THESIS FOR DOCTOR OF PHILOSOPHY

PROGRESSIVE BUCKLING OF LARGE-DIAMETER MONOPILES DUE TO BOULDER COLLISION DURING INSTALLATION

BOHAN CHEN

Wolfson College, University of Oxford

Department of Engineering Science – Renewable Energy Marine Structures



Supervisors:

Prof Byron Byrne

Prof Chris Martin

Hilary Term 2024

ABSTRACT

PROGRESSIVE BUCKLING OF LARGE-DIAMETER MONOPILES DUE TO BOULDER COLLISION DURING INSTALLATION

This research aims for an improved description of the progressive buckling phenomena of large-diameter monopiles due to boulder collision during the installation progress. This description contributes to a more reliable predictions of the possibility and the severity of progressive buckling *in situ* during the design process. This improved description benefits from establishing a calculation approach that leads to reliable 3D simulations of progressive buckling, given 2D benchmark models.

Adopting the numerical technique, Coupled Eulerian-Lagrangian (CEL) method, the deliverables are generated from three stages of research. The first stage contains parametric studies based on 2D plane-strain plate installation models exploring variation of material properties, installation conditions, boulder shapes, and tip geometries. It is found that the boulder size was most influential to the tip deflections, followed by the boulder embedment and the soil strength.

Laboratory-scale physical modelling is then introduced during the second stage to ensure validation of the 2D models. Soil movements during plate installation are revealed using Particle Image Velocimetry (PIV) analysis. Together, these two stages provide confidence in the use of numerical methods for 3D geometries.

The third stage explored truncated 3D simulations, reducing the problem to a quarter section of the pile, and examining the impact of the ratio between the pile diameter and the pile wall thickness. These 3D models build links between the 2D benchmarks and 3D simulations, to complete the calculation approach for reliable simulation of the progressive buckling phenomena of monopiles during installation. The numerical results allow safety envelopes to be established with respect to the boulder diameter, the contact eccentricity, the boulder depth, and the relative strength between the pile and the soil. These envelopes provided a quick evaluation of whether the tip deflection would happen with corresponding parameters.

ACKNOWLEDGEMENT

As I reflect on the journey that has led to the completion of this thesis, it is truly surprising to see how far I have come. I would like to express my sincere gratitude to all those who have supported and guided me throughout the process of completing this thesis.

First, I would like to express my heartfelt appreciation to my supervisors, Prof Byron Byrne and Prof Christopher Martin. Thank them for their generous support in conveying the knowledge. Their invaluable encouragement and inspiration illuminated the path of my work. Without them, this thesis would not have been possible.

I would also like to thank Prof. Orestis Adamidis, Prof Harvey Burd, and Prof Guy Houlsby for their diligent review and insightful suggestions of my work during the examinations of Transfer and Confirmation of Status. Their expertise and feedback significantly contributed to the refinement of my work.

My gratitude also goes to Dr Miad Saberi and Dr Stephen Suryasentana, for their valuable guidance on numerical simulation at the commencement of my work. The experimental phase started amidst the challenges of the Covid-19 pandemic and finished when mask-wearing became less of a concern. Thank Dr Zhenghui Qiu, Dr Geyang Song, and Dr Kunwei Wu for their generous support during this challenging period. Thanks also go to Mr. Clive Baker, for his great tolerance after seeing my red clay spreading all over the laboratory.

Furthermore, thank Dr Iona Richards, Dr Toby Balaam, and Mr Sanjeev Malhotra for their valuable advice on career development. My gratitude also goes to my friends in the department and Wolfson College, including Dr Sarah Martin, Dr Jingyi Yang, Ms Xiaotian Yu, Dr Luc Simonin, and Dr Yiu Siu for their unreserved kindness over the years.

I extend my deepest thanks to my parents for nurturing my personality and being exemplary role models as engineers. Thank my siblings for their, albeit sometimes annoying, yet mostly joyful companionship throughout my growth. Additionally, I appreciate my grandparents for their unwavering support and unbreakable confidence in me. Finally, thank my little parrot, Lujia, for keeping me company throughout the thesis writing process.

TABLE OF CONTENTS

Chapter 1 Introduction 1
1.1 Renewable Energy and Offshore Wind 1
1.2 Offshore wind structures and foundations 4
1.3 Monopiles and monopile installations 7
1.4 Tip distortions and historical cases 9
1.5 Offshore soil conditions in the UK 14
1.6 Research problem definition 16
1.7 Overall methodology and thesis outline 17
Chapter 2 Literature Review 20
2.1 Monopile design codes for tip distortion 20
2.1.1 API RP2A (API, 2014) 20
2.1.2 DNV-ST-0126 (DNV, 2016) 21
2.1.3 EN 1993-1-6 (2007) 22
2.1.4 ISO 19902 (ISO, 2020) 24
2.1.5 NORSOK N-004 (Norsok, 2012) 24
2.1.6 DNV-RP-C202 (DNV, 2019) 25
2.1.7 Summary and comparison of design codes 26
2.2 The current state of research 27
2.2.1 Progressive buckling in structural engineering 28
2.2.2 Tip buckling of pile in geotechnical engineering 30
2.3 Gaps between the practice and research 54
Chapter 3 Two-Dimensional Plate Penetration 57
3.1 Coupled Eulerian-Lagrangian method 57
3.2 Benchmark models for plane-strain models 59
3.2.1 Strip footing penetration model 59

3.2.2 Square boulder rotation model 63
3.3 Plate penetration model 67
3.3.1 Model description 67
3.3.2 Element selection 70
3.3.3 Penetration speed 76
3.3.4 Soil weight 79
3.4 Parametric studies of independent factors 83
3.4.1 Effect of boulder dimension 85
3.4.2 Effect of contact eccentricity 88
3.4.3 Effect of boulder embedment depth 90
3.4.4 Effects of relative stiffness 91
3.4.5 Effect of relative strength 93
3.4.6 Parameter sensitivity analysis 96
3.4.7 Coupling effects 97
3.4.8 Effect of boulder shape 100
3.4.9 Effect of chamfer geometry 106
3.5 Concluding remarks 108
Chapter 4 Laboratory-Scale Physical Modelling 110
4.1 Apparatus setup 111
4.1.1 Calibration chamber 111
4.1.2 Loading and measurement devices 112
4.1.3 Data acquisition and processing 113
4.1.4 Accessories: lateral supports and edge wrapping 114
4.2 Components and material properties 116
4.2.1 Plate 116
4.2.2 Boulder 119
4.3 Particle image velocimetry analysis setup 120

4.3.1 Resolution requirements and digital equipment 121
4.3.2 Image quality control 122
4.3.3 Control point and coordinate calibration 124
4.4 Preliminary testing in sands 127
4.4.1 Preparation of soil samples 127
4.4.2 Camera setup 128
4.4.3 Preliminary results 130
4.5 Clay testing 134
4.5.1 Artificial texture setup 134
4.5.2 Preparation of soil samples 135
4.6 Numerical model refinements 139
4.6.1 Initial component positions in physical models 139
4.6.2 Interfacial contacts 141
4.6.3 Reduction of computing cost 144
4.6.4 Mitigation of oscillations 148
4.6.5 Effects of refinements 152
4.7 Result comparison 154
4.8 Soil function analysis 161
4.9 Concluding remarks 163
Chapter 5 Three-Dimensional Pile Penetration 166
5.1 Introduction of truncated 3D simulation 166
5.1.1 Model geometry 166
5.1.2 Material properties 167
5.1.3 Boundary conditions and motion control 168
5.2 Viability of truncated model 169
5.3 Model construction 171
5.3.1 Eulerian domain and soil generation 171

5.3.2 Pile and pile sleeve generation 175
5.3.3 Boulder generation 176
5.3.4 Surface definitions and reference points 179
5.3.5 Calculations of effective volume fraction 181
5.4 Investigation of model robustness 182
5.4.1 Mesh sensitivities 183
5.4.2 Contact properties 187
5.4.3 Mass scaling 188
5.5 3D parametric study 189
5.5.1 Effect of D/t ratio 190
5.5.2 Effect of contact eccentricity 195
5.5.3 Effect of boulder depth 198
5.6 Connection between 2D and 3D simulations 201
5.6.1 Connection establishment 201
5.6.2 Tip deflection generalisation 206
5.7 Concluding remarks 211
Chapter 6 Conclusion 214
6.1 Objectives and outcomes 214
6.2 Chapter summaries and contributions 216
6.3 Limitations and future work 221
References 224

CHAPTER 1 INTRODUCTION

1.1 RENEWABLE ENERGY AND OFFSHORE WIND

The *Paris Agreement* released in 2015 aimed at limiting the global average temperature increase to 2℃ higher than pre-industrial levels (United Nations, 2015). To meet such a target necessitates a transition from conventional fuel energy to renewable sources.

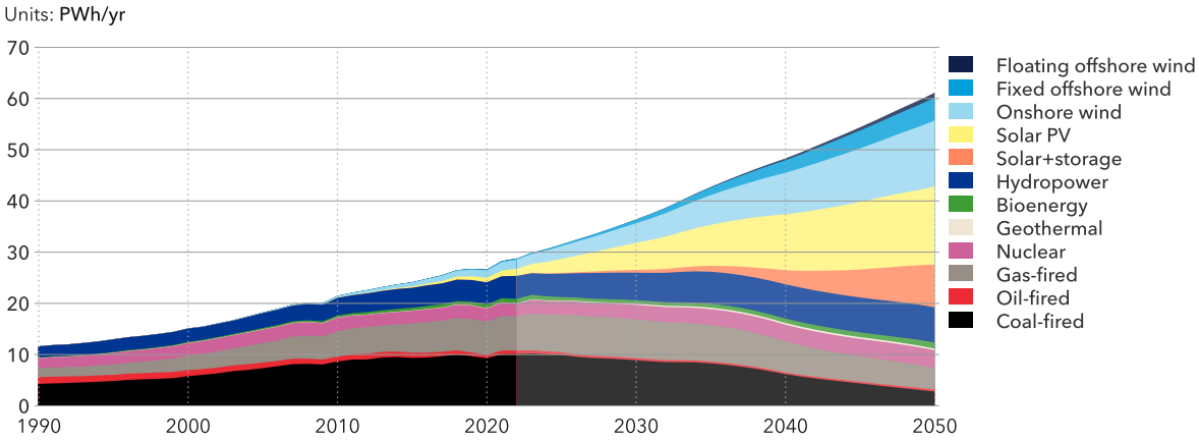


Figure 1-1 World grid-connected electricity generation by power station type (DNV, 2023)

Figure 1-1 shows the evolution in global energy sources from 1990 to 2022, with the forecast extending through 2050 (DNV, 2023b). It is anticipated that 30% of the power supply will be wind-generated, with around 21% from onshore, and 9% from offshore turbines. With the goal

to achieve net-zero emissions, a *UN Energy Compact* was signed in 2021 by GWEC (Global Wind Energy Council) and IRENA (International Renewable Energy Association), targeting a total deployable offshore wind energy of 2,000 GW by 2050 (GWEC, 2023a). This target entails an average new offshore wind installation of 35 GW annually until 2030, increasing to 70 GW annually between 2030 and 2050 (GWEC, 2023b). This trajectory is evaluated based on the current global installation of around 60 GW (GWEC, 2023a). Figure 1-2 shows the anticipated annual installation of offshore winds with the Compound Annual Growth Rate (CAGR), indicating high growth (CAGR > 31%) over the next five years until 2027.

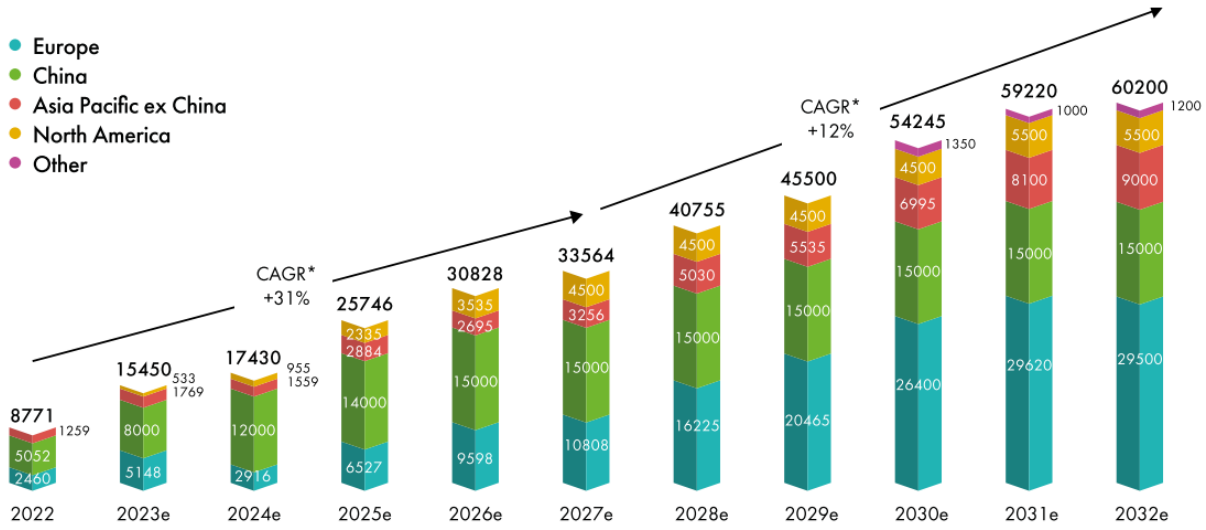


Figure 1-2 Global new offshore wind installations in MW (GWEC, 2023a)

Numerous regions and countries have proposed corresponding policies and investments to attain the zero-emission objective. The UK, for example, is aiming to elevate their installed capacity for offshore wind generation to 40 GW by 2030, resulting in an overall wind capacity of 50 GW (DESNZ, 2023)[1]. Floating wind would likely contribute 1 GW of the overall anticipated capacity and fixed facilities would contribute the remainder (The Crown Estate, 2023). By the end of 2022, the UK had achieved 28% of this goal (The Crown Estate, 2023).

[1] DESNZ: Department for Energy Security and Net Zero, UK Government.

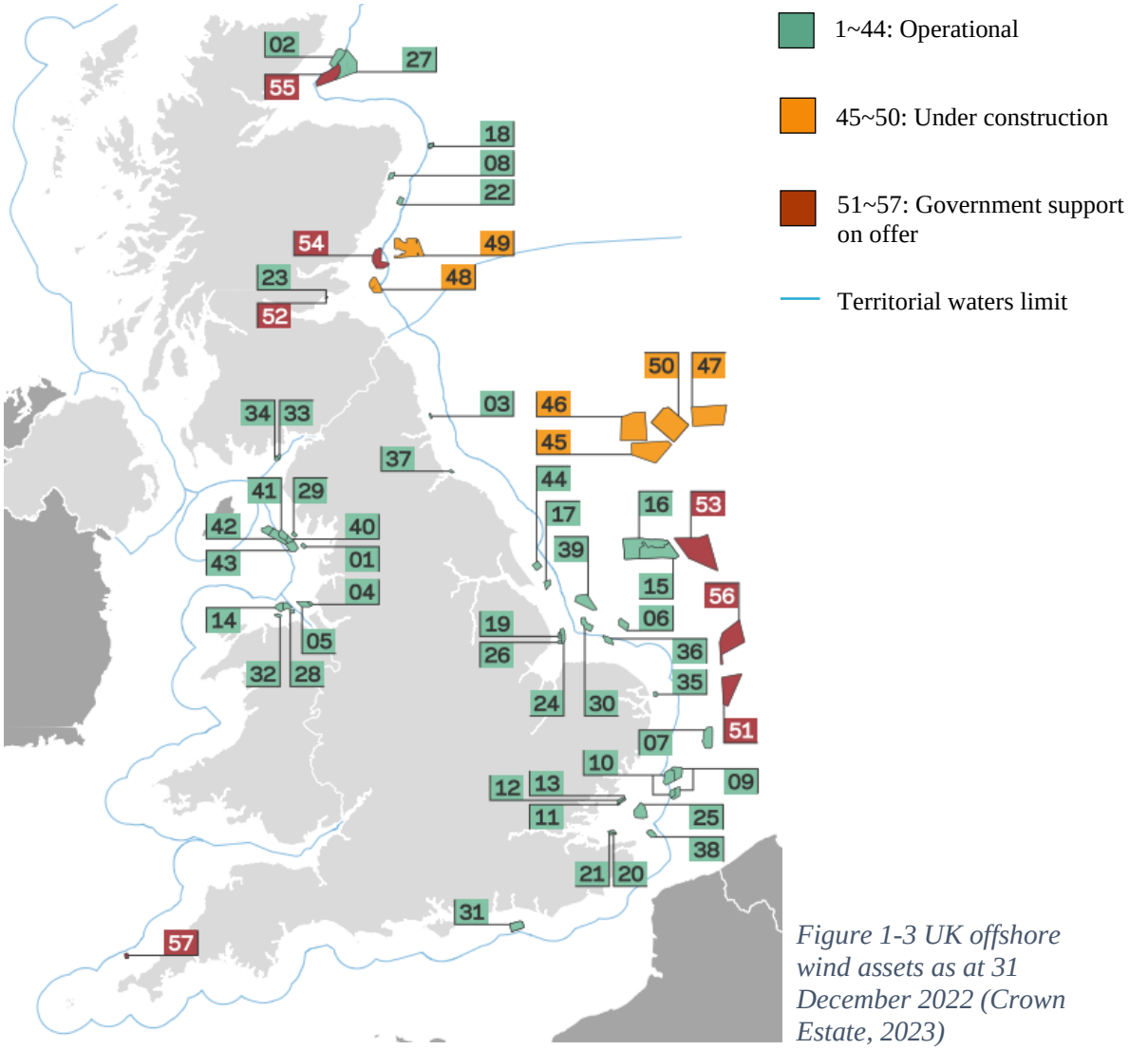


Figure 1-3 UK offshore wind assets as at 31 December 2022 (Crown Estate, 2023)

Figure 1-3 shows a map of the UK offshore wind assets, recorded by the end of 2022, where 44 wind farms were fully commissioned, containing a total number of 2652 turbines (The Crown Estate, 2023). These wind farms generated 24% of global offshore wind capacity and contributed 14% of the total UK electricity (around 45 TWh), supporting 41% of UK homes (The Crown Estate, 2023). Since the world's largest offshore wind farm, Hornsea 2 (No. 16 in Figure 1-3), entered operation, the average size of UK offshore wind farms increased to 1.1 GW, with an average individual turbine size of 9 MW (The Crown Estate, 2023).

As suggested by Figure 1-4, the current size of European wind turbines is typically in the range of 7 ~ 9 MW (Rystad Energy, 2023). However, this range is predicted to increase to 18 ~ 20 MW by 2030, with an average of 15 MW (Rystad Energy, 2023). This size increase could be driven by cost reductions (Rystad Energy, 2023), but represents a challenge for the design of supporting structures, especially foundations.

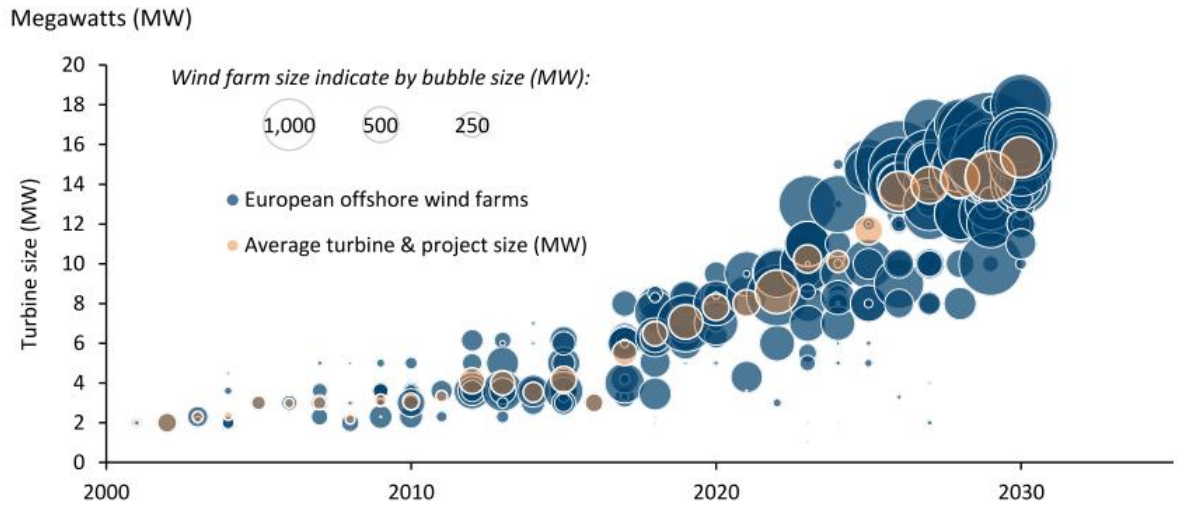


Figure 1-4 European offshore wind farms by start-up year, turbine size, and capacity (Rystad Energy, 2023)

1.2 OFFSHORE WIND STRUCTURES AND FOUNDATIONS

A wind turbine has four primary components: the rotor, the nacelle, the tower, and the foundation (Li *et al.*, 2022). The global average tower height recorded in 2022 was 116.6 m, with an average rotor diameter of 174.6 m (U.S. Department of Energy, 2023). This means that the average total height of the turbine was around 203.9 m. As turbine capacities increase, total heights of up to 300 m can be envisaged in the near future (OWIC, 2019).

The rotor plays an important role in electricity generation, however, the turbine foundation is the most expensive component, contributing around 35% of the total installation cost of a turbine (Byrne and Houlsby, 2015). As turbines become larger, there will be an escalating

demand for improved foundation design, especially in terms of the foundation stiffness and capacity, the installation procedure, and the cost efficiency.

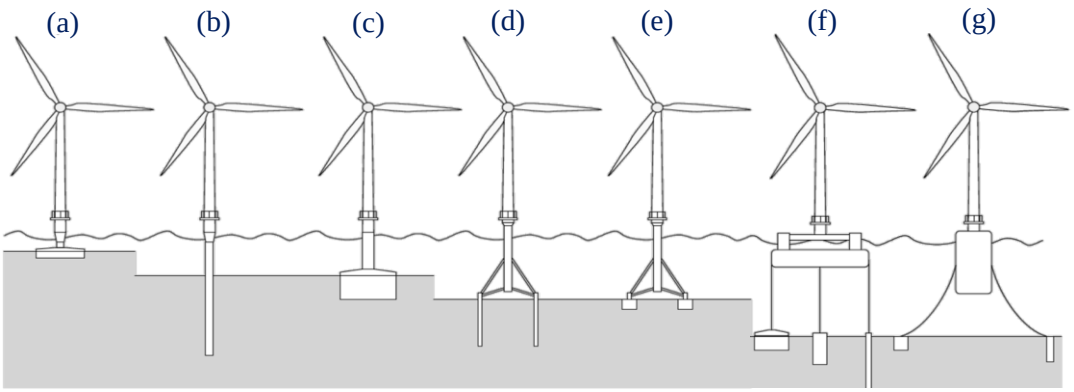


Figure 1-5 Offshore turbine foundation types (after Byrne, 2011)

(a) Gravity base; (b) Monopile; (c) Mono-caisson; (d) Multi-pile; (e) Multi-caisson; (f) Tension-leg platform; (g)Spar

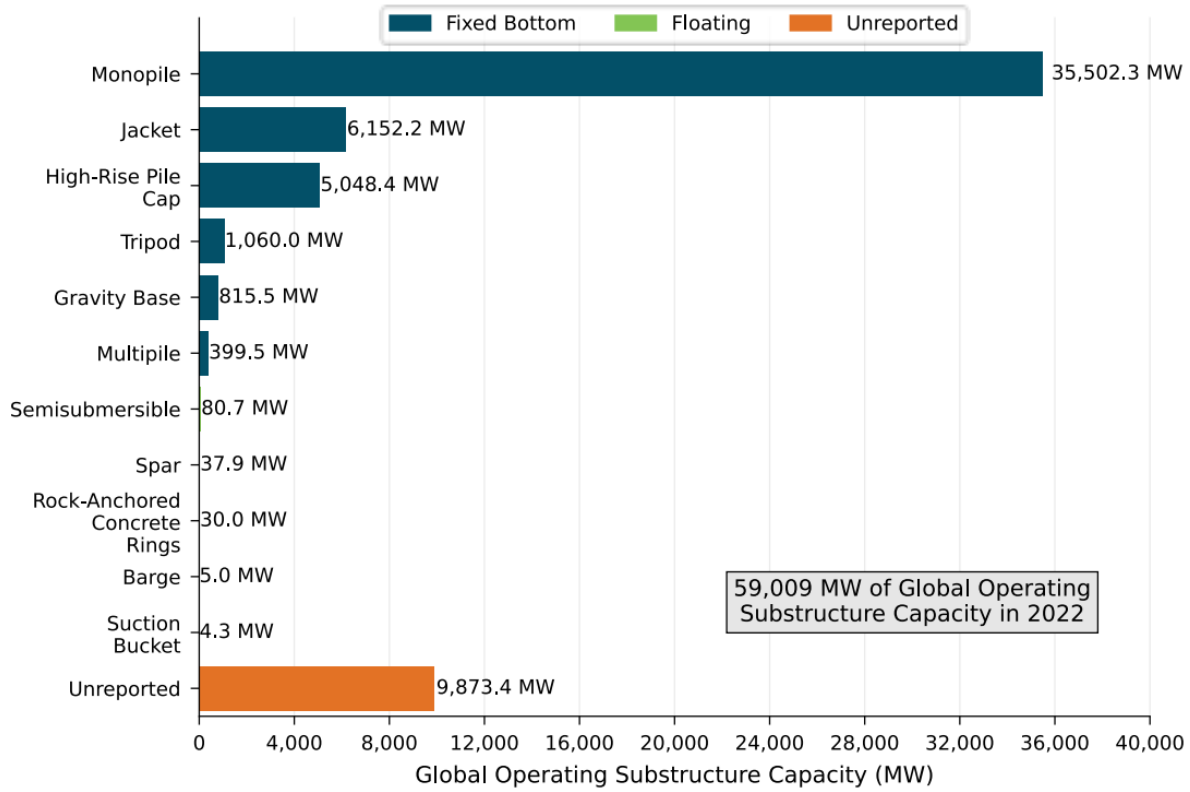


Figure 1-6 Global offshore wind turbine foundations used in operating projects (U.S. Department of Energy, 2023)

As shown in Figure 1-5, various foundation types are adopted to cope with different soil conditions and water depths (Byrne, 2011). Fixed foundations, Figure 1-5 (a) to (e), are

applicable in shallow-sea areas where the water depth is typically less than 50 m, while floating foundations, Figure 1-5 (f) to (g), are preferable for deeper water. Innovative foundation types, such as helical piles (Byrne & Houlsby, 2015), might also be used to reduce installation noise.

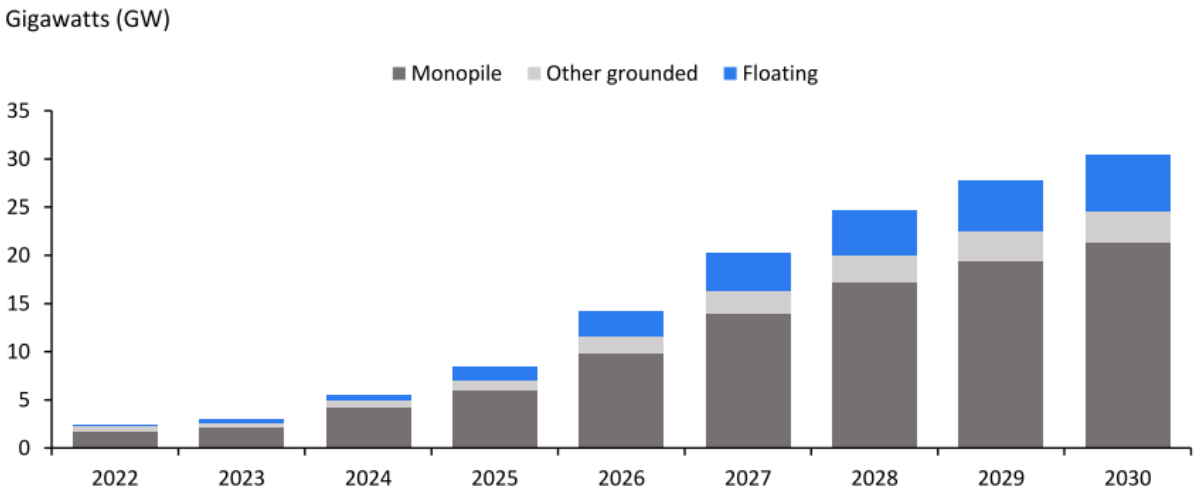


Figure 1-7 Predictions of European offshore wind capacity additions by foundation type (Rystad Energy, 2023)

For turbines installed to date, monopiles have outnumbered the other foundation types. The monopile foundation for an offshore turbine usually consists of a single open-ended steel tube. Figure 1-6 shows the foundations for operating offshore wind farms on a global scale in 2022, where 60% of capacity was generated by monopile-supported turbines (U.S. Department of Energy, 2023). According to Wind Europe (2021), monopiles accounted for 81.2% of installed turbine foundations by the end of 2020. In the first half of 2023, 235 out of 360 (65.3%) turbines that were newly connected to the grid were founded on monopiles (Wind Europe, 2023). The Rystad Energy (2023) forecast, as shown in Figure 1-7, suggests that the monopile will remain the dominant option for future offshore wind turbines until 2030, despite an increasing percentage of floating turbines. The prevalence of monopiles in the current wind industry can be attributed to their manufacturing and installation processes, which are comparatively simpler and more cost-efficient than those of the other foundation types. In Europe, the shallow

water depth and strong soil in the North Sea make monopiles most suitable (RenewableUK, 2016).

1.3 MONOPILES AND MONOPILE INSTALLATIONS

A monopile classification based on the pile diameter, D [m], and the turbine capacity is shown in Table 1-1. The majority of monopiles in 2022 were in the categories of "Regular and XL", with 5 m < D < 8 m, while larger piles in the categories "XXL and XXXL", with D > 8 m will be demanded by the future offshore wind industry (Rystad Energy, 2023). A comparison between the predicted monopile demand and the announced capacity by the manufacturers is shown in Figure 1-8. The manufacturing capacity is affected by various factors, such as the supply chain of the raw material and, more importantly, the techniques of producing thick steel plates for offshore use (GWEC, 2023a).

Table 1-1 Monopile classification (Rystad Energy, 2023)

Class	Typical diameter [m]	Typical turbine capacity supported
Regular	5 ~ 6	< 6 MW
XL	6 ~ 8	6 ~ 10 MW
XXL	8 ~ 11	10 ~ 14 MW
XXXL	> 11	> 14 MW

The normal thickness of manufactured steel plate is in the range of 10 mm to 60 mm for general use (GWEC, 2023a), however, the monopile wall thickness is typically 40 mm to 150 mm (Anandavijayan *et al.*, 2018). Therefore, most steel plates for offshore monopiles are beyond the common capacity of typical steel manufacturers to produce (GWEC, 2023a). The production of the steel plates could be limited by the supply chain of the original materials, which is affected by the regional policies of the source (GWEC, 2023a). The thick wall, in addition, also brings challenges for the monopile installation process.

In practice, prefabricated monopiles are transported to their proposed installation position via a barge. Either a jack-up vessel or a heavy lift vessel is then used to lift the monopile to an upright position (BOEM, 2020; Jiang, 2021). After manoeuvring to the designated location, the pile will gradually sink into the seabed under its own weight. Further penetration is typically achieved using a hydraulic pile-driving hammer, aided by pile-handling devices to facilitate pile positioning (Jiang, 2021). Vibratory installation is also a promising alternative, particularly due to its potential for noise reduction. However, a thorough study of its offshore application is still necessary (Holeyman *et al.*, 2020).

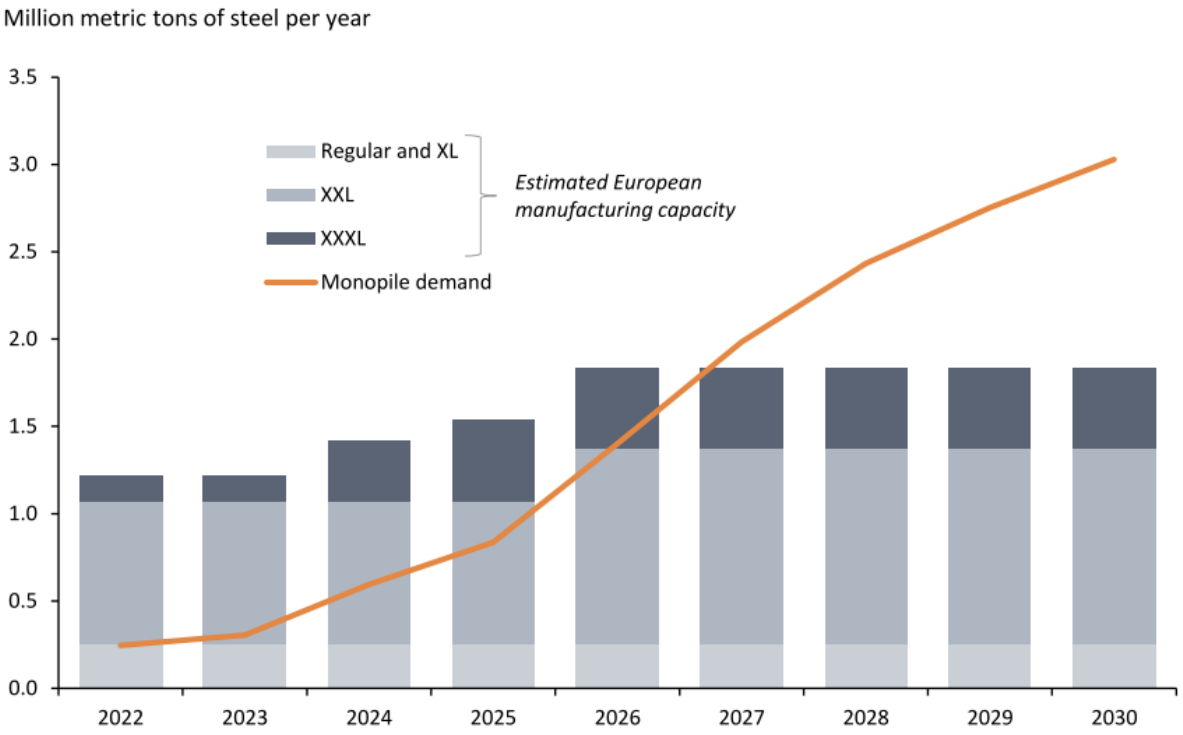


Figure 1-8 Monopile manufacturing capacity and demand in Europe (Rystad Energy, 2023)

During installation, it is crucial to ensure that the monopile inclination falls within an acceptable range. Excessive lateral stress at the pile tip due to inclination could result in significant distortion, and eventually lead to premature refusal of the pile. A pile which fails to reach the designated target depth may not provide adequate support to the upper structure.

1.4 TIP DISTORTIONS AND HISTORICAL CASES

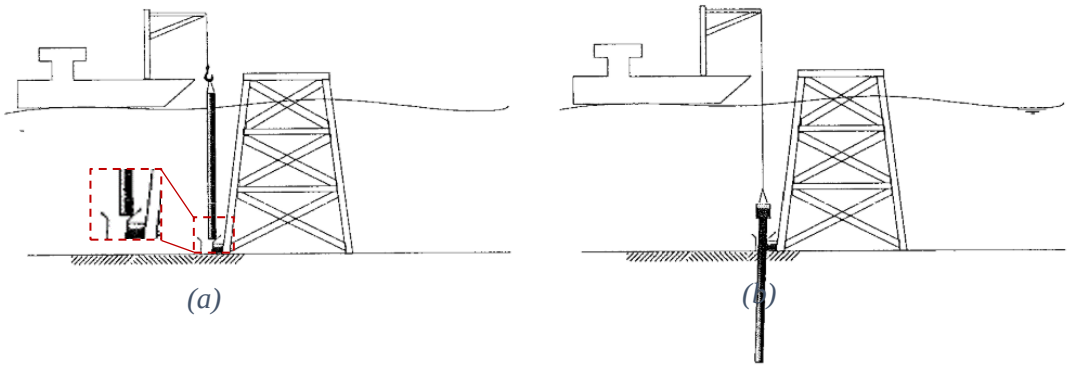
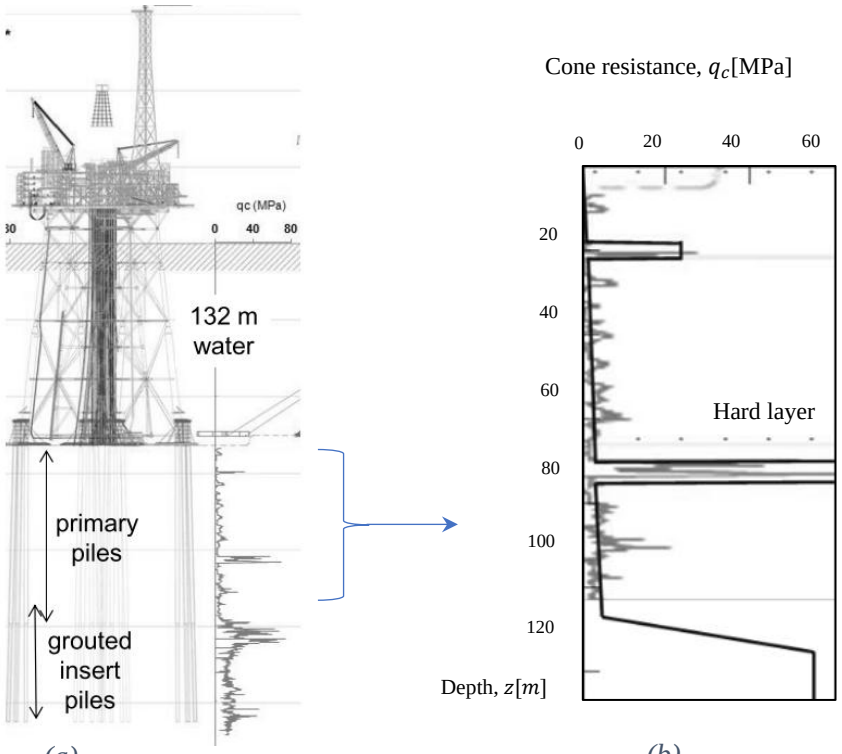


Figure 1-9 Pile installation for Goodwyn-A (after Kramer, 1996)
(a) Contact moment between primary pile and pile sleeve; (b) Penetration of primary pile

Tip distortion was discovered among a group of piles during the construction process of the Goodwyn-A platform in Australia (Kramer, 1996). The Goodwyn-A piles had two sections: the primary piles and the inserted piles. The primary piles were first driven into the ground through a pile sleeve, as shown in Figure 1-9. The soil plugs within the piles were then removed to create cavities for the inserted piles. During the soil removal, however, 15 out of 20 primary piles were found to be distorted, with the circular annulus at the tip deformed into peanut shapes, making the installation of the inserted piles impossible (Erbrich *et al.*, 2011; Kramer, 1996). Further studies showed that this buckling likely developed from a small dent caused by the collision of the pile tip and the pile sleeve during the process shown in the inset of Figure 1-9 (a). The primary pile was 133 m in length (L [m]), with a diameter (D [m]) of 2.65 m and a pile wall thickness (t [m]) of 0.045 m, which gives $L/D = 50$ and $D/t = 58.9$ (Kramer, 1996). The platform profile and the piles are shown in Figure 1-10 (a). The distortion was evident from a depth of 80 m below the seabed, following penetration through a hard layer of calcareous silt and sands. This layer was of 3 to 5 m thick, with a cone resistance, q_c [MPa], of up to 60 MPa, as shown in Figure 1-10 (b) (Randolph, 2018). This hard layer exacerbated the

small dent caused by the collision. The small dent then propagated throughout the pile length, resulting in the premature refusal of the pile (Kramer, 1996).



(a) *(b)*

Figure 1-10 Soil profile under Goodwyn-A platform (after Randolph, 2018)
(a) Profile of platform and piles; (b) Soil profile from CPT test

Another example of progressive buckling was found in a demolition project called Amazonhaven in Rotterdam. As shown in Figure 1-11, the piles were extracted from the ground and found to be buckled at the tip. These piles, with a diameter-to-wall-thickness ratio (D/t) of 1420 mm/17 mm = 83.5, had been supporting an inclined combi-wall for over 20 years before the demolition in 2010 (Mourillon, 2015), with the buckling issue undetected. Closer investigations suggested three possible reasons leading to tip buckling: 1) loss of steel strength due to temperature increase during installation; 2) an increase of soil effective stress due to an installation halt for hammer shifting; 3) propagation of small dents induced by the inclination during installation (Broos *et al.*, 2017).



Figure 1-11 Tip buckling of piles extracted from Rotterdam basin (after Broos et al., 2017)

Case studies of tip distortion found three primary causes (Randolph, 2018):

1) Collision with heterogeneities in soil, such as boulders or hard layers,
2) Highly differential internal and external soil pressure,
3) Propagation of an initial imperfection due to either manufacturing or transportation.

Figure 1-12 gives an illustration of the geometry of progressive distortion and the causes. Considering that the soil plugging is unlikely to happen for offshore monopiles with large diameters, the uneven pressure (Cause 2) could be induced by the abnormal pile geometry resulting from either heterogeneity collision (Cause 1) or manufacturing imperfections (Cause 3). The kinematic mechanism of further development of the imperfection can be seen in Figure 1-13 (a).

Figure 1-13 (a) shows the loading condition of the deformed pile section as it penetrates into a deeper soil layer. After ovalisation, the external pile wall experiences excessive pressure perpendicular to the minor axis of the pile section. This, together with the excessive pressure

on the inner side that is perpendicular to the major axis, further exaggerates the ovalisation of the pile. Described as a "*feedback loop*" by Randolph (2018), this mechanism triggers the distortion of subsequent pile sections as penetration proceeds. Eventually, it results in the progressive distortion of the entire pile. The pile chamfer could also result in uneven pressure. As shown in Figure 1-13 (b), the soil pressure perpendicular to the chamfered face could lift the pile tip and thus result in progressive distortion. This failure was found in the Valhall platform in the North Sea, where five out of eight piles reached premature refusal after the chamfered pile tip penetrated through a layer of very dense sand (Alm *et al*., 2004).

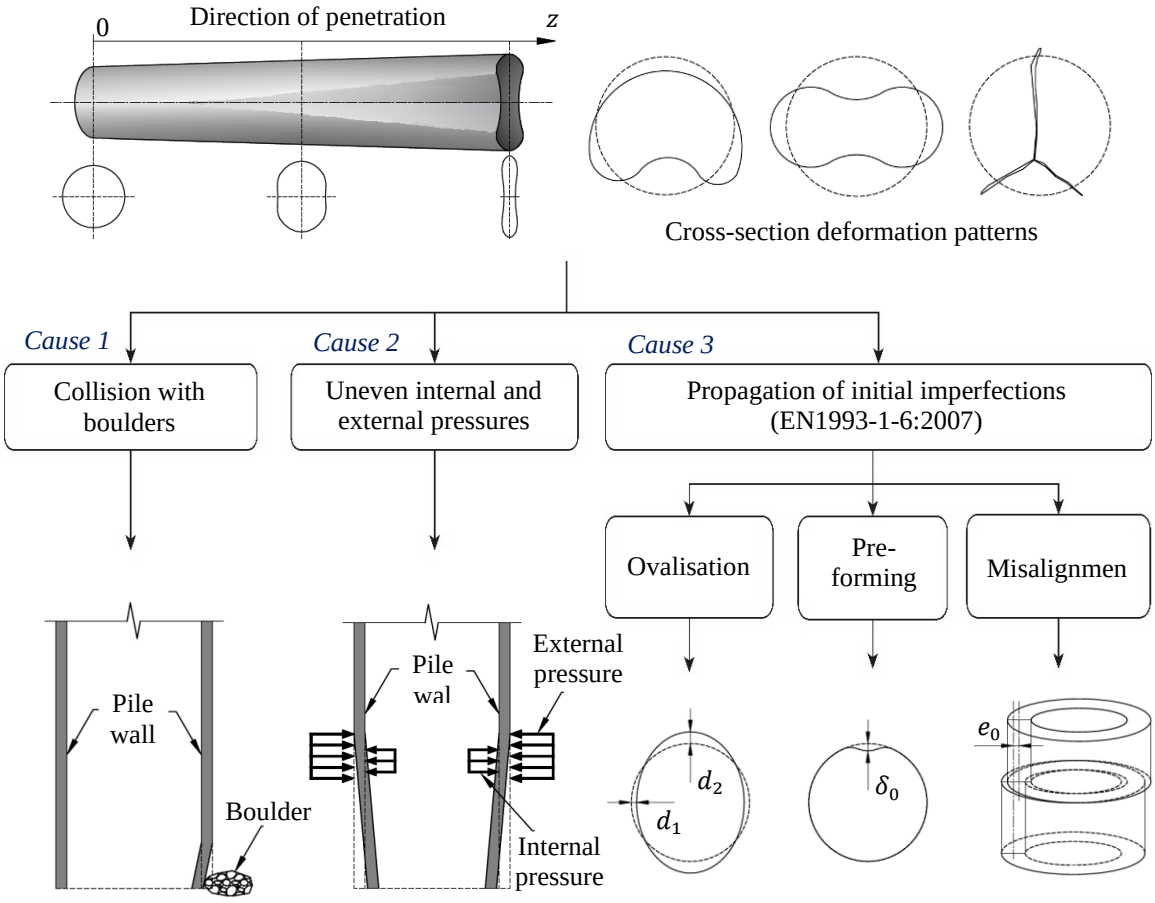


Figure 1-12 Geometries and mechanisms of progressive buckling

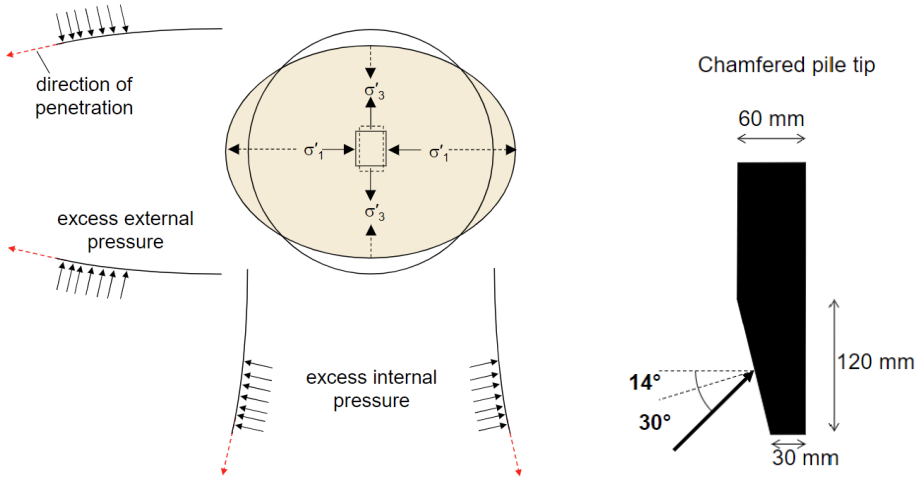


Figure 1-13 The mechanism of progressive distortion and the chamfer effect (Randolph. 2018) (a) The kinematic mechanism of pile cross-section ovalisation; (b) Chamfer effects

To mitigate the risk of buckling due to initial imperfections, API Specification 2B gives manufacturing tolerance regarding three major imperfections (API, 2002): ovalisation, pre-forming, and misalignment, as illustrated in Figure 1-12. A similar but perhaps less predictable cause of tip distortion, by comparison with geometrical imperfections induced by manufacturing and transportation, is boulder collision (Cause 1).

In this situation, a small imperfection could form at the pile tip, following an interaction with a buried boulder, with the imperfection then propagating along the entire pile length. This problem is more likely when piles are driven through glacial tills, where boulders buried within the soil could be sufficiently large to distort the pile. As offshore wind turbine sizes continue to increase, monopiles with ever-larger diameters are being employed. However, such an increase in size also makes the monopiles more vulnerable to this type of buckling failure. While using thicker pile walls is a possible solution, the high costs of foundation manufacturing and installation mean that optimising the pile wall thickness is important. With the aim of producing a reliable calculation approach for such a problem, the scope of this research, including the applicable soil conditions and pile geometry, is introduced.

1.5 OFFSHORE SOIL CONDITIONS IN THE UK

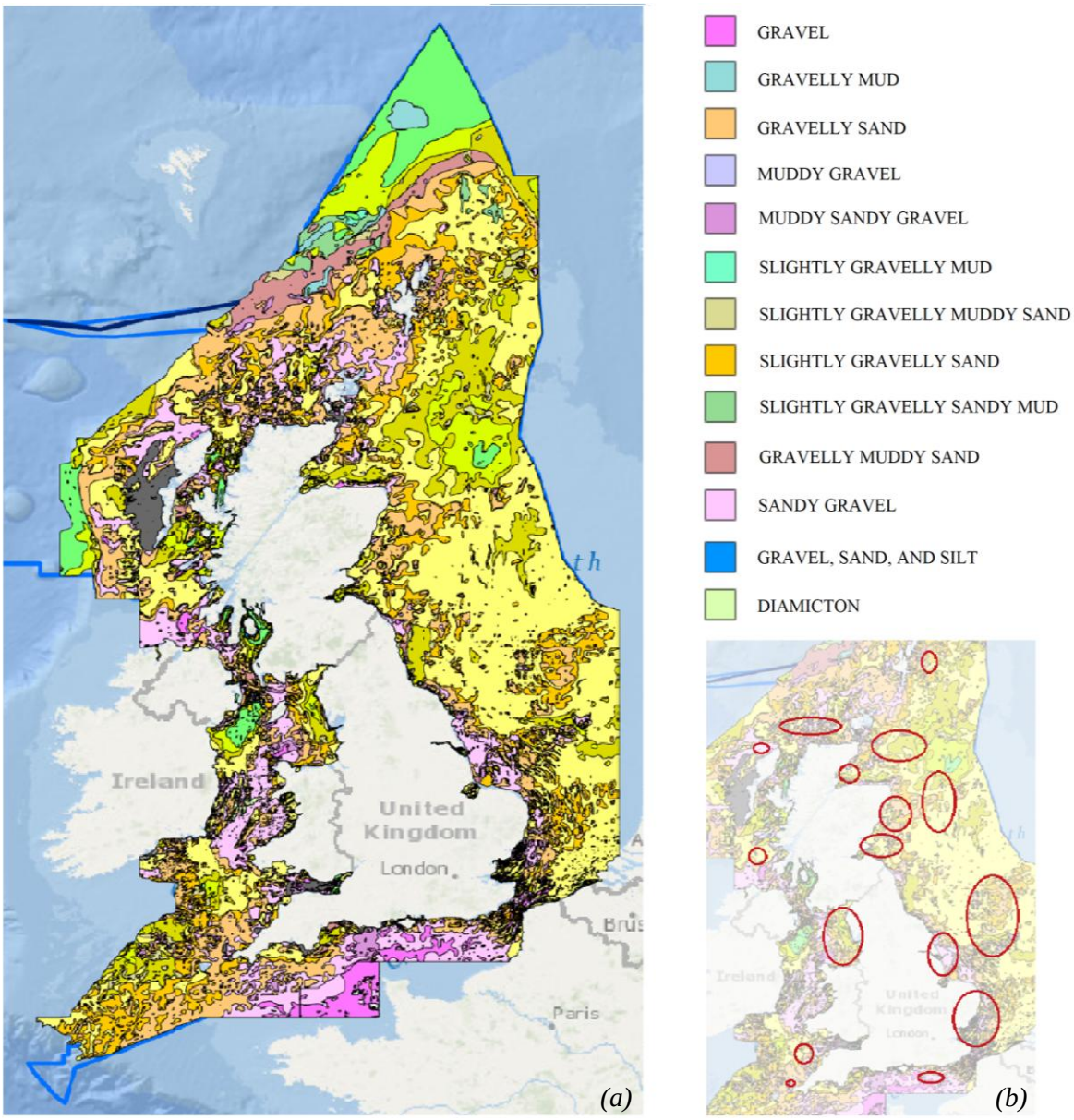


Figure 1-14 Offshore soil conditions and distribution of OWT within UK EEZ Limit
(a) Distribution of gravelly soils (after BGS, 2022); (b) Distribution of OWT in operation, in construction, or pre-construction by 2023 (after RenewableUK, 2022)

The interaction between piles and boulders could be a common scenario encountered in offshore wind farm construction. Figure 1-14 (a) presents the distribution of Holocene submarine sediments within the Exclusive Economic Zone (EEZ) of the UK (BGS, 2022), categorised using the Folk Classification (Folk, 1959). To produce a clear view, only the

legends of the gravelly soils are kept in the figure. These gravelly soils are primarily distributed around the North Sea, the Irish Sea, and the English Channel. Figure 1-14 (b) presents the distribution of OWTs in the UK by 2023 (according to RenewableUK (2022)), showing those which overlap with gravelly soil areas.

The gravelly soil tends to provide challenges for pile penetration, where the heterogeneities within the soil could cause the initial dent at the pile tip. Boulder clay, or glacial till, could be even more problematic than gravelly soils. Figure 1-15 presents the properties of the glacial till collected by Clarke (2018) from north-eastern England, which reveals the typical features of glacial till – high undrained shear strength with significant over-consolidation. The scatter among these data, in addition, could be attributed to the complex composition of the soil, as a result of its deposition and consolidation mechanisms.

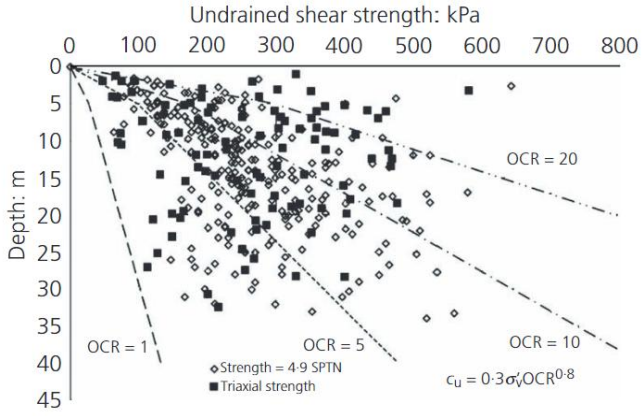


Figure 1-15 Undrained shear strength and over consolidated ratio (OCR) of glacial till samples in north-eastern England (Clarke, 2018)

Four primary mechanisms of glacial sedimentation, summarised by Benn & Evans (2010), include lodgement, friction retardation, melt-out, and gravity. These sediments were usually formed in different locations before they were transported by the glacier (Clarke, 2018). A broadly accepted definition refers to the glacial till as "*sediment that has been transported and deposited by or from glacial ice, with little or no sorting by water*" (Benn & Evans, 2010;

Dreimanis, 1989). This definition indicates that the glacial till could contain soils from all four soil categories in the engineering classification standards: very coarse-grained, coarse-grained, fine-grained, and organic soils (Clarke, 2018).

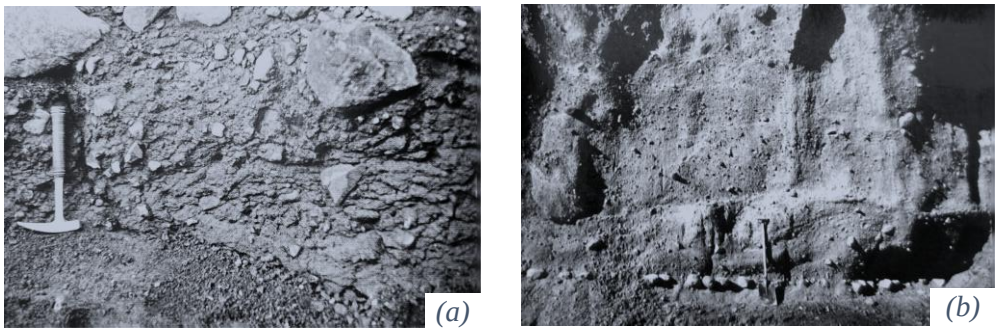


Figure 1-16 Glacial tills (Benn and Evans, 2010)
(a) Matrix-supported diamiction; (b) Boulder pavement

Figure 1-16 (a) shows a representative example of the subglacial till with stratified textures and scattered boulders, while an example of more clustered boulders, named boulder pavement, is given in Figure 1-16 (b). Boyce & Eyles (2000) suggested that the boulder pavement represented an interface between the historic glaciers and associated subglacial till. Other explanations for the boulder pavement, such as boulder sinking and excavational deformation, were summarised by Benn and Evans (2010, sec. 10.3.4). The uncertainties around its formation mechanism indicate that the interaction between the boulder and the surrounding soil requires consideration. The interaction between multiple boulders within a soil matrix could also be worth investigating but is beyond the scope of this research due to its complexity.

1.6 RESEARCH PROBLEM DEFINITION

This research aims to develop an improved description of the progressive buckling phenomena of large-diameter monopiles due to boulder collision during installation. The description intends to improve the understanding of the two aspects:

1) The sensitivity of the influencing factors, including the material properties, installation conditions, and structure geometries,
2) The deforming procedure as the pile penetrates into the soil, after boulder collision.

This description will contribute to more reliable predictions of the possibility during the design process, as well as the severity of progressive buckling in situ. This improved description includes the establishment of a calculation approach that leads to reliable 3D simulations of progressive buckling, given 2D benchmark models. The outcomes of this research also apply to other large-diameter cylindrical shell structures used in geotechnical engineering, such as suction caissons.

1.7 Overall methodology and thesis outline

For the research, the properties of glacial till were simplified to be homogeneous stiff clay with a floating boulder. The pile dimensions covered by this research were in alignment with the larger sizes used in current industrial practice, as well as those forecast to be relevant in the future.

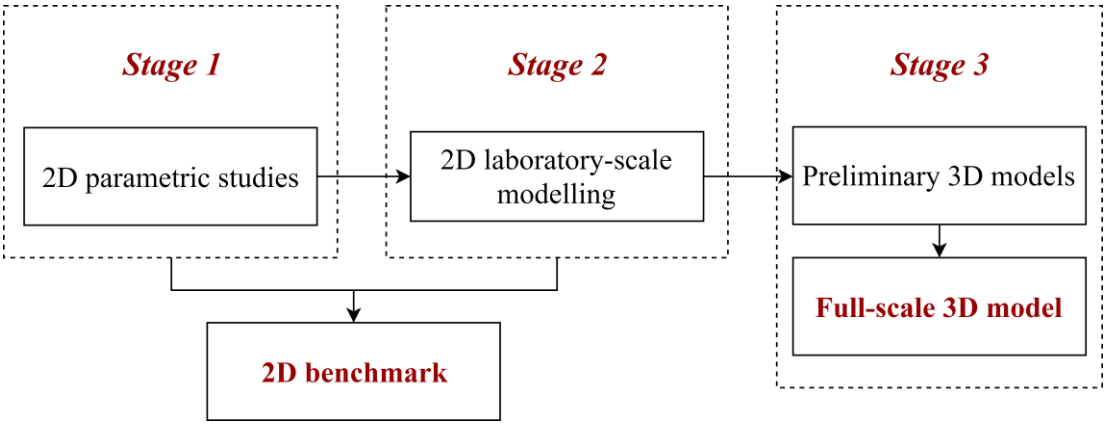


Figure 1-17 Research framework

Built upon the numerical technique, Coupled Eulerian-Lagrangian (CEL) method, the deliverables are generated from three stages of research, as illustrated in Figure 1-17, each comprising one chapter from Chapter 3 to Chapter 5. The objectives of each stage (or chapter) and the corresponding methodologies are listed as follows:

Chapter 3: The first stage contained parametric studies based on 2D plate installation models in relation to the material properties, installation conditions, and structure geometries. Piecewise equations were derived from the simulation results as numeric fits, providing the relationship between the tip deflection and the corresponding parameters. A sensitivity index was also established to quantify the parameter sensitivity. This stage enhances the understanding of the progressive buckling of monopiles by identifying the worst conditions that may arise in situ.

Chapter 4[2]*:* To validate the numerical simulations in stage 1 (Chapter 3), laboratory-scale physical modelling is introduced in the second stage. During this stage, each experiment was simulated using the numerical techniques in stage 1. The reaction forces and tip trajectories of the plate were extracted from the experiments and compared with their numerical counterparts, serving as a reference for calibrating the numerical techniques. Soil movements during plate installation were monitored using Particle Image Velocimetry (PIV) analysis and also compared with the numerical models qualitatively. The function of the soil in the process of progress buckling was also investigated. After calibration, the consistency of the results from these two stages provides confidence in the chosen numerical methods for application to the 3D geometries in the third stage.

[2] The content of this chapter was published as a conference paper: Chen, B., Byrne, BW., Martin, CM. (2023). The interaction of thin metal plate and circular rigid boulder in undrained clay:2D physical and numerical models. *Proceedings to conference SUT OSIG 2023*. London, UK

Chapter 5: Stage 3 investigates the effect of the pile curvature using 3D simulations. Prior to the full-scale 3D simulation, preliminary 3D models were established to examine the model properties, giving a stable state of the simulation. An algorithm was established using the piecewise equations in Chapter 3 (stage 1), building links between the 2D benchmarks and 3D simulations. This algorithm also facilitated a rapid assessment of the tip deflection and generated safety envelopes of the corresponding parameters.

In addition to Chapter 3 to Chapter 5, this thesis comprises six chapters. The literature review in Chapter 2 focuses on the current state of the design techniques recommended in the prevalent design codes, as well as the previous research in relation to the progressive buckling of monopiles. The literature review revealed the gaps between the current research and the practice, setting a guideline for this study. The concluding chapter, Chapter 6, summarises the established calculation approach, with discussions of its reliability and the potential further work. The chapter was also a condensed version of the thesis, outlining the detailed methodology of each chapter along with their respective outcomes and contributions.

CHAPTER 2 LITERATURE REVIEW

2.1 MONOPILE DESIGN CODES FOR TIP DISTORTION

The prevalent design codes set guidelines for the design and construction of offshore structures. To understand the state of art, the literature review first looks into the common practice presented by six offshore design codes, each composing a sub-section from Section 2.1.1 to Section 2.1.6. Finally, the summary in Section 2.1.7 provides a comparison of the various design codes, highlighting their specific focus and applicable regimes.

2.1.1 API RP2A (API, 2014)

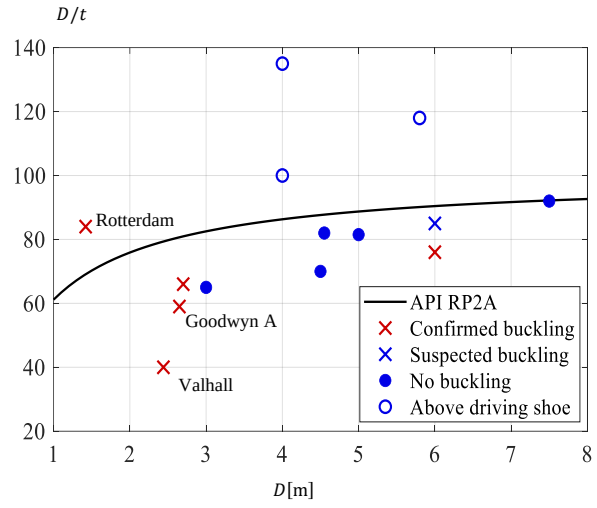
Focusing on maintaining the integrity of the pile tip, API RP2A (API, 2014) suggests that the pile wall thickness (t [mm]) should be no less than

$$t = 6.35 + D/100 \qquad \textit{Eqn. 2-1}$$

where D [mm] is the outer diameter of the pile. Apart from Eqn. 2-1, the code also suggests a general rule for the selection of pile wall thickness, stating that:

> *"The pile wall thickness in the vicinity of the mudline, and possibly at other points, is normally controlled by the combined axial load and bending moment which results from the design loading conditions for the platform."* (API, 2014)

The reliability of Eqn. 2-1 was examined by (Randolph, 2018) from a review of construction sites with confirmed buckling failures. Figure 2-1 shows that some pile designs that conformed to this equation still experienced buckling (Randolph, 2018). This deviation is likely attributed to gaps between early structural engineering studies and offshore geotechnical applications. For example, the allowable stress design in API RP2A follows the AISC specifications of compact hot-rolled steel sections, coded as AISC335-89 (AISC, 1989), adopting numeric fits of laboratory-scale experiments. However, these experiments excluded the soil-structure interactions (Sherman, 1977), especially the influence of soil heterogeneity.



Pile geometries and soil conditions

Site	$\boldsymbol{D}[\mathbf{m}]/\boldsymbol{t}[\mathbf{m}]$	Soil type
Goodwyn A, Australia	$\frac{2.65}{0.045} \cong 59$	3 ~ 5 m calcareous silt and sand
Valhall, North Sea	$\frac{2.44}{0.06} \cong 40$	Dense sand $q_c = 80$ MPa
Rotterdam	$\frac{1.42}{0.017} \cong 84$	Medium-dense sand, $q_c =$ 25 ~ 40 MPa

Figure 2-1 Practice and API RP2A recommendation (Randolph, 2018)

2.1.2 DNV-ST-0126 (DNV, 2016)

Instead of specifying a dimension-control equation such as Eqn. 2-1, another commonly used design code, DNV-ST-0126 (DNV, 2016), suggests that monopiles fulfilling the criteria for *compact sections* undergo the strength assessments outlined in DNV Classification No.30.1 (DNV, 2018), superseded by DNV-CG-0128 (DNV, 2023a). Compact sections are defined based on the D/t ratio of the tubular section, given as

$$\frac{D}{t} \leq 50\varepsilon^2, \qquad \varepsilon = \sqrt{\frac{235}{f_y}} \qquad \textit{Eqn. 2-2}$$

where f_y [MPa] is the minimum yield strength of the material. The definition of compact sections varies in different codes: in API RP2A (API, 2014) and NORSOK N-004 (Norsok, 2012) it is defined as $D/t < 60$, while in EN 1993-1-1 (2005), $D/t < 21150/f_y$. The compact section is regarded less likely to fail due to local buckling and an axial stress equal yield strength can be achieved (Norsok, 2012). Therefore, the analysis in DNV-CG-0128 (DNV, 2023a) emphasises the global buckling in relation to the slenderness of the component.

If the criteria of compact sections are not met, EN 1993-1-6 (2007) may be used for monopiles with $D/t < 250$, while ISO 19902 (ISO, 2020) or NORSOK N-004 (Norsok, 2012) for $D/t < 120$, as suggested by DNV-ST-0126 (DNV, 2016). Alternatively, DNV-RP-C202 (DNV, 2019) can also be used for the uncompacted sections, without specific applicable D/t range.

2.1.3 EN 1993-1-6 (2007)

DNV-ST-0126 (DNV, 2016) suggests that EN 1993-1-6 (2007) is suitable for piles with $D/t < 250$. However, the code is applicable to a wider range of cylindrical shell structures with D/t from 20 to 5000, such as silos and chimneys. This is probably because, instead of piecewise equations rooted in experiment results, EN 1993-1-6 (2007) provides a group of buckling analysis methods based on numerical simulations.

A representative design philosophy adopted by the code is the *Overall Method*, the workflow of which is shown in Figure 2-2. The method uses Linear Bifurcation Analysis (LBA) to determine the elastic critical buckling resistance, and Material Nonlinear Analysis (MNA) for

the plastic limit load (Taras *et al.*, 2014). Together, LBA and MNA give an overall slenderness, determining the reduction factor of local buckling strength (Taras *et al.*, 2014).

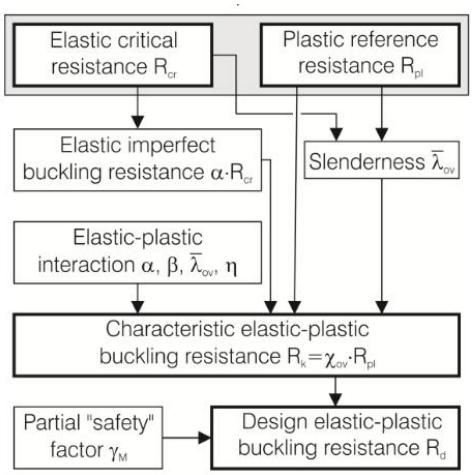


Figure 2-2 Overall method workflow in EN 1993-1-6 (Taras et al., 2014)

A more advanced method, Geometrically and Materially Nonlinear Imperfection Analysis (GMNIA), is also acknowledged in the code. The method considers the imperfections in geometries, boundary conditions, and residual stresses. A bifurcation eigenvalue check is required at each load level, based on the shell bending theory and large-deflection theory (EN 1993-1-6, 2007). A reduction factor is then obtained from GMNIA analysis, giving the local buckling strength of the imperfect structure.

The reduction factor in the code is only suitable for steel shell structures subjected to quasi-static loads. Reliable validations, in addition, are also needed for the numerical simulations, especially for GMNIA. As the imperfections addressed in GMNIA simulations are typically case-specific, they lack established experimental or theoretical references. Nevertheless, GMNIA is a promising approach to capture the reactions of monopiles in the design stage, provided that the working mechanisms of shell structures, especially their interaction with soils, are well understood.

2.1.4 ISO 19902 (ISO, 2020)

ISO 19902 gives instructions on the buckling analysis using numerical simulations, taking account of the material and geometry nonlinearity. Piecewise equations are also provided for the quick evaluation of local buckling strength, f_{yc} [Pa], based on the elastic local buckling strength, f_{xe} [Pa]

$$f_{xe} = 2C_x Et/D \qquad \textit{Eqn. 2-3}$$

where E [Pa] is the Young's modulus of the material, while C_x is the elastic critical buckling coefficient taking account of the geometry imperfections. A reduction factor as a function of f_{xe} is then added to the yield strength, f_y [Pa], giving the value of f_{yc} (ISO, 2020, sec. 13.2.3.3).

Though no specific limitation is given in relation to the minimum wall thickness, the code emphasises that the geometry imperfection at the pile tip can lead to progressive buckling during installation for piles with high D/t ratios (ISO, 2020, sec. 17.3.6). The use of an external chamfer, in addition, may increase the potential for pile refusal especially in very dense sands (ISO, 2020, sec. A.17.3.8). However, similar to the minimum wall thickness, no specific guidance is given in the code.

2.1.5 NORSOK N-004 (NORSOK, 2012)

NORSOK N-004 identifies that the possibility of local buckling would increase as the D/t ratio gets larger. Instead of a safe range of D/t ratio, the code points out that the elastic local buckling strength in ISO 19902 (ISO, 2020), as shown in Section 2.1.4, is conservative for cylinders with $t > 6$ mm and $D/t < 120$ (Norsok, 2012, sec. Comm. 6.3.3). However, the

code does not provide explicit instructions on mitigating the conservatism, apart from advising that any members beyond the specified range should refer to DNV-RP-C202 (DNV, 2019).

2.1.6 DNV-RP-C202 (DNV, 2019)

DNVGL-RP-C202 focuses on the shell buckling problem. It gives a brief instruction on the numerical analysis of the problem using the Finite Element Method (FEM), with four key aspects that need to be covered (DNV, 2019, sec. 1.3): imperfections, material nonlinearities, residual stresses, and possible interaction between local and global buckling. In contrast to the limited instruction on FEM analysis, the code provides explicit piecewise equations for the characterisation of the structural strength.

For uncompacted and unstiffened tubular, DNVGL-RP-C202 suggests a characteristic elastic buckling strength (DNV, 2019, sec. 3.4.2) based on Timoshenko's critical compressive stress σ_{cr} $[Pa]$ of thin plates:

$$\sigma_{cr} = C\frac{\pi^2 E}{12(1-\nu^2)}\frac{t^2}{l^2} \qquad \textit{Eqn. 2-4}$$

where C is a unitless coefficient concerning dimensional effects; E [Pa] and ν are Young's modulus and Poisson's ratio, respectively; and l [mm] refers to the length of the plate specimen (Timoshenko & Gere, 1985, figs. 9–4) or the cylinder length. In the case of a stiffened cylinder, l refers to the distance between adjacent ring frames (DNV, 2019). Eqn. 2-4 was to describe the buckling behaviour of simply supported rectangular plates with longitudinally uniform compression (Timoshenko & Gere, 1985, sec. 9.2). This equation emphasises the influence of the in-plane compressive stress, which, in the circumstance of pile installation, is comparable to the soil resistance perpendicular to the pile base. The possible contributions of lateral soil resistance to the out-of-plane deflections of piles are also neglected by Eqn. 2-4.

2.1.7 SUMMARY AND COMPARISON OF DESIGN CODES

Table 2-1 Summary and comparison of the design codes

Design code	**Applicable D/t**	**Compact section D/t range**	**Recommended approach**
API RP2A	$D/t < 300$	$D/t < 60$	Work stress design using piecewise equations
DNV-ST-0126	No specific range	$D/t \leq 50\left(\sqrt{\frac{235}{f_y}}\right)^2$	Partial safety factor method using piecewise equations, with implementation guidance of other design codes
Eurocode 3 EN 1993-1-1 & EN1993-1-6	$20 \leq \frac{D}{t} \leq 5000$ $t > 3$ mm	$D/t < 21150/f_y$	Limit state design mainly relying on numerical simulations, with piecewise equations as guidelines
ISO 19902	$\frac{f_y D}{Et} \leq 0.069$	$f_y/f_{xe} \leq 0.170$	Limit state design mainly relying on numerical simulations, with piecewise equations as guidelines
NORSOK N-004	$D/t < 120$ $t > 6$ mm	$D/t < 60$	Limit state design using piecewise equations
DNV-RP-C202	No specific range	Not defined	Piecewise equations characterising thin shell buckling behaviours

Table 2-1 gives a summary of the discussed design codes. The summary of the recommended approach primarily focuses on the calculation of the buckling behaviour. Though the codes tend to provide guidance on both numerical simulations and piecewise equation methods for determining buckling behaviour, they emphasise these approaches differently. Most of the codes (four out of six) follow the more conventional approach, predominantly relying on piecewise equations to characterise the buckling resistance of the tube, while the other two (Eurocode 3 and ISO 19902) focus on numerical simulations. Given the complex loading conditions in the scenario of a pile-boulder impact within the soil, using the simple piecewise

equations in current design codes may not be sufficient. Therefore, numerical simulations considering material and geometric nonlinearities, as recommended in Eurocode 3, represent the most promising approach for addressing the progressive buckling of piles due to boulder collision.

2.2 THE CURRENT STATE OF RESEARCH

Numerous studies have been carried out in relation to the progressive buckling of steel tubulars in the field of structural engineering. These studies focused on the structure itself, identifying piecewise equations to characterise the buckling phenomenon using both theoretical and experimental methods. The loading conditions in these studies adopt a concentrated force, sometimes with hydrostatic pressure, as shown in Figure 2-3, Section 2.2.1. However, these reviews focus on the progressive buckling of offshore pipelines, where the steel tubular is subjected to hydrostatic pressures.

The pile failure in Goodwyn-A brought the tip buckling of the pile into focus. The new research considered not only the pile itself, but also the interactions between the pile and external components, such as soil and pile sleeve. Numerical techniques are commonly used due to the complexity of the problem. Physical models, meanwhile, have been adopted to provide a more straightforward view of the structural interactions and facilitate understanding. Theoretical methods derived in previous studies in structural engineering, however, were not integrated with geotechnical studies. This was probably due to complex loading conditions from the soil. These studies are shown in Section 2.2.2 in chronological order. Finally, Section 2.3 discusses the gaps between the practice and research, identifying directions for this research.

2.2.1 PROGRESSIVE BUCKLING IN STRUCTURAL ENGINEERING

Study in the field of structural engineering combines the shell theory and plastic hinge models. A denting force was determined using a plastic hinge model on a perfect cylindrical shell, then a propagation force was derived by sequentially relocating the plastic hinge. A typical plastic hinge model is given in Figure 2-3, while a list of representative piecewise equations is given in Table 2-2. The research in the field of structural engineering tends to exclude the consideration of soils. Therefore, these studies may have limited contributions to the monopile buckling problems in geotechnical engineering, where the effect of highly non-linear soil reactions cannot be neglected. However, these studies could provide a different perspective on geotechnical research and are presented here to provide a comprehensive view.

Table 2-2 Piecewise equations of progressive buckling

Reference	**Equation**	**Technique**
Kyriakides & Babcock (1982)	$\frac{P_P}{\sigma_Y} = \left[10.7 + 0.54\left(\frac{E_P}{\sigma_Y}\right)\right]\left(\frac{t}{D}\right)^{2.25}$	Empirical
Steel & Spence (1983)	$\frac{P_P}{\sigma_Y} = \frac{\pi}{4}\left(\frac{t}{R}\right)^2\left[1 + 2.07\left(\frac{t}{R_p}\right)^{0.35}\left(\frac{E_P}{\sigma_Y}\right)^{0.12}\right]$	Analytical + Numeric fit
Wierzbicki & Bhat (1986)	$P_P \cong \left\{3 + 12\left(\frac{1}{3}\frac{E_p}{\sigma_Y}\frac{t}{D}\right)^{0.7}\right\}\sigma_Y\left(\frac{t}{D}\right)^2$	Analytical + Numeric fit
	$\frac{P_I}{P_P} = 0.41\frac{\ln(D/D^*)}{(D/D^* - 1)^2}$	Analytical
Calladine (1986)	$P_I = \begin{cases}\pi\sigma_Y t^2 = P_0, & w \le t \\ 1.22P_0\sqrt{r^2/Rt}, & w > t\end{cases}$	Analytical

Nomenclatures			
t	Pipe thickness, m	E_P	Strain hardening modulus, Pa
w	Magnitude of indentation, m	P_I	Pressure/Force to initiate buckling, Pa/N
D	Pipe diameter, m	P_P	Propagation pressure, Pa
D^*	Minor axis of deformed section, m	R_p	Pipe radius, m
		σ_Y	Yield strength, Pa

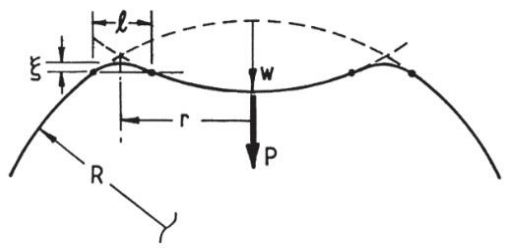


Figure 2-3 Plastic hinge model (Calladine, 1986)

The first three studies focus on the progressive buckling of offshore pipelines, where a steel tubular is subjected to hydrostatic pressure. Kyriakides & Babcock (1982) developed a pressure tank to investigate the propagation pressure of a pipe, giving a piecewise equation using numeric fit. The numerical simulation conducted by Steel & Spence (1983) and Wierzbicki & Bhat (1986) used the same assumptions: 1) the material had a rigid-linearly strain hardening uniaxial behaviour; 2) the tubular deformation is inextensional. The first assumption could be regarded as a simplification for the convenience of computation, while the second was based on the *a priori* knowledge that the extension and shear effects were negligible in the propagation of buckling (Wierzbicki & Bhat, 1986). The plastic hinge in Wierzbicki & Bhat (1986) would split into two as the tubular deformed, while in Steel & Spence (1983), the hinges remained the same regardless of the geometry change. However, the two solutions gave similar descriptions of the propagation force and were underestimations compared to the empirical equation from Kyriakides & Babcock (1982).

Another crucial feature is the force or pressure initiating the progressive buckling. Wierzbicki & Bhat (1986) investigated the buckling initiation pressure of a dented tubular, giving a singularity point at $D^*/D = 1$, where D^* [m] was the minor axis of the deformed cross-section. The equation indicated the occurrence of progressive buckling following the formation of a dent, but did not clarify whether the dent would originate from a perfectly tubular structure.

Calladine (1986), meanwhile, suggested that when the deflection w [m] was smaller than the shell thickness t [m], the shell would behave like a flat plate with four edges fully clamped. This analogy gave the force initiating a dent on a perfect cylinder when $w \leq t$. As the deformations increased, the change of topology was considered by relocating the plastic hinge on the circumference, as shown in Figure 2-3. The propagation force was then obtained.

The equation given by Calladine (1986) was based on a tubular subjected to a concentrated force only, while the other approaches adopted hydrostatic loading conditions. The hydrostatic pressure is different from the soil pressure during pile installation. However, these equations offer the potential to address the progressive buckling issue through analytical methods. This is provided that the non-linear soil behaviour can be accurately captured as a substitute for hydrostatic pressure. The cavity expansion theory should be a promising approach to realise this substitution. However, efficient validation and calibration methods are still necessary, whether based on numerical or experimental approaches. An example of the application of these analytical descriptions is presented in Cai & Deeks (2005). Their paper aimed at simulating the progressive buckling of an impact-driven pile during installation due to its initial out-of-roundness. However, as a preliminary study, this analysis did not consider the effects of soil.

2.2.2 TIP BUCKLING OF PILE IN GEOTECHNICAL ENGINEERING

Research in relation to the tip buckling of an advancing pile started from Kramer (1996), following the pile failure in the Goodwyn-A platform. However, subsequent literature appears to offer limited further research in this area. This is probably because buckled piles are usually not detected unless they are extracted from the ground or experience premature refusal during installation. Most existing research, as shown in this section, is case-specific and lacks a unifying concept or systematic framework. Therefore, this section first reviews the research

independently in chronological order, while a summary and comparison is provided in Table 2-3 in the end

Kramer (1996)

Kramer (1996) identified that the progressive buckling of Goodwyn-A piles initiated from a dent due to the impact between the pile tip and the pile sleeve. This small indentation then propagated after the pile penetrated through a hard layer. The study had a dual focus: the force initiating a dent at the pile tip, and the magnitude of the deformation at a designated penetration depth.

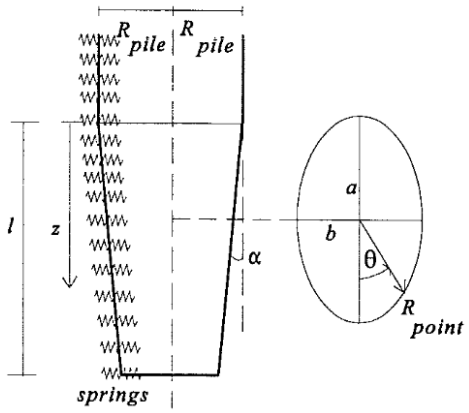


Figure 2-4 Nomenclature definitions of pile-soil interaction model (Kramer, 1996)

The research of Kramer (1996) started with a structural analysis of the pile using yield-line theory. A denting force, P_0 [N], was calculated based on an analogy of a flat plate subjected to a point load at the midpoint on a free edge,

$$P_0 = \sqrt{2}\sigma_Y t^2 \qquad \textit{Eqn. 2-5}$$

Eqn. 2-5 is similar to the solution given by Calladine (1986), which is given as $P_0 = \pi\sigma_Y t^2$, as listed in Table 2-3. The different constants in the equations could be due to the different boundary conditions that were adopted in the analyses. Calladine (1986) assumed

that the unloaded plate edges were fully clamped. Though the detailed calculation was not given by Kramer (1996), a reproduction of Eqn. 2-5 suggested that a simply-supported condition was used for Eqn. 2-5. This denting force is indicative when the dent occurs before the pile penetrates into the soil. However, its applicability may be limited in scenarios where the advancing pile encounters a buried boulder within the soil, as the equation does not account for the effects of the soil around the pile.

To predict the magnitude of deformation, a pile-soil interaction model was then established, with an initial ovalisation assigned to the pile. As shown in Figure 2-4, the soil reactions are represented by a series of elastic springs. A dimensionless parameter, h/d, is adopted to quantify the extent of distortion, where h [m] is the undeformed length after penetration; and d [m] is the penetration depth. The value, $h/d = 0$, indicates negligible change in the pile after penetration, while a value of 1 means the maximum deformation. By equating the radial stresses in pile and soil, the h/d ratio is given as

$$\frac{h}{d} = \frac{1}{1 + \frac{1.6}{3}\frac{E_s}{E_p}\left(\frac{D}{t}\right)^3} \qquad \textit{Eqn. 2-6}$$

where E_s [Pa] and E_p [Pa] are the Young's modulus of the soil and the pile, respectively (Kramer, 1996). The radial tip deflection, u_r [m], thus become

$$u_r = h \tan \alpha \qquad \textit{Eqn. 2-7}$$

A laboratory-scale test was also established to validate the theoretical solutions in Eqn. 2-6 and Eqn. 2-7. The comparison of results showed good agreement, where 15 out of 17 results were consistent. This test also provided a parametric study of the initial tip deflection (characterised by α), D/t ratio, and the pressure placed on the soil sample. The experiment suggested that the

three parameters presented a positive correlation with the radial deformation of the pile tip, with α being the dominant factor (Kramer, 1996).

The research of Kramer (1996) marked the commencement of the investigation of the progressive buckling of monopiles. However, the research was constrained by the techniques available at the time, leading to significant simplifications on the pile-soil interaction model, including the pile geometry and the soil reaction. The application of the deflection angle α is only valid under the condition that the pile deformation is linearly propagated throughout the penetration length. Using linear springs to represent the soil, meanwhile, excludes the frictional effects on the pile wall, as well as the non-linear plastic behaviour of the soil. In addition, the coupling effects of different soil layers are also neglected by using independent springs. These simplifications, however, are reasonable for analytical calculations. Alternatively, more advanced numerical techniques are required to accurately capture the complex behaviour of both the pile and the soil.

Aldridge et al. (2005)

For thin shells, Aldridge *et al.* (2005) built a plastic-hinge model for localised buckling due to concentrated forces. The loading condition of the model and the nomenclatures are shown in Figure 2-5. However, instead of a cylinder, the calculation was probably based on a flat plate, with the same conditions as that in Kramer (1996). The minimum lateral force to initiate a dent, $F_{lateral}$ [N], is given as (Aldridge *et al.*, 2005)

$$F_{lateral} = 1.4\sigma_Y t^2 \qquad \textit{Eqn. 2-8}$$

Eqn. 2-8 is 15% larger than the minimum dent force, Q_{tip} [N], suggested in HSE (2001),

$$Q_{tip} = 1.2\sigma_Y t^2 \qquad \textit{Eqn. 2-9}$$

This deviation results from a safety criterion set by HSE (2001), that a pile is regarded as failed when the tip deflection, δ [m], fulfils the condition $\sqrt{\delta/D} \geq 0.1$.

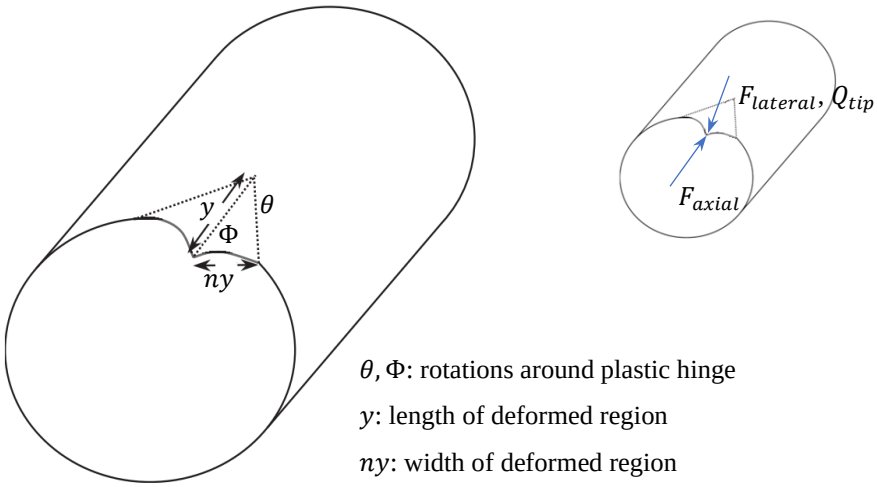


Figure 2-5 Local tip buckling model (after Aldridge et al., 2005)

Apart from the analytical calculation, the axial denting force, F_{axial} [N], was given by a combination of experimental and FEM analyses (Aldridge *et al.*, 2005),

$$F_{axial} = 2.8\sigma_Y t^2 \qquad \textit{Eqn. 2-10}$$

Eqn. 2-8 to Eqn. 2-10 were derived from the structural analyses of the pile, without the effect of soil.

By equating the inward deflection of the pile wall to the lateral displacement of a rigid circular area with the same D [m] within the soil, Aldridge *et al.* (2005) developed a safe criterion for the D/t ratio,

$$\left(\frac{D}{t}\right)^3 < \frac{5(1-\nu_s^2)E_p}{E_s} \qquad \textit{Eqn. 2-11}$$

where ν_s is the Poisson's ratio of soil. This equation assumes that the soil pressure is applied at the pile tip over an arc length of $0.5D$. The derivation of Eqn. 2-11 was conducted in the elastic range. It implies that the progressive buckling would only occur when the soil stiffness

is larger than that of the pile (Aldridge *et al.*, 2005). Otherwise, the pile deflection in the elastic range will recover, and progressive buckling will be unlikely to occur.

In addition to the relative stiffness, another failure criterion was established based on the relative strength, given as

$$\sigma_{soil} > \frac{3\sigma_Y t^2}{y^2} \qquad \textit{Eqn. 2-12}$$

where σ_{soil} [Pa] is the yield strength of the soil; y [m] is the initial buckled length of the pile. Eqn. 2-12 was formulated under the premise that the soil strength should be sufficiently large to amplify the initial dent and initiate progressive buckling (Aldridge *et al.*, 2005).

The reliability of Eqn. 2-11 and Eqn. 2-12 is hard to evaluate as the validation method is not available. The equations establish criteria for progressive buckling in the presence of a pre-existing dent. However, this exclusion is only applicable when the preceding dent does not affect the performance of the remaining part of the pile, as well as the loading conditions on the pile wall. The effects of the magnitude of the initial imperfections, in addition, are also excluded from the equations. Provided that the initial deformation is in the plastic range, a calculation relying solely on elastic properties, such as Eqn. 2-11, may not be sufficient. Nevertheless, the research was the first to point out the inadequate considerations of the tip buckling problem in the current design code. The equations, in addition, represented a preliminary attempt to integrate criteria of tip integrity into the design code.

Erbrich et al. (2011)

To investigate the progressive buckling due to initial imperfection, Erbrich *et al.* (2011) developed a Bucket Adjusted Soil Installation Loading (BASIL) model. The model has two components: 1) the tubular pile with uniform user-defined shell elements with hardening

effects; and 2) layers of BASIL soil springs radiating from the centre line of the pile. The model geometry is shown in Figure 2-6, where the red dots symbolise the joints between the pile and the soil springs.

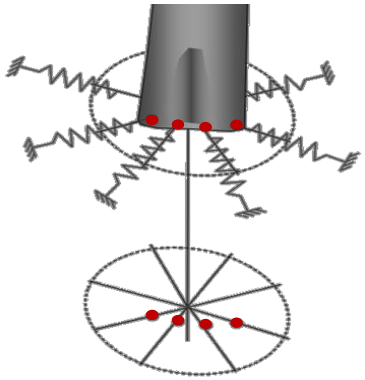


Figure 2-6 BASIL soil springs and pile tip (after Randolph, 2018)

The BASIL soil springs are non-linear Ramberg-Osgood models calibrated against cavity expansion analysis. Given that BASIL springs can only be activated in the direction of compression, the effects of the soil plug are excluded. At the onset of analysis, the pile is assumed to be embedded at a small depth, with nodal forces representing soil reactions applied to the pile tip. The initial imperfection is defined by a set of nodal forces on the bottom elements. The model is imported into the software Abaqus, using an iterative calculation procedure at each penetration interval. The pile advancement is at one element length per interval. The deformed geometry from the last interval is represented by a new set of nodal forces on the pile.

Apart from presenting the calculation procedure of the BASIL model, the paper presented a case study of an ovalized pile penetrating through a hard layer. Figure 2-7 shows the tip trajectories of the pile, where an increase of the gradient appears in the cemented layer, symbolising an accelerated tip deflection.

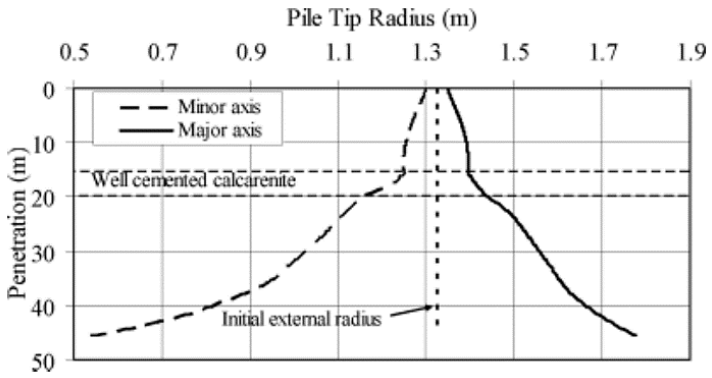


Figure 2-7 Tip trajectories from BASIL model (Erbrich et al., 2011)

Though the reaction of the soil plug was not included, Erbrich *et al.* (2011) provided an efficient numerical approach to describe the buckling process. Classical FEM has difficulties dealing with the large deformation in the soil during pile installation. A remap of the mesh is usually required to avoid the model collapse due to the severe element distortion. This remap, however, is time-consuming. The BASIL model, on the other hand, considers the installation procedure of the pile by simply changing the nodal forces on the pile. In this way, it saves computing time by avoiding the mesh remap. Though no physical model was provided for validation, the application of the cavity expansion theory enhances its reliability, given its extensive long history in solving pile installation problems. Therefore, the BASIL model could be regarded as a promising approach for addressing progressive buckling due to initial imperfections in piles. However, when a third object like a boulder is introduced into the model, its effectiveness may diminish due to the absence of reliable reference or validation methods.

Holeyman et al. (2015)

Following the Wave Equation Analysis (WEA) approach, Holeyman *et al.* (2015) proposed a 1D model conducted in GRLWEAP. An illustration of the model is shown in Figure 2-8. This is the first model available in the literature that describes the interactions between a pile, a boulder, and the soil.

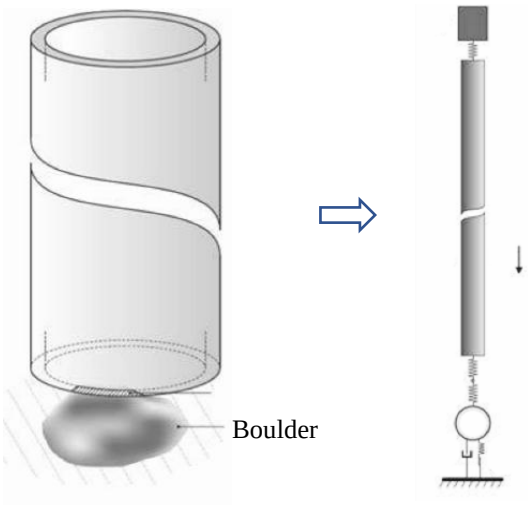


Figure 2-8 Pile-soil-boulder model (after Holeyman et al., 2015)

The pile is represented by its impedance with a downward force transmitted to the base. A boulder, on the other hand, is modelled as a standard pile element in classical WEA. The boulder resistance to vertical displacement, R_B [N] is assessed as

$$R_B = N_c s_u \pi a^2 \qquad \textit{Eqn. 2-13}$$

where N_c is a shape factor of sphere penetration, which was taken as 15 in the model; s_u [Pa] is the undrained shear strength of the soil, which was stiff glacial till for the calculation example in the paper; and a [m] is the horizontal radius of the ellipsoidal boulder (Holeyman *et al.*, 2015). The Hoek-Brown rock failure criterion is adopted to characterise the boulder strength. For larger boulders, the Heuze scaling law is applied to address potential weaknesses associated with increased size. The splitting resistance of the boulder, $T_{b,split}$ [N], is therefore obtained. Figure 2-9 gives the variation of boulder governing forces, R_B and $T_{b,split}$, against a.

The contact between the pile and the boulder was assumed in an elastic range, represented by two stiffness factors with Hertz contact theory. For the convenience of computation, the contact eccentricity between the pile and the boulder was neglected. Two calculation examples gave the contact force between the pile tip and the boulder, marked as black triangles in Figure 2-9.

The possibility of tip buckling is thus obtained by comparing the contact force with $T_{b,split}$, the yield strength of the pile, and R_B.

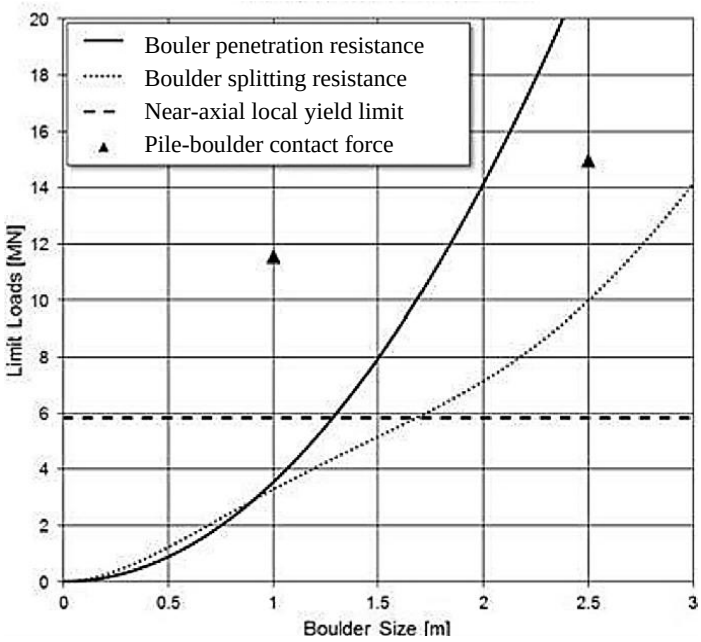


Figure 2-9 Variation of boulder governing forces (Holeyman et al., 2015)

The paper provided a quick calculation approach based on the 1D WEA model. The model does not predict the magnitude of the tip deflection; instead, it indicates the possibility of tip deflection using the comparison between forces, as shown in Figure 2-9. However, this comparison may not be sufficient to determine whether the buckling would occur. Take the boulder size $a = 1$ m for example, as shown in Figure 2-9, the instant contact force is much larger than the other three forces. But it does not necessitate the tip deflection, as the boulder may be crushed or pushed away after the contact. The same obscurity also occurs for the example with $a = 2.5$ m, where the boulder may be crushed before the tip buckles. Nevertheless, the research proves that larger boulders pose greater challenges for pile installation, and provides a quick evaluation method for assessing pile buckling due to boulder impact.

Gargarella (2018)

Gargarella (2018) conducted more detailed research on boulder movement in soil using an analogy of flint moving in chalk. The research, similar to Holeyman *et al.* (2015), starts with the investigation of the splitting force of a flint, F_{split} [N] obtained from the Brazilian test, given as

$$F_{split} = \frac{1}{2}\sigma_t \pi d \qquad \textit{Eqn. 2-14}$$

Eqn. 2-14 assumes a unit plane thickness, where σ_t [Pa] is the tensile strength of the boulder; d [m] is the boulder diameter. The splitting force is then compared with the plane-strain bearing capacity failure force from the T-bar solution,

$$F_{lim} = 12 s_u d \qquad \textit{Eqn. 2-15}$$

The ratio between the two gives a criterion determining that the flint would split when $s_u/\sigma_t < 0.13$ after contact, otherwise, it would penetrate into the soil as the pile moves. This theoretical criterion was then compared with the numerical simulation of boulder penetration. The comparison indicates that the boulder will move within the soil if s_u is 10% lower than σ_t, otherwise, it will be crushed.

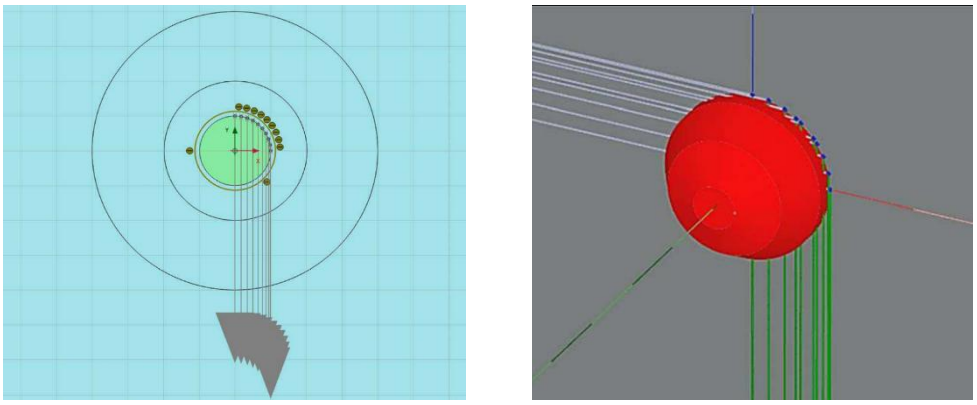


Figure 2-10 Boulder movement model in 2D (left) and 3D (right) in PLAXIS (Gargarella, 2018)

Numerical models were then established using PLAXIS to derive the failure envelope of boulders under static loads. The geometries of 2D and 3D models are presented in Figure 2-10, where the boulder is simulated as a rigid body, and the undrained soil is represented as a homogeneous material adhering to the Tresca failure criteria.

Three types of point loads were included in the parametric study for the failure envelope: the horizontal (F_x [N]), the vertical (F_y [N]), and the inclined loads. The inclined force is represented by its angle to the vertical. The vertical and horizontal loads, meanwhile, are depicted by the angle formed between the connection line from the load position to the origin and the vertical line. The locations of these loads are marked in Figure 2-10. A comparison of the 2D and 3D results is shown in Figure 2-11, indicating the consistency between the two models. The 3D parametric study suggests that the boulder would have a rotational failure when the angle of the inclined force exceeds 10°, otherwise, a bearing capacity failure of the soil occurs.

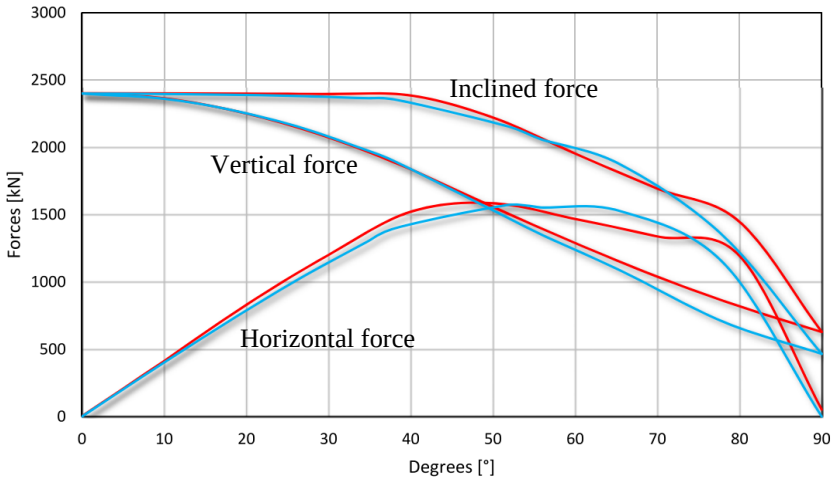


Figure 2-11 Comparison between 2D (red) and 3D (blue) results (Gargarella, 2018)

A dynamic analysis was also conducted on the pile and the boulder. The analysis for the pile was based on the software, GRLWEAP. The dynamic force of the pile was extracted as an input for the dynamic analysis of the boulder in PLAXIS. A relationship between the peak

force and the corresponding permanent displacement of the flint was accordingly established, given as

$$u_y = \frac{F_y^2}{144 s_u E_s d^2 L}, \qquad if\ F_y > 0.3\sqrt{s_u E_s} dL \qquad \textit{Eqn. 2-16}$$

$$u_x = \frac{F_x^2}{30 s_u E_s d^2 L}, \qquad if\ F_x > 0.13\sqrt{s_u E_s} dL \qquad \textit{Eqn. 2-17}$$

where d [m] is the boulder diameter, L [m] is the boulder length in a plane-strain condition, and E_s [Pa] is the Young's modulus of the soil using the Mohr-Coulomb criterion. The threshold in Eqn. 2-16 and Eqn. 2-17 symbolised the commencement of plastic deformation of the soil, below which $u_y = 0$ and $u_x = 0$.

Gargarella (2018) assumed that the presence of a boulder would not affect the global performance of the pile, such as its advancement with each hammer blow, but rather lead to local changes, such as tip buckling. Therefore, the tip buckling can be avoided by limiting the advancement of the pile with each hammer blow to a smaller amount than the permanent boulder displacement.

This research provides a quick evaluation method of the possibility of pile buckling incorporated with the software GRLWEAP. It gives a thorough investigation of the performance of a boulder moving within the soil. However, because the pile and the boulder were analysed independently, the complex interaction between the two components was neglected. For example, the failure envelope of the boulder was based on the static load, where the loading position remained unchanged. In reality, however, the deformation of the pile tip will continuously change the contact condition between the pile and the boulder. The localised buckling caused by the boulder, in addition, may also lead to a global response of the pile, such as premature refusal or a change in the penetration rate. Nevertheless, the research provides an

analysis approach that combines WEA and FEM, saving the effort of defining a wave absorption boundary condition for FEM models, while still keeping the dynamic analysis valid.

Stevens et al. (2019)

Stevens *et al.* (2019) built a hammer-pile-soil system using 1D to 3D models. Each model helped the understanding of different parts of the system. The 1D WEA was implemented for the interaction between the hammer and the pile using the software GRLWEAP. The model indicated the forces propagated downwards from the hammer, and the impedance change from the pile wall to the thicker driving shoe. The model indicates that the stress propagating to the pile toe could be twice the impact stress from the hammer when there is no shaft resistance. This scenario can be approximated to the case where the pile encounters a hard layer at the surface. A 2D model was then established to investigate the reactions within the hard layer after the impact from the pile.

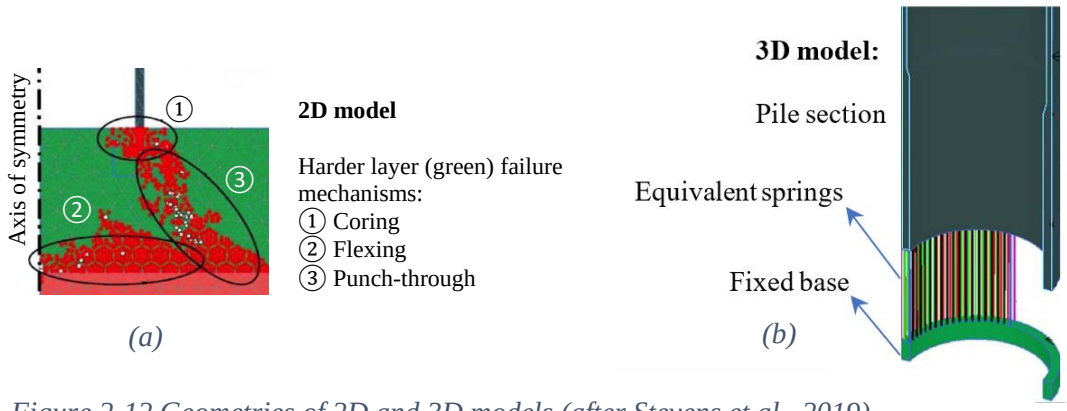


Figure 2-12 Geometries of 2D and 3D models (after Stevens et al., 2019)
(a) Three failure mechanisms in 2D models; (b) Tip subjected to boulder

The 2D symmetric model contained a rigid pile wall and a hard rock layer that behaved according to the Hoek-Brown criterion. A degradation factor was included to capture crack propagations under the pile tip due to the brittleness of the rocks. The model reveals three failure mechanisms, as shown in Figure 2-12 (a). At the start of penetration, a region of rock

proximate to the pile tip first loses its bearing capacities (*coring failure*). Sequentially, the exceedance of tensile limits appears at the bottom of the rock layer, initiating beneath the pile tip, and expanding laterally (*flexing failure*). Finally, *punch-through failure* occurred as the pile further advanced, where shearing failure initiated at the pile tip and propagated outwards through the bottom, provided that the rock layer was sufficiently thick.

To investigate the stress distribution due to collision with a boulder, a quadrant of the pile was simulated in the 3D model, including with a pile shoe. Instead of introducing a second solid body, the boulder was represented by partially distributed vertical springs, fully fixed with a rigid base as shown in Figure 2-12 (b). Two contact conditions were considered, where the boulder springs occupied 50% and 33% of the tip perimeter, respectively. Studies have shown that stress concentrations appear at both the contacting area and the zone where the wall thickness changes. Furthermore, a smaller contact area will result in higher stress increases in these regions. Given that the force applied to the pile remained constant, this conclusion is not surprising.

This paper reveals the key feature of a pile interacting with a hard layer and a boulder. Though it did not provide a specific safe range of the D/t ratio in pile design, it pointed out that the application of driving shoes may introduce additional challenges around the area where the wall thickness changes. Meanwhile, the boulder movement after the impact will change the contact condition with the pile. Therefore, using a group of vertical springs to represent the boulder impact may not be sufficient.

Bakroon et al. (2019)

Bakroon *et al.* (2019) conducted a study of the relationship between buckling patterns, types of initial imperfections, and boulder collision. The 3D analyses were conducted in LS-

DYNA/Explicit based on a user-defined technique, the Multi-Material Arbitrary Lagrangian-Eulerian (MMALE) method. This allows multiple materials to coexist in one Eulerian element. The model contained three major components: Lagrangian pile meshed with uniform shell elements; Eulerian domain filled with soil; and a layer of void Eulerian elements allowing soil heave. The geometry of the model is shown in Figure 2-13 (a).

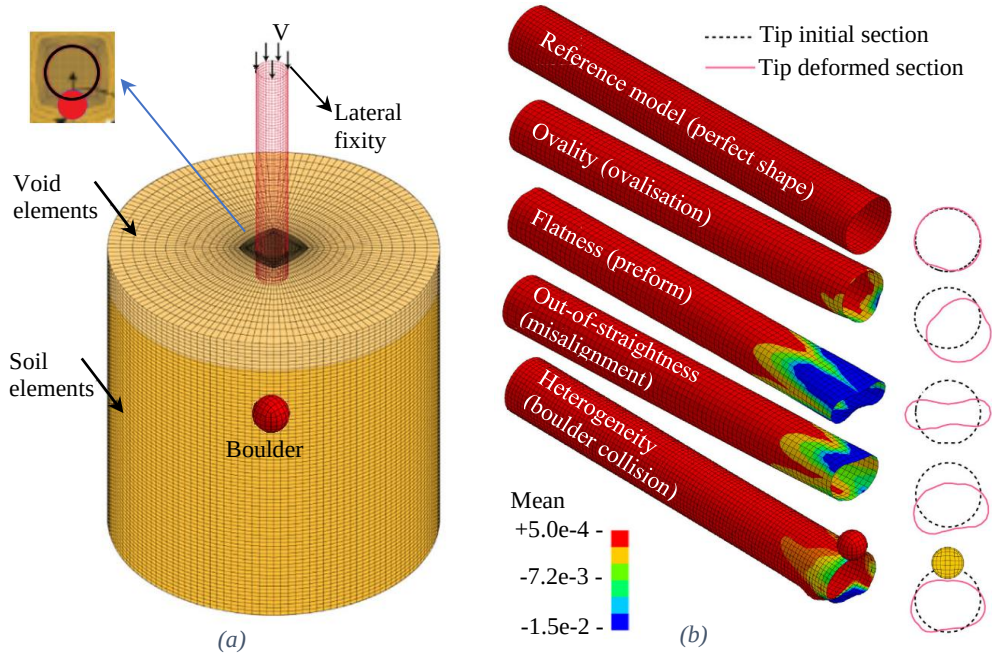


Figure 2-13 Numerical simulation in LS-DYNA (after Bakroon et al., 2019)
(a) Model geometry; (b) Imperfections and deformations

The simulation covers the progressive buckling due to the initial imperfections of the pile and the presence of the boulder. Figure 2-13 (b) shows the links between the different types of influencing factors and the deformed shape of the pile by the end of the penetration. To ensure the collision between the pile and the boulder, the boulder is fixed in the soil rather than left to "float", thus constraining its deviation from the predefined position. These limitations, however, are appropriate, given that a complete computation of this 3D model would take around two months on a normal computer, and two days on a supercomputer. A parametric study, including batch computation, was felt impractical. The heavy computation cost is a key

feature of numerical techniques for large-deformation problems. Nevertheless, the MMALE model revealed two effects of imperfections and boulders:

1) The penetration rate would decrease close to buckling and result in a shallower penetration depth compared to that of perfectly-shaped piles,
2) More internal energy accumulated within the pile, despite their shallower penetration. This implies that more energy would be required for pile buckling and lateral displacement.

Bakroon *et al.* (2019) gave a qualitative description of the failure model of the pile and the initial imperfections. The study was the pioneer in addressing the progressive buckling problem using numerical techniques for large-deformation problems. However, a quantitative evaluation of the possibility and the severity of the buckling is still required. An effective reference model is also needed to support the validity of the numerical model. These gaps were then addressed by Nietiedt (2022).

Nietiedt (2022)

Nietiedt (2022) undertook a comprehensive study containing a set of centrifuge tests, and the corresponding 3D numerical simulation of the tests.

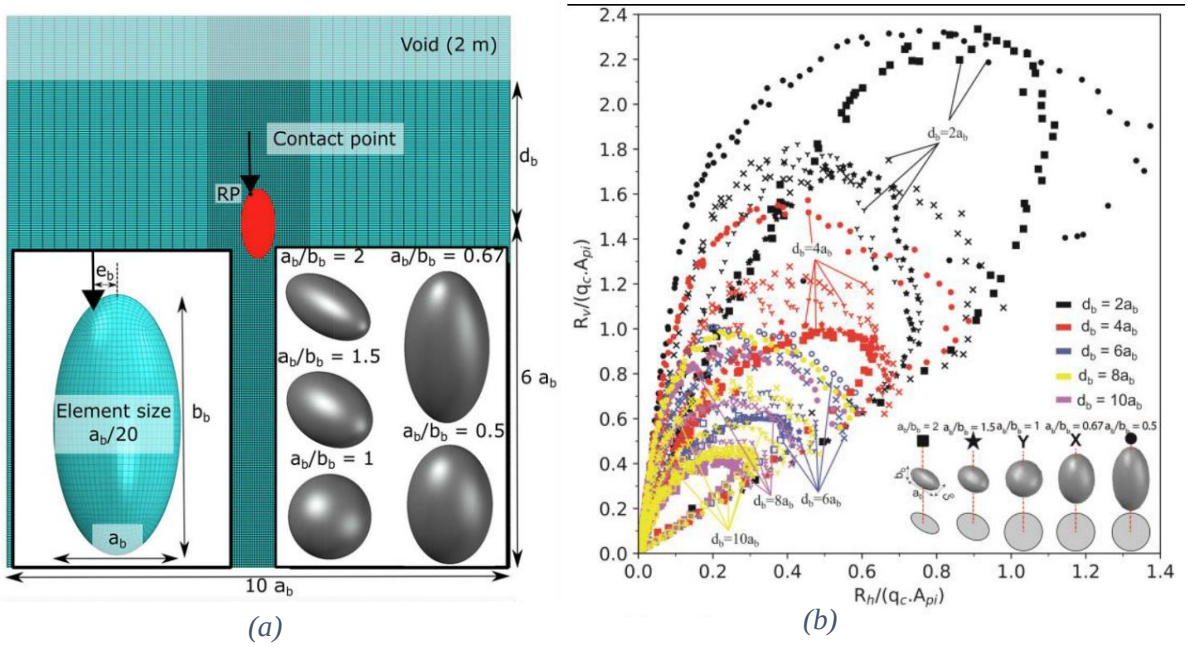
The centrifuge test contained two types of heterogeneities that could lead to progressive buckling, the inclined hard layers and the horizontal boulder layers. During the test, the pile was hammered into the dense dry sand at a model acceleration of 80g, resembling a pile with $D = 4$ m and $t = 40$ mm ($D/t = 100$). These tests were then simulated using Abaqus CEL, the consistency of the numerical and the physical model proved that the developed centrifuge test could serve as a validation for the numerical simulation.

Two sets of 3D numerical parametric studies were conducted independently to investigate the imperfection force at the pile tip and the boulder reaction force subjected to point loads in the sand. The imperfection study conducted in Abaqus/Standard gave a piecewise equation regarding the radial displacement of the pile tip, δ_p [m],

$$\frac{\delta_p}{\sqrt{Dt}} = 0.73\left(\frac{s_{load}D^2}{t^3}\right)^{0.335}\frac{\sigma_Y}{E_p} \qquad \textit{Eqn. 2-18}$$

where s_{load} [m] is the length of the line load applied at the pile tip. The imperfection force, F_p [N], is given as

$$\frac{F_p}{\sigma_Y t^2} = 0.17\left(\frac{s_{load}D}{t^2}\right)^{0.7}\frac{\sqrt{Dt}}{\delta_p}\frac{\sigma_Y}{E_p} \approx 0.25\left(\frac{s_{load}}{t}\right)^{0.4} \qquad \textit{Eqn. 2-19}$$

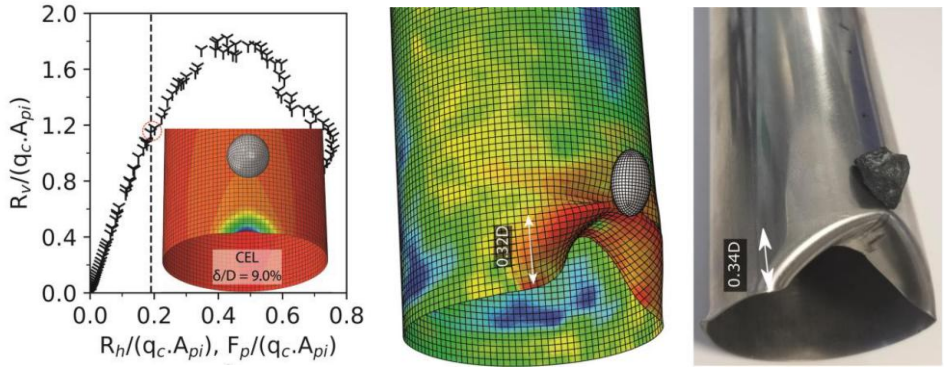


(a) *(b)*

Figure 2-14 Parametric study of boulder reaction forces (after Nietiedt, 2022)
(a)Model geometry; (b) Map of boulder reaction forces

The model geometry for the boulder reaction force study is shown in Figure 2-14 (a), with the definition of the nomenclatures. The model was built in Abaqus CEL, with a rigid boulder and

non-associative linear Drucker-Prager sand. A concentrated load was applied to the boulder. A preliminary parametric study indicates that the worst condition is when the load eccentricity becomes 0.1 times the horizontal length of the boulder, namely $e_b = 0.1a_b$. Figure 2-14 (b) presents a map of the normalised boulder reaction forces with different shapes and boulder depths at $e_b = 0.1a_b$. The vertical and the horizontal axes symbolise the normalised vertical and horizontal reaction forces, respectively. The study suggests that the boulder will continue rotating up to a maximum angle of 45° to 90° after the pile contact when $R_h < F_p$, where R_h is the horizontal reaction force of the boulder, and F_p is calculated using Eqn. 2-19. Otherwise, a plastic dent will occur at the pie tip.



(a) *(b)* *(c)*

Figure 2-15 Numerical simulations and their validations (Nietiedt, 2022)

(a) Comparison between the numerical model and the boulder reaction forces; (b) P6 numerical model; (c) P6 centrifuge test

A pile-boulder-soil interaction model was also built using Abaqus CEL. The shell element, S4, was used to model the pile, with a rigid boulder and Drucker-Prager sand. The model was first compared with the map of boulder reaction forces. An example is shown in Figure 2-15, and the vertical line symbolises the position of F_p calculated from Eqn. 2-19. The contact length between the pile and the boulder is assumed to be $5\%D$, giving the value of s_{load}. If the vertical line has an intersection with the map of R_v-R_h, the pile will buckle, as suggested in the example; otherwise, the buckling will be negligible.

Figure 2-15 (b) and (c), in addition, give a comparison of the pile deformation in a numerical simulation, coded as P6, and its centrifuge test. During the centrifuge test, the pile was hammered into the dense sand at a model acceleration of 80g. A layer of boulder was buried at the designated depth with selected dimensions. The tip deflections in the two models are $0.32D$ and $0.34\,D$, respectively, showing good consistency. Therefore, the centrifuge test can effectively validate the numerical models developed using Abaqus CEL.

After determining the possibility of initial imperfections, another set of numerical simulations was conducted to investigate the force propagating the dent. The propagation force, F_d [N], is given as a proportion to the imperfection force, F_p,

$$\frac{F_d}{F_p} = 3.8\left[1 - \exp\left(-\frac{5\delta/\delta_p}{28}\right)^{1.6}\right] \qquad \textit{Eqn. 2-20}$$

where δ [m] is the dent depth, and F_p and δ_p can be obtained from Eqn. 2-18 and Eqn. 2-19, respectively. Nietiedt (2022) provides an efficient method to evaluate the possibility of tip buckling using a map of boulder reaction forces, Figure 2-14 (b), and an equation of the imperfection force, Eqn. 2-19. The centrifuge test, in addition, serves as an effective validation for the numerical simulations, proves the reliability of the latter. However, the contact eccentricity between the pile and boulder remained undefined during the centrifuge test. While the numerical model could give a comparable tip deflection, the method for determining the contact eccentricity remains unclear. Using shell elements to model the pile, in addition, merits further consideration, particularly given the increased thickness of offshore piles.

Another assumption in the study was the value of F_p, which was taken as $5\%D$. However, it may be more indicative if a parametric study can be carried out in relation to the effect of this value. Nevertheless, Nietiedt (2022) gives a feasible and rather convenient solution for the

evaluation of the possibility of tip buckling. Though the research was carried out in dense sand, extending it to stiff clay does not appear to be a significant challenge.

Palmieri et al. (2023)

To save computing time, Palmieri *et al*. (2023) used a series of non-linear springs to represent the soil resistance. The model components and geometries are presented in Figure 2-16, where the boulder was modelled as an elastic solid and the pile as a cylindrical shell. Laboratory and *in situ* tests were conducted to determine the soil properties that defined the springs. These test results, combined with 3D numerical results of cavity expansion, determined the properties of the soil spring.

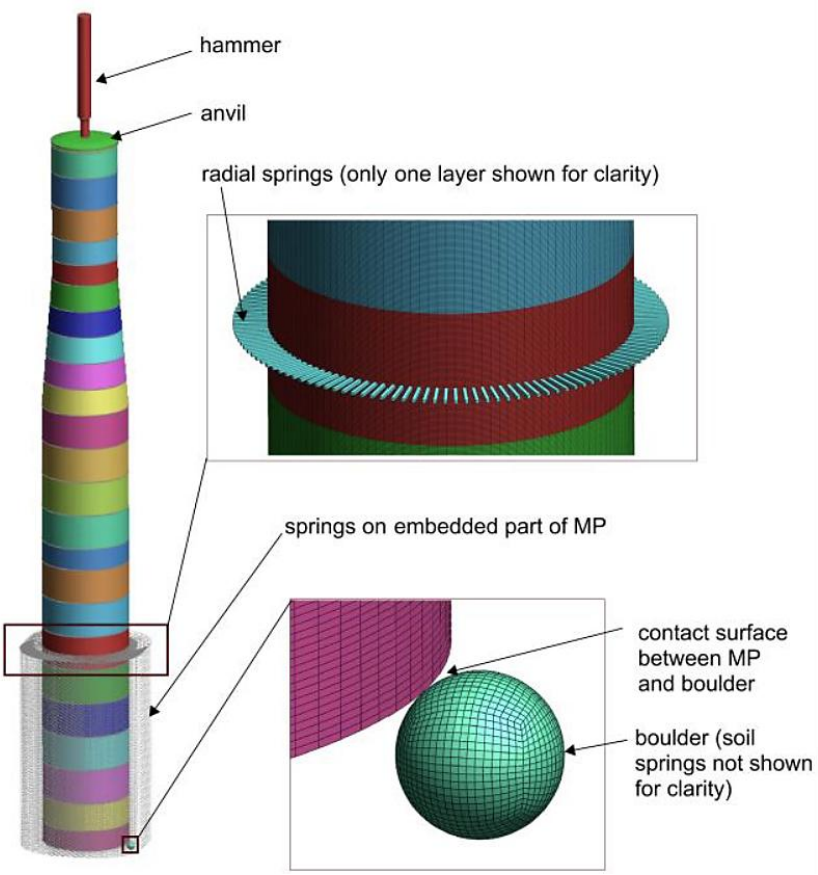


Figure 2-16 Soil spring model (Palmieri et al., 2023)

Two types of over-consolidated clay were investigated, one with a lower strain stiffness and undrained shear strength (denoted LB soil) compared to another (denoted UB soil). The research shows that the pile tip would continue buckling after boulder impact in UB soil, while, in LB soil, the buckling will reach to a plateau after a certain depth. The research also contains a parametric study of the contact angle between the line connecting the pile tip to the boulder centre and the horizontal axis. It suggests that the contact angle of 75° would cause the largest distortion, while 90° the least. However, the highest plastic strain was found at the angle of 90°, with the largest reduction in penetration depth under the same hammer blow.

The model, similar to the BASIL model (Erbrich *et al.*, 2011), provides an efficient tool for the evaluation of the tip buckling. While it considers the elasticity of the boulder, limited parametric studies have been conducted in relation to the effects of this elasticity. Meanwhile, although the boulder was pushed into the soil for a considerable distance, especially in the models with LB soils, the potential gaps formed due to the boulder movement were not sufficiently considered[3]. This gap could be addressed by incorporating a tension cut to the soil spring opposite to the direction of boulder movement. The application of the soil spring also made the boulder rotation excluded from the calculation. The boulder rotation, however, could be an important factor affecting the tip deflection. For example, considering an ellipsoidal boulder, the rotation can alter the projected area of the boulder in the horizontal plane, leading to varying degrees of obstruction to the pile trajectory. A potential solution could be to add slider elements or perpendicular springs to the original ones at each node. Nevertheless, this spring model can be a preliminary study for an alternative calculation approach compared to FEM analysis.

[3] This information was obtained from a discussion with the author during the conference SUT 2023.

Le et al. (2023)

Le *et al*. (2023) established a laboratory-scale model test to investigate the pile-boulder interactions in sand, and the geometry of the model is shown in Figure 2-17. During the test, the pile was hammered into the sand, where a steel boulder was placed midway through the penetration depth during the pluviation. The boulder was painted with marks, helping reconstruct the trajectories and the rotations of the boulders. The pile had a D/t ratio at $200\ \text{mm}/1\ \text{mm} = 200$, while the boulder diameter was 50 mm. The plastic strain of the pile tip was assessed using a 3D scanning system with white light fringe projection technology. Two surcharge load levels were tested, given that the higher stress level would result in higher distortion at the pile tip.

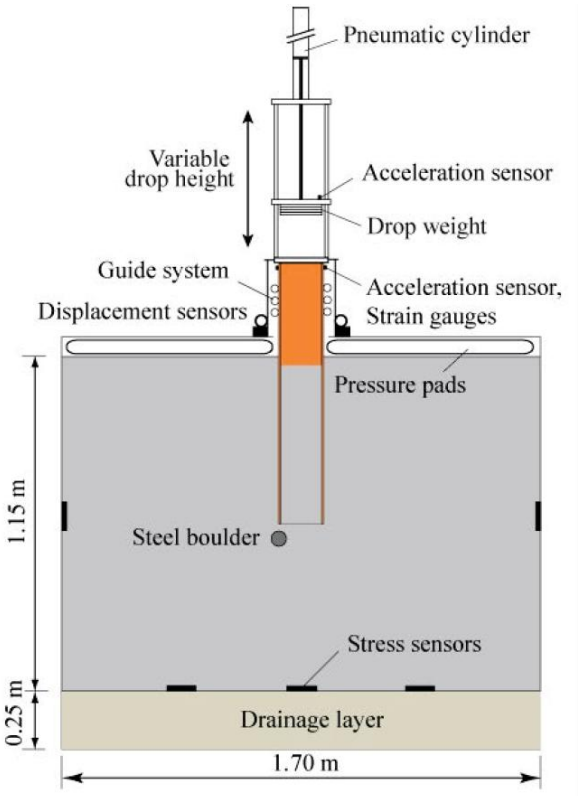


Figure 2-17 Model test setup (Le et al., 2023)

The presented model test is part of a project aiming to understand the behaviours of the pile and the boulder after the impact. A subsequent 3D analysis will be constructed to recreate the

test. Similar to the test conducted by Nietiedt (2022), the boulder in the test was placed into the dry sand with surcharge loads. Though boulders are less likely to be found in sand, this practice is understandable, as it can be challenging to maintain the boulder in the designated location within the clay after consolidation. The marks on the boulder may be able to indicate the contact point, however, the interacting procedure between the pile and the boulder still remains unknown. It would therefore be useful to create a test enabling clear observation of the process.

Summary and comparison of the research

An overview of the existing research is presented in Table 2-3, with Bakroon *et al.* (2019) marking the initial application of numerical techniques for high-speed large-deformation problems. A detailed discussion of the gaps between the current research and the practice can be seen in the next section.

Table 2-3 Summary of current research on the progressive buckling of piles

Reference	**Contribution**	**Technique**	**Limitations**
Kramer (1996)	Recreation of Goodwyn-A pile failure; parametric studies of the initial dent, D/t ratio, cell pressure; maximum deformation at given penetration depth	Analytical solution and lab test of denting force; numerical model based on the analytical solution	The soil reaction was represented by a series of elastic springs
Aldridge *et al*. (2005)	Vertical and horizontal concentrated denting forces at the tip of a perfect cylinder	Plastic-hinge model and FEM analysis	The plastic-hinge model was based on a flat plate; the soil effect was excluded
Erbrich *et al*. (2011)	BASIL soil spring model for advancing piles	In-house numerical simulation	The effects of the soil plug were excluded; the introduction of a boulder may be difficult
Holeyman *et al*. (2015)	The possibility of pile failure due to boulder impact in the vertical direction	Modified 1D wave propagation model	The pile deformation was excluded

Gargarella (2018)	A failure envelope of boulder movement in the plane of F_y-F_x; Relationship between the peak contact force and the boulder displacement	GRLWEAP, PLAXIS simulation, and boulder fracture test	The pile deformation and boulder movement were analysed independently
Stevens *et al*. (2019)	The interaction between an advancing pile and a hard layer; stress distribution in the pile after boulder impact	1D to 3D numerical simulation	The boulder was simplified into a series of vertical springs at the pile tip
Bakroon *et al*. (2019)	Relationship between the failure modes of piles and their initial imperfections; relationship between the penetration rate and the pile buckling	LS-DYNA simulation	The boulder was fully fixed within the soil
Nietiedt (2022)	Failure envelopes indicating the denting force with corresponding parameters	Centrifuge test and Abaqus CEL simulation	The research was based on sands
Palmieri *et al*. (2023)	A soil spring model for quick evaluation; parametric study of the contact angle of boulder impact	In-house numerical simulation	The potential gaps formed within the soil due to boulder movement were neglected
Le *et al*. (2023)	Lab-scale test in dry sand; parametric study of surcharge load	Lab-scale model test	The test was based on sands and the boulder positioning technique was not clear

2.3 GAPS BETWEEN THE PRACTICE AND RESEARCH

The review of the current standards and research suggests that the studies on piles and boulders are typically conducted independently. The tip imperfection force and the boulder resistance are then compared with each other, giving a possibility of tip buckling (Gargarella, 2018; Holeyman *et al*., 2015; Nietiedt, 2022). This methodology might favour the pile design in practice and can be easily incorporated with the current design code. However, there are still several uncertainties, which may not necessarily be unconservative, but could be improved with further study.

Parametric study of imperfection force

The studies of the imperfection force in geotechnical engineering either rely on simple plastic-hinge models (Aldridge *et al*., 2005; HSE, 2001; Kramer, 1996), or classical FEM simulations (Aldridge *et al*., 2005; Gargarella, 2018; Nietiedt, 2022). An advantage of such methods is the conciseness of the analytical expressions, especially compared with those presented in Section 2.2.1. However, the possible resistance from the soil plug is neglected. Because it is usually hard to effectively measure the imperfection force during an experiment, evaluating the accuracy of the solutions becomes difficult. One potential solution to this problem could involve conducting a parametric study using the FEM for large-deformation problems, where the pile is wished-in-place within the surrounding soil. A simpler alternative, meanwhile, would be to add soil springs on the internal side of the pile wall, with tension-cutoffs on the external springs where applicable.

Instead of using a wished-in-place pile, this research investigates the pile buckling behaviour of an advancing pile with a boulder buried within the soil. This is because the dynamic effects of the advancing pile can influence the magnitude of the contact force at the moment of pile-boulder collision.

Evaluation of boulder behaviour

The evaluation of boulder behaviour is primarily based on numerical techniques (Gargarella, 2018; Nietiedt, 2022), either in the regime of small-deformation or large-deformation calculations. These studies give the failure pattern or failure envelope of the boulder under a point load at a static location. In practice, however, the contact point between the pile and the boulder would continuously change as the penetration proceeds. Therefore, rather than remaining within a single failure envelope, the trajectory of the boulder reaction force may

span across multiple envelopes as the contact eccentricity changes. However, obtaining the instantaneous boulder reactions during the experiment seems unachievable. Numerical simulation may be the only viable option, provided that its validity is effectively proved by physical models.

Instead of a failure envelope of the boulder, this research establishes a connection between the tip deflection and the factors in relation to the boulder mobility and the pile capacity (as shown in Chapter 4). A laboratory-scale physical modelling approach, in addition, is established to calibrate the numerical model, ensuring its validity.

Pile simulation using shell elements

Another common practice in numerical simulations is to use shell elements to model the pile (Bakroon *et al*., 2019; Erbrich *et al*., 2011; Nietiedt, 2022; Palmieri *et al*., 2023). In fact, regarding the thick pile wall as a shell structure is also the practice in the current offshore design codes (see Section 2.1). Whether the pile can be regarded as a shell structure should be determined by the pile geometry and the loading condition. However, in numerical simulations, the shell element may become problematic when it needs to interact with other structures, especially the surrounding soil. This is because the resistance from the pile wall thickness may not be sufficiently accounted for. A calculation example is presented in Chapter 3 to address this issue.

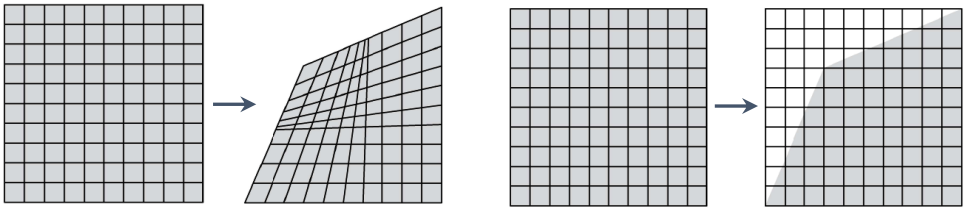
CHAPTER 3 TWO-DIMENSIONAL PLATE PENETRATION

3.1 COUPLED EULERIAN-LAGRANGIAN METHOD

The Finite Element Method (FEM) developed in the 1960s' has become one of the most prevalent numerical techniques in the engineering field. Analyses that use FEM for large-deformation problems have two categories: meshed or meshless methods. Meshed methods apply the concept of *domain discretisation* and have two main variants based on the descriptions of material deformation (Qiu *et al*., 2011a), as shown in Figure 3-1, where the material flow is coloured with grey:

1) *Lagrangian description*, which is the basis of classical FEM, gives a velocity field of material as a function of initial coordinates and time, namely, $V = f(x_0, y_0, z_0, t)$. This means that meshes deform with the domain and the boundaries of different materials can be explicitly tracked. However, unless remeshing is performed, the Lagrangian description can only be used for small-deformation problems where mesh distortion is not too severe to maintain the accuracy of predictions;
2) *Eulerian description* gives a velocity field of material deformation as a function of position and time, namely, $V = f(x, y, z, t)$, which treats the material as flowing

through a constant meshed domain. This means that the mesh does not deform with the material, which eliminates mesh distortion and thus enables the analysis of large-deformation problems, but at the price of greater difficulty tracing interfaces between different materials.



(a) *(b)*

Figure 3-1 Mesh and material
(a) Lagrangian description; (b) Eulerian description

To capture the features of high-speed problems in fluid mechanics, such as gas explosions, a hydrocode incorporating the advantages of both Lagrangian and Eulerian descriptions was developed by Noh (1963) named as the *Coupled Eulerian-Lagrangian (CEL) method*, mathematical derivations of which can be referred to Benson (1992).

An analysis based on CEL starts with a conventional Lagrangian phase with nodes attached to the deformed material, followed by a remapping phase where the displaced nodes are remapped back to the Eulerian mesh along with the convected state variables (Kong, 2015). The degree of material occupancy in an Eulerian element is measured by a coefficient, Eulerian Volume Fraction (EVF), ranging from 0 (void element) to 1 (fully filled element). Material boundaries within a partially-filled element can be calculated based on the EVF of surrounding elements in an average sense (Abaqus, 2014). To obtain a smooth and rational profile of material boundaries, fine meshes with regular shapes and small dimensional variations are therefore required.

In geotechnical engineering, CEL, along with the related methods, Arbitrary Lagrangian-Eulerian (ALE) method, has proved to be effective for the simulation of large-deformation problems including rigid pile installation in both undrained and drained soils (Qiu *et al*., 2011; Hamann *et al*., 2015; Rooz and Hamidi, 2019), buckling of offshore pipeline (Kong, 2015; Kong *et al*., 2017), the interaction between soil and thin-shell foundations (Ko *et al*., 2017; Bakroon *et al*., 2018; Xiao *et al*., 2019), and the progressive buckling of monopiles due to boulder impact (Nietiedt, 2022).

3.2 BENCHMARK MODELS FOR PLANE-STRAIN MODELS

Prior to the full-scale simulation of monopile penetration, 2D models were constructed for an initial validation study, based on the in-built CEL algorithm in Abaqus/Explicit 2019. Using 2D plane-strain models could save computing time, but it is not possible in Abaqus CEL since the software supports 3D CEL analysis only. The most efficient solution is to use a unit element length and a single layer of elements in the out-of-plane direction so that the 3D model performs equivalently to a 2D plane-strain model. Because there was only one element throughout the Z-direction (into the page), and the stress state along this direction was considered uniform, the structure was considered less likely to distort in the out-of-plane direction. Certain boundary conditions, as discussed in Section 3.2.1 and Section 3.2.2, were also applied to ensure a plane-strain modelling condition. Two benchmark models, in addition, were created to evaluate the reliability of this equivalent 2D model in Abaqus CEL for solving geotechnical problems involving the penetration of objects into undrained clay.

3.2.1 STRIP FOOTING PENETRATION MODEL

Reference solution: In the absence of surcharge load and soil weight, the exact solution for the bearing capacity of a strip footing on a semi-infinite elastic-perfectly plastic soil is obtained

using the Prandtl mechanism (Prandtl, 1921). The normalised strip footing bearing capacity factor N_c is

$$N_c = \frac{V}{s_u BL} = 2 + \pi \approx 5.14 \qquad \textit{Eqn. 3-1}$$

where V is the vertical reaction force at failure, s_u is the undrained shear strength of the soil, and B, L are the width and length of the footing, respectively. However, Eqn. 3-1 is only suitable for small-deformation scenarios where no significant footing penetration occurs. Further studies on the bearing capacity of an embedded strip footing led to an empirical expression for N_c (Salgado *et al*., 2004),

$$N_c = (2 + \pi)\left(1 + 0.27\sqrt{\frac{d}{B}}\right) \qquad \textit{Eqn. 3-2}$$

where d is the embedment depth. Eqn. 3-2 has been validated against experimental and numerical data (Salgado *et al*., 2004; Gourvenec *et al*., 2006) and thus can be used to validate the present strip footing modelling. However, it should be noted that Eqn. 3-2 pertains to a footing that has been "wished-in-place" at a predefined embedment, rather than being continuously penetrated from the surface as is done in the analysis described below.

Model properties: Instead of modelling the entire domain, only half of the domain was simulated using symmetrical boundary conditions to save computing time, as presented in Figure 3-2 (a). The model was composed of three parts: Eulerian domain, Lagrangian rigid strip footing of width $B = 1$m, and meshless soil material. The tangential interactions between the footing and the soil were simulated with the in-built frictionless (smooth) interface of Abaqus. According to the stress contours in preliminary trials (not shown) and the suggestions in Kong (2015), the width of the Eulerian domain was $W = 5B$, and the height was $H = 5B$ to eliminate the boundary effect. The depth of the undeformed soil domain was $D = 4.5B$, with

a void layer with a height of $0.5B$, enabling the soil heave as shown in Figure 3-2 (a). To obtain an equivalent 2D plane-strain condition in 3D space, the assembly had unit thickness, $L_z = B$, in the Z direction.

The behaviour of the rigid strip footing was governed by a reference point at its geometric centre which was subjected to displacement control. The final penetration depth d was divided by the total step period T, which then gave the penetration speed as $v = d/T$. In the models presented in this chapter, $v = 0.1B$/s.

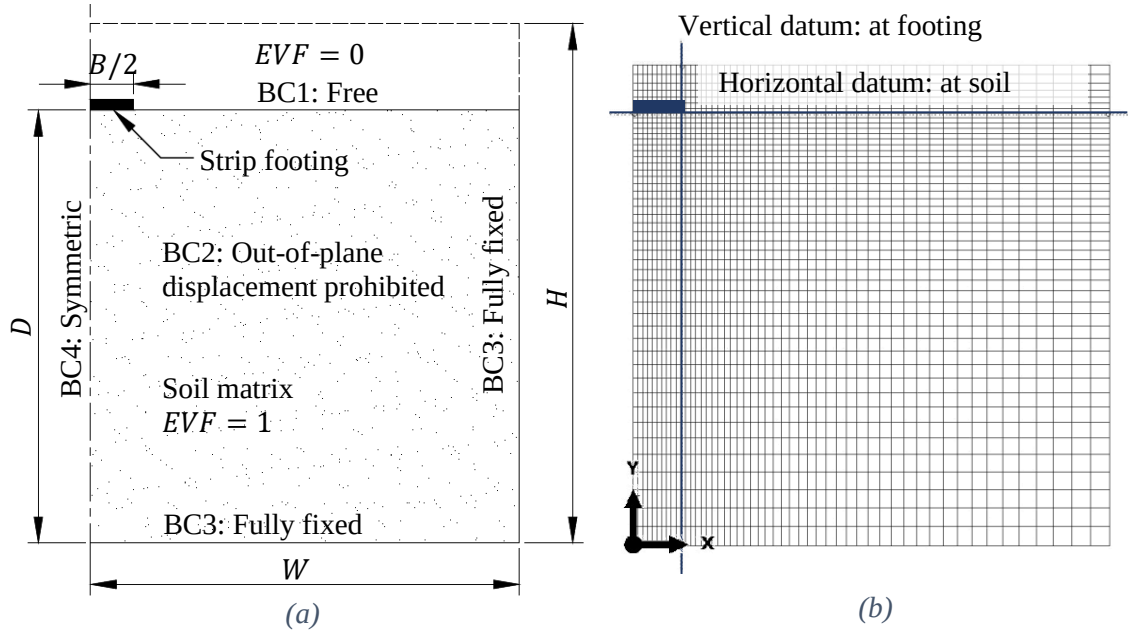


Figure 3-2 Strip footing penetration model
(a) Model geometry and boundary conditions; (b) Meshing scheme

Material properties: The soil was modelled as a weightless elastic-perfectly plastic material with the von Mises failure criterion, with density $\rho_s = 0.1$ kg/m^3, and Young's modulus E_s defined as a multiple of s_u, $E_s = 500 s_u$. The soil matrix is incompressible under undrained conditions, and its Poisson's ratio was therefore modelled as $\nu = 0.49$. Abaqus follows the classical definition of tensile yield strength of metals, while the geotechnical characterisation

of soil failure is governed by the shear strength s_u. Therefore, in the input to Abaqus, s_u needs to be replaced by the corresponding tensile stress F_t following the relationship $F_t = \sqrt{3}s_u$.

Table 3-1 SFP models for mesh sensitivity test

Model	L_{min}	L_{max}	No. of elements, N
SFP1	0.10B	0.20B	1225
SFP2	0.05B	0.20B	2448

Meshing scheme: Figure 3-2 (b) gives the meshing strategy for the Strip Footing Penetration (SFP) model. Elements with the minimum side length, L_{min}, are clustered around the edge of the footing, then gradually increased to the maximum length, L_{max}, as shown in Figure 3-2 (b). Two models were constructed with different element counts for the mesh sensitivity test, using the mesh sizes and element counts, N, listed in Table 3-1. The reaction force on the footing, R_{sf}, was normalised following Eqn. 3-1 as $\tilde{R}_{sf} = R_{sf}/s_u BL$, and compared with Eqn. 3-2 using the error measure L_2-norm, defined as

$$L_2 = \sqrt{\Sigma\left(\tilde{R}_{sf} - N_c\right)^2 / \Sigma(N_c^2)} \qquad \textit{Eqn. 3-3}$$

where N_c was calculated using Eqn. 3-2 by substituting the instantaneous penetration depth at the corresponding $\tilde{R}_{sf}$. As shown in Figure 3-3, significant differences occurred at the start of penetration, where the soil first experienced elastic compressive deformation; a better approximation of rigid-plastic behaviour could be obtained by increasing the soil stiffness, E_s. The calculation of Eqn. 3-3 started from $d/B = 0.1$ to exclude these large differences. Mesh SFP1 gave results higher than Eqn. 3-2 with $L_2 = 5.40\%$. Mesh SFP2 decreased this value to $L_2 = 1.17\%$, which indicated quick convergence of the model. Further refinement of the elements could give improved results, but with a price of higher computational cost.

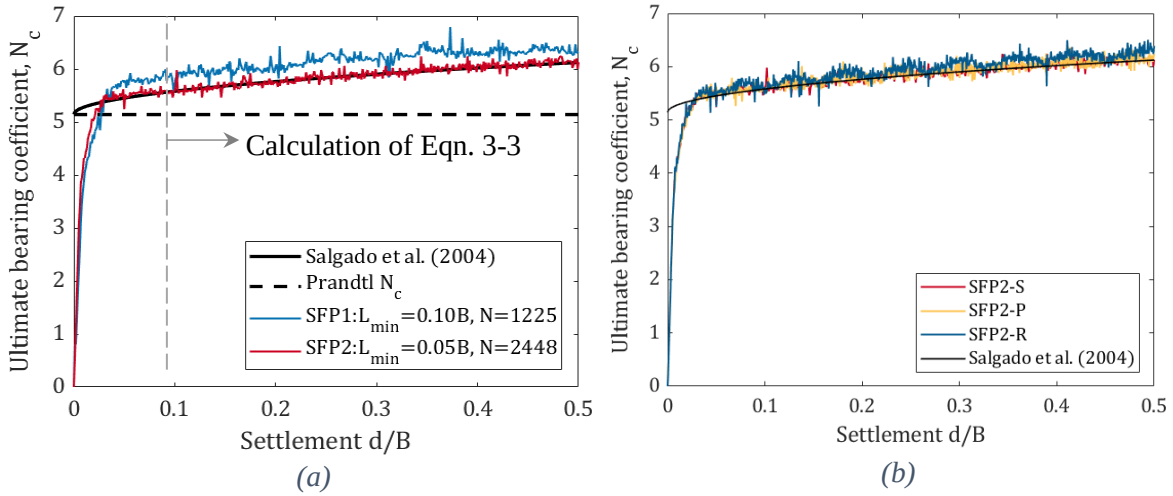


Figure 3-3 Abaqus CEL results and reference solution
(a) Mesh sensitivity; (b) Effects of contact property

Given that Eqn. 3-2 should not be affected by the interface roughness of the footing, two additional tangential interactions were introduced to model SFP2. With smooth interaction on all surfaces, SFP2 is referred to as SFP2-S in Figure 3-3. SFP2-P refers to the penalty condition on all surfaces with frictional coefficient $\mu = 0.5$, and the allowable maximum shearing stress set to be $\tau_{max} = s_u$. The in-built rough surface condition was implemented for SFP2-R. The normalised reaction force $\tilde{R}$ was again compared with Eqn. 3-2. The consistency between the computational results and the reference solution in Figure 3-3 suggests that the same bearing capacity obtained from the Abaqus CEL model is insensitive to the interface conditions.

3.2.2 SQUARE BOULDER ROTATION MODEL

A more complex problem is the bearing capacity of a shallow strip foundation subjected to combined loadings, including vertical F_y and horizontal F_x forces, and moment around the Z axis M_z. Previous studies related to this topic (Houlsby & Puzrin, 1999; Martin, 1994; Richards *et al.*, 2021) suggested a failure envelope in the shape of a rugby ball in F_x-F_y-M_z space. This idea of a failure envelope can also be applied to boulder-soil interaction and a study with respect to a 2D circular boulder can be seen in Gargarella (2018). Considering the interaction between

a penetrating pile and a boulder, a more relevant scenario would be a boulder subjected to F_y at an eccentricity e, which is equivalent to a force F_y along the central line of the boulder with a simultaneous moment $M_z = F_y e$ taking account of the effect of eccentricity.

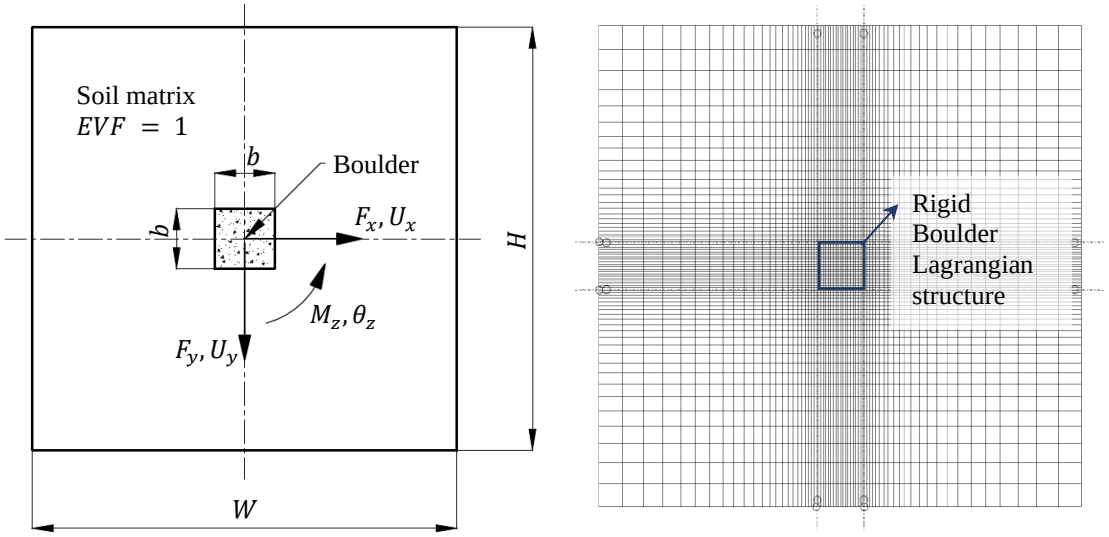


Figure 3-4 Square boulder rotation model

(a) Model geometry and parameter conventions; (b) Meshing scheme

Model properties: Figure 3-4 (a) presents the geometry of the Square Boulder Rotation (SBR) model in Abaqus CEL. The meshless soil occupied the entire Eulerian domain except for the boulder area ($b \times b$ with $b = 1$ m). The four sides of the Eulerian domain were fully fixed with width (W) and height (H) at $10b$. Similar to the SFP model, out-of-plane displacements were prohibited to mimic 2D plane-strain conditions with the 3D model. As shown in Figure 3-4 (b), finer elements were clustered around the boulder with a side length of $0.05b$, with coarser elements at $0.5b$ spread along the outer boundaries. The failure envelope in Abaqus CEL was obtained using displacement-controlled probe tests – the model had a vertical displacement U_y and a rotation θ_z assigned at the reference point of the rigid boulder. The reference point was defined as the geometric centre of the boulder in Figure 3-4 (a). For dimensionless analysis, a combination of U_y and θ_z was assigned to the boulder with a ratio:

$$r = \theta_z b / U_y \qquad \textit{Eqn.3-4}$$

As U_y and θ_z increase from zero to their assigned final values, the reaction-force trajectory extracted from the reference point of the boulder, or the load path in M_z-F_y space, departs from zero, reaches the failure envelope, and travels along the envelope afterwards. For the dimensionless study, M_z and F_y were normalised following

$$\tilde{M}_z = \frac{M_z}{s_u b^2}, \qquad \tilde{F}_y = \frac{F_y}{s_u b} \qquad \textit{Eqn.3-5}$$

Focusing on the first quadrant of the $\tilde{M}_z$-$\tilde{F}_y$ plane, the ratio r is in the range $r \in [0, +\infty)$, where $r = 0$ denotes pure downward movement and $r \to +\infty$ denotes pure rotation. To exclude the influence of friction, a smooth tangential interaction between boulder and soil was introduced to the model using in-built functions. Considering an undrained condition with Poisson's ratio $\nu = 0.49$, the soil was modelled as a weightless elastic-perfectly plastic material with the von Mises failure criterion, with density $\rho_s = 0.1\text{kg/m}^3$, and Young's modulus E_s defined as a multiple of s_u, $E_s = 500 s_u$.

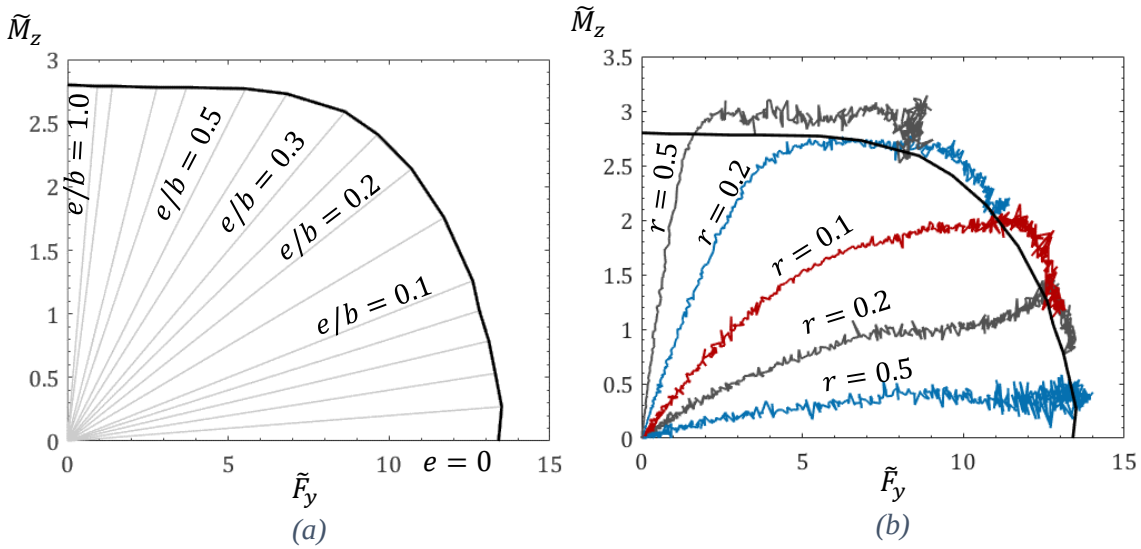


Figure 3-5 Failure envelope in the first M_z-F_y quadrant

(a) Load paths in OxLim2D; (b) Failure envelope obtained from Abaqus CEL and OxLim2D

Verification technique: Independent verification of the SBR model in Abaqus CEL was conducted using OxLim2D, which was designed for plane-strain analysis under the framework of Finite Element Limit Analysis (Martin, 2011). The program calculates the upper bound (UB) and lower bound (LB) solutions simultaneously, and the best estimation is given as the average (AVG) of the two with an error measure ($err\%$) (Dunne, 2017):

$$AVG = \frac{UB + LB}{2}, \qquad err\% = \pm\frac{UB - LB}{UB + LB} \times 100 \qquad \textit{Eqn.3-6}$$

Adaptive mesh refinement is conducted until $err\%$ reaches a predefined tolerance, which was $\pm 2\%$ in this research. Compared with Abaqus CEL, OxLim2D has four major differences in modelling:

1) OxLim2D simulated the boulder as a square hole with four rigid edges within the soil domain instead of an independent rigid body. Smooth tangential interaction was imposed on the boulder edges by defining the interface $s_u = 0$, and tensile stress in the normal direction was prohibited by the in-built tension cut-off function, which allowed for potential separation between boulder and soil, and kept the model features consistent with those in Abaqus CEL,
2) OxLim2D has an in-built Tresca criterion, which is equivalent to the von Mises criterion under plane-strain conditions. Thus, s_u was directly used as the input strength,
3) Instead of seeding edges with specified element sizes, only a maximum triangle area was needed, with adaptive mesh refinement taking place at each iteration until the target $err\%$ was reached,
4) A combination of M_z and F_y was directly assigned to the boulder in OxLim2D so that e was simply the ratio of M_z to F_y. The load paths, presented as grey lines in Figure 3-5 (a), depart from the origin and stop extending when they reach the failure envelope.

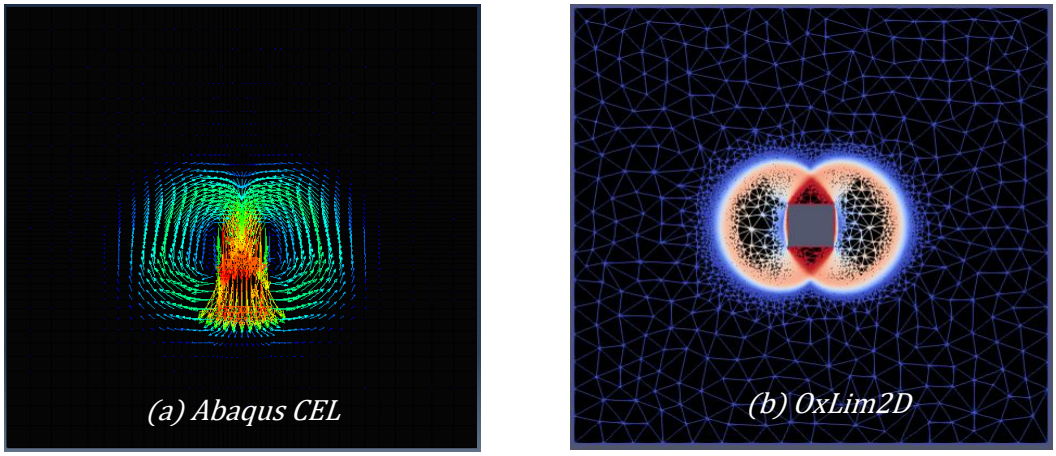


Figure 3-6 Total velocity field of soil around square boulder moving downward (colours indicate velocity magnitude)

A comparison of the results obtained from Abaqus CEL and OxLim2D in Figure 3-5 (b) shows that Abaqus CEL overestimated the failure envelope by ~5%. A comparison of the velocity field in the soil around the boulder showed that both Abaqus CEL and OxLim2D gave the same flow-round failure mode. An example in relation to a downward-moving boulder is given in Figure 3-6.

3.3 PLATE PENETRATION MODEL

The 2D modelling of plate-boulder interaction assumes that the localised behaviour of a monopile with an extremely large D/t ratio can be represented by a plate strip in the longitudinal direction of the cylinder. It can be regarded as a combination of the two benchmark models considered earlier in this chapter, where the advancing pile is equivalent to the penetrating strip footing, albeit with added complexities due to the plate flexibility.

3.3.1 MODEL DESCRIPTION

Model components and boundary conditions: Figure 3-7 (a) shows the geometry of a typical Plate Strip Penetration (PSP) model with a square boulder. For dimensionless analysis, the model dimensions were defined as multiples of the plate thickness, t, which was taken as $t =$

1 m. The Abaqus CEL model contained four Lagrangian components (plate sleeve, plate cap, plate, boulder) and a soil block ($W \times H = 200t \times 200t$) lying in the Eulerian domain with three edges fully fixed (BC2). A void layer with a height $H_0 = 25t$ was defined above the free soil surface (BC1) to permit soil heave. Few studies have investigated the influence of boundary effects; it was assumed that positioning the boundaries at 200 times the plate thickness and at least ten times the boulder size should be sufficient, based on our experience with the two benchmark models.

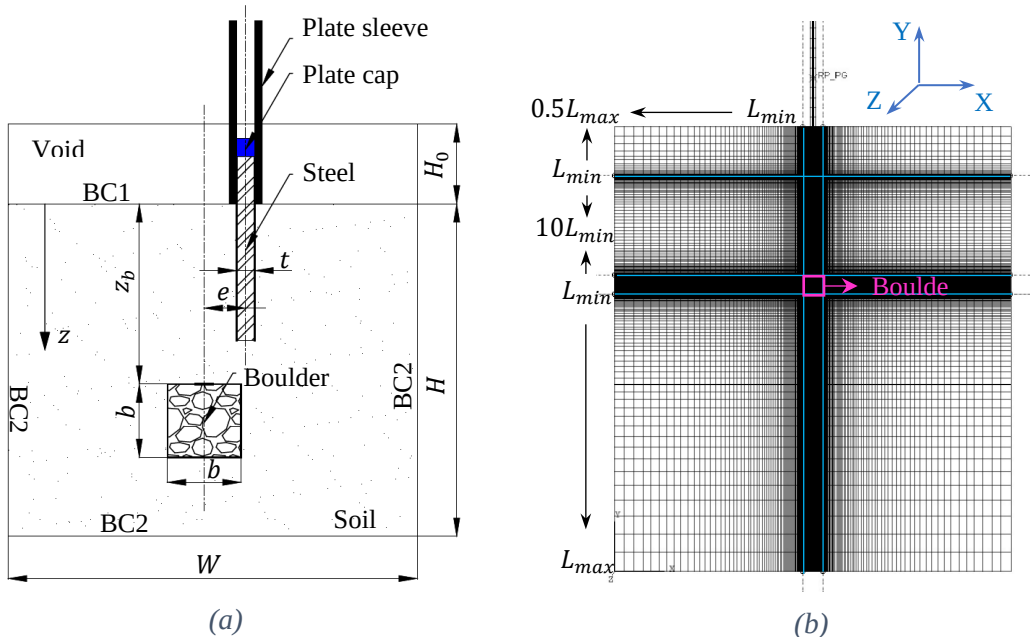


Figure 3-7 2D plate penetration model

(a) Geometry and boundary conditions; (b) Meshing scheme example with global coordinates

With elastic-plastic material properties and a length of $100t$ assigned to the plate, it was not ideal to assign displacement directly on the plate. Instead, a rigid plate cap was placed onto the top of the plate, through which the plate was jacked into the ground at a speed $v = 0.1t/\text{s}$ under displacement control. The penetration direction is denoted by local coordinate z in Figure 3-7 (a). To prevent possible Euler buckling of the plate in the space above the soil, a pair of fixed rigid plate sleeves was introduced as a penetration guide. The boulder was modelled as a rigid

body “floating” (i.e., free to displace) within the soil, with its shape, dimensions, and embedment depth becoming three variables for the parametric study. In this way, the model was able to capture the boulder movement in three degrees of freedom (two transitional, one rotational) under the plane-strain condition.

Contacts: For simplicity, the contact conditions at all interfaces were defined as “Frictionless” in the tangential direction and “Hard” in the normal direction using the in-built functions in Abaqus. To be specific, the model did not incorporate frictional behaviour for interactions between the pile and boulder, pile and soil, or boulder and soil.

Material properties: Both the soil and the plate were simulated as elastic-perfectly plastic materials using the von Mises failure criterion. Given the likely field scenario of the plate penetrating into undrained stiff clay, typical ranges of material properties for both steel and soil are listed in Table 3-2. These typical values gave two variables representing the relative strength (r_σ) and stiffness (r_E) between plate and soil:

$$r_\sigma = \frac{\sigma_Y}{s_u} = 690\sim6500, \qquad r_E = \frac{E_p}{E_s} = 840\sim21000 \qquad \textit{Eqn. 3-7}$$

Table 3-2 Likely range of material properties in field scenario

Material	Strength	Young’s modulus	Poisson’s ratio
Steel (pile)	$\sigma_Y = 345 \sim 650$MPa	$E_p = 210$GPa	$\nu_p = 0.3$
Stiff clay	$s_u = 100 \sim 500$kPa	$E_s = 100 \sim 500 s_u$	$\nu_s = 0.49$

These material properties were considered reasonable based on *a priori* knowledge from the literature. However, the output could potentially be applied more generally with careful normalisation schemes.

Meshing scheme: Element sizes as multiples of t in the Eulerian domain are presented in Figure 3-7 (b). Elements with minimum side length at $L_{min} = 0.2t$ were clustered around the boulder and the trajectory of the plate, then gradually became coarser towards the model boundaries. Elements with lengths equal to the plate thickness, t, were uniformly distributed throughout the plate, which means that only one element was placed across the plate thickness, as shown in Figure 3-8.

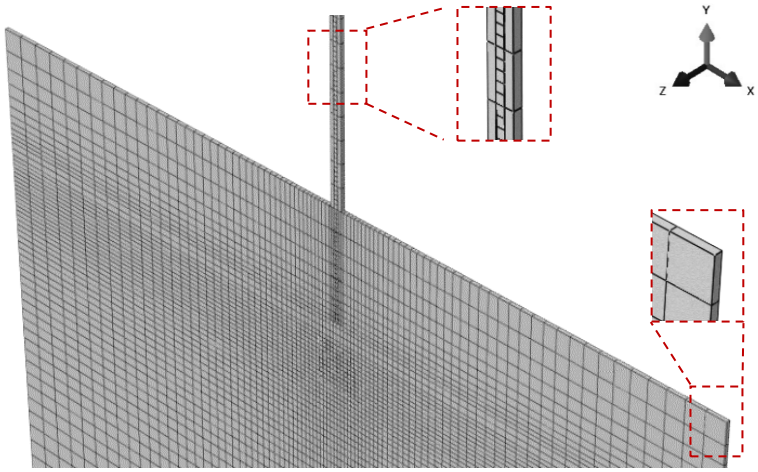


Figure 3-8 View of mesh showing single element in Z-direction (global coordinate)

3.3.2 ELEMENT SELECTION

The element in the Eulerian domain is coded as EC3D8R, the mechanical response of which corresponds to the 3D eight-node Lagrangian hexahedral element with reduced integration and viscous hourglass control, coded as C3D8R (Abaqus, 2014). A second-order advection scheme is implemented in each element to ensure the monotonic advection of material flow (Abaqus, 2014). This Eulerian element, EC3D8R, is used by default in Abaqus for nonthermal problems and cannot be modified. Therefore, the selection of suitable elements for this simulation focused on the Lagrangian structures, the flexible plate and the rigid boulder.

Plate

The plate can be simulated by shell or solid elements, and the former has been more common in the research related to piles, such as Bakroon *et al*. (2018) and Nietiedt (2022). However, the shell element may be problematic when interacting with the Eulerian material. This is because the normal direction of the element face is not uniquely defined, and the shell thickness may not be sufficiently considered.

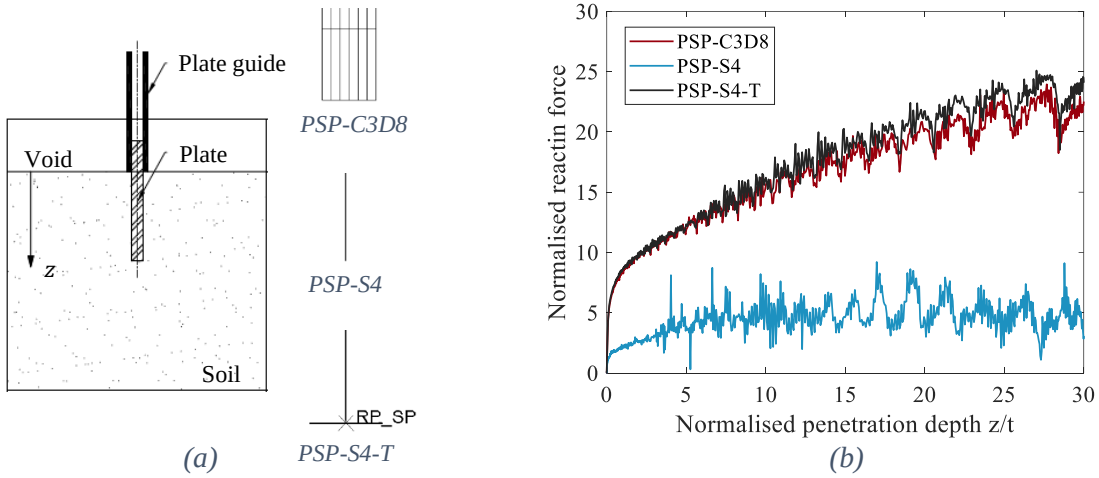


Figure 3-9 Plate penetration without boulder
(a) Model geometry and tip geometry; (c) Result comparison

An exploratory study is shown in Figure 3-9, where a flexible plate strip with a thickness of t [m] was pushed into the homogeneous soil. The linear hexahedral element, C3D8, and the linear quadrilateral shell element, S4, were used to simulate the plate for the investigation.

As shown in Figure 3-9 (a), six C3D8R elements were assigned across the thickness of the plate in model PSP-C3D8R, enabling consistent performance with plates modelled by S4 shell elements. Two tip geometries were tested for the plate modelled by S4, a straight-line shape in PSP-S4 and a T-shape in PSP-S4-T. In PSP-S4-T, a platform of the width t was attached to the plate tip (Figure 3-9 (a)). This platform was modelled rigid to prevent deformation during

penetration and thus became comparable to the base of the plate modelled by C3D8 continuous elements. The same meshing scheme was implemented in the Eulerian domain, with the smallest element under the plate tip having a width $t/6$, gradually increasing to the maximum, $10t$, around the model boundary. This meshing scheme was tested in preliminary studies (not shown) and ensured a converged result in both solid-element and shell-element models.

To compare the performance of the elements, the vertical reaction force at the plate head, F_p, was extracted and normalised following the equation,

$$\tilde{F_p} = F_p/s_u t M_t \qquad \textit{Eqn. 3-8}$$

where M_t was the model thickness, which was of unit element length, t. The penetration depth, z, was also normalised as $\tilde{z} = z/t$.

Figure 3-9 (b) indicates that the shell elements, PSP-S4, tended to underestimate the reaction forces at the plate tip compared with PSP-C3D8R. This underestimation could be due to the loss of the normal resistance provided by the shell thickness. The rigid platform in PSP-S4-T, acting as an "artificial shell thickness", could compensate for this and restore the correct bearing capacity at the plate tip. However, this rigid platform could be problematic when the boulder is introduced to the model and interacts with the plate tip. Therefore, the solid element would be preferable for the simulation of the flexible plate to give reliable predictions of the reaction force at the plate tip.

In addition to the bearing capacity, the element used for simulation was expected to capture the possible lateral buckling behaviour of the plate. This meshing scheme, therefore, was then tested using linear perturbation analysis based on a bottom-fixed cylindrical tube subjected to longitudinal compression.

The tube had a wall thickness of t, an outer diameter $100t$, and a length $100t$. Six eigenvalue-buckling modes were analysed, with the first being compared with the Timoshenko critical buckling stress (Timoshenko & Gere, 1961)

$$\sigma_{cr} = \frac{Et}{R\sqrt{3(1-\nu^2)}} \qquad \textit{Eqn. 3-9}$$

where E is the Young's modulus of the material, ν is the Poisson's ratio, and R is the radius of the tube. Substituting the model properties, $E = 210$ GPa, $\nu = 0.3$, and $R = 50t$, the critical buckling stress of the simulated tube is $\sigma_{cr} = 2.54$ GPa.

Four types of elements were investigated using Buckling of Cylindrical Tube (BCT) models, with the same element size equal to t uniformly distributed throughout the tube. The fully-integrated shell element, S4, and the solid element, C3D8, were again tested, the models denoted as BCT-S4 and BCT-C3D8, respectively. The elements with reduced integration, S4R and C3D8R, were also tested. Although the quadratic hexahedral element with reduced integration, C3D20R, cannot be used in Abaqus CEL, it was tested to provide a complete picture. The first buckling modes of the four models are shown in Figure 3-10 (a) to (d), and the computed critical buckling stress of each model is listed in Table 3-3, with the relative error ($err\%$) presented as the percentage of Timoshenko's critical buckling stress, for the models with solid elements, n_t denotes the number of elements across the thickness of the tube.

Table 3-3 Result comparison of critical buckling stress

Model	σ_{cr}**[GPa]**	$err\%$
Timoshenko and Gere (1961)	2.54	-
BCT-S4R	2.52	1.0
BCT-S4	2.52	1.0
BCT-C3D8R-$n_t = 1$	0.26	89.9
BCT-C3D8R-$n_t = 2$	2.22	12.7
BCT-C3D8-$n_t = 1$	2.05	19.5
BCT-C3D20R-$n_t = 1$	2.53	0.5

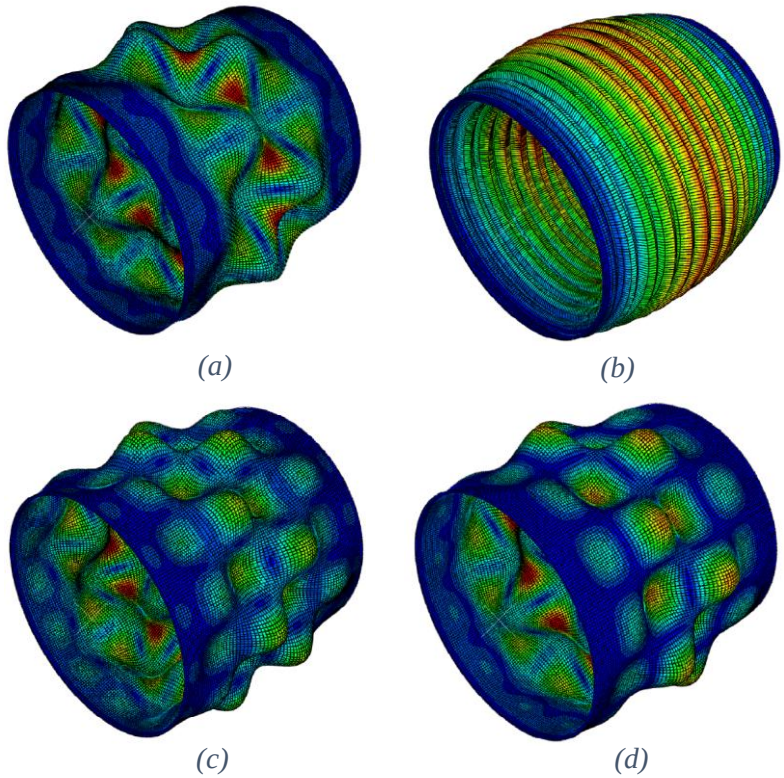


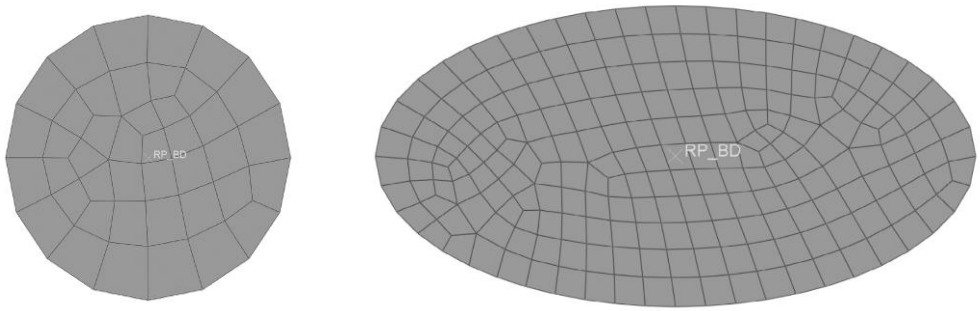
Figure 3-10 First eigenvalue-buckling mode
(a) BCT-S4; (b) BCT-C3D8R-$n_t = 1$; (c) BCT-C3D8-$n_t = 1$; (d) BCT-C320R-$n_t = 1$

Both shell elements, S4 and S4R, provide results comparable to the analytical solution. With a single element across the wall thickness, the quadratic solid element C3D20R performs the best among the solid elements. For linear solid elements, however, the full-integration formulation, C3D8, gives improved results compared to reduced integration, C3D8R, with $n_t = 1$. This finding is consistent with those of Bakroon *et al*. (2019). However, C3D8R gives slightly better prediction with $n_t = 2$. This is because the element C3D8R has only one integration point, which makes it difficult to capture the highly non-linear buckling behaviour of the structure, unless an increased number of elements are used.

A summary of the previous tests suggested that, though capable of capturing the buckling behaviour of the structure, the shell elements may not be suitable for the simulation of monopile installation in soil. On the contrary, the unique outward normal direction on a solid element

surface could give more explicit definitions of contacting conditions when the Eulerian material flows around the Lagrangian structure (Abaqus, 2014). Therefore, a balance between the accuracy of describing the eigenvalue-buckling behaviour and the end-bearing capacity of a thin-walled tubular pile should be considered. Given that the computing time is determined by the smallest element size, the plate is modelled by C3D8, with one element across the thickness.

Boulder



(a) *(b)*

Figure 3-11 Meshed boulders with curvatures
(a) Circular boulder, diameter 5t; (b) Elliptical boulder, 20t × 10t

Since it is modelled as a rigid body, the boulder has less stringent requirements on the mechanical response. However, the element length should be sufficiently small to approximate the curvatures of circular and elliptical boulders using straight element edges. The Lagrangian element C3D8R was used for these simulations, with the element length equal to the plate thickness, t. With the smallest diameter of the circular boulder at $5t$, this element length gave a polygon with at least 16 sides, which was considered sufficient to simulate the response of a circular boulder. With the increase of boulder dimensions, this curvature simulation became increasingly accurate with the increased number of polygon sides. The circular boulder with a diameter of $5t$ is presented in Figure 3-11 (a), along with an example of an elliptical boulder

in Figure 3-11 (b). In this case, the major and minor axes of the elliptical boulder are $20t$ and $10t$, respectively.

3.3.3 PENETRATION SPEED

In addition to the element size, the accuracy of an Abaqus CEL simulation of plate penetration is also influenced by the penetration speed. The rapid penetration tends to result in larger reaction forces from the pile top. This section intends to find a normalisation scheme to eliminate this speed effect. The dynamic effect in relation to the tip deflection, meanwhile, will be discussed in Chapter 4, along with the calibration of numerical models.

Seven models with different penetration depths were first established for the investigation. Because the duration of the penetration process is one second for all models, the penetration depth (as a multiple of t) can be equivalent to the penetration speed, v, symbolised by the constant in the model code z1 to z20. An alternative is to keep the penetration depth unchanged, but vary the duration of the penetration process. However, this alternative would significantly elongate the computing time.

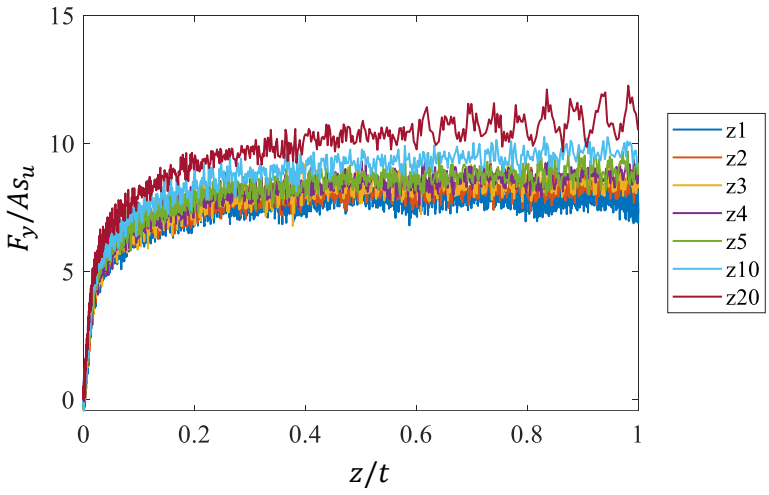


Figure 3-12 Effects of pile penetration speed

Figure 3-12 shows the comparison between the normalised vertical reaction force at the plate top, with the variation of the penetration speed. The comparison only covers the penetration depth up to $z = t$, because the model had the shallowest penetration depth of $z = t$. It is clear that the reaction force increases with the increase of the penetration speed. A normalisation scheme mitigating the effect of penetration speed is therefore given as

$$\widetilde{F_y} = \frac{F_y}{As_u} \times \left(\frac{\sqrt{E_s/\rho_s}}{v}\right)^{1/10} \qquad \textit{Eqn. 3-10}$$

where A is the base area of the plate; s_u is the undrained shear strength of soil; E_s is the Young's modulus of the soil; and ρ_s is the density of saturated soil.

The term $\sqrt{E/\rho}$ is the wave speed in an isotropic elastic solid, which, despite the existence of plastic deformation, is borrowed for the soil to normalise the penetration speed. The exponent $1/10$ is from trial and error, giving the best performance within the comparison range $z = t$, as shown in Figure 3-13.

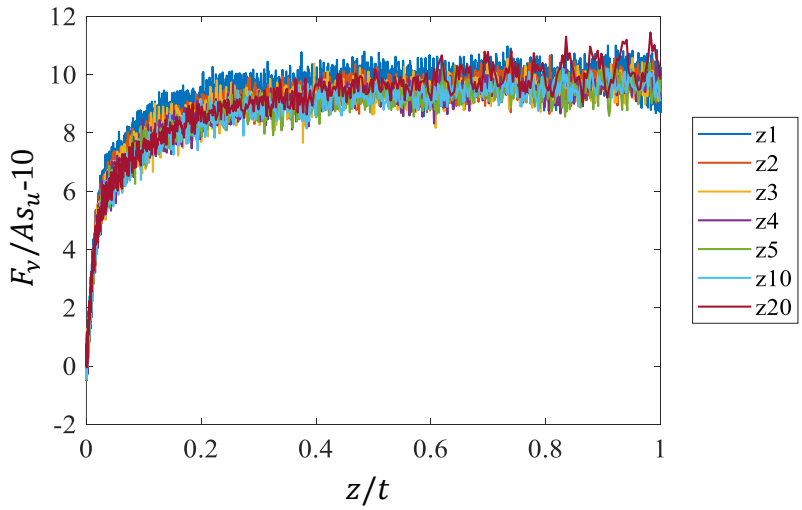


Figure 3-13 Results of index 1/10 in Eqn.3-10

Another group of models, meanwhile, was also carried out to investigate whether further decreasing the penetration speed below $v = t$ would change the model performance. Three

penetration speeds, $v = 1t$, $0.5t$, and $0.1t$/s, denoted as z1, z0.5, and z0.1, were analysed. The result comparison in Figure 3-14 suggests that the model reached a stable state $v = 1t$/s. Penetration slower than this will not affect the reaction force of the plate. Similar to Figure 3-13, because the shallowest penetration depth was $z = 0.1t$ in model z0.1, the result comparison only covers the range of $z = 0.1t$ in Figure 3-14. The Youngs's modulus of the soil was also increased from $E_s = 500s_u$ to $E_s = 5000s_u$ to ensure that the soil deformation enters the plastic range within the shallow penetration depth of $z = 0.1t$.

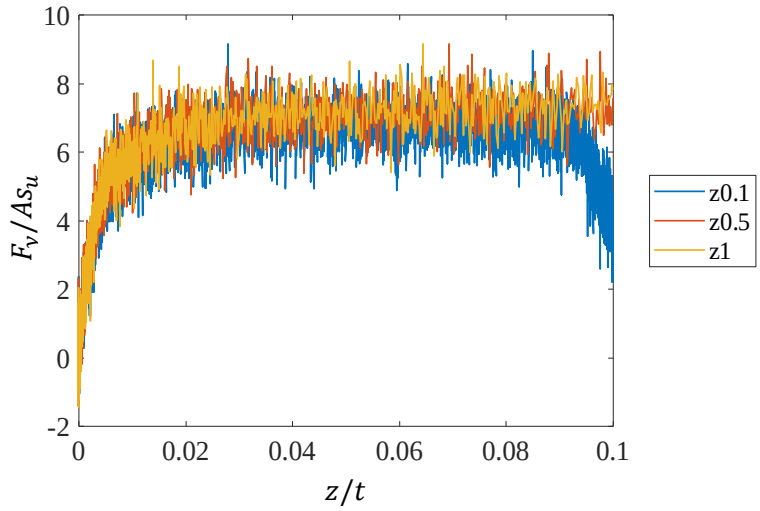


Figure 3-14 Results of penetration speed $v \leq t$

However, the slow penetration speed in a full-scale model would require a longer time length in one step, and thus higher computing cost. To figure out whether the penetration speed would have an influence on the plate deformation, the vertical logarithmic strain, LE33, was then extracted from models z1, z5, and z10 for comparison. Figure 3-15 suggests that the strain variations of the three models are consistent with each other. The deviations in model z1, meanwhile, were perhaps due to the use of smooth amplitude variation (Figure 3-15), which would lead to an extremely slow movement in the later part of the simulation.

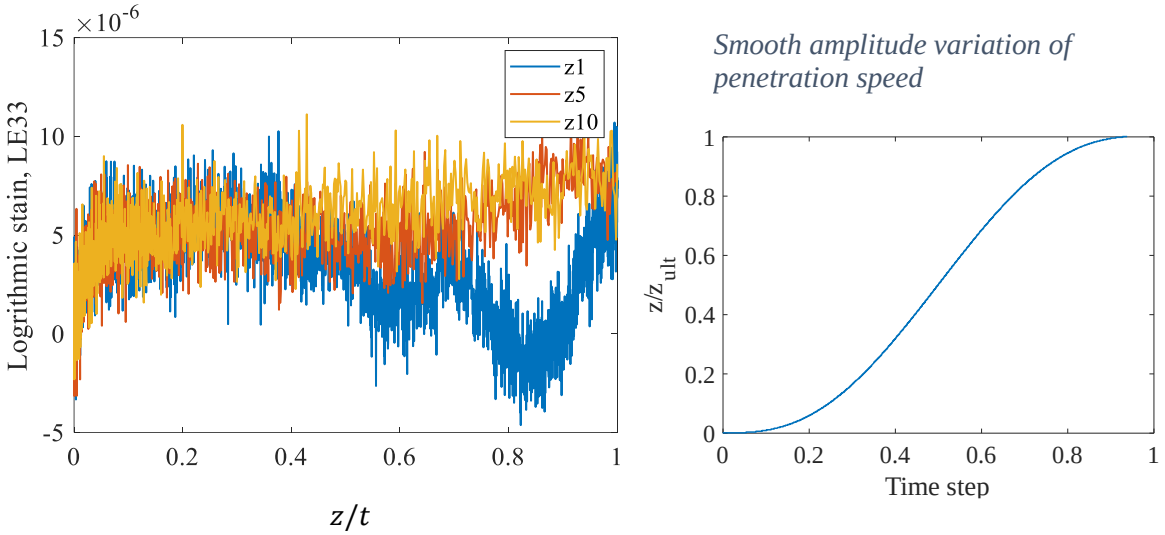


Figure 3-15 Comparison of LE33 (z_{ult}, ultimate penetration depth)

In the full-scale simulation, it is therefore recommended that the penetration should be completed within one second to save computing time. This would lead to an overestimation of the reaction force at the pile head, but may not cause a severe difference in the pile deflection. In addition, the reaction force can be calibrated using Eqn. 3-10 when necessary.

3.3.4 SOIL WEIGHT

Gravitational forces can affect the failure mechanism of the soil, especially when the boulder movement results in large gaps within the soil. Introducing gravity to the model, however, may bring additional stress waves to the model before the penetration starts. These stress waves were first observed in the 2D strip footing penetration models (not shown), which could be due to the sinking of soil subjected to self-weight. An additional calculation step can be added prior to the pile installation for these gravity-induced settlements. In this way, the settled soil would stay still at the start of pile penetration. However, unlike those in PLAXIS, this gravity-induced soil settlement cannot be reset in Abaqus.

To investigate the effects of gravity, the pile is removed from the model, leaving a buried boulder vertically penetrated into the soil. These analyses consider a Circular Boulder (CB).

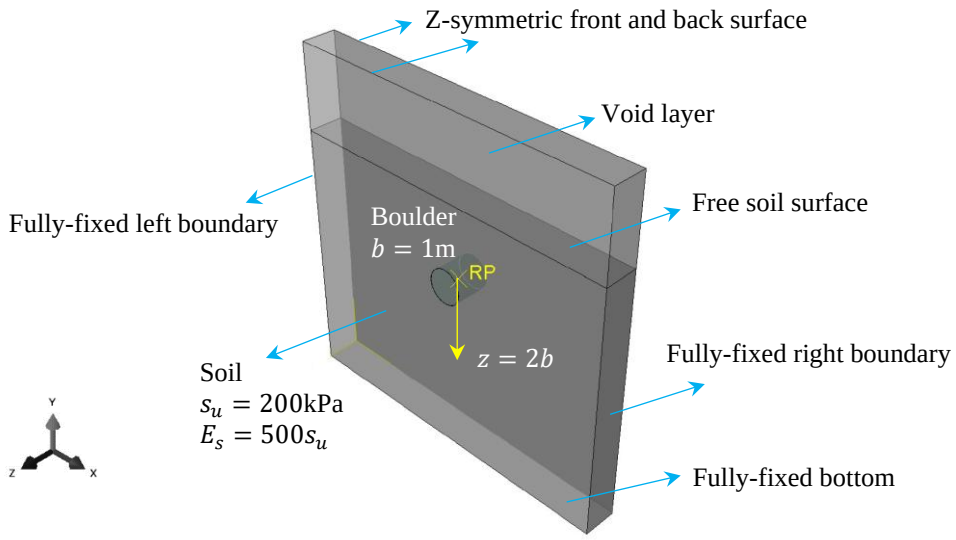


Figure 3-16 Boulder penetration model

As shown in Figure 3-16, the boulder with a diameter of 1 m is pushed downward until $z = 2b$ at a constant speed. The soil is 7.5 m in height and 10 m in width, with a 2.5 m void layer above the free surface, allowing soil heave. Fully-fixed boundary conditions are defined on the left, right, and bottom of the domain. Smooth boundary conditions were assigned on the front and the back surfaces to simulate a plane-strain condition.

The soil weight is defined as $\gamma_s = \beta g \rho_s$, where g is gravitational acceleration, taken as 9.81 $\mathrm{m/s^2}$, $\rho_s = 2000\ \mathrm{kg/m^3}$, and β is a coefficient for varying the soil weight. Because the boulder motion is controlled by its Reference Point (RP in Figure 3-16), this modification does not lead to the boulder sinking in addition to the predefined displacement. Four β values are investigated ($\beta = 0, 1, 5, 10$), the corresponding model of which is coded as CB-βg.

Figure 3-17 shows the deforming pattern at the end of the simulation (time step = 1000) and the velocity field of the soil at time step 100. With $\beta = 0$, the downward movement of the boulder results in a void area within the soil. The soil in this area is pushed away by the

trajectory of the boulder, leading to soil heave at the free surface. As the soil weight increases, from CB-1g to CB-10g, the soil wall collapses, filling the void area, mitigating the soil heave. The velocity field in the soil, however, shows a contrary trend with an increase of β, especially at the soil surface. As shown in Figure 3-17, the soil surges upward to the surface in CB-10g, while in CB-0g, the soil surface is less disturbed. The soil surging in CB-10g, however, is then compensated by the gap filling due to the weight effect, ending up with negligible soil heaving at the free surface at the end of the analysis.

A quantitative comparison of the force penetrating the boulder is presented in Figure 3-18. The normalisation scheme for the strip footing penetration ($\tilde{F}_y = F_y/As_u$), is again applied as a baseline. For the circular boulder, A refers to the projected area of the boulder on the X-Z plane. This baseline, as shown in Figure 3-18 (a), suggests a positive correlation between the reaction force and the soil weight from model CB-1g to CB-10g. An optimised normalisation scheme is therefore given as

$$\tilde{F}_y = \frac{F_y}{As_u} \times \left(\frac{\gamma_s b}{s_u}\right)^{-1/8} \qquad \textit{Eqn. 3-11}$$

Because few differences were noticed between CB-0g and CB-1g in Figure 3-18 (a), the soil weight in CB-0g is also taken as $\gamma_s = g\rho_s$ to fulfil the mathematical requirement of Eqn. 3-11. Figure 3-18 (b) shows the plot of the optimised normalisation scheme. The normalised state of the force, however, could not lead to a normalised state of the pile deflection. The soil surging and the gap-filling mechanisms in Figure 3-17 indicate that the soil weight tends to affect the interactions between the pile and soil in deeper areas. Details of this aspect will be discussed along with the results from the parametric study below, which uses weightless soil to maintain the model stability.

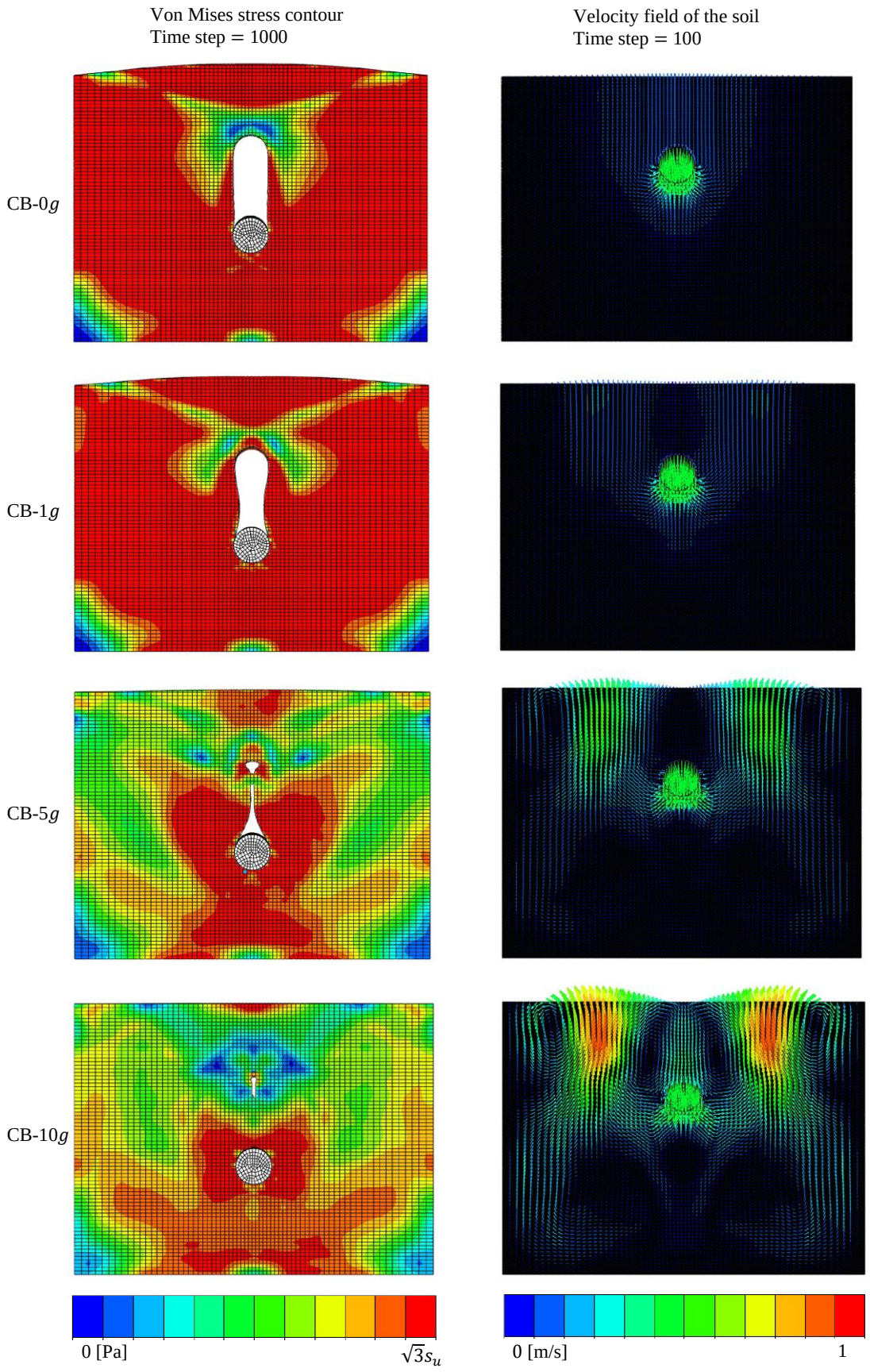


Figure 3-17 Stress contour, soil collapse, and the velocity field of the soil

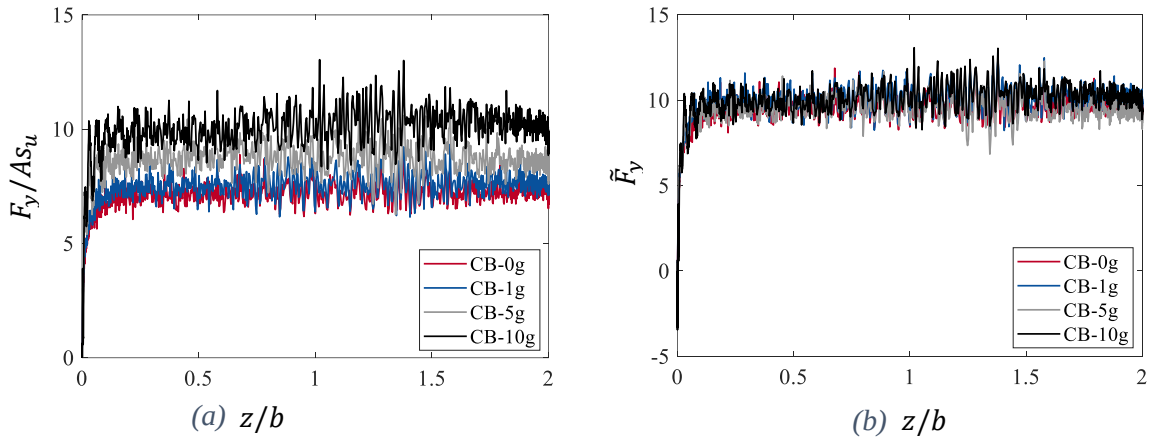


Figure 3-18 Normalisation of vertical reaction forces

(a) Baseline normalisation scheme; (b) Optimised normalisation using Eqn. 3-11

3.4 PARAMETRIC STUDIES OF INDEPENDENT FACTORS

For the convenience of explaining the parameters related to the model geometry, Figure 3-7 (a) is again presented here for reference. Assuming that the monopiles are perfectly manufactured, the occurrence of buckling during pile jacking or driving tends to be affected by nine parameters falling into two categories (see Figure 3-7 (a) for dimensions):

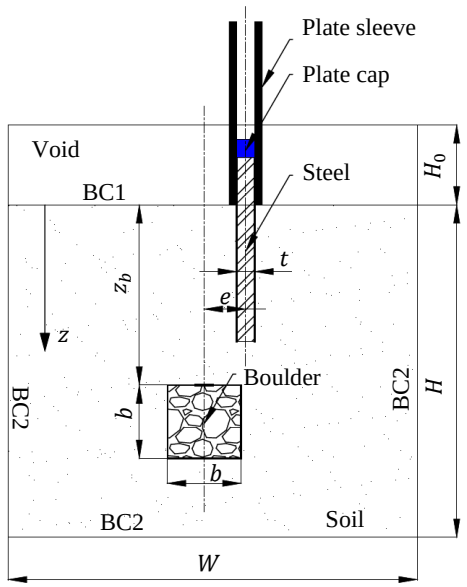
1) The boulder mobility – how easily the boulder can move within the soil, which depends on the following:
    a. Soil stiffness, E_s
    b. Soil strength, s_u;
    c. Boulder dimension, b;
    d. The embedment depth of the boulder, z_b;
    e. The contact eccentricity between the plate and boulder, e;
    f. The boulder shape.
2) The pile capacity – how easily the pile wall can deform, which depends on the following:

a. The stiffness of the steel, E_p;

b. The yield strength of the steel, σ_Y;

c. The chamfer profile of the pile tip.

The effect of varying the penetration speed, v, though it could decrease the oscillations of the computed reaction forces, was not investigated in this parametric study to save computing time.



Recall – Figure 3-7 (a) Geometry and boundary conditions of 2D plate penetration model

The normalisation schemes were as follows (see Figure 3-7 (a) for dimensions):

Relative stiffness	$r_E = \frac{E_p}{E_s}$
Relative strength	$r_\sigma = \frac{\sigma_Y}{s_u}$
Normalised boulder dimension	$\tilde{b} = b/t$
Normalised boulder embedment	$\tilde{z}_b = z_b/z_{ult}$
Normalised eccentricity	$\tilde{e} = e/b$

When varying the parameters r_E and r_σ, the pile properties remained the same, while only the soil properties were changed. The severity of buckling was evaluated using the horizontal displacement of the plate tip, U_1, at the end of the simulation, normalised as

$$\widetilde{U_1} = U_1/z_{ult} \qquad \textit{Eqn. 3-12}$$

where z_{ult} is the ultimate penetration depth of the plate. This normalisation emphasizes the relationship between the plate deflection and the penetration depth. The buckling can become increasingly severe as the penetration continues, until premature refusal occurs. Similarly, rather than using a ratio of t, the boulder embedment is normalised against the ultimate penetration depth z_{ult}. For the parametric study, z_{ult} was taken as a constant with a value of $100t$.

The effects of five quantifiable parameters are discussed individually from Section 3.4.1 to Section 3.4.5. Piecewise equations are also given to approximate the relationship between the tip deflection of the plate and the corresponding parameter. These equations were later used in Chapter 5 for the generalisation of 2D results and the construction of the safety envelope. The sensitivities of these parameters are then evaluated and compared in Section 3.4.6.

3.4.1 Effect of boulder dimension

This parametric study was performed using circular boulders. The normalised boulder dimension, $\tilde{b}$, was evaluated using the boulder diameter. The model code "PP" stands for Plate Penetration model, and "C" stands for the Circular boulder. The constant in the model code symbolises the value of $\tilde{b}$. For example, the model PP15C means that the plate penetration model has a circular boulder with a diameter of $\tilde{b} = 15$. The models used for the investigation of the effect of boulder diameter are listed in Table 3-4.

Table 3-4 Models with various boulder diameters

Model code	Normalised boulder diameter $\tilde{b}$
PP05C	5
PP10C	10
PP15C	15
PP20C	20
PP25C	25

In the models, boulders of various sizes were placed at $z_b = 0.05z_{ult} = 5t$. The boulder was placed at such shallow depths because, from a preliminary study, a shallower boulder tended to have more significant effects on the tip deflection than a deeper one. Details of the effect of boulder depth are presented in Section 3.4.3. The centrelines of the plate and the boulder coincided, which means no contact eccentricity was introduced into the model. The mechanical properties were taken as $r_\sigma = 1000$, $r_E = 10000$.

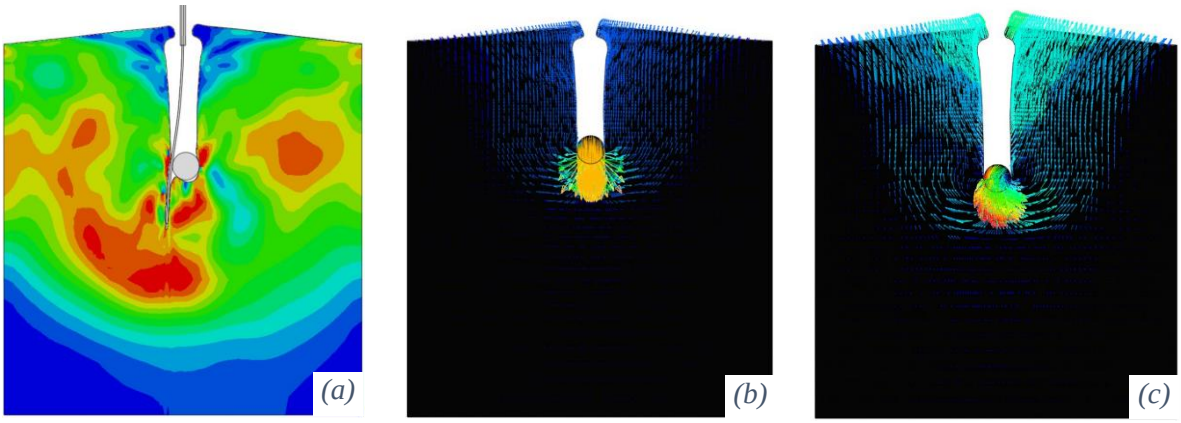


Figure 3-19 Pile and soil deformation in model PP15C

(a) Deformation and stress contour at time step 1000; (b) Velocity field at time step 500; (c) Velocity field at time step 575

Taking the model PP15C as an example, the deformation of the plate and the soil is shown in Figure 3-19 (a). The velocity field during the downward and lateral movement of the boulder is shown in Figure 3-19 (b) and (c), respectively. With $\tilde{b} = 15$, the boulder is first pushed

downward until $0.6z_{ult}$ before the plate tip slides off and deforms laterally. The subsequent lateral movement and rotation of the boulder result in a final deflection plate around $\widetilde{U}_1 = 0.09$.

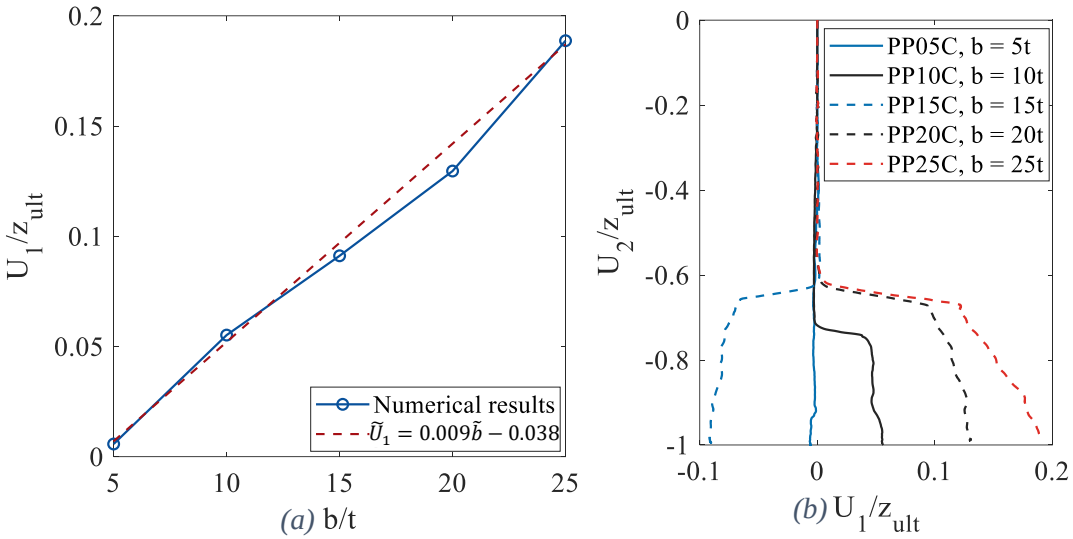


Figure 3-20 Effect of (circular) boulder size

(a) Numeric fit of the deflection trend; (b) Trajectories of plate tips

The parametric study of boulder diameter covers a range $\tilde{b} = 5$ to 25, increasing with an interval of 5. Figure 3-20 (a) shows an essentially linear relationship between $\widetilde{U}_1$ and $\tilde{b}$, the correlation coefficient of which is $R^2 = 0.99$. Figure 3-20 (b) shows the tip trajectories in various analyses, where U_2 is the instantaneous vertical displacement of the plate tip. With $\tilde{b} = 5$, the boulder was pushed by the advancing plate until z_{ult} was reached, with minor deflections ($\widetilde{U}_1 = 0.007$) occurring in the later stage of the penetration, from around $0.9z_{ult}$. The onset of tip deflection starts earlier with the increase of boulder size, until $\tilde{b} = 15$. Beyond this point, the plate starts deflecting around $0.6z_{ult}$ regardless of the further increase of $\tilde{b}$. In all models, the plate reached the prescribed penetration depth.

3.4.2 EFFECT OF CONTACT ECCENTRICITY

Models with a normalised boulder dimension $\tilde{b} = 10$ were used to investigate the effect of varying the normalised contact eccentricity, $\tilde{e}$. In these models, the boulder was embedded at a shallow depth of $z_b = 0.05 z_{ult}$. The mechanical properties were $r_\sigma = 1000$, $r_E = 10000$. The parametric study covers a range of normalised eccentricities $\tilde{e}$ from 0 to 0.4. In the model code, the value of $\tilde{e}$ is represented by the percentage values following the letter "E", which symbolises "eccentricity". Table 3-5 gives a model list with corresponding $\tilde{e}$, while the code "PP10C" has the same meaning as those in Section 3.4.1.

Table 3-5 Models with various contact eccentricities

Model code	Normalised contact eccentricity $\tilde{e}$
PP10CE00	0
PP10CE05	0.05
PP10CE10	0.10
PP10CE20	0.20
PP10CE30	0.30
PP10CE40	0.40

Figure 3-21 shows the final tip deflection as $\tilde{e}$ increases from 0.05 to 0.2. With the increase of $\tilde{e}$, both the downward movement of the boulder and the tip deflection become smaller. A quantitative analysis in Figure 3-22 (a) suggests an exponential relationship between $\widetilde{U}_1$ and $\tilde{e}$. In the fitting equation, Euler's number is denoted by a bold $\boldsymbol{e}$ to distinguish it from the contact eccentricity, e. The correlation coefficient, R^2, between the equation and the numerical data is 0.959. The peak deflection tends to occur around $\tilde{e} = 0.05$ in the numerical models and 0.04 is suggested by the equation. This observation is comparable to the finding of Nietiedt *et al.* (2022), who gave a critical eccentricity of $\tilde{e} = 0.1$ based on Abaqus CEL models with an

ellipsoidal boulder buried in sand. The different boulder shapes and soil conditions could be the reason leading to the different critical contact eccentricities. Though the analysis of boulders in sand was beyond the scope of this research, the effects of boulder shape have been investigated and are discussed in detail in Section 3.4.8.

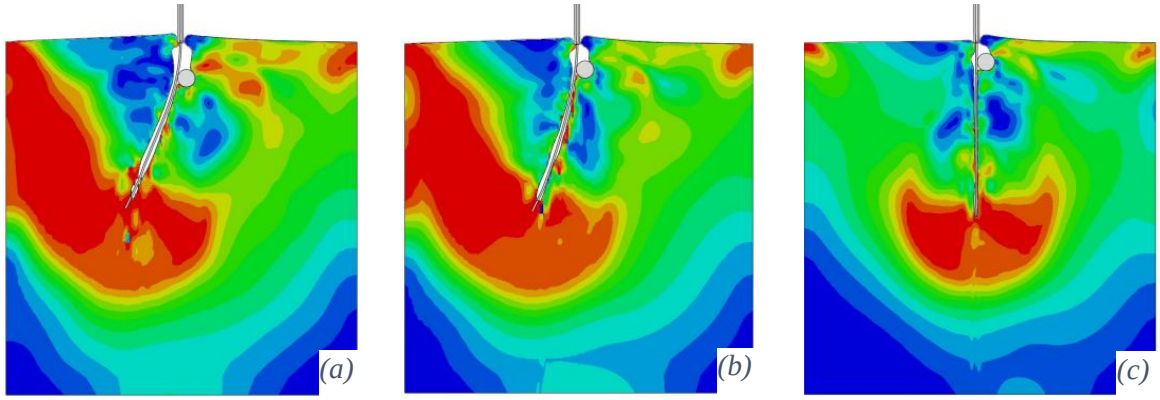


Figure 3-21 Tip deflections in models with (a) $\tilde{e} = 0.05$; (b) $\tilde{e} = 0.1$; (c) $\tilde{e} = 0.2$

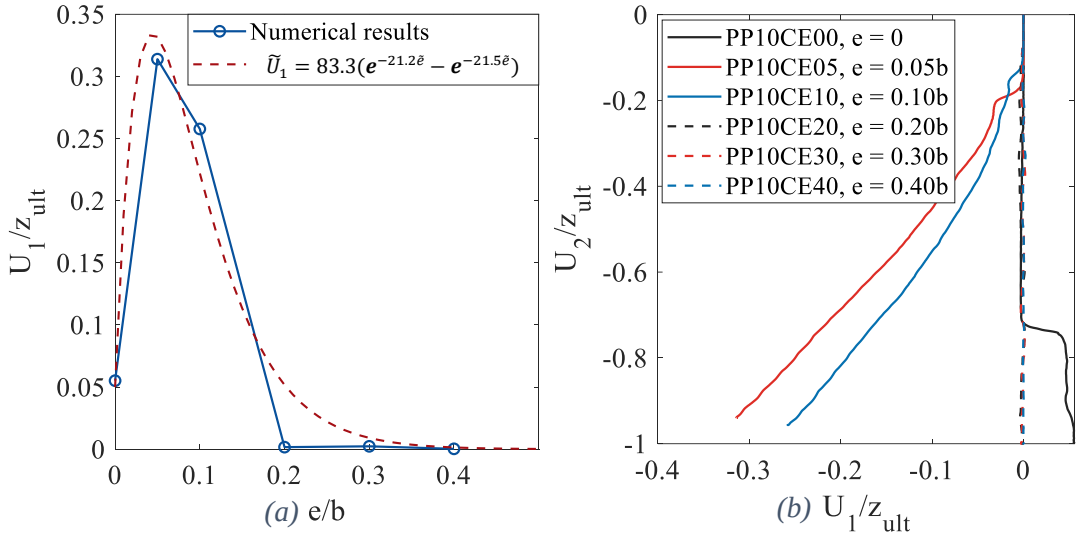


Figure 3-22 Effect of contact eccentricity
(a) Numeric fit of the deflection trend; (b) Trajectories of plate tips

Figure 3-22 (b) shows the trajectories of the plate tip. With no eccentricity, the plate first pushes the boulder downward until approximately $0.7z_{ult}$ before it deflects. In models PP10CE05 and PP10CE10, when small contact eccentricities are introduced, plate deflection starts much

earlier. Due to the large deflection, the prescribed z_{ult} was not reached in these two models. This effect of eccentricity diminished after $\tilde{e}$ reached 0.2. In models PP10CE20, PP10CE30, and PP10CE40, the plate pushed the boulder out of the way and remained straight during the penetration.

3.4.3 Effect of boulder embedment depth

The models with $\tilde{b} = 10$ were again used to investigate the effect of varying the normalised boulder depth $\tilde{z}_b$. No contact eccentricity was included in these models ($\tilde{e} = 0$). The mechanical properties were $r_\sigma = 1000$, $r_E = 10000$. Table 3-6 lists the models and the corresponding $\tilde{z}_b$. In the model code, the value of $\tilde{z}_b$ is represented by the percentage values following the letter "Z", while the code "PP10C" has the same meaning as those in Section 3.4.1.

Table 3-6 Models with various contact eccentricities

Model code	Normalised boulder depth $\tilde{z}_b$
PP10CZ05	0.05
PP10CZ15	0.15
PP10CZ25	0.25
PP10CZ35	0.35
PP10CZ50	0.50

The normalised embedded depth of the boulder was increased from 0.05 to 0.5, with a rapid decrease in tip deflection observed between 0.25 and 0.35, as shown in Figure 3-23 (a). A power equation was used to approximate the variation of $\tilde{U}_1$ within the range 0 to 0.35, with a correlation $R^2 = 0.99$. Beyond 0.35, a plateau of variation was considered to be reached, and a further increase of $\tilde{z}_b$ would not lead to a significant change in the tip deflection.

Figure 3-23 (b) shows the trajectories of the plate tip in the corresponding models. The boulders at shallower depths (0.05 to 0.25) were pushed into the soil until the plate started to deflect when $0.7z_{ult}$ was reached for $\tilde{z}_b = 0.05$ and 0.15, and around $0.97z_{ult}$ for $\tilde{z}_b = 0.25$. Boulders buried deeper than $0.35z_{ult}$ have a negligible effect on the final tip deflection of the plate. An observation of the models $\tilde{z}_b = 0.05$ to 0.25 suggests that the plate starts to deflect after the boulder is pushed downward for a distance of 0.55 to $0.70z_{ult}$. For cases where $\tilde{z}_b \geq 0.35$, though the deeper soil has higher confining stress, the tip deflection may not have sufficient distance to develop after the boulder collision, with the given total penetration distance in the present analyses. This aspect will be explained in more detail in Chapter 5, based on the 3D analysis.

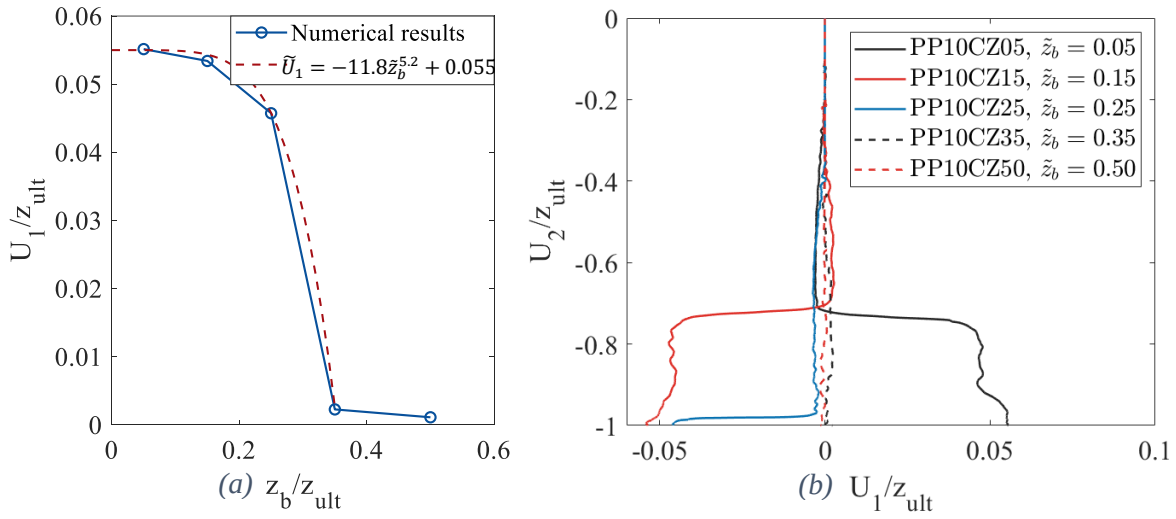


Figure 3-23 Effect of boulder embedment depth
(a) Numeric fit of the deflection trend; (b) Trajectories of plate tips

3.4.4 Effects of Relative Stiffness

The model used for this part of the study included a boulder buried at $\tilde{z}_b = 0.05$ and of a size $\tilde{b} = 10$. No contact eccentricity existed between the plate and the boulder ($\tilde{e} = 0$). The relative strength between plate and soil remained $r_\sigma = 1000$. Table 3-7 gives a list of models and the

corresponding r_E values. The models are coded numerically from 1 to 6, corresponding to increasing values of r_E ranging from 500 to 20000. The term "sti" in the code represents "stiffness", while "PP10C" has the same meaning as those in Section 3.4.1.

Table 3-7 Models with various contact eccentricities

Model code	Relative stiffness r_E
PP10Csti1	500
PP10Csti2	2500
PP10Csti3	5000
PP10Csti4	7500
PP10Csti5	10000
PP10Csti6	20000

Figure 3-24 (a) shows the variation of $\widetilde{U}_1$ for relative stiffness within the range $r_E \in [500, 20000]$. The plateau of this plot indicates that $r_E \in [2500,10000]$ have little influence on $\widetilde{U}_1$. Though a decrease of $\widetilde{U}_1$ occurs outside the range, the slopes of the variation are negligible, being 6e-6 in the lower end and 2.1e-6 in the higher end. These small slopes indicate that the relative pile-soil stiffness r_E tends to have little influence on $\widetilde{U}_1$.

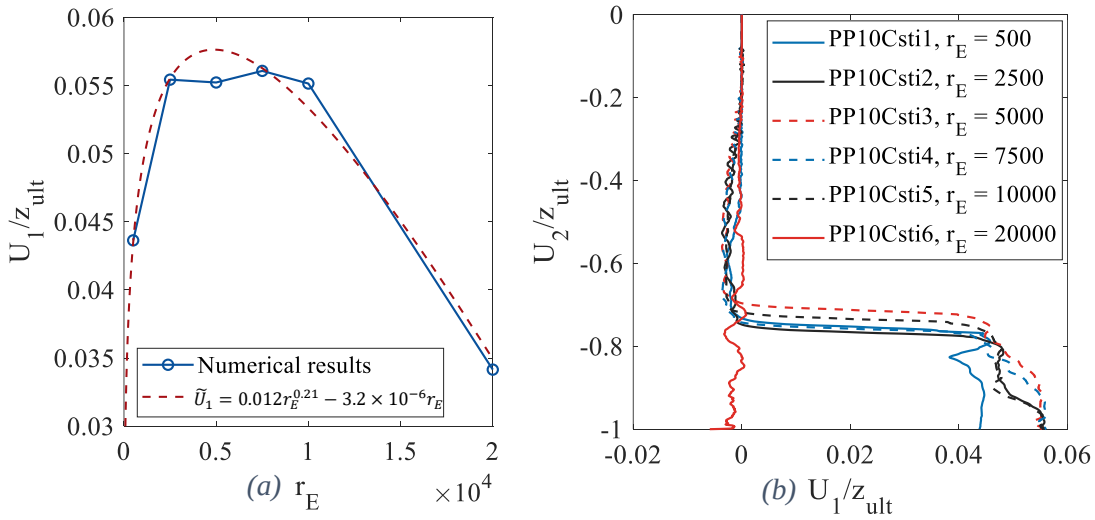


Figure 3-24 Effects of relative stiffness

(a) Numeric fit of the deflection trend; (b) Trajectories of plate

Figure 3-24 (b) gives the trajectories of the plate. These are consistent when $r_E \leq 10000$, with boulders pushed throughout the entire penetration depth. The same boulder movement is found when $r_E = 20000$, but the plate is generally kept straight.

3.4.5 EFFECT OF RELATIVE STRENGTH

These models included a boulder buried at $\tilde{z}_b = 0.05$ with $\tilde{b} = 10$ and $\tilde{e} = 0$. The relative stiffness between the plate and soil remained $r_E = 10000$. The effect of varying the relative strength, r_σ, was investigated with a range from 100 to 3000. This was achieved by modifying the undrained shear strength of the soil only, while the yield strength of the steel plate remained constant. The highest soil strength ($r_\sigma = 100$) would not appear in reality, but was presented here for the interest of research. Table 3-8 gives a list of models with corresponding r_σ values. The models are coded numerically from 1 to 6, corresponding to increasing values of r_σ. The term "str" in the code represents “strength”, while “PP10C” has the same meaning as those in Section 3.4.1.

Table 3-8 Models with various contact eccentricities

Model Code	Relative strength r_σ
PP10Cstr1	100
PP10Cstr2	500
PP10Cstr3	1000
PP10Cstr4	1500
PP10Cstr5	2000
PP10Cstr6	3000

As shown in Figure 3-25, the tip deflection, $\widetilde{U}_1$, monotonically decreases within $r_\sigma \in [500, 2000]$, and reaches a plateau of minimum afterwards. The lower value of $\widetilde{U}_1$ at $r_\sigma = 100$

does not imply a safer trend of pile installation in extremely stiff clays; instead, it was a consequence of severe distortion and premature refusal of the plate.

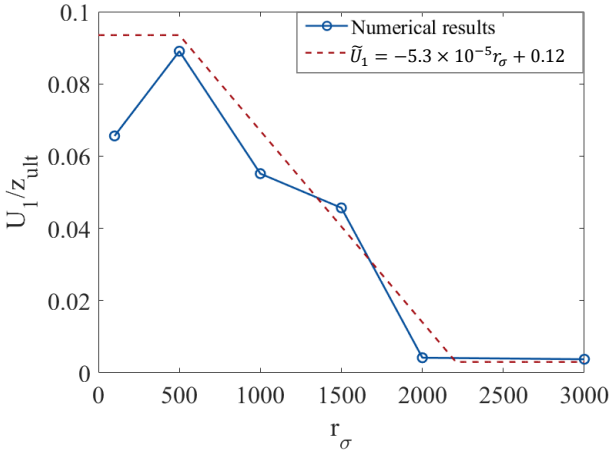


Figure 3-25 Effect of relative strength – numeric fit of deflection trend

As shown in Figure 3-26 (a), all plates with $r_\sigma \geq 500$ reach the designated penetration depth, though with different amounts of lateral deflection. In the analysis with $r_\sigma = 100$, the plate stops at $z = 0.4z_{ult}$ and an Euler buckling mode appears in the plate segment above the boulder. The final elasto-plastic deformation of the plate at $z = 0.41z_{ult}$ can be seen in Figure 3-26 (c), although the elastic Euler buckling initiated much earlier.

A comparison of the Euler critical buckling load and the vertical reaction force, F_y, is shown in Figure 3-26 (b). The critical buckling load, P_{cr}, was calculated following

$$P_{cr} = \frac{\pi^2 I}{(KU_2)^2} \qquad \text{Eqn. 3-13}$$

where I is the second moment of area of the plate strip. U_2 is the penetration depth of the plate tip, which was considered the same length as the unsupported part of the penetrating plate. This, however, was a slight overestimation due to the neglect of the buried part below the boulder. The column effective length factor, K, is taken as $K = 2.0$ to simulate a column with one end free and the other fully fixed. Figure 3-26 (b) suggests that F_y first exceeds P_{cr} at

around $z = 0.23z_{ult}$ when $r_\sigma = 100$, which implies the initiation of Euler buckling and is slightly earlier than $z = 0.31z_{ult}$ as shown in Figure 3-26 (a). This discrepancy is because of the overestimation of the unsupported length in Eqn. 3-13. In model PP10Cstr5, when $r_\sigma = 2000$, F_y does not exceed P_{cr}. Therefore, only negligible deflection is found in the model (Figure 3-26 (a)), and the boulder is pushed downwards throughout the penetration.

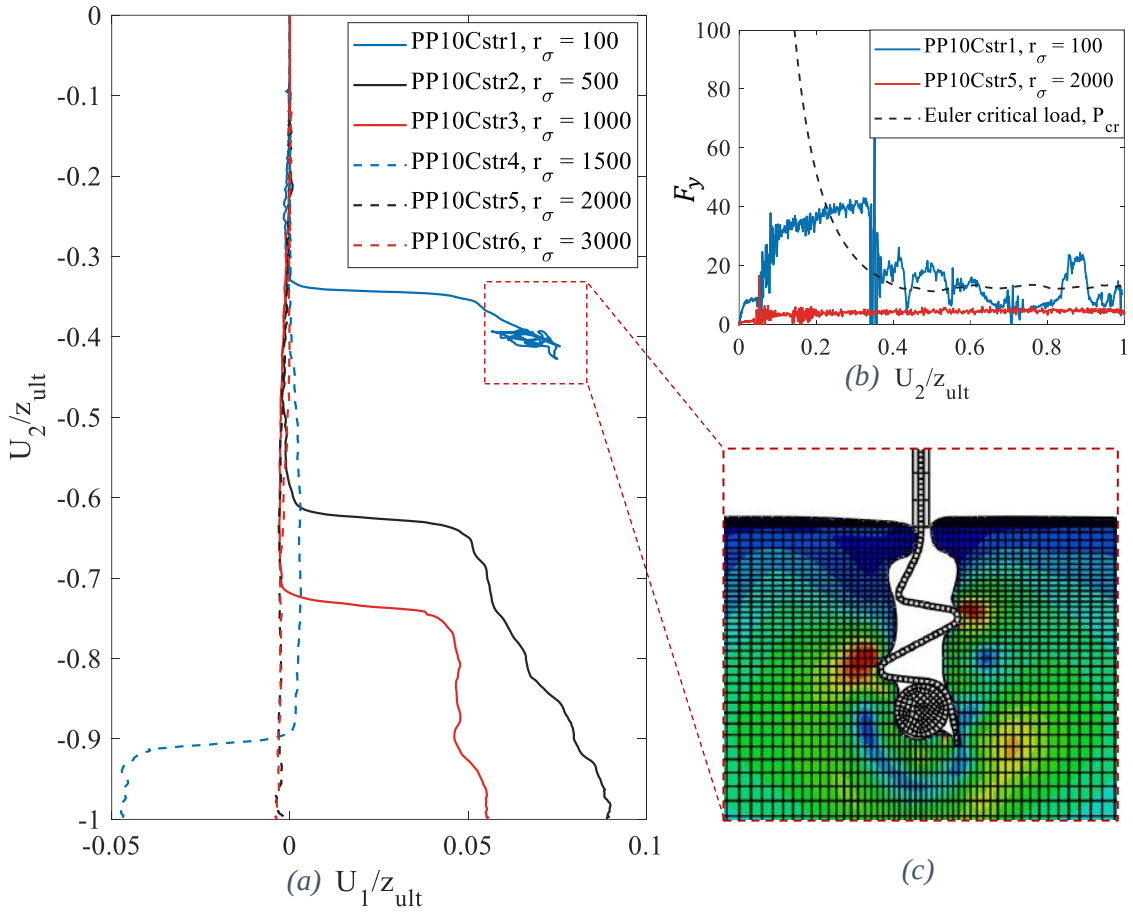


Figure 3-26 Numerical results

(a) Trajectories of plate tips, (b) Euler buckling load and vertical reaction force
(c) Severe tip distortion at $r_\sigma = 100$

The comparison between P_{cr} and F_y is most relevant in stiff-clay scenarios, where gaps tend to form due to the movement of boulders. Meanwhile, an increase of P_{cr} can be envisaged when the soil collapses towards the boulder under gravity and fills in the gaps to a deeper depth. In

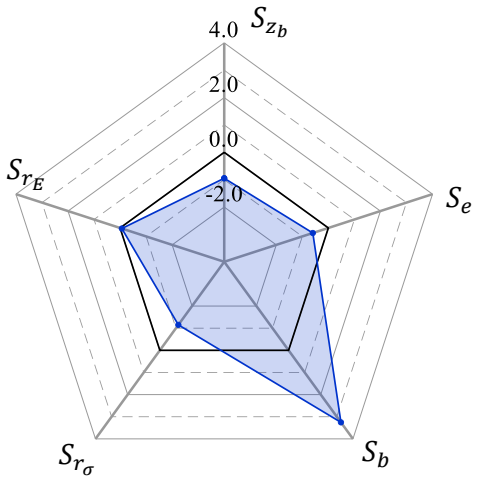
non-cohesive soils, however, Eqn. 3-13 is no longer applicable as the soil particles fill the gaps and provide additional lateral support to the embedded pile.

3.4.6 PARAMETER SENSITIVITY ANALYSIS

The parameter sensitivity can be evaluated based on the rate of change of the horizontal displacement of the plate tip, U_1, against the rate of change of the corresponding parameter. A *sensitivity index*, S_χ, is defined correspondingly as

$$S_\chi = \frac{1}{n}\sum_{i=1}^{n}\frac{(|U_{1_{i+1}}| - |U_{1_i}|)\chi_i}{|U_{1_i}|(\chi_{i+1} - \chi_i)} \qquad \textit{Eqn. 3-14}$$

where the subscript i denotes the individual model, n is the total number of models concerned, and χ is the corresponding parameter. A positive S_χ indicates a positive correlation between the tip deflection and the influencing factor, while the negative S_χ indicates the opposite. Following Eqn. 3-14, a radar plot was obtained for the models with circular boulders, as shown in Figure 3-27, with the values of sensitivity indices listed on the right.



Boulder depth	S_{z_b}	-0.95
Contact eccentricity	S_e	-0.60
Boulder diameter	S_b	3.25
Relative strength	S_{r_σ}	-1.15
Relative stiffness	S_{r_E}	-0.07

Figure 3-27 Radar plot of sensitivity index

The plot suggests that boulder size is the most critical factor influencing the tip deflection, followed by the soil strength and the boulder embedment. In practice, the soil strength and stiffness are determined with reasonable certainty in the site investigation. The more uncertain site-dependent factors among the five are the boulder size ($\tilde{b}$), boulder embedment ($\tilde{z}_b$), and the contact eccentricity ($\tilde{e}$). Both $\tilde{b}$ and $\tilde{z}_b$ tended to have monotonic relationships with the ultimate deflection, as discussed in Section 3.4.1 and Section 3.4.3. The contact eccentricity, $\tilde{e}$, however, could be an uncertain factor with the existence of critical value. An investigation of two-parameter coupling effects was therefore conducted for $\tilde{b}$-$\tilde{e}$ and $\tilde{z}_b$-$\tilde{e}$.

3.4.7 COUPLING EFFECTS

The coupling effects of $\tilde{b}$-$\tilde{e}$ and $\tilde{z}_b$-$\tilde{e}$ are discussed in this section. Coupling effects involving multiple parameters (≥ 3) may also exist and are worth investigating for actual design cases. However, parametric studies on these complex parameter combinations may not be practical due to the required number of models. Therefore, this research mainly focused on the coupling effects of two parameters.

Boulder size and contact eccentricity, $\tilde{b}$-$\tilde{e}$

To investigate the $\tilde{b}$-$\tilde{e}$ effect, the boulders were placed at $z_b = 0.05z_{ult}$, with diameters ranging from $5t$ to $25t$. The contact eccentricities covered the range $\tilde{e} = 0{\sim}0.2$, which includes the critical value obtained from Section 3.4.2. The mechanical properties of the models were $r_\sigma = 1000$, $r_E = 10000$. The models were coded following the same principles as those outlined in previous sections, while an example of code explanation is presented in Figure 3-28.

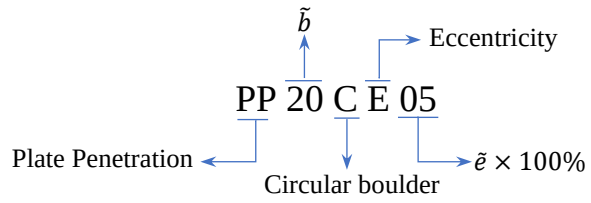


Figure 3-28 Model code explanation

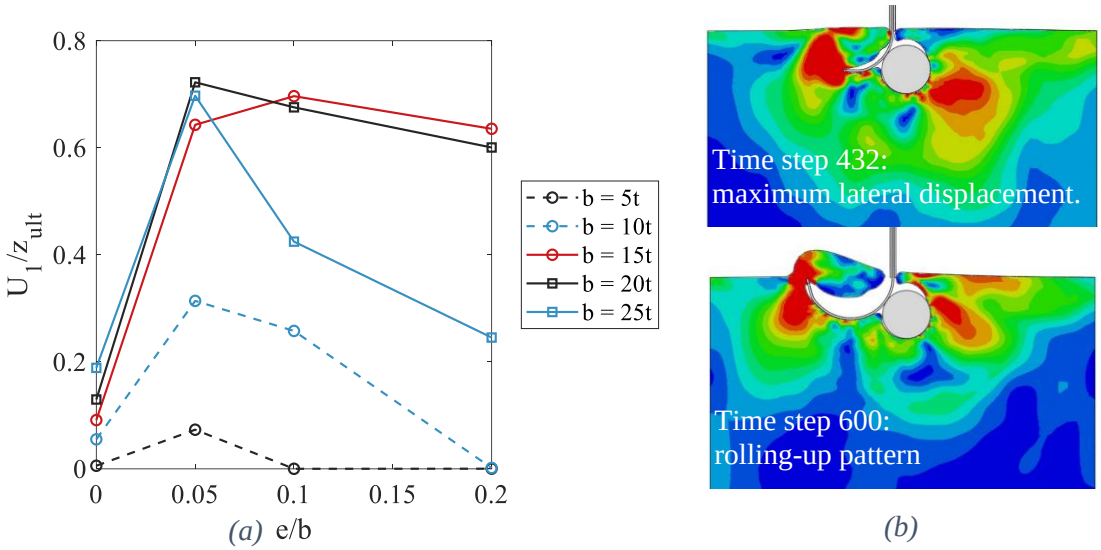


Figure 3-29 Coupling effects of boulder size and contact eccentricity

(a) Plot of tip deflection against eccentricity; (b) Maximum lateral displacement and rolling-up pattern in model PP25CE20

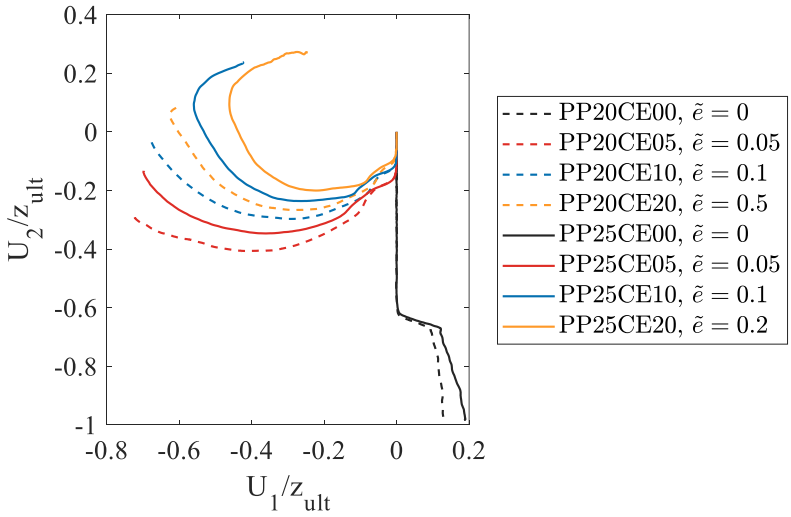


Figure 3-30 Trajectories of plate tips

Figure 3-29 (a) shows the tip deflections obtained with different boulder sizes and contact eccentricities at the final computation step. The critical contact eccentricity is between $\tilde{e} = 0.05$ and 0.1 for all models. In general, the deflection becomes more severe with the increase of boulder size. The exceptions in models $\tilde{b} = 20$ and 25 are due to excessive plate deflection where, instead of penetrating downward, the plates rolled upwards after the boulder collision. In this pattern, the plate tip first advances laterally to a maximum value, then approaches the plate head with a gradual decrease of $\tilde{U}_1$. This rolling-up pattern would not occur in circular piles, but it could correspond to the premature refusal of a monopile during installation when the open-ended pile is significantly distorted and becomes fully closed. Figure 3-29 (b) shows an example of this rolling-up pattern using model PP25CE02, while the tip trajectories of the model with $b = 20t$ and $25t$ are shown in Figure 3-30.

Boulder depth and contact eccentricity, $\tilde{z}_b$-$\tilde{e}$

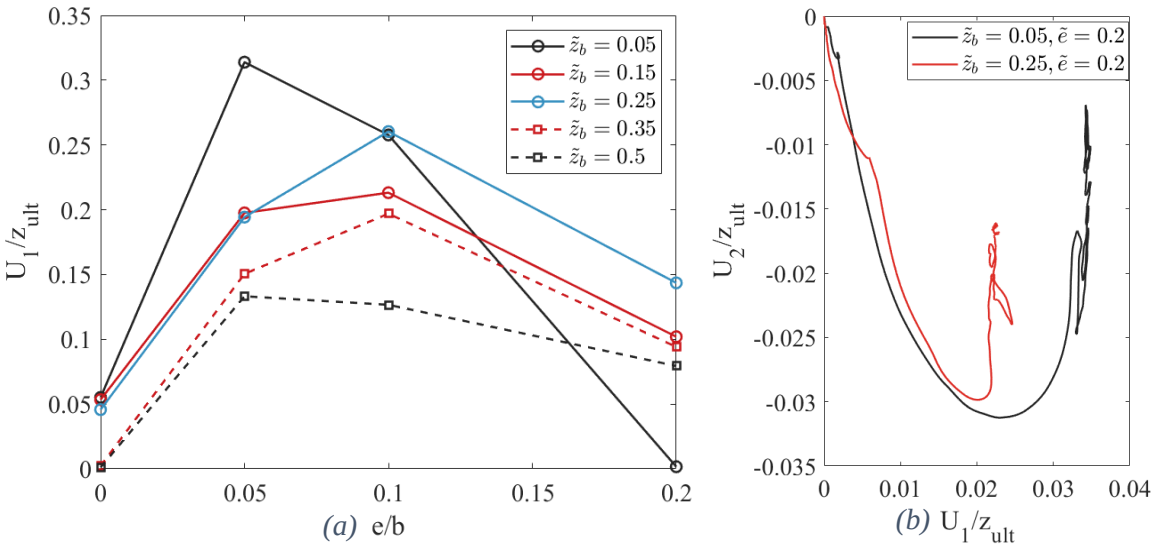


Figure 3-31 Coupling effect of boulder depth and contact eccentricity
(a) Variations of final tip deflections; (b) Comparison of boulder trajectories

These models involved boulders of constant size $\tilde{b} = 10$ buried from the shallowest depth $\tilde{z}_b = 0.05$ to the deepest, $\tilde{z}_b = 0.5$. The mechanical properties of the models remained constant at $r_\sigma = 1000$, $r_E = 10000$.

As suggested in Figure 3-31 (a), the critical contact eccentricity moves from $\tilde{e} = 0.05$ to $\tilde{e} = 0.1$ as $\tilde{z}_b$ increases from 0.15 to 0.35, while remaining at $\tilde{e} = 0.05$ for the shallowest ($\tilde{z}_b = 0.05$) and deepest ($\tilde{z}_b = 0.5$) boulder depths. In general, the tip deflection, $\widetilde{U}_1$, increases as the boulder becomes shallower. However, exceptions appear at $\tilde{z}_b = 0.05$ and 0.15, where the decrease of $\widetilde{U}_1$ occurred at $\tilde{e} = 0.1$. This is because, with less soil lying above, the boulders were more easily displaced at a shallower depth. Figure 3-31 (b) shows the boulder trajectories when $\tilde{z}_b = 0.05$ and 0.25, suggesting a broader movement range in the former.

3.4.8 Effect of boulder shape

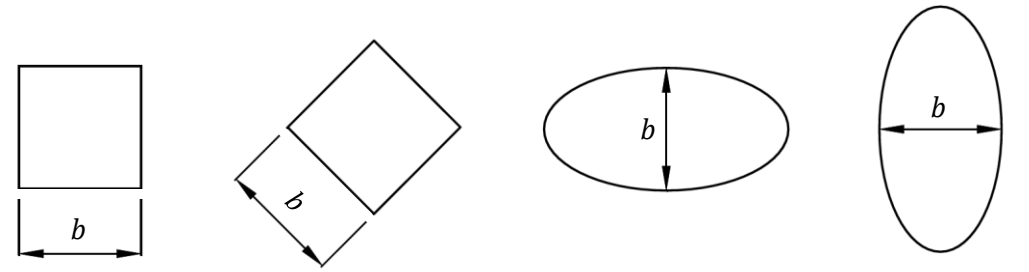


Figure 3-32 Boulder size characterisation for different shapes

The intention of this investigation was to build a map of different boulder shapes, which was constrained by the computing time. Instead, four simple shapes, Circular (C), Square (S), Diamond (D), and elliptical (H and V), were included in the simulations. Despite their simplicity, their variedness was sufficient to prove that the boulder shape would significantly affect the tip deflection.

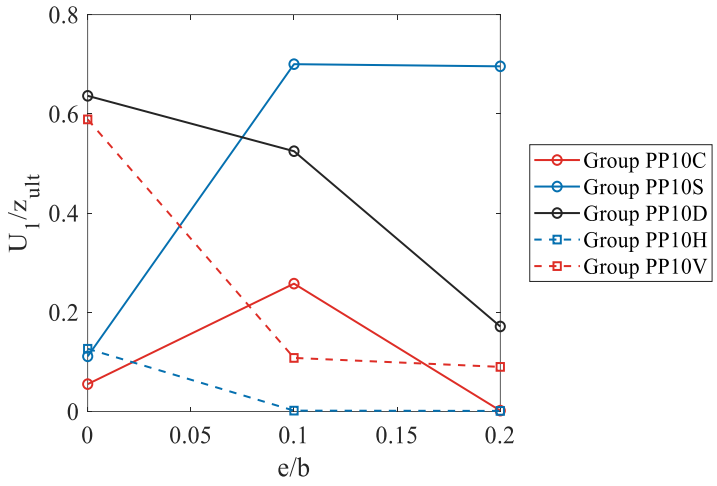


Figure 3-33 Tip deflections at ultimate penetration depth

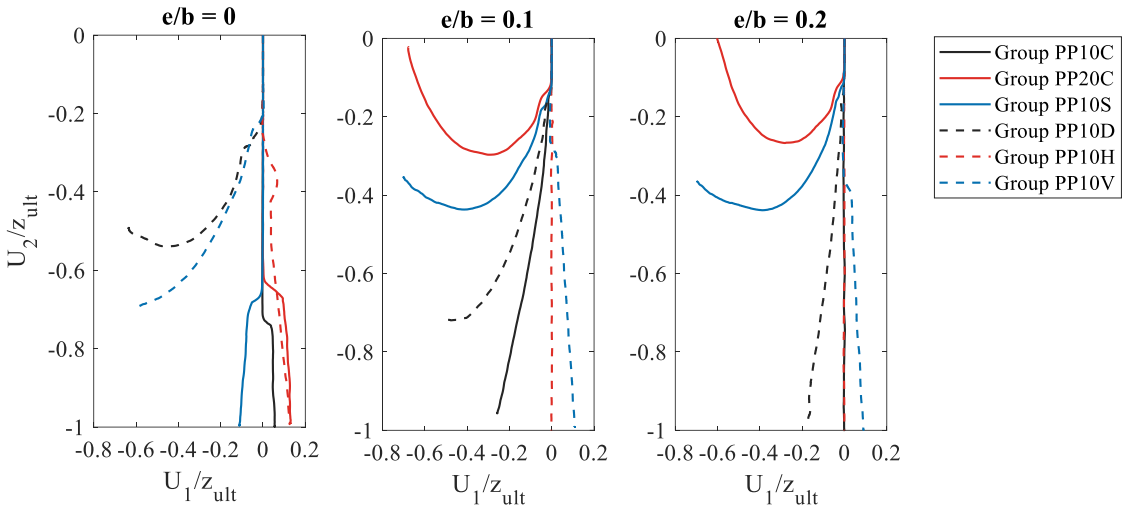


Figure 3-34 Tip trajectories

The major axis of each elliptical boulder was twice the minor axis. The normalised boulder size, $\tilde{b} = b/t$, of each shape was characterised based on the geometrical lengths b marked in Figure 3-32. The model code shown in Figure 3-32 combines the value of $\tilde{b}$ with a letter (C, S, D, H, or V) indicating the boulder shape. Because of computing time limitations, only one boulder size, $\tilde{b} = 10$, was investigated for each shape, with three eccentricities $\tilde{e} = 0$, 0.1, and 0.2. The boulders were buried at a constant depth $\tilde{z}_b = 0.05$.

Figure 3-33 shows the variations of final tip deflection with contact eccentricity in each group of models. The boulder shape did affect the tip deflection, and each followed a unique $\widetilde{U}_1$-$\tilde{e}$ trend.

Detailed plots of tip trajectories in the various models are presented in Figure 3-34. The model group PP20C was introduced to compare with PP10H because, in these models, the horizontal axes of the boulders were identical and equal to 20*t*.

A key factor determining the severity of tip deflection at $\tilde{e} = 0$ was whether "balance" could be kept at the tip-boulder contact point. Subjected to perfectly symmetrical impact conditions at $\tilde{e} = 0$, the boulder tended to be pushed downward until 1) the balance at the contact point was lost, and the boulder started to rotate, or 2) the reaction force from the soil was sufficiently large for the plate to deflect.

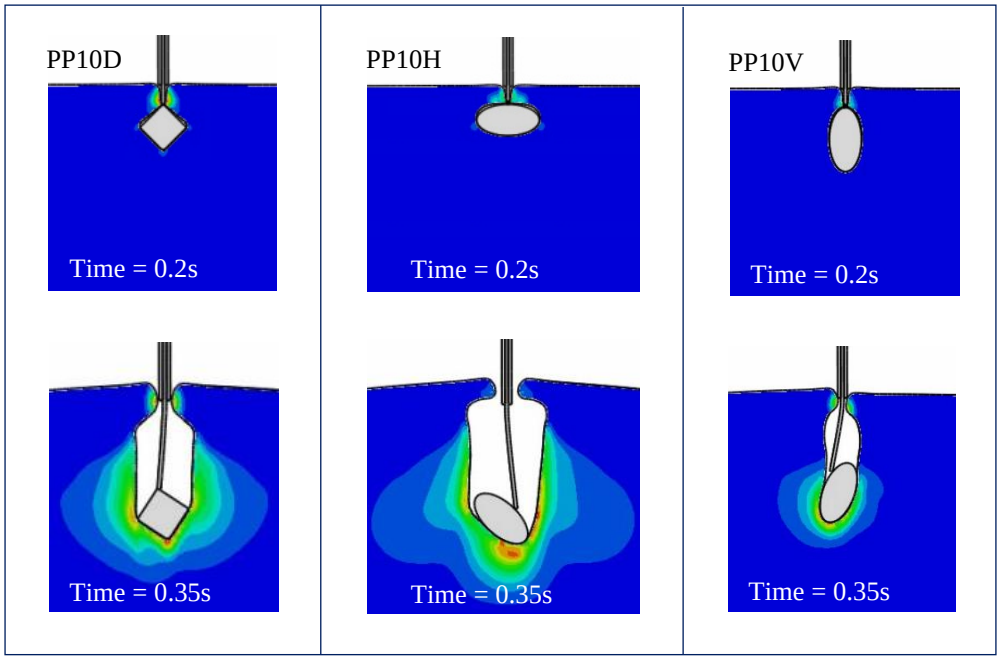


Figure 3-35 Loss of contact balance in PP10D, PP10H, and PP10V

Examples of losing balance can be found in models PP10D, PP10H, and PP10V. Figure 3-35 gives the positions of the plate and boulder in each model at two essential time steps,

corresponding to the initial plate-boulder collision and the onset of balance loss. This loss of balance could be due to the small contact area between the plate and boulder, as in PP10D. With only one boulder node contacting the plate tip, the balance brought by the symmetrical impact conditions could not be preserved throughout the penetration. For the elliptical boulders in PP10H and PP10V, the small contact area was no longer the primary reason for early tip deflection. Compared to the circular boulder with comparable dimensions, the elliptical boulder was more flexible with a unique "flipping" mechanism due to insufficient resistance from the overlying soil at shallow embedment depth. Recalling Figure 3-33, the critical eccentricity for the elliptical boulders (Group PP10H and Group PP10V) was $\tilde{e} = 0$, which was different from $\tilde{e} = 0.1$ suggested by Nietiedt (2022). This difference can be explained by the flipping mechanism of the elliptical boulder at a shallower depth. The shallowest embedment depth of the boulder investigated by Nietiedt *et al.* (2022) was $2b$, which varied depending on the boulder size. The embedment depth in this study, however, is a constant fraction of the penetration depth, giving an embedment of $0.5b$ for Group PP10V and $0.25b$ for Group PP10H.

The flipping mechanism, furthermore, can be exaggerated by the contact eccentricity $\tilde{e}$. Figure 3-36 shows the plate-boulder movement in models PP20CE10 and PP10HE10, where the letter "E" denotes "Eccentricity" and the number after "E" is the percentage value of $\tilde{e}$. In both models, the boulder dimensions in the horizontal direction were $20t$, with $\tilde{e} = 0.1$. The elliptical boulder tended to flip upright ($> 90°$ anticlockwise) and moved away from the trajectory of the plate at shallow depths. This flipping mechanism did not occur for the circular boulder. Instead, the circular boulder was pushed away through a short distance with rotation around its centre until the resistance from the soil was large enough to cause the plate deflection.

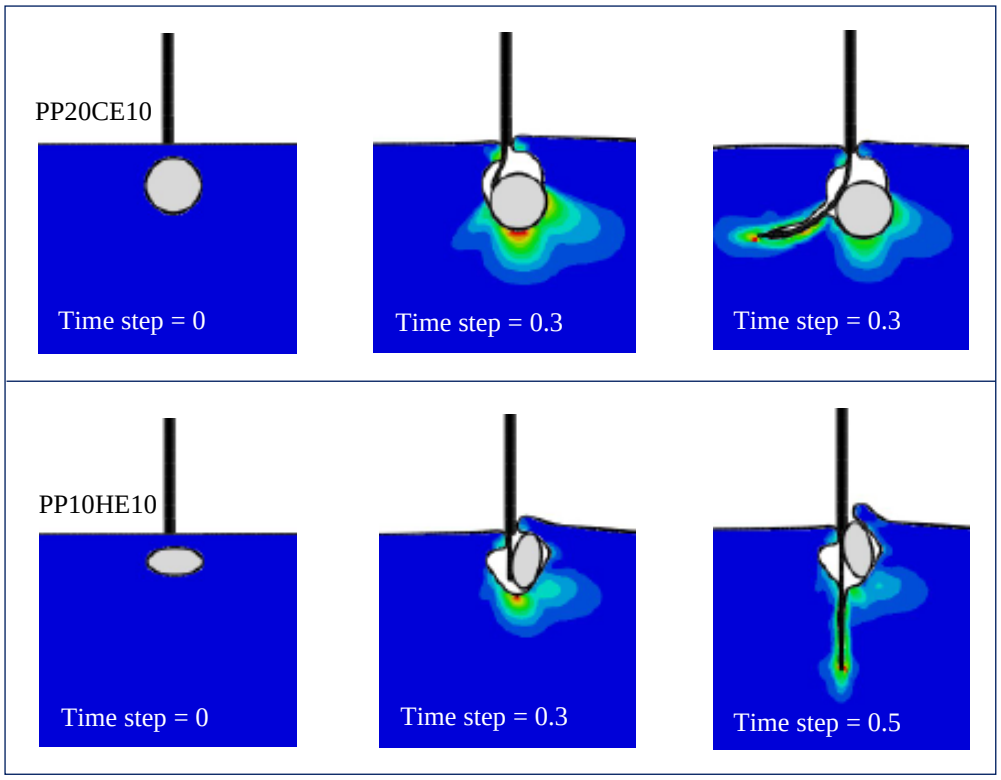


Figure 3-36 Boulder movements in PP20CE10 and PP10HE10

A similar comparison was also conducted on models PP10CE10 and PP10VE10. As was the case in PP10HE10, the flipping mechanism of the vertical elliptical boulder in PP10VE10 also led to smaller tip deflection than the circular boulder in PP10CE10, but larger deflections compared to the horizontal elliptical boulder. As shown in Figure 3-37, after rotating around 90° clockwise, the vertical boulder lay horizontally in the soil, leaving the longer axis occupying the penetration path and causing larger tip deflections. The same scenario also appeared for diamond and square boulders.

Figure 3-38 compares the boulder movement in models PP10DE10 and PP10SE10. In PP10DE10, the diamond boulder rotated anticlockwise after plate contact. The length of the horizontal boulder axis then shortened due to this rotation, leaving a flat surface occupying the plate trajectory and causing less tip deflection. In PP10SE10, on the other hand, the horizontal

boulder axis that occupied the plate trajectory became longer after the same anticlockwise rotation. The tip deflection thus became larger compared to that of a diamond boulder.

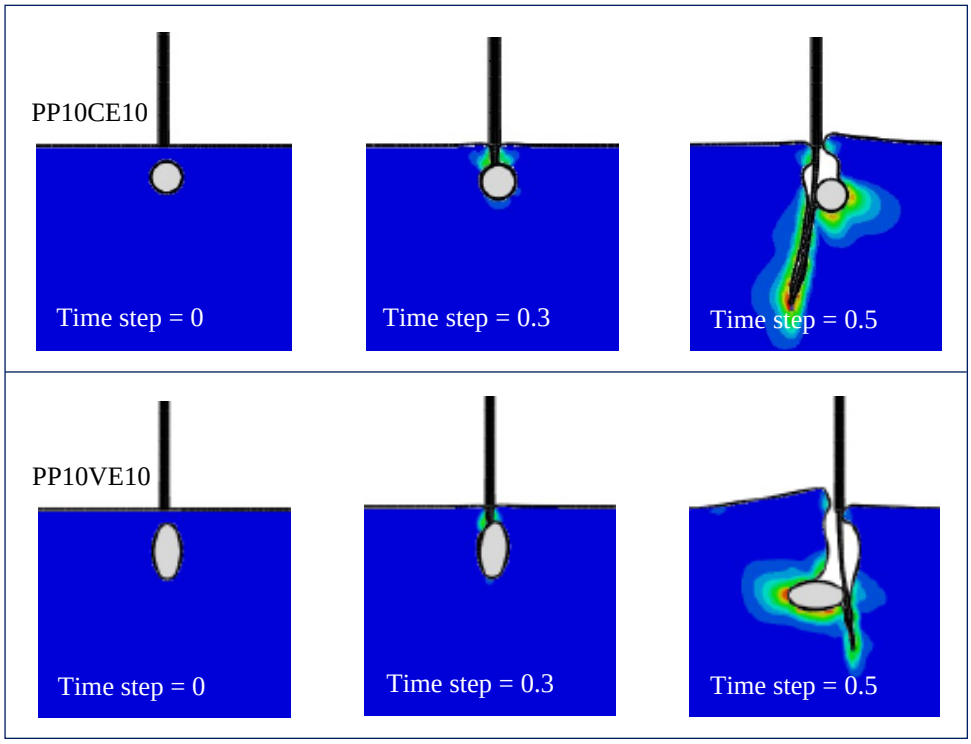


Figure 3-37 Boulder movement in PP10CE10 and PP10VE10

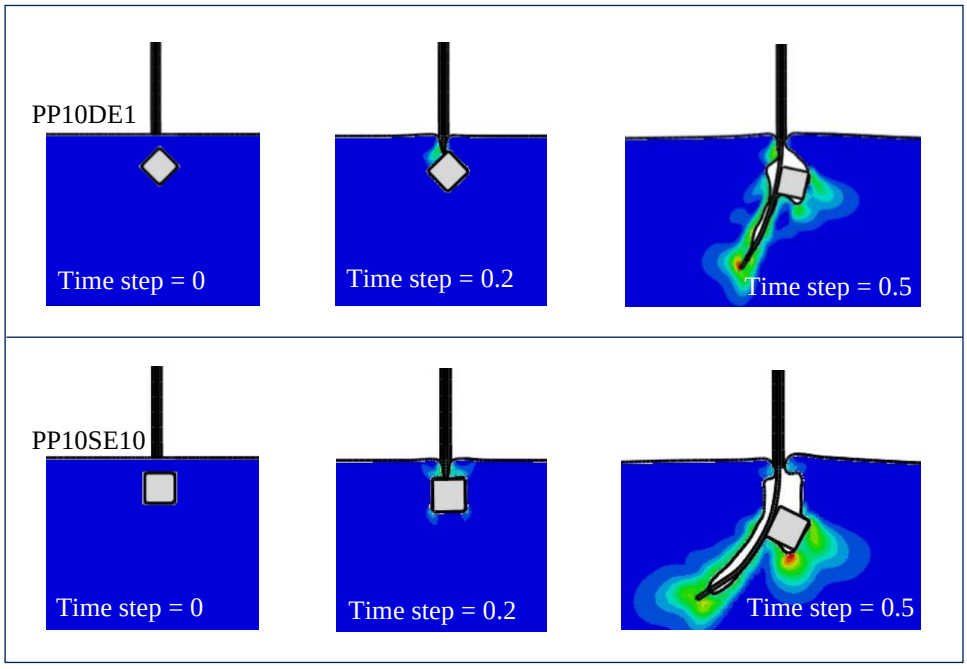


Figure 3-38 Boulder movement in PP10DE10 and PP10SE10

Though it was hard to quantify the effects of different boulder shapes, the qualitative discussions above here indicated that the boulder shape can affect the tip deflection with two mechanisms:

1) The small contact area between the plate tip and the boulders with sharp angles or large curvatures can lead to the loss of rotational balance after a plate-boulder collision. The early boulder rotation due to this balance loss can lead to a more significant tip deflection.
2) Boulders with different-sized axes can influence the tip deflection by the longer axis interfering with the plate trajectory after boulder rotation. Longer axes tend to lead to more significant tip deflection.

In practice, the boulder shape can be more complicated and the initial position of a boulder can be difficult to determine prior to the pile installation. However, two conditions should be emphasised during the design stage: the vertical elliptical boulder with a long major axis and no contact eccentricity, and the circular boulder with a large diameter. In addition, the boulder axis that occupies (perpendicular to) the tip trajectory by the end of boulder rotation would affect the tip deflection most. The longer the axis is, the larger the tip deflection will be.

3.4.9 Effect of chamfer geometry

Chamfered tips are commonly used on prefabricated piles, such as concrete piles and timber piles, to facilitate the installation process (Elkhouly, 2020; Gerwick Jr., 1968). They can also appear on the external of the thickened driving shoe for offshore steel piles as a minor design (Durning & Rennie, 1978; Randolph & Gourvenec, 2011). However, the chamfered tip may lead to progressive buckling by increasing the external radial stresses on the pile (Merritt *et al*.,

2012; Randolph, 2018). An example of such failure was found in the piles of the Valhall water injection platform, where 5 of the 8 piles encountered premature refusal (Randolph, 2018).

The models used to investigate the effect of chamfered tips in this section involved boulders with $\tilde{b} = 10$ buried at $z_b = 0.05$. The mechanical properties of the models remained $r_\sigma = 1000$, $r_E = 10000$. Figure 3-39 (a) shows the geometry of the simulated chamfer. A parameter, $\alpha = 2\Delta d/t$, was created to characterise the vertical extent of the chamfer. Two chamfer geometries, $\alpha = 20$ and 40, were investigated as the contact eccentricity $\tilde{e}$ varied from 0 to 0.2.

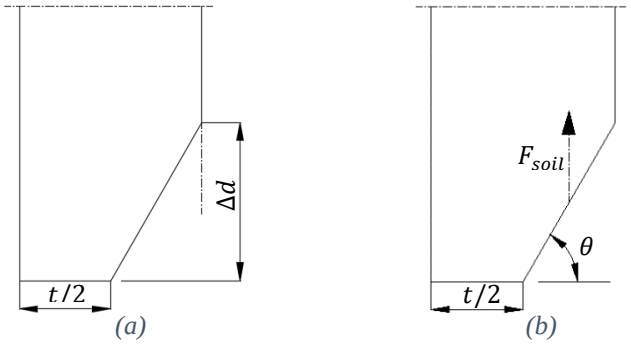


Figure 3-39 (a) Chamfer geometry; (b) Chamfer subjected to vertical soil forces

Figure 3-39 (b) shows the loading condition of an undeflected chamfered tip subjected to soil resistance only. The vertical resultant force from the soil is denoted as F_{soil} [N/m], taken as

$$F_{soil} = \frac{s_u t}{2\cos\theta} = \frac{1}{2} s_u t\sqrt{1+\alpha^2} \qquad \text{Eqn. 3-15}$$

Therefore, with the increase of α, the resultant force to the inclined surface will become larger. The tip, in addition, is prone to more considerable deflections with less steel mass providing resistance simultaneously. Figure 3-40 shows the trajectories of plate tips. The critical contact eccentricity (giving the largest final tip deflection) remains $\tilde{e} = 0.1$ for the chamfered plates. In general, the chamfer decreases the lateral resistance of the tip. Without eccentricity, the two

shapes of chamfers have consistent tip deflection. With eccentricity, however, the tip deflection increases as α becomes larger. This finding is consistent with the simple calculation provided in Eqn. 3-15.

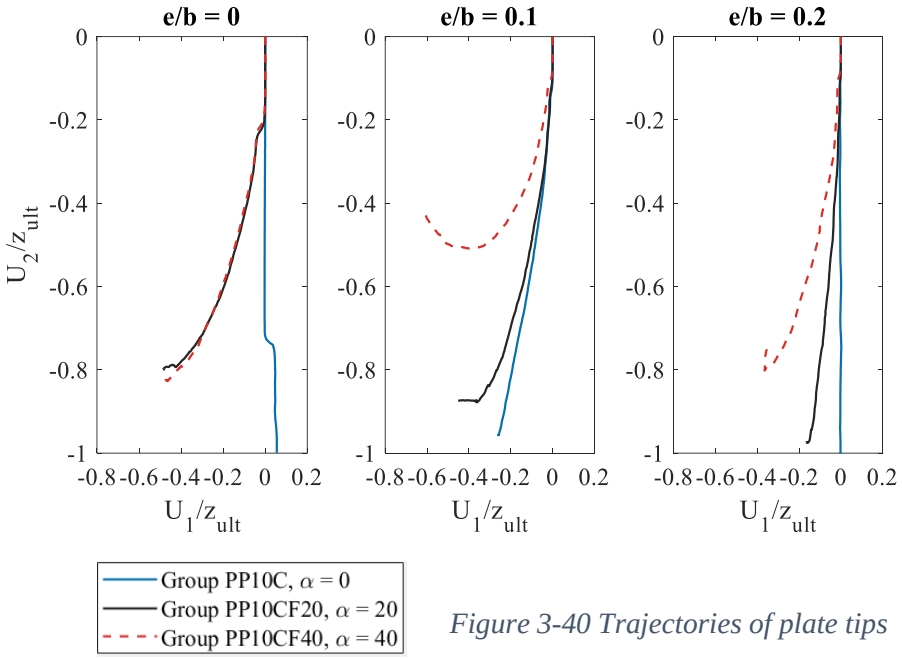


Figure 3-40 Trajectories of plate tips

3.5 CONCLUDING REMARKS

This chapter presented the parametric study of the tip deflection due to boulder collision during plate penetrations. The study was based on equivalent 2D models in that the model thickness was much smaller than its width and height.

Five normalised parameters were investigated individually based on models with circular boulders. To evaluate and compare the parameter sensitivities, a new parameter, *sensitivity index*, was calculated based on the tip deflection at the end of plate penetration. These indices showed that the boulder size was most influential to the tip deflections, followed by the boulder embedment and the soil strength in the second place. However, the index cannot reveal the relationship between the parameter and the tip deflection. Because Eqn. 3-14 was a simple linearisation and cannot represent the high-order relationship that possibly existed. Due to the

same reason, the index was not suitable for evaluating the coupling effects of multiple parameters.

The coupling effects of parameters were also investigated for boulder size and eccentricity, as well as boulder embedment and eccentricity. The critical contact eccentricity was found within 0.05 and 0.1 times the diameter of the circular boulder. However, the critical values might change with various boulder shapes.

The investigation of the boulder shape effects, though hard to quantify, delivered two mechanisms of the plate-boulder interaction:

1) The small contact area between the plate tip and the boulders could lead to more significant tip deflection due to the loss of balance.
2) The axis occupying the plate trajectory after boulder rotation determines the tip deflection. Longer axes would lead to more significant tip deflection.

For chamfered tips, the critical eccentricity remained consistent with the unchamfered ones. However, the chamfer would decrease the tip resistance. It was also found that the tip deflection positively correlated to the chamfered area – the larger the chamfered area was, the larger the tip deflection would be. The contact eccentricity, meanwhile, tended to magnify this decrease.

Apart from the parameters and factors covered in this research, more detailed investigations could still be done by, for example, including the coupling effects of multiple (≥ 3) parameters, or using smaller incremental steps of individual parameters. However, these detailed investigations would lead to a significant increase in model numbers. A much more computational cost would be required, but probably without much more information. Nevertheless, the detailed investigation may still be of interest if more efficient computation methods are established.

CHAPTER 4 LABORATORY-SCALE PHYSICAL MODELLING

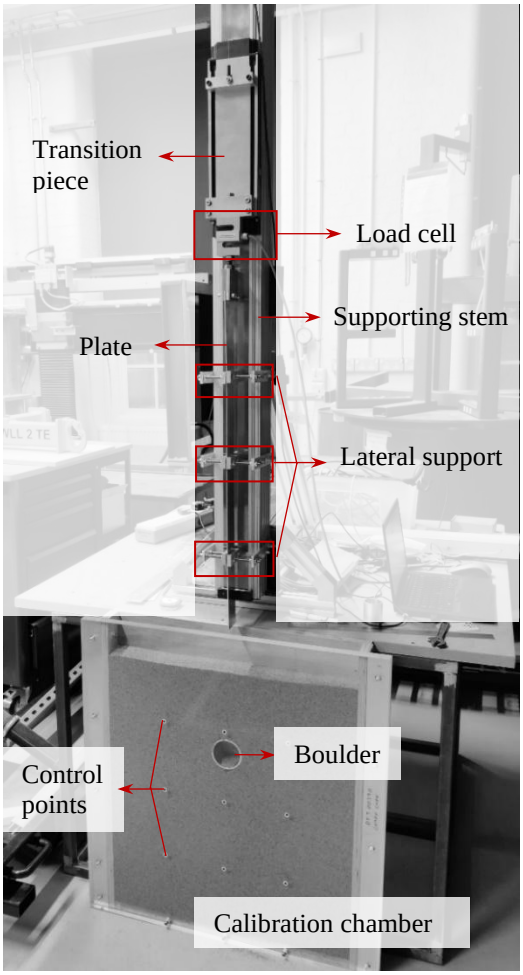


Figure 4-1 Apparatus for preliminary sand tests (motor not shown)

4.1 APPARATUS SETUP

The apparatus has three major components, the calibration chamber (Section 4.1.1), the loading and measurement devices during plate jacking (Section 4.1.2), and the accessories (Section 4.1.3). An overview of the apparatus for preliminary sand tests can be seen in Figure 4-1.

4.1.1 CALIBRATION CHAMBER

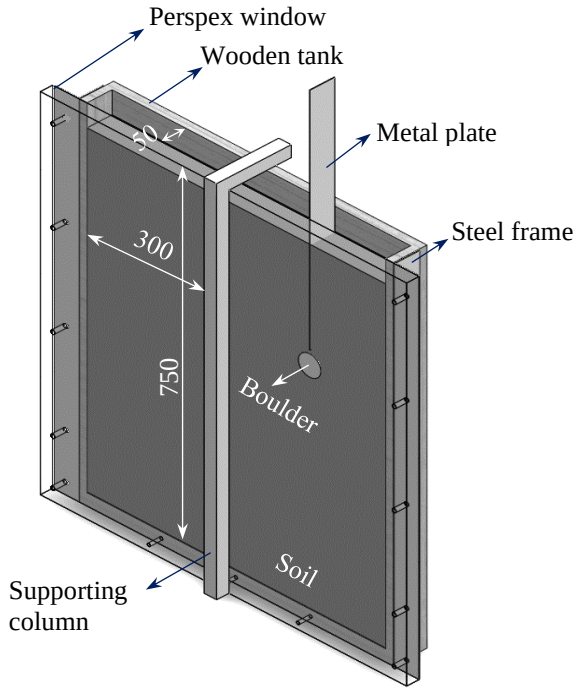


Figure 4-2 CAD models of calibration chambers, unit: mm

The calibration chamber contains three major components: the Perspex sheet, the wooden tank, and the steel frames. A Computer-Aided Design (CAD) model of the chamber can be seen in Figure 4-2. Though a 25 mm thick Perspex sheet was selected, the out-of-plane curvature of the Perspex still exceeded the acceptable range due to the contained volume of soil, interfering with the tests, especially for the sand specimen. Therefore, as shown in Figure 4-2, a vertical supporting column was introduced to maintain the gap between the Perspex and the wooden frame at 50 mm. The column also divides the chamber into two, providing two observation

windows of dimensions 300 mm and 750 mm. Since the gap between the sheet and wooden tank is much smaller than the length and height of the chamber and limited out-of-plane deformation could occur, tests conducted in this calibration chamber approximate a plane-strain condition.

4.1.2 LOADING AND MEASUREMENT DEVICES

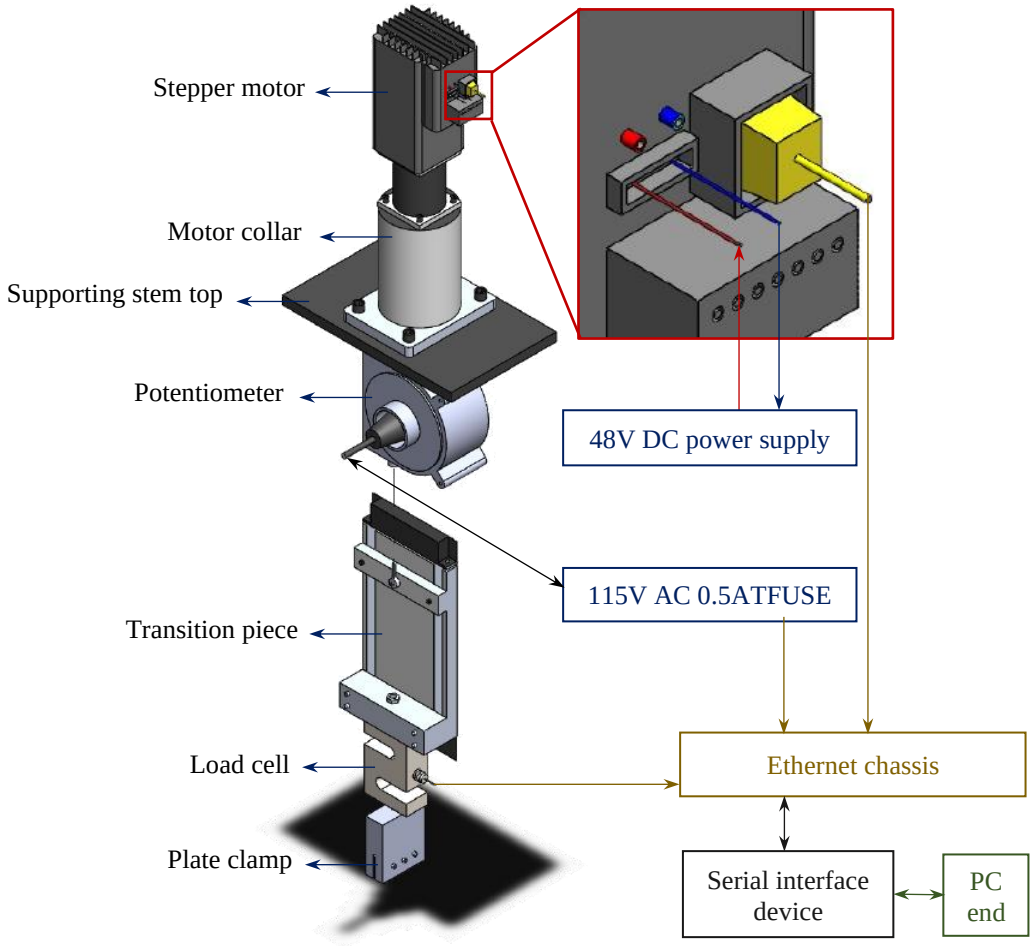


Figure 4-3 CAD model of loading and measuring devices (supporting stem not shown)

The arrangement of the loading and measurement devices is presented in Figure 4-3 as a CAD model. During the test, the plate was jacked into the soil via displacement control, using a stepper motor (STM23Q-3AE from Mclennan Ltd.). With a 48V DC input voltage, the stepper motor delivers a steady torque of ~1.48N·m with a speed of five revolutions per second (rps).

The power supply (PS320A48 from Mclennan Ltd.) provided a regulated output voltage for the stepper motor at 48V with an output range from 43.2V to 52.8V. A transition piece was attached to the supporting stem to transmit the jacking forces from the motor to the plate. The moving end of the potentiometer (SP2-50 from Measurement Specialist) was attached to the transition piece to record the penetrating depth of the plate. A power supply (provided by the University of Oxford) of 115V AC was used for the potentiometer.

An S-beam load cell (LCM105-500 from Omegadyne Inc.) was attached to the bottom of the transition piece and the top of the plate clamp to measure the plate reaction force during installation. The maximum capacity of the load cell was ~4.9 kN, which was sufficient for the intended tests. The load cell, along with the motor and potentiometer, was linked to the Ethernet chassis (cDAQ-9188 from National Instruments) for the data collection. Communication with the PC was through the interface device (USB-RS232 from National Instruments). Detailed procedures for the calibrations of the instruments can be seen in Mayall (2018). The sensitivities of the load cell and potentiometer were:

Load cell	1634.94	N/(mV/V)
Potentiometer	137.63	mm/V

4.1.3 DATA ACQUISITION AND PROCESSING

The LabVIEW code used for the experimental control and data acquisition was developed by Mayall (2018) for cone penetrometer testing (CPT). The structure of the program is shown in Figure 4-4. The code was modified to accommodate the new test arrangement.

The synchronised data processed by the LabVIEW code were primarily for test monitoring, with analysis of the test results based on the raw data. The raw data, with units [mV/V] for the load cell and [V] for the penetrometer, were delivered from the instrumentation at

approximately 1.6 kHz. This frequency was the property of the instrument, while the experiment itself did not need such a high rate. The resolution of data acquisition was 32 bits. Fluctuations were found in the data due to the oscillated electric signals. A MATLAB script was thus built to smooth the data by taking the data average within every integer second. The smoothed data from the load cell and potentiometer were then converted to [N] and [mm], respectively, based on the sensitivities listed in Section 4.1.2.

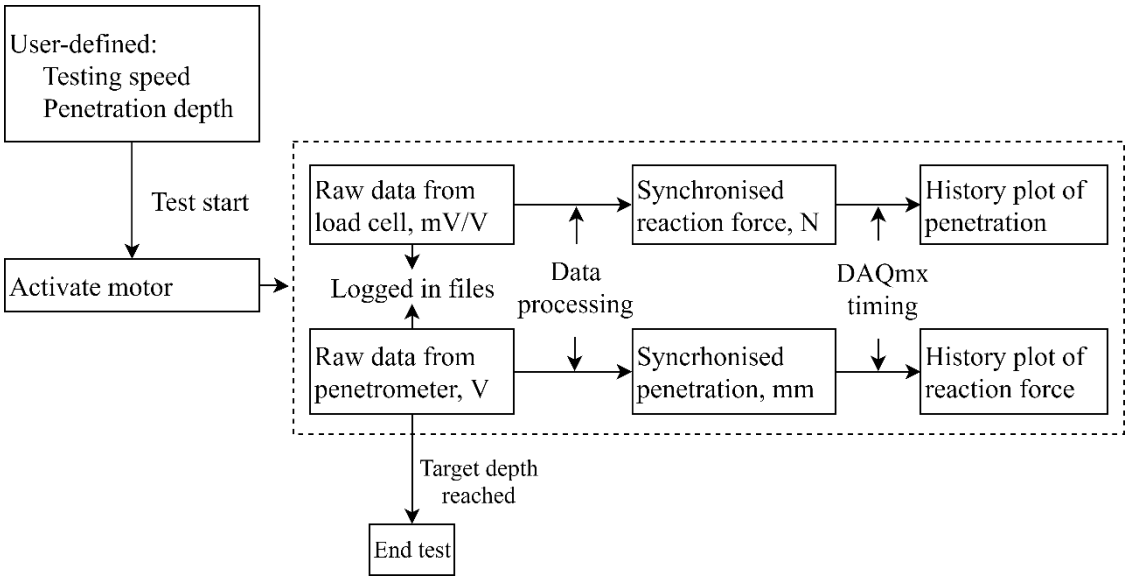


Figure 4-4 Structure of LabVIEW code

4.1.4 ACCESSORIES: LATERAL SUPPORTS AND EDGE WRAPPING

To improve the performance of the test, two types of accessories were added to the plates.

Lateral supports

Three pairs of lateral supports were placed along with the height of the plate, as shown in Figure 4-1. A detailed view of one support is shown in Figure 4-5. The functions of these supports were twofold: they (a) prevented the plate from excessive Euler buckling in the air during penetration; and (b) ensured the plate was jacked into the soil at the desired location. Small

gaps, up to 2mm, were reserved between the plate and each lateral support to decrease the friction due to surface pressure. Therefore, friction between the plate and lateral supports only occurred after the plate came into contact with the lateral supports due to Euler buckling.



Figure 4-5 Lateral support of plate (one pair)

Edge wrapping

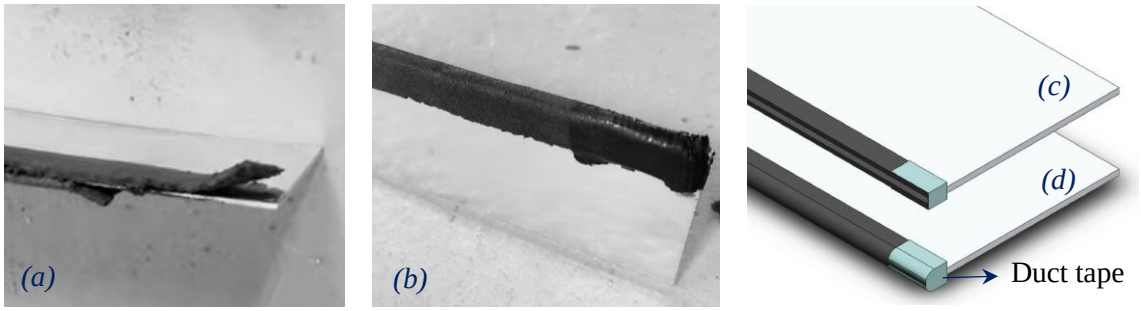


Figure 4-6 Edge wrapping

(a) Photograph of Wrapping A (ruptured); (b) Photograph of Wrapping B;
(c) CAD model of Wrapping A; (d) CAD model of Wrapping B

The edge wrapping was used to prevent the soil particles from falling in front of the plate, especially in the sand tests, and intervening in the observation of the plate trajectory. Two types of edge wrapping, as presented in Figure 4-6, were attempted for the test. Wrapping A (Figure 4-6 (a) and (c)) had two layers of 3mm rubber sheet adhered to the plate. The tip was wrapped in duct tape (Figure 4-6(c)) to prevent the rupture of the rubber sheet (Figure 4-6 (a)) due to friction from the soil particles. Wrapping A was used for the preliminary test in sands, but was

then replaced by Wrapping B (Figure 4-6 (b) and (d)), which had better resistance to the falling sand particles and generated less soil friction. Similar to Wrapping A, 3 mm rubber sheets were used for Wrapping B in the sand tests. In the clay tests, however, 0.6 mm foam tape was used to decrease the movement of soil particles due to the additional width brought to the plate by the wrapping, thus enabling more accurate descriptions in the PIV analyses.

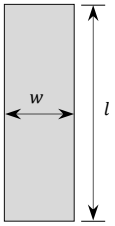
4.2 COMPONENTS AND MATERIAL PROPERTIES

The tests focused on the interactions of three components: the plate, the artificial boulder, and the soil (loose dry sand or soft clay). The preparation of the soil sample is discussed in detail in Section 4.4 for loose sand, and Section 4.5 for soft clay, together with the corresponding tests. The mechanical properties of the plates and boulders were consistent for all tests, and are presented in Section 4.2.1 and 4.2.2, respectively.

4.2.1 PLATE

Table 4-1 Dimensions of tensile test specimens

No.	Thickness, t [mm]	Length, l [mm]	Width, w [mm]		Average cross-section area, A_a [mm^2]
			End 1	End 2	
1	1.47 (~1.50)	121	24.70	24.40	38.09
2			25.79	24.14	36.70
3			24.95	25.43	37.03
4			24.42	24.48	35.94
5			25.15	24.80	36.71
6			25.29	24.65	36.71



The metal for the plate manufacturing was selected to be sufficiently soft and flexible so that the buckling phenomena could be triggered in the laboratory-testing conditions. Therefore,

high-strength steels commonly used in the offshore industry were replaced by Duralumin. A programme of ultimate tensile tests was conducted to obtain the mechanical properties of the Duralumin used for this research.

During the test, tensile loading was applied to the specimen using displacement control. The upper grip, shown in Figure 4-7 (a), moved upwards at a slow rate, 0.002 mm/s, to minimise material hardening due to dislocations at high loading rates. Six rectangular plate specimens were tested, the dimensions of which are provided in Table 4-1.

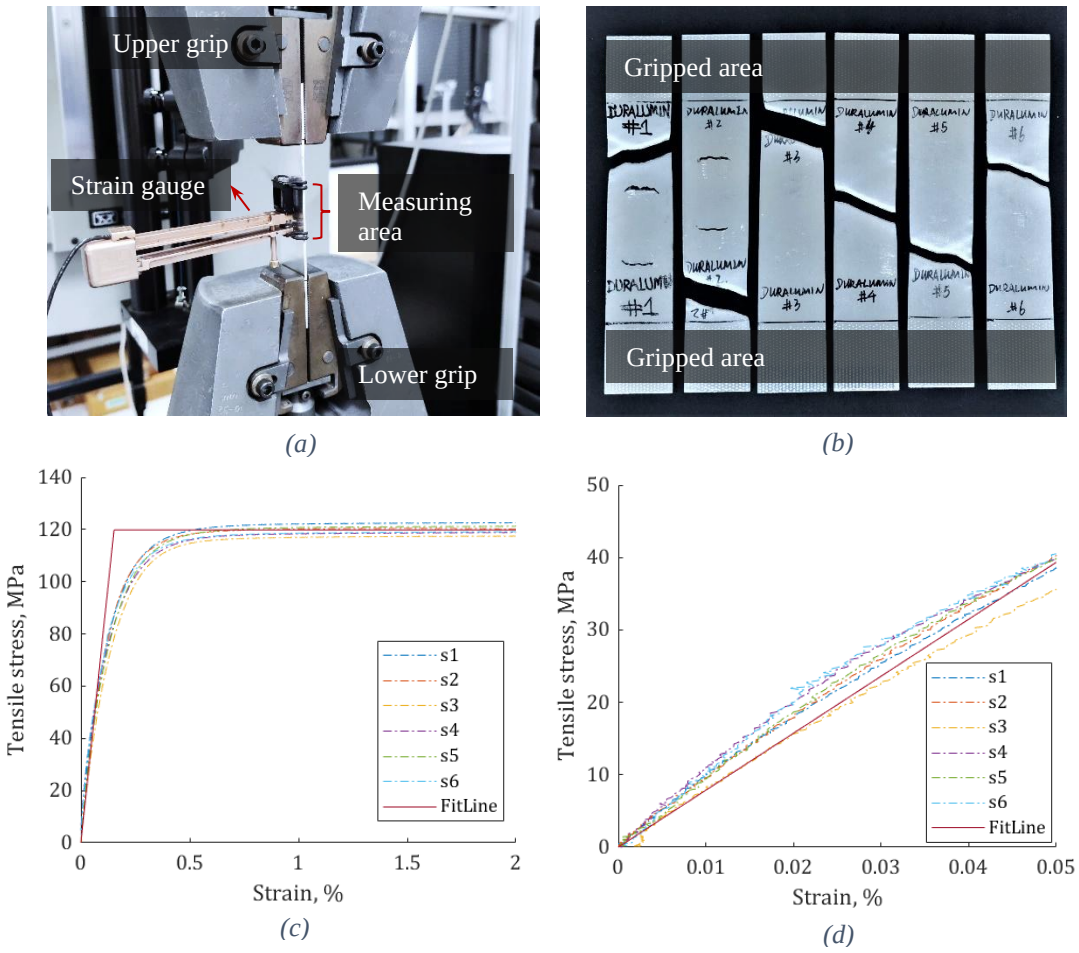


Figure 4-7 Photographs and results of plate ultimate tensile tests

(a) Gripped sample and strain gauge position;
(b) Duralumin samples (ruptured, left to right, s1~s6);
(c)Complete stress-strain plots;
(d) Stress-strain plots within 0.05% strain range

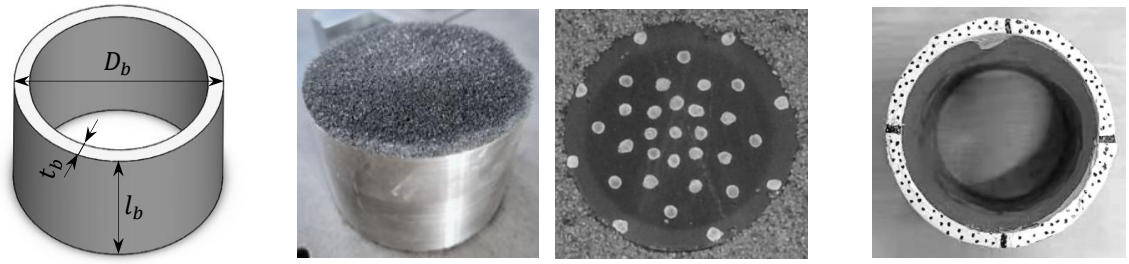
According to the standard BS EN 10002-1:2001 (2001), dumbbell-shaped specimens should be used for the tensile testing to ensure that failures occur in the midspan, within the measuring area of the strain gauge (Figure 4-7 (a)). The manufacturing of the dumbbell-shaped specimen, however, was rather complex due to the accuracy requirement. Rectangular specimens, such as those used for these tensile tests, give random locations of failures, especially in the proximity of the grips due to stress concentrations. Therefore, the elongation measured by the strain gauge could be less than its real value and lead to stiffer estimated material properties. As shown in Figure 4-7 (b), three out of six plates ($s1$ to $s3$) had failures close to the grips, outside of the measuring area of the local strain gauge. However, this random failure distribution did not lead to significant discrepancies amongst the test results (Figure 4-7 (c)). Therefore, the results from the rectangular specimens were deemed acceptable for use in the numerical simulations covered in Section 4.2.1.

The average value of the yield strength, σ_Y [Pa], was first calculated based on the plateau of the stress-strain plots (Figure 4-7 (c)), giving $\sigma_Y = 119.83$ MPa. Since the Duralumin used for the tensile test was a ductile material, there was no distinguishable "turning point" symbolising the transition from elasticity to plasticity. To ensure the material was still in its elastic region, the results in a small strain range of 0 to 0.05% (Figure 4-7 (d)) were used to determine the Young's modulus, E_p [Pa], giving an average value of $E_p = 78.69$ GPa. A fit line was plotted using the determined E_p and σ_Y, as shown in Figure 4-7 (c) and (d).

During the plate penetration experiments in the soil chamber, the thickness of the plate remained $t_p = 1.47$ mm, but the width and length became $w_p = 50$ mm and length $l_p = 750$ mm, respectively, to accommodate the testing conditions.

4.2.2 BOULDER

The boulder was made of thick-walled brass tube to simulate the rigid-body condition in the numerical models. A CAD model can be seen in Figure 4-8 (a). The wall thickness of the tube was adjusted to make the density of the boulder equal to the density of the saturated clay, which was assumed to be $25\ \mathrm{kN/m^3}$. The value, $25\ \mathrm{kN/m^3}$, is an empirical density of saturated clay, and the density match of the boulder and the clay was to prevent the boulder from sinking prior to the pile penetration. Two boulders were produced with different outer diameters, the detailed dimensions of which are listed in Table 4-2. The boulder length was made slightly smaller than 50mm to fit into the chamber.



(a) *(b)* *(c)* *(d)*

Figure 4-8 Boulder geometry

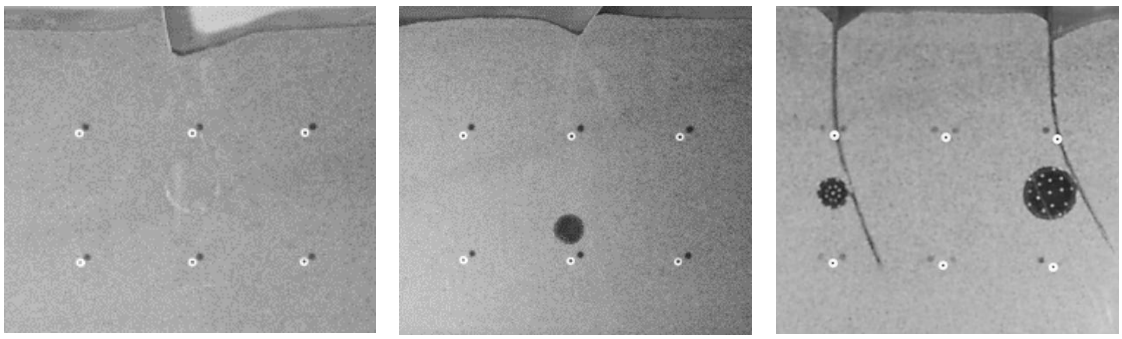
(a) CAD model of boulder; (b) Boulder with foam cover;
(c) Boulder with textured foam cover; (d) Boulder with textured edge

Table 4-2 Boulder dimensions

No.	Length, l_b[mm]	Outer diameter, D_b[mm]	Wall thickness, t_b[mm]
$b1$	49 (~50)	75	5.5
$b2$		45	6.5

Similar to the edge wrapping of the plate, a layer of 3 mm rubber sheet was attached to the front face of the boulder for the sand tests, as shown in Figure 4-8 (b) and (c). This prevented the soil particles from falling in front of the boulder and interfering with the observation. A

comparison of the test performance with and without the rubber covering or edge wrapping can be seen in Figure 4-9. Textures were painted onto the coverings at a later stage to record boulder displacements and rotations in the PIV analysis. Despite its effectiveness in the sand tests, the covering was removed in clay tests, and the textures were only painted on the top edges of the boulder (Figure 4-8 (d)). This was because, when the boulder was pushed into the saturated clay, the rubber covering became an air seal, restricting the placement of the boulder. A detailed description of the sample preparation for the clay test is given later in Section 4.5.2.



(a) *(b)* *(c)*

Figure 4-9 Effects of boulder covering and plate edge wrapping in sand testing
(a) no covering or wrapping; (b) with covering but no wrapping; (c) with covering and wrapping

4.3 PARTICLE IMAGE VELOCIMETRY ANALYSIS SETUP

Particle Image Velocimetry (PIV) originated from the measurement of instantaneous field variables in fluid mechanics (Adrian, 1991), and was first implemented in geotechnical problems by White *et al.* (2001). Compared with conventional image-capture methods, PIV requires a less stringent arrangement of marking points on samples, but provides descriptions of the velocity field based on the spatial variation of brightness (White *et al.*, 2003).

The PIV analysis conducted in this research was based on GeoPIV-RG developed by Stanier *et al.* (2016). This program has enhanced precision of displacement measurement. Previous

researchers proved the effectiveness of the program in relation to the measurement of rigid body displacements (Wheeler *et al*., 2016) and soil movement (Stanier *et al*., 2016). Though the measurement of the plate deformation in this research did not fall into either of the two categories, GeoPIV-RG was still capable of measuring the trajectory of the plate, the displacement of the boulder, and the movement of soil particles. A detailed discussion of this is found in Section 4.6 for the tests in clay.

4.3.1 RESOLUTION REQUIREMENTS AND DIGITAL EQUIPMENT

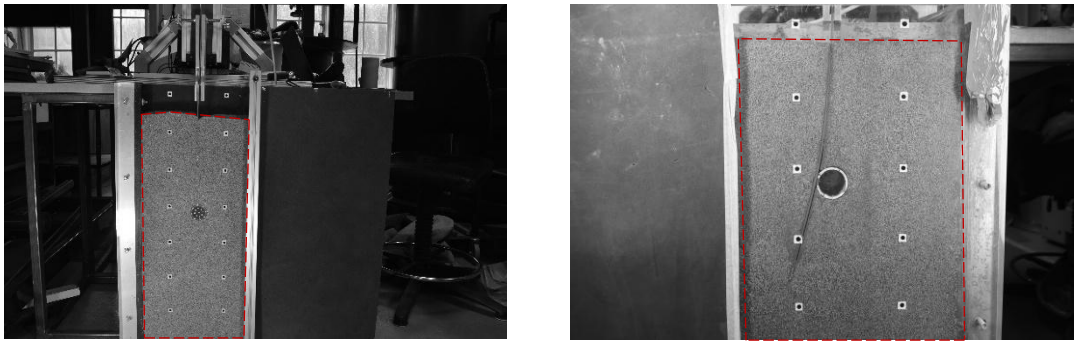
The resolution requirement of photographs used for PIV analysis was determined based on the 2D numerical model. Table 4-3 gives the minimum scale of displacements in the 2D numerical models, including the horizontal displacement of the pile tip, U_{p1} [mm], the horizontal and vertical displacement of the boulder, U_{b1} [mm] and U_{b2} [mm]. For the convenience of generalisation, these parameters were normalised against the total penetration depth of the plate $Z_{tot} = 100t$, where t [mm] was the plate thickness, and the parameters became $\widehat{U}_1 = U_1/Z_{tot}$, $\widehat{U}_2 = U_2/Z_{tot}$.

Table 4-3 Scale of deformation in the 2D numerical models

Location	Pile tip	Boulder vertices	
Component	$\widehat{U}_{p1}$	$\widehat{U}_{b1}$	$\widehat{U}_{b2}$
Min. scale	6.26E-3	1.2E-3	2.42E-2

With the total penetration depth at 300 mm in the proposed experiments, the minimum displacement to be captured was around 0.36 mm. It was anticipated that the PIV apparatus would be able to capture small displacements in the scale of 0.001 mm. Given that the precision of detected rigid-body displacements by GeoPIV-RG could reach ~0.001pixel (px), the anticipated nominal image scale for the experiments was 1mm/px. Assuming that the Region

of Interest (RoI) was equal to the maximum interaction domain of each test, which was 300mm × 700mm, the minimum requirement of the image dimensions was therefore 300px × 700px.



(a) *(b)*

Figure 4-10 Experiment image and region of interest
(a) NIKON D3200 image; (b) Canon G7 image

During the experiment, two cameras were used. The first camera, NIKON D3200, gave the total image dimensions at 6016px × 4000px. An example of an experimental image taken by the NIKON D3200 is shown in Figure 4-10 (a). The RoI, marked by the red lines, possessed an area of 1265px × 2687px. A second camera, Canon PowerShot G7 X Mark II (abbreviated as "Canon G7"), provided total image dimensions at 5472px × 3648px. The RoI of Figure 4-10 (b) taken by the Canon G7 was 5472 px × 3129 px. Both images satisfied the minimum requirement of 300px × 700px. The displacement at the scale of 0.001mm could be captured by GeoPIV-RG, as anticipated.

4.3.2 IMAGE QUALITY CONTROL

During the PIV analysis, the RoI of each photograph was discretised into a grid of "test patches" (White *et al.*, 2003). Patches of the image at a later time step (t_{n+1}) are compared with ones at an earlier time step (t_n) pixel by pixel using cross-correlation (White *et al.*, 2003). The pair of patches in two images with the highest correlation coefficients are regarded as

identical with the distance between the two patches recorded as displacements. One key factor affecting the precision of this process is the spatial brightness frequency (White *et al.*, 2003). In coloured images, the brightness frequency may be disturbed by the dispersion of lights in the camera lens. As shown in Figure 4-11, the sand particles in the coloured image partially turn into red or green due to dispersion, which would then affect the calculation accuracy. Therefore, monochrome images, which have more consistent brightness frequencies, were taken for the PIV analysis during the experiment. To enhance the image quality, the focal length and the aperture diameter were locked once the experiment commenced to prevent the focus changing due to the movement of the plate, while also keeping the light environment of all images consistent throughout the test.

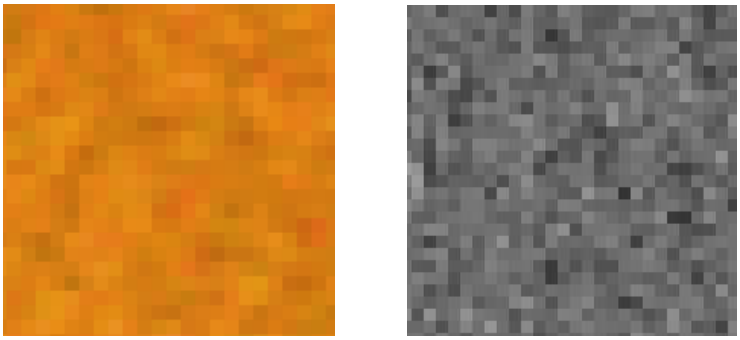


Figure 4-11 Comparison of sand patches in coloured and monochrome images

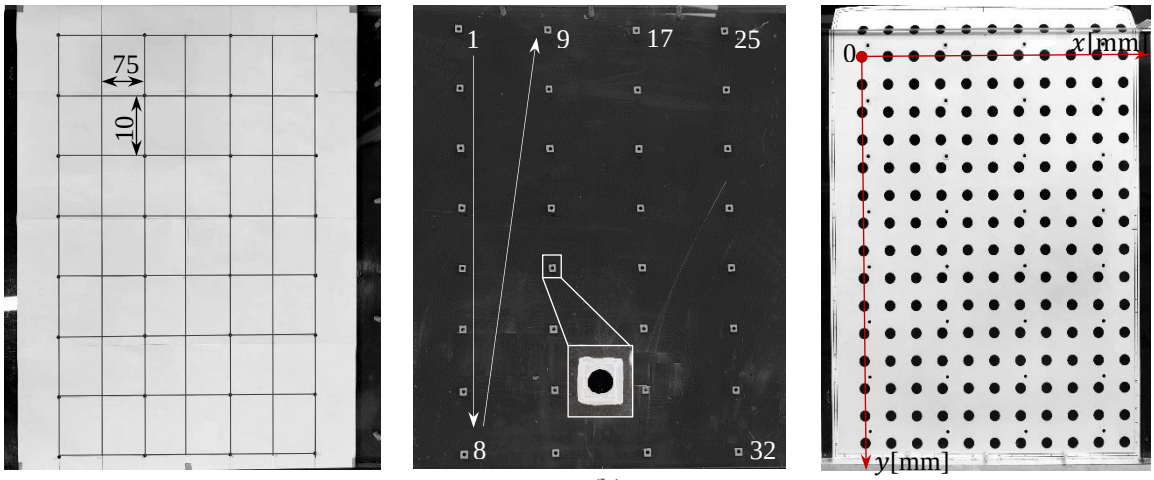
Table 4-4 Photographing control parameters

Camera	**NIKON D3200**	**Canon G7**
Control method	Wired remote controller with self-timing	Bluetooth controller with no self-timing
ΔT[s]	1	5
$\boldsymbol{v_p}$**[mm/s]**	2	0.4

Because the test patches were compared using cross-correlation, the relative deformations between two images need to be sufficiently small for the calculation to proceed effectively.

Excessively large relative deformations might confuse the patch comparison procedure in the program, leading to "wild vectors". A balance between the time step, ΔT [s], of photographs and the penetration speed of the plate, v_p [m/s], was found through trial and error. Different ΔT and v_p were used for the two cameras to accommodate their control methods, as summarised in Table 4-4.

4.3.3 CONTROL POINT AND COORDINATE CALIBRATION

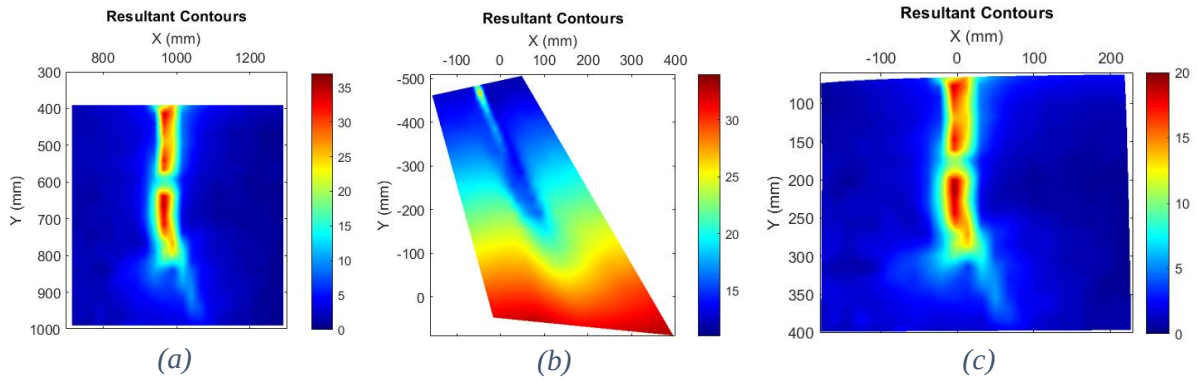


(a) *(b)* *(c)*

Figure 4-12 Photographs of control point geometry and calibration
(a) Paper grid for initial CP locating (unit, mm*); (b) Painted CP; (c) CP calibration*

After the cross-correlation calculation, the results based on image pixels, or Image-Space Coordinates (ISC), are converted to displacements in the Object-Space Coordinates (OSC). To navigate this conversion process, 32 Control Points (CPs) were manually painted on the Perspex window. The control points were expected to cover the entire interaction space, including the void layer above the soil surface to record the soil heaving. A paper grid, as shown in Figure 4-12 (a), was placed on the Perspex sheet for the initial locations of the CPs. The paper grid had horizontal intervals every 75 mm, and vertical intervals every 100mm. The CPs were placed on the grid at every second horizontal interval (150 mm) and every vertical

interval (100 mm). Figure 4-12 (b) presents the distribution of the painted CPs and their numbering, which started from the top left and proceeded by columns. Each CP was a black circle with a diameter of 5 mm, and surrounded by a 10 mm × 10 mm white square (enlarged image in Figure 4-12 (b)). To avoid shadows casting on the soil surface through the thick Perspex sheet, the CPs were painted on the inner side of the Perspex, against the soil. Both the colouring and geometry of the CP accommodated the definition of CPs in GeoPIV-RG.



(a) *(b)* *(c)*

Figure 4-13 Resultant displacement contour comparison (origin of y-axis in the middle)
(a) Image-space displacements; (b) Uncalibrated object-space displacement;
(c) Calibrated object-space displacement

Though the paper grid gave the initial locations of the CP, the accuracy of these initial values cannot be guaranteed by manual measurements. Figure 4-13 shows a comparison of two object-space resultant displacement contours converted from the same image-space contour (Figure 4-13 (a)) based on uncalibrated (Figure 4-13 (b)) and calibrated CP locations (Figure 4-13 (c)). It can be seen from the figure that, though the errors between the initial and the calibrated CP coordinate in this case were no more than 5mm, significant twisting of the output contours can appear from the PIV analysis.

Two calibration methods can be used for CP coordinates. The first, named as “stitching”, is described in detail by Song (2020, sec. 4.2.3). This method uses a high-accuracy dot mesh, Fixed Frequency Grid Distortion Targets (FTGD), to calibrate the manually painted CPs.

Though high accuracy can be achieved, this method can only calibrate a limited number of CPs at one time, as the largest dimension of FTGD was $150\text{mm} \times 150\text{mm}$ (EdmundOptics, 2022). Repetitive calibrating procedures are then required to cover the entire CP domain. Additional CAD software, such as SOLIDWORKS, was also needed to integrate the calibrated CPs.

An alternative method was to replace the FTGD with Printer Printed Dots (PPD). As shown in Figure 4-12 (c), the PPD in A2 size was placed against the inner side of the Perspex window, on the same side with the painted CPs. Both the vertical and horizontal distance between the centres of two adjacent dots were 50mm precisely. Together, these dots could form reference coordinates in the units of [mm] for the painted CPs. The calibrated coordinates of CPs, (x_{ccp}, y_{ccp}) can then be obtained following the control point analysis procedure in GeoPIV-RG using the point-by-point method, the workflow of which is shown in Figure 4-14.

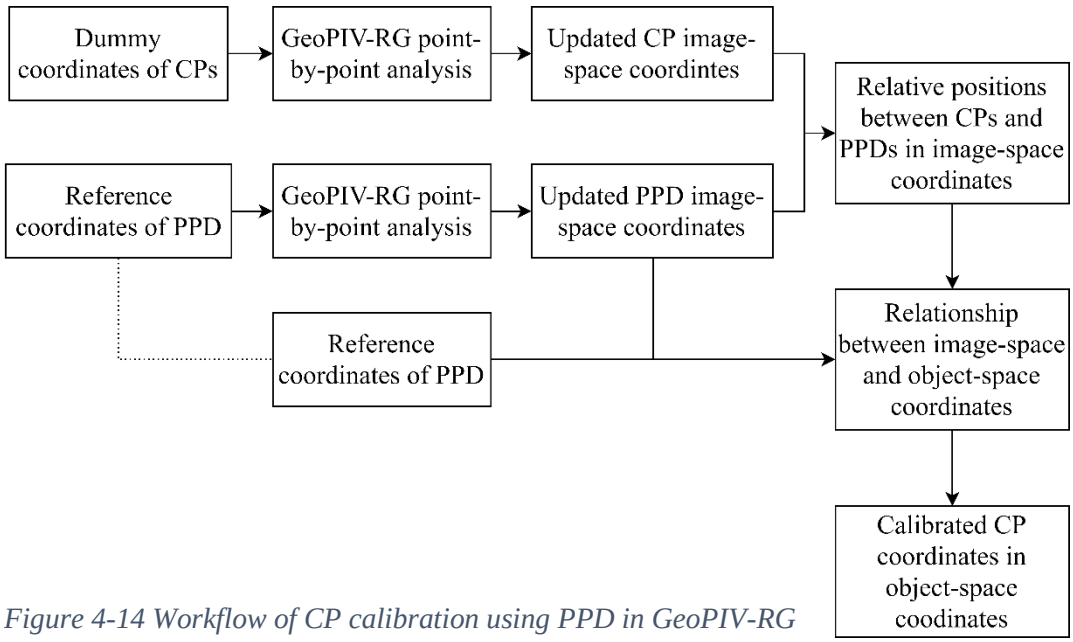


Figure 4-14 Workflow of CP calibration using PPD in GeoPIV-RG

4.4 PRELIMINARY TESTING IN SANDS

A number of preliminary tests were performed on loose sand to trial different apparatus setups and operational procedures, to establish the optimum configuration. The quantitative comparison of the sand test was excluded because of two reasons: 1) a robust constitutive model of the sand was difficult to implement in Abaqus CEL, and 2) boulders are less likely to appear in sands. Instead, the results of these preliminary tests were used for qualitative evaluations to find the most effective experimental conditions for the PIV analysis.

4.4.1 PREPARATION OF SOIL SAMPLES

Dry Yellow Leighton Buzzard sand was used for the preliminary testing. This type of sand had been used for a number of research projects in Oxford, the particle size of which is presented in Figure 4-15.

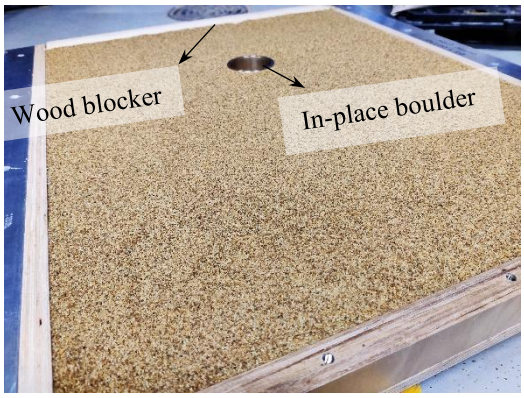


Figure 4-15 Photograph of loaded and flatted sand (rubber sealing not shown)

Particle size (Richards, 2019)	
d_{10}	0.56 mm
d_{30}	0.69 mm
d_{50}	0.81 mm
d_{60}	0.87 mm

To begin the preparation of the soil sample, the calibration chamber is laid horizontally, with a wooden blocker sealing the open end, as shown in Figure 4-15. The boulder was placed in the designated position, before the sand is then loaded into the tank using air pluviation. To create

a flat surface, an aluminium sheet of length 750 mm (longer than the width of the chamber) was scraped against the right and left edges of the chamber to remove excess sand. The Perspex window was then screwed into the frame on top of the sand surface, with painted calibration points on the inner side. After this, the calibration chamber was lifted to the upright position.

The sand was loaded horizontally instead of vertically with two primary considerations. First, the sand test was to find the optimum operating procedure for the clay test. This operating procedure, loading the soil with the tank lying on the floor, was adopted by the clay tests, as described in Section 4.5.

Each component of the calibration chamber was designed to be sufficiently tight, to seal the soil particles during the uplifting (from horizontal to vertical), however this was not perfectly achieved due to deformations of the Perspex and the wood panel given self-weight loading, and wear and tear from repetitive use. To resolve this, in the subsequent experimental stages, a layer of rubber sheet was adhered to the wood frame edges in contact with the Perspex sheet. The loaded chamber was positioned horizontally to obtain the anticipated contact eccentricity between the plate and the boulder. However, both the eccentricity of contact and the embedment depth of the boulder could not be precisely controlled or adjusted to accurately achieve the anticipated position. The inaccuracy of eccentricity was due to the friction between the heavy chamber and the laboratory floor. The inaccuracy of boulder embedment was caused by the downward movement of the loose sand and the boulder under gravity. Strategies to cope with these issues were introduced for the clay test, presented in Section 4.5.

4.4.2 CAMERA SETUP

The camera was positioned to cover the region of interest. A thin layer of void area above the free surface of the soil was included to capture soil heave. The bottom boundary of the camera

domain was at least 50mm lower than the expected ultimate penetration depth of the plate, to give a complete picture of the soil flows. The left and right boundaries of the test were also covered to provide a complete view of the interacting area.

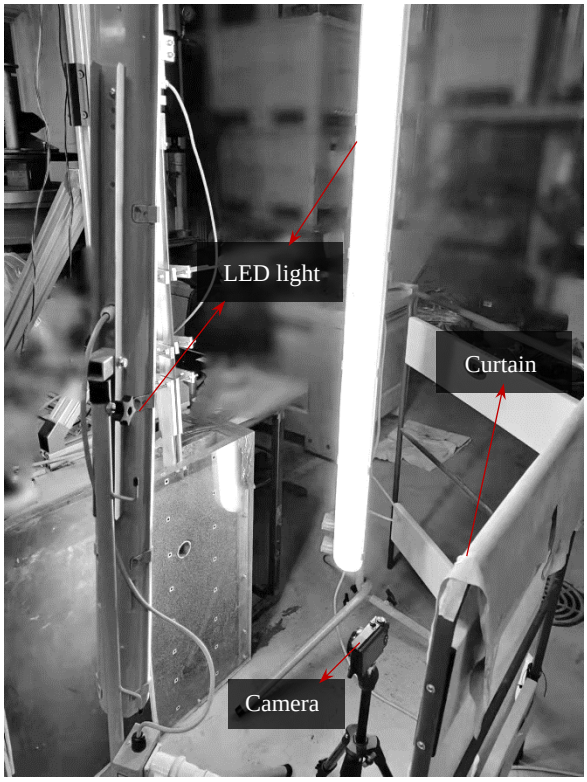


Figure 4-16 Lighting of experiments

The auto-adjustment of the camera focus position was turned off during the test to keep the brightness frequency of pictures consistent. A short exposure time of $1/125$s was selected to capture the detailed movement of soil particles at each time interval. The f-number was adjusted accordingly to $f/1.8$, correlating to an aperture diameter near its upper limit and subsequently more light was allowed to reach the server. To enhance the brightness and eliminate shadows from the apparatus, two 110V 30W LED tripod lights were placed in front of the chamber, as presented in Figure 4-16. A sheet of uniform colour was placed behind the camera, with sufficient size to avoid perturbation of brightness frequency from reflections over the entire area of the exposed Perspex window.

4.4.3 PRELIMINARY RESULTS

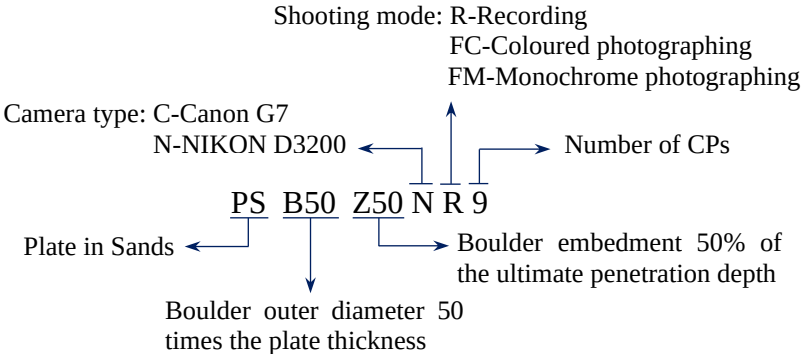
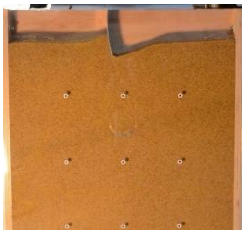
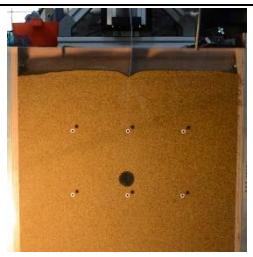
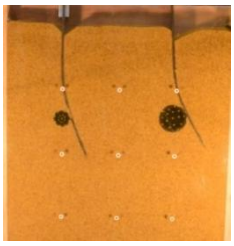
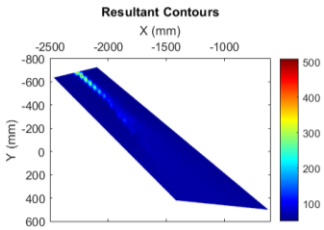
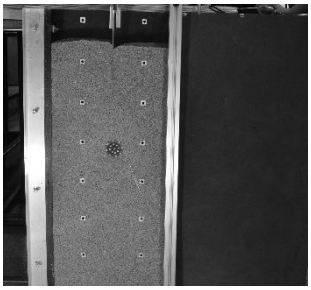
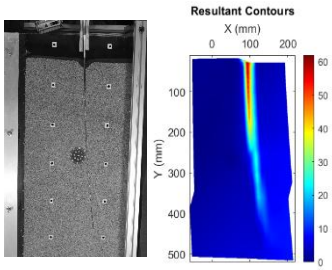


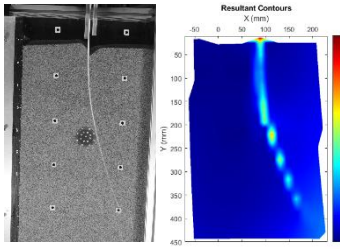
Figure 4-17 Test code interpretation for sand tests

In the preliminary tests, the plate was penetrated 500mm into the sand, with a focus on determining the optimum operation strategy for subsequent tests, in a larger range of soils. Table 4-5 lists the milestones of the preliminary testing stage. Not all of these milestones had satisfactory results, but they contributed to further improving the experiment. The improved aspects are listed in Table 4-5. A test labelling code was developed which included the intended initial position of each component, an example is shown in Figure 4-17. For the video-recorded test using NIKON D3200, a program was written in Python to convert the video file (.mp4) to the image files (.jpeg) by frames at a user-defined frame interval. These images were then used for the PIV analysis.

Table 4-5 Milestones of preliminary tests

Test code	Test results	Improvement
PSB50Z20NR9		The rubber covering, discussed in Section 4.2.2, was added to the test.

PSB30Z50NR9		The lateral supports were extended to the free surface of the soil to prevent Euler buckling of the plate at this point; the edge wrapping of the plate (see section 4.2.1) was introduced afterwards.
PSB30Z50NR9 & PSB50Z50NR9		First attempt of two experiments being conducted in tandem in the same soil sample for time efficiency; markers on the boulder covering were added to the test.
PSB50Z20NR9		The twisting of displacement contours in OSC first became a significant issue. Debugging of the test procedure started.
PSB30Z50NFM32		32 calibrated CPs were used for the tests; the monochrome image of the test was taken at every second when the penetrating speed of the plate was 5mm/s, slower penetrating speed was used for later tests; thinner edge wrapping was used for the plate, as discussed in Section 4.2.1.
PSB30Z50NFM32		The penetrating speed of the plate was reduced to 1mm/s. First promising results were obtained, further refinement started.

PSB30Z50NFM32		Satisfactory results were obtained in sand tests; the preliminary testing stage ended.

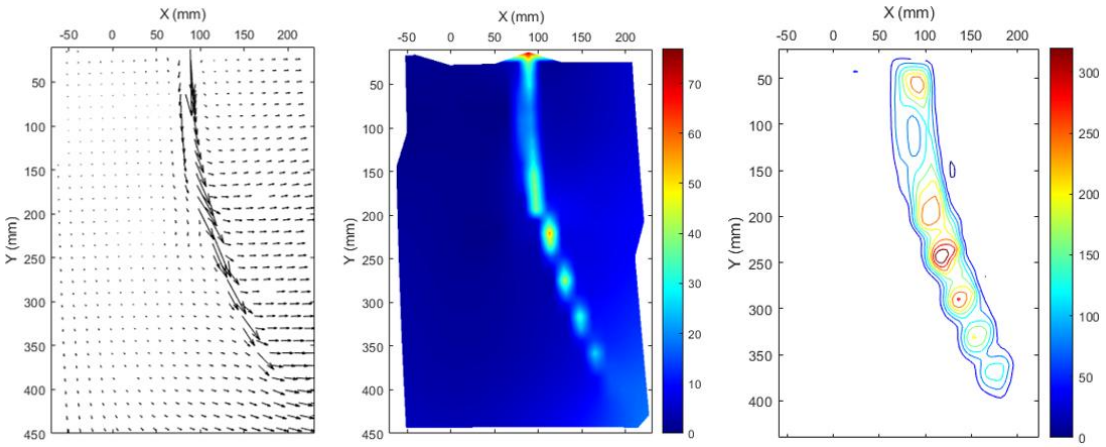


Figure 4-18 Results from PIV analysis of PSB30Z40NFM32
(a) Displacement vectors; (b) Resultant displacement contour; (c) Incremental strain plot

PSB30Z50NFM32 was the last test conducted in the preliminary stage. The penetration depth of the plate was decreased from 500 mm to 350 mm to be consistent with the testing conditions proposed for clays. The penetration speed was further decreased to 0.4 mm/s (stepper motor 0.5 rps), with images taken every second. Over the duration of the test, 799 images were obtained for the PIV analysis. The "leapfrog" algorithm was used for both control-point analysis and the soil-flow calculation. The total computing time of the two processes was around 16 h, with each of the two parts taking around 8 h. Figure 4-18 presents the results obtained from the PIV analysis, including the displacement vectors (Figure 4-18 (a)), the resultant displacement contours (Figure 4-18 (b)), and the incremental strain plot (Figure 4-18 (c)). These plots revealed movements of soil particles consistent with those observed

experimentally. The discontinuity in the lower part of the plate trajectory was due to sand falling in front of the plate edge. Any sand that fell in front of the plate edge was carried by the plate for a small distance, and finally was abandoned by the plate coming to rest in the surrounding soil.

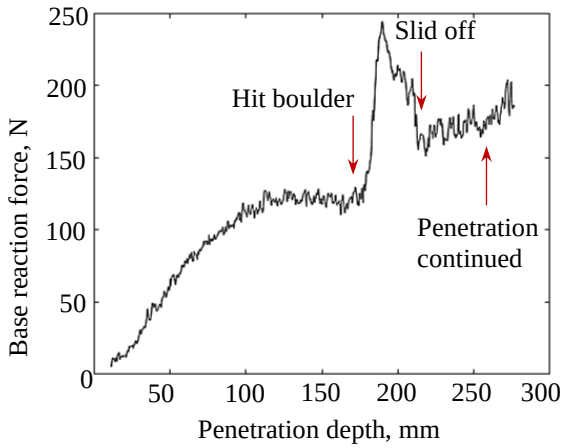


Figure 4-19 Force-penetration plot of PSB30Z40NFM32

Figure 4-19 shows the reaction force plotted against the penetration depth over the range of 0 to 300 mm, with the key features of the test annotated. The plate first hit the boulder at around 175mm, which was consistent with the design embedment depth of the boulder (50% of the total penetration depth 350 mm). Reaction forces continued to rise until the plate tip slid off the boulder. This led to the rapid drop of the reaction force after the peak. Once the plate tip was no longer in contact with the boulder, the reaction force increased steadily as the plate kept penetrating into the soil. This style of force-penetration behaviour was also found in the numerical models. At this point, the qualitative evaluations from the preliminary testing were considered to prove that the testing procedure for the PIV analysis was capable of giving satisfactory results in sand, and should also be suitable for testing in clay.

4.5 CLAY TESTING

The clay testing aimed at validating the numerical models under comparable experimental conditions. Stiff clay was selected for the first stage of the clay tests and was purchased from the company "Ketley Bricks". However, the forces were too large and so soft clay became the target material. A softening procedure was applied to Ketley stiff clays to produce the softer clay material. The mechanical properties and the preparation of samples are shown in Section 4.5.2. Firstly, the application of artificial textures on the clay surface for the PIV analysis is presented in Section 4.5.1. The results of the clay testing are discussed and compared with the numerical simulations in Section 4.6.

4.5.1 ARTIFICIAL TEXTURE SETUP

The density of artificial textures on fine-grained soils, such as the clay used for this research, could impact the accuracy of PIV analysis (White *et al*., 2003). Two texturing methods were found in the literature – flock fibres (White *et al*., 2001) or small diameter particles (Zhang *et al*., 2005). For the particle texturing method, studies show that the performance of PIV analysis would not be further affected by the densities of the particles, once a minimum threshold was reached (6 to 8 particles per patch) (Zhang *et al*., 2005). In addition, particles with smaller diameters favour the accuracy of analysis (Zhang *et al*., 2005). The dry Yellow Leighton Buzzard sand used in preliminary testing was used initially to provide the artificial texture. A thin layer of sand particles was scattered uniformly onto the clay surface after the clays were loaded into the calibration chamber and the surface flattened. This thin layer of sand does not affect the properties of the clay, nor the interaction between the plate and soil. The high density of small-size particles in each test patch was expected to favourably impact the performance of PIV analysis.

4.5.2 PREPARATION OF SOIL SAMPLES

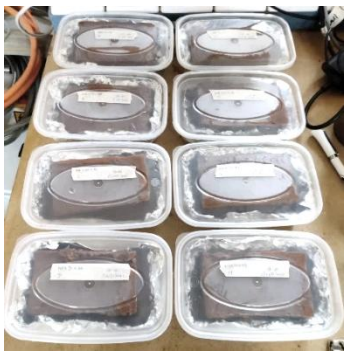


Figure 4-20 Clay softening for UU tests

Table 4-6 Variations of water content and s_u

Clays	Water content, w%	s_u[kPa]
OS	15.02	66.48
S24	19.93	23.87
S72	24.49	13.02

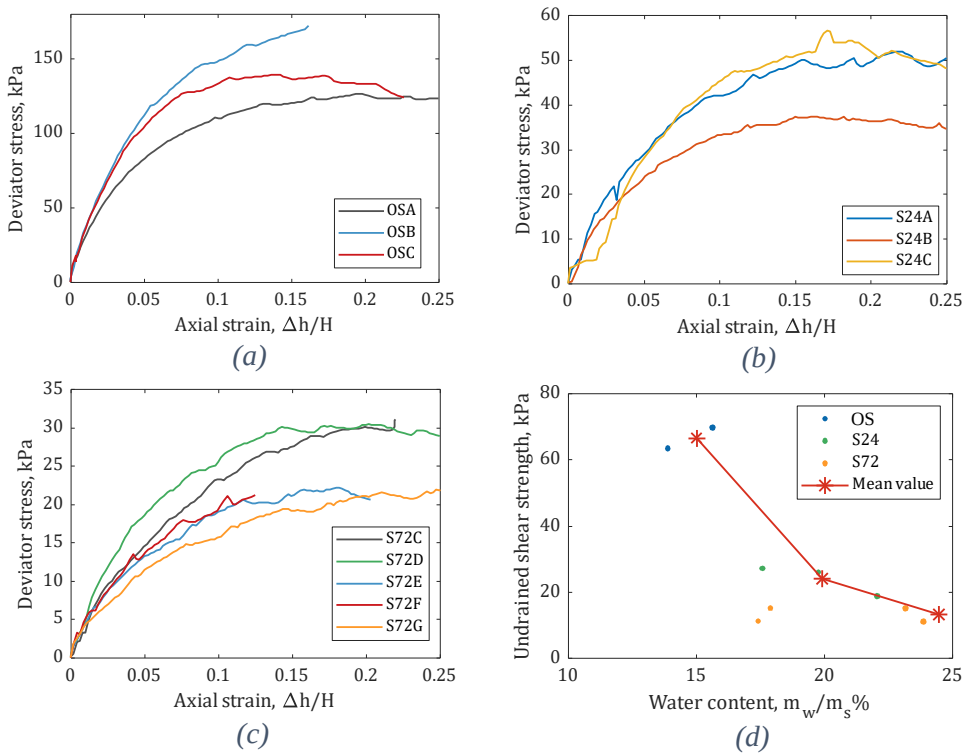


Figure 4-21 UU triaxial test results of clays and water content variations

(a) UU tests for OS blocks; (b) UU tests for S24 blocks; (c) UU tests for S72 blocks; (d) Strength variation against water content

Blocks of the Ketley stiff red clay were used for the experiments. Undrained Unconsolidated (UU) Triaxial tests were conducted for the Original Soil (OS) blocks, as well as for blocks after 24h (S24) and 72h (S72) of softening. The softening of clay samples for testing is shown in

Figure 4-20, where the clay bricks were cut into small blocks, with dimensions of 115 mm × 75 mm × 45 mm, chosen to match the sample box size. Water was poured into the sample box, with the surface just above the clay. The sample box was then sealed and kept at room temperature until the desired softening time had been reached.

Figure 4-21 (a) to (c) show the UU test results for the original and softened clays, while a summary plot can be seen in Figure 4-21 (d). This plot shows a rapid decrease in undrained shear strength, s_u [kPa], as the water content, $w\%$, increases. The red line symbolises the average values for the test results, as listed in Table 4-6.

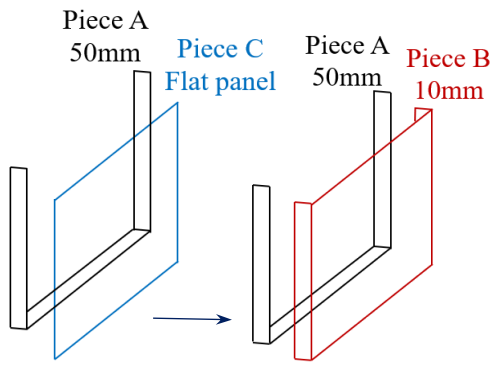


Figure 4-22 Modified tank

The standard Ketley clay block, with dimensions 225 mm × 105 mm × 1100 mm, was cut into four equal parts during the sample preparation, to reduce the drainage path for clay softening. In general, the softening of the clay block followed the same procedure as the softening of clay samples for the UU tests, only with a larger water tank and longer softening time. To remove the softer surface material due to water absorption, the original wood tank of the calibration chamber was modified to allow soil scraping. As shown in Figure 4-22, an additional piece, B, with a 10mm gap, was added to the original 50mm frame of the chamber and replaced the flat back panel (Piece C) before the soil was loaded. The procedure of clay softening, and sample

preparation in the calibration chamber can be seen in Figure 4-23. Detailed descriptions of each step are as follows:

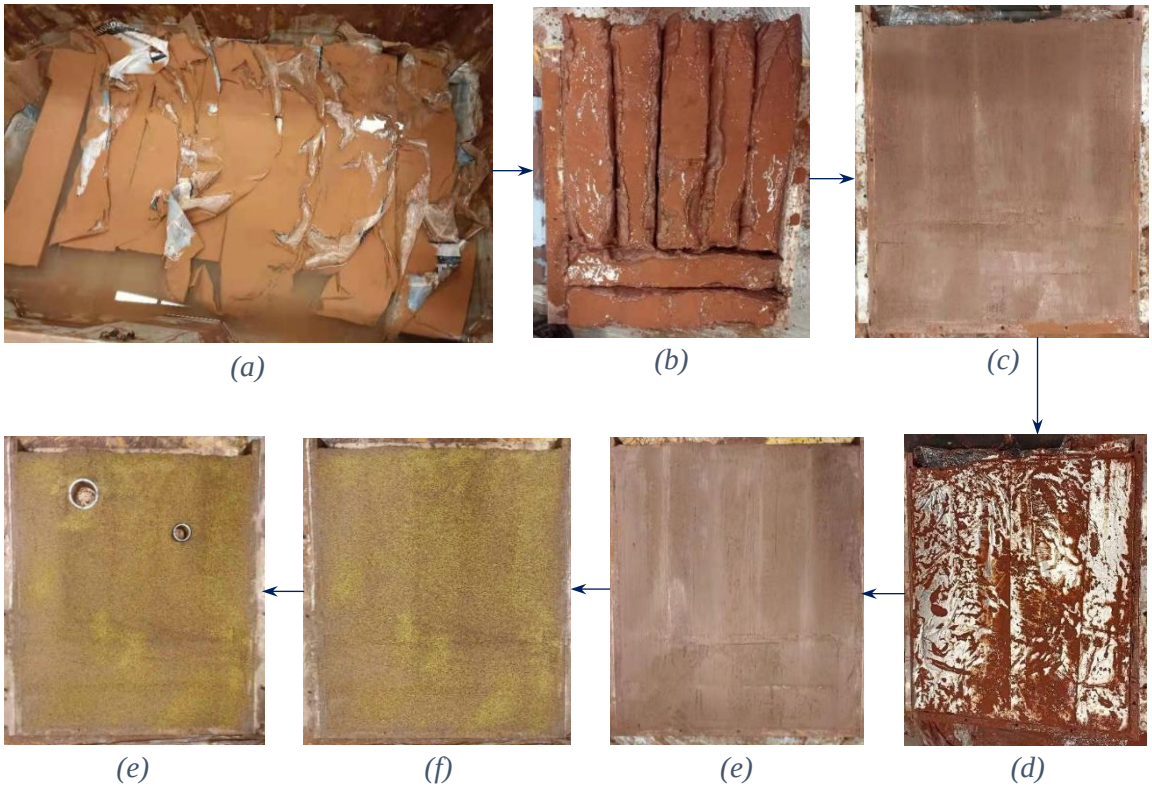


Figure 4-23 Preparation of Ketley clay samples

Figure 4-23 (a): The cut clay blocks, with dimensions 110 mm × 105 mm × 550 mm, were loaded into a sealed water tank wrapped with plastic sheets. The plastic wrapping here had the same function as the previously mentioned foil sheet to conveniently lift the clay blocks out of the water tank.

Figure 4-23 (b): The clay blocks were lifted from the water tank after being softened for a week. This softening time was selected based on trial and error, with the target of reducing the strength to $s_u = 15 \sim 20$ kPa. To avoid discontinuities at the interface of different blocks, the clays were first placed vertically in the upper part of the chamber, upon two layers of clay blocks on the bottom. Piece B, covered with a layer of foil sheets, was mounted on Piece A as the tank base, which gave the 60 mm total inner height of the tank.

Figure 4-23 (c): Considering the dimensions of the clay block, the loaded clay was at least 45mm higher than the top edge of the wood tank. Most of the excess material was scraped off using a steel cable. The clay surface was then flattened using an aluminium sheet. Similar to the surface flattening for sand tests, this aluminium sheet was used to scrape off small amounts of remaining excess clay, while filling any small valleys on the clay surface. After this, a temporary protection panel would cover this flattened surface and the entire wood tank would be flipped over.

Figure 4-23 (d): Removing Piece B, the excess clay with a height of 10 mm was ready to be removed. The foil sheets prevented the clay from adhering to Piece B, which then protected the flattened surface in Figure 4-23 (c) from damage due to the removal of Piece B.

Figure 4-23 (e): The same flattening procedure as in Figure 4-23 (c) was applied to the back surface. The flat wood panel Piece C (Figure 4-22) was mounted onto Piece A and the wood tank was flipped over again to its front side.

Figure 4-23 (f): The temporary protection panel was removed, and a thin layer of sand particles was scattered on the clay surface uniformly.

Figure 4-23 (e): The boulder was gently pushed into place, and the clay within the boulder ring was removed. The sample preparation was then finished, and the Perspex window would then be installed on the front face of the chamber, against the textured clay surface. Finally, the calibration chamber was lifted, and positioned horizontally to obtain the designated contact eccentricity between the plate and boulder.

4.6 NUMERICAL MODEL REFINEMENTS

The numerical models in Abaqus CEL had the same horizontal and vertical dimensions as the experiment, while the thickness was a unit element length to simulate the plane-strain conditions in the 3D environment. The boundary conditions were consistent with the 2D models in Chapter 3: fully fixed right, left, and bottom sides; Z-symmetric conditions on the front and back plane; and free surface on the top of the soil. The material properties of the Duralumin plates were consistent with those described in Section 4.2.1, while the brass boulders were modelled as rigid bodies. The soil strength, s_u, was measured by Shear Vane Tests (SVT) or Fall Cone Tests (FCT) after each test and these test-specific values were used in the models.

The key variables to be determined were the initial positions of the plate and boulder, as presented in Section 4.6.1. The contact properties between the plate, boulder, and soil were determined using trial and error, the process of which can be seen in Section 4.6.2. The optimisation of numerical models in terms of calculation precision and time will be discussed in Section 4.6.3, and the mitigation of result oscillations is in Section 4.6.4. The result comparison of numerical and physical modelling of three clay tests is presented in Section 4.7.

4.6.1 INITIAL COMPONENT POSITIONS IN PHYSICAL MODELS

Though certain controlling methods were applied during the tests to keep components in the anticipated positions, the accuracy of these positions cannot be guaranteed with manual operations. More accurate initial positions of the boulder and soil were obtained using a similar procedure to the control point calibration, described in Section 4.3.3. An example of this process is presented based on test PKB30Z25NFM32 (K: Ketley clay).

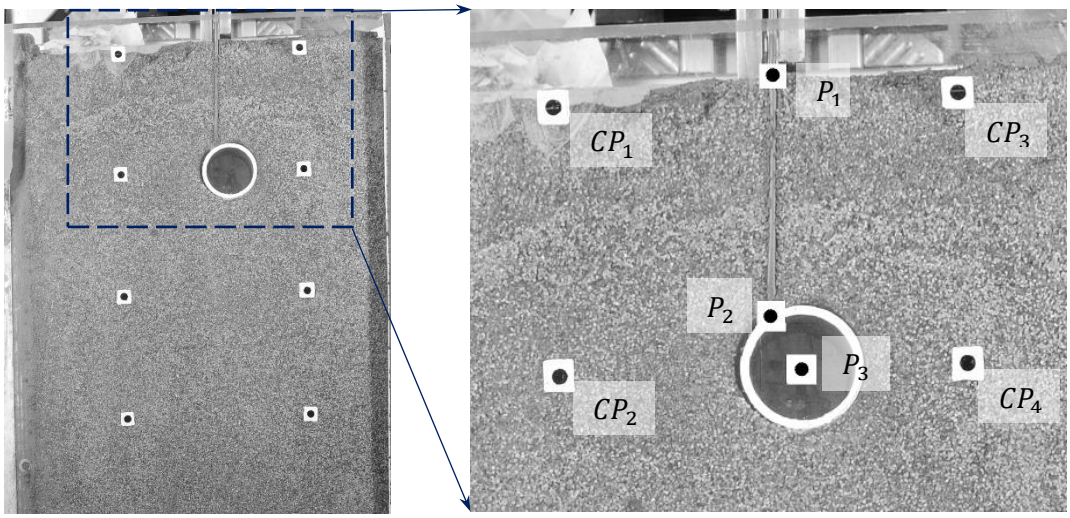


Figure 4-24 Determination of initial component positions - PKB30Z25NFM32

Figure 4-24 presents the image taken at time step 85, immediately before the plate hit the boulder. Three additional Locating Points (LP), P_1 to P_3, were added manually using Microsoft Paint. P_1 determined the position of the soil surface and the starting point of plate penetration; P_2 located the contact position, or the contact eccentricity e [m], of the plate and boulder; P_3 was the centre of the boulder, which, combined with P_1, gave the initial embedment depth of the boulder. The four Control Points, CP_1 to CP_4, were among the 32 CPs calibrated in Section 4.3.3, with accurate object-space coordinates. Therefore, CP_1 to CP_4 were used as reference points for converting between image-space and object-space coordinates, such as the PPDs in Section 4.3.3.

After calibration using GeoPIV-RG, the true object-space coordinates of the LPs were used to obtain the parameters for the numerical simulation, including:

Embedment of boulder, Z_b[m]	$Z_b = y_{P_3} - y_{P1} + r_b$
Normalised contact eccentricity, $\hat{e}$	$\hat{e} = \left(x_{P_3} - x_{P_1}\right)/d_b$

where r_b [m] and d_b [m] denote the radius and the boulder diameter, respectively. These parameters were then used in the numerical models, which had two computing stages, before and after the contact, following the steps below:

a) The horizontal coordinate of the boulder was determined by putting the vertical central line of the boulder consistent with that of the model, termed as R_x. The vertical coordinate of the boulder was then determined using Z_b.

b) The plate was located level with the soil free surface. The initial horizontal coordinate of the plate base was calculated by $PB_{x0} = R_x - (x_{P_3} - x_{P_1})$.

c) The inclination between P_1 and P_2 was due to the initial imperfection, specifically out-of-straightness, of the Duralumin plate. This imperfection was considered in the first computing stage as a horizontal displacement, $\Delta x = x_{P_2} - x_{P_1}$, imposed on the plate base. The vertical displacement was imposed on the plate head as $\Delta Z_1 = y_{P_2} - y_{P_1}$, which was negative to accommodate the coordinate conventions defined in Abaqus. This computing stage will be referred to as the 'pre-contact stage' in the following discussions.

d) Both Δx and ΔZ_1 were then deactivated in the second stage after contact. A new vertical displacement was imposed on the pile head, $\Delta Z_2 = Z_{ult} - \Delta Z_1$, where Z_{ult} was the ultimate penetration depth. This computing stage will be referred to as the 'post-contact' stage in the following discussions.

4.6.2 INTERFACIAL CONTACTS

The contact properties of the interface between components, particularly interface friction, have an influence on the rotation of the boulders and the magnitude of reaction forces. One

major source of friction, apart from the interactions between tested components, was the contact between the plate and its lateral supports in the air.

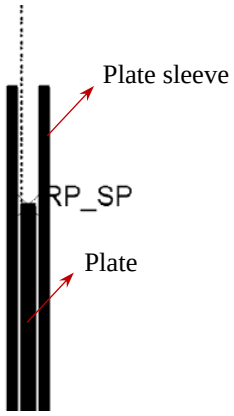


Figure 4-25 Plate and plate sleeve

Difficulties of determining the contact properties between the plate and the lateral support were due to the unknown contact conditions. Instead of tightly "clamping" the plate throughout the entire test, a small gap was reserved between the plate and the lateral support to reduce the influence of the lateral support on the test results. This small gap allowed a negligible scale of Euler buckling of the plate, which had little effect on the motions of the plate in the soil but could generate large frictions when the plate and lateral supports came into contact.

A compromised method was implemented in the numerical models to mimic realistic contact properties between the plate and the lateral support. Instead of modelling the true locations of three pairs of point supports, the lateral support in the numerical model was replaced by a continuous "sleeve" support of the plate above the soil surface.

Table 4-7 Contact properties of models

No.	Metal-Metal	Metal-Soil	Global
Fr1	0.3	0.3	Frictionless
Fr2	0.2	0.2	
Fr3	0.2	0.125	
Fr4	0.2	0.05	
Smooth	Frictionless in the entire domain		

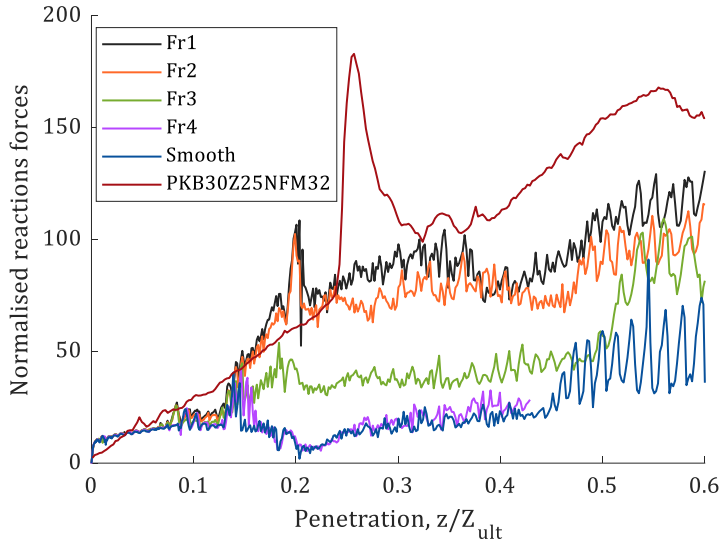


Figure 4-26 Result comparison – effects of friction coefficients

Each side of the sleeve had a gap of 0.5mm between it and the plate. Similar to the experimental setup, this gap restrained the magnitude of lateral Euler buckling and allowed the build-up of friction due to the increase in normal forces at the contact point(s). During the numerical simulation, the tangential contact property was defined using the in-built penalty algorithm in Abaqus CEL and separation after contact was allowed. Therefore, the only parameter that needed to be determined at this stage was the friction coefficient, μ, in the penalty algorithm. Four models (Fr1~Fr4) with different μ were established, while an additional model (smooth) with 'frictionless' contact in the entire domain was also established for a complete view. The selected values of μ in each model have been listed in Table 4-7. A common practice in

literature was first attempted, while a more suitable value was then determined based on the comparison between the numerical model and the experiment. The result comparisons focused on the normalised reaction forces at the pile head, as shown in Figure 4-26 in terms of

Among the four models, Fr1 had the best performance by comparison with the experiment. Therefore, the friction coefficient $\mu = 0.3$ was used for both metal-metal and metal-soil interactions. Because of the gaps between the plate and the plate sleeve, the friction can only occur when the plate experienced Euler buckling and contacted the sleeve. Therefore, the penetration speed of the plate should not affect the value of the friction coefficient. Results presented in Figure 4-26, in addition, were based on the models with artificially softened plates, whose strength and stiffness were $1/1000^{th}$ of the true values. This softening had the benefit of reduced computing time but led to an abnormal deformation pattern in the soil, as discussed in detail in Section 4.6.3, with other alternative methods to save computing costs.

4.6.3 Reduction of computing cost

The stable time increment, ΔT [s], of the explicit algorithm in Abaqus is dependent on three major factors: material stiffness, material density, and minimum element length. An estimation of ΔT could follow the equations below (ABAQUS, 2014, sec. 6.3.3):

$$\Delta T \approx \frac{L_{min}}{c_d} \qquad \textit{Eqn. 4-1}$$

$$c_d = \sqrt{\frac{\hat{\lambda} + 2\hat{\mu}}{\rho}} \qquad \textit{Eqn. 4-2}$$

where c_d is the current dilatational wave speed in the element and ρ [kg/m^3] is the density of materials. $\hat{\lambda}$ [Pa] and $\hat{\mu}$ [Pa] are the effective Lamé constants, which are, for isotropic-elastic materials, the same as the Lamé constants λ_0 [Pa] and μ [Pa], defined as follows:

$$\lambda_0 = \frac{E\nu}{(1+\nu)(1-2\nu)} \qquad \textit{Eqn. 4-3}$$

$$\mu_0 = \frac{E}{2(1+\nu)} \qquad \textit{Eqn. 4-4}$$

where E [Pa] is Young's modulus and ν is the Poisson's ratio of the material. Therefore, the component with the highest material stiffness and the smallest element length becomes critical, in this case, the elements in the Duralumin plate.

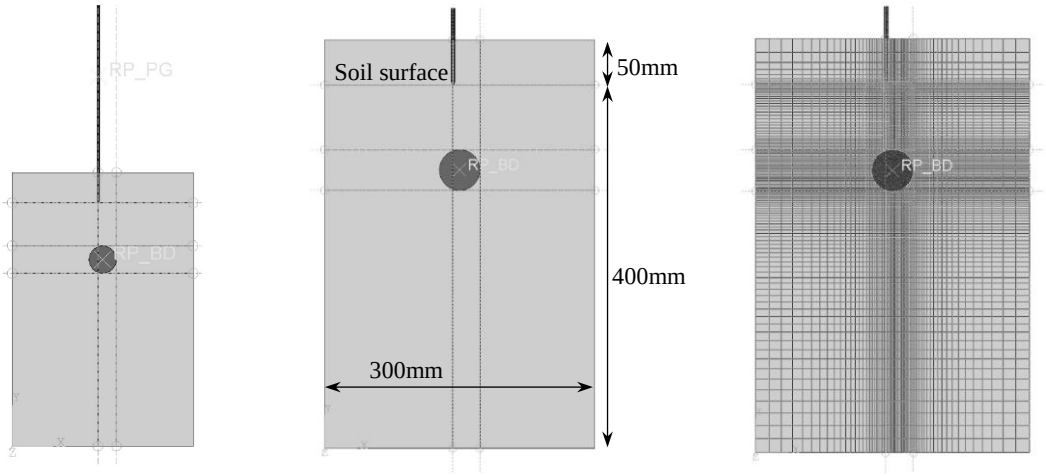


Figure 4-27 Experiment simulation, test PKB30Z25NFM32
(a) Model geometry; (b) Details of Eulerian domain; (c) Meshing scheme of Eulerian domain

A general view of the model can be seen in Figure 4-27 (a), which followed the framework of the conceptual 2D models in Chapter 3. To save computing time, the minimum RoI of each experiment was selected for the simulation, the dimensions of which were height × width = 450 mm × 300 mm (300t × 200t), as presented in Figure 4-27 (b). As for the conceptual model, horizontal and vertical datum lines were applied on the Eulerian domain to support the meshing scheme, where finer elements with element length $L_{elem} = t$ were distributed within the interacting area of the plate and boulder, and coarser elements with $L_{elem} = 10t$ were distributed around the model edges, as seen in Figure 4-27 (c). This meshing scheme gave a

total number of elements, N_{elem}, ranging from 7475 to 12615, depending on the size of the boulder, and thus the size of the interacting area. Single elements were applied across the thickness of the Duralumin plate with $L_{elem} = t$. Therefore, with slightly larger dimensions compared to the conceptual 2D model in Chapter 3 (250*t* × 200*t*), the model dimensions for the experiment simulations had an increased number of elements and therefore increased computing time. The estimated stable time increment using the true mechanical properties of the Duralumin plates in Section 4.2.1 and SI units was approximately 1.17×10^{-9}, which would take around 36 days to finish one model. Other techniques were then applied to attempt to find an appropriate compromise between accuracy and reduction in computing time: (1) mass scaling, (2) time scaling, and (3) material softening, following the essence of Eqn. 3-1 and Eqn. 4-2.

Mass scaling

Mass scaling is to increase the density of material ρ which then decreases the dilatational wave speed c_d in Eqn. 4-2, and thus increases the stable time increment ΔT in Eqn. 3-1. This method, however, could lead to abnormal distortions of the Lagrangian elements due to excessive deformation wave speed, and thus crash the simulation. Though a mass scaling factor could be defined for each analysis step in Abaqus, the mass scaling in these simulations was realised by altering the material density directly.

In the simulations, the material density was magnified by a factor of 10^4 based on trial and error. The soil density became 2.5×10^7 kg/m^3, and the Duralumin density which was then in the scale of 2.79×10^7 kg/m^3.

Time scaling

As discussed in Section 4.3.2, the testing speed of the experiment was either 2 mm/s, or 0.4 mm/s to accommodate the camera conditions. Therefore, it took either 175 s or 875 s for the plate to reach the designated penetration depth, $Z_{ult} = 0.35$ m. These time scales were decreased to a unit value of 1 s for both pre-contact and post-contact stages based on trial and error, which indicated that the testing procedure was compressed to 2 s in the simulation. Further reduction of time scales could lead to excessive distortions in Lagrangian elements, or excessive oscillations of data (presented in Section 4.6.4).

Material softening

The material softening concerned the effective Lamé constants in Eqn. 4-2. Attempts were made including adding a softening factor of 10^{-3} to material strength and stiffness for both the soil and the plate. However, abnormal deforming patterns occurred. An example of this can be seen in Figure 4-28. Therefore, the approach of material softening is not appropriate for the numerical simulation, and the original material properties were used for the following simulations.

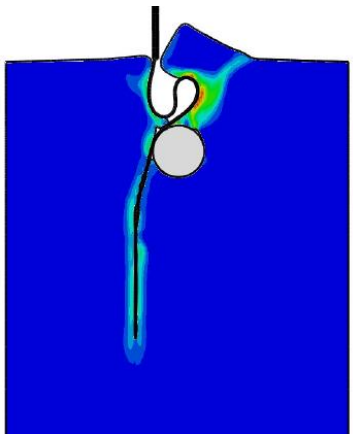


Figure 4-28 Plastic strains in Eulerian domain – abnormal pattern

4.6.4 MITIGATION OF OSCILLATIONS

With the above refinements, the stable time increment was increased to 3.67×10^{-7}. Accordingly, computing time was decreased from approximately 36 days to 10 ~ 20 hours depending on the number of elements, N_{elem}, in the Eulerian domain, but with the price of inducing large data oscillations to the model due to the large mass scaling and compressed time scale. Figure 4-29 shows a comparison example of the oscillated numerical result, M0, and the experiment result PKB30Z25NFM32. Additional measures were then taken to smooth the numerical data.

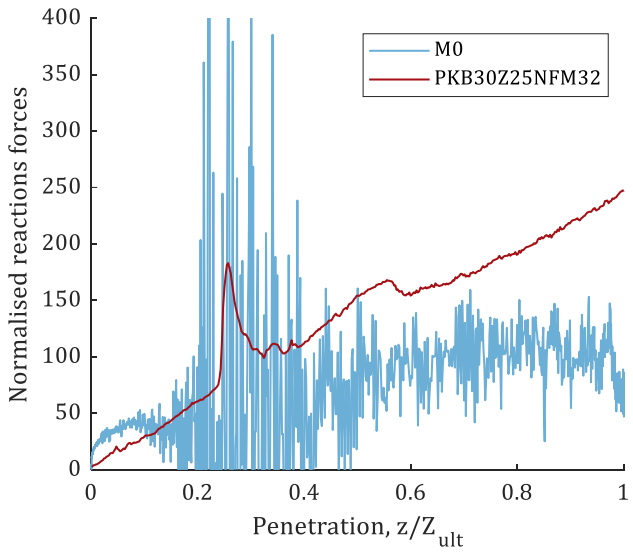


Figure 4-29 Oscillated data using quadratic elements

To capture the non-linear deformation pattern of the plate, the conceptual 2D model used linear hexahedral elements (type C3D8) with second-order accuracy. However, this could lead to significant data jumps at the contact between the Lagrangian body and the rigid body, the plate and boulder in this research. Therefore, C3D8R with reduced integration and hourglass control were applied to the following models instead.

Eight models (M1 to M8) were established. The tested factors included (1) the scaling factor of the material density $\hat{\rho}$, (2) time scale of computing stage T, (3) element size L_{elem} in the Eulerian domain, (4) bulk viscosity ζ, and (5) total number of requested output data points N_{rd}. Detailed model properties of these values have been listed in Table 4-8.

Table 4-8 Model properties

No.		$\hat{\rho}$	T [s]		L_{elem} [m] Min, Max	N_{elem}	ζ		N_{rd}
			T_1[s]	T_2[s]			ζ_l	ζ_q	
M1		1e7	1	1	t, 10t	7475	0.06	1.2	1000
M2		1e6	0.5	1	0.5t, 8t	20736	0.06	1.2	1000
M3	×	1e6	0.5	1	0.5t, 10t	15960	0.12	2.4	1000
M4	×	1e6	0.5	1	t, 10t	7475	0.12	2.4	4000
M5	×	1e7	0.5	1	t, 10t	7475	0.08	1.6	4000
M6	×	1e7	0.5	1	t, 10t	7475	0.075	1.5	4000
M7		5e7	1	1	t, 10t	7475	0.08	1.6	4000
M8		1e6	1	1	t, 10t	7475	0.12	2.4	4000

Four out of eight models (M3 ~ M6) were aborted before the simulation was completed, marked with "✕" in Table 4-8. This model failure was primarily due to the modification of the default model viscosities, which ruptured the model stability. However, the results of these models will still be discussed below to present the complete process of oscillation reduction for the numerical models.

M1~M2: effects of refined elements, L_{elem}

With refined elements and a smaller mass scaling factor, the results of M2 were broadly consistent with the experiment, even though the time scale was further compressed to 0.5s

during the pre-contact stage. However, negative reaction forces still appeared around contact, as shown in Figure 4-30.

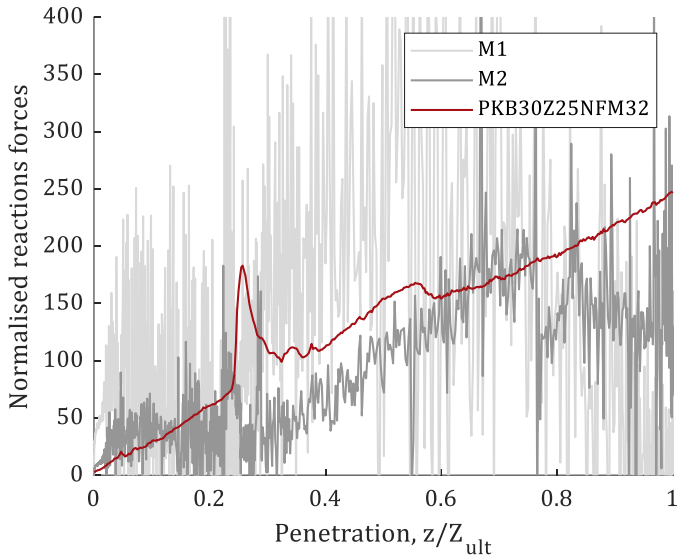


Figure 4-30 M1~M2 results

M2~M4: Effects of bulk viscosity, ζ, and the requested data points, N_{rd}

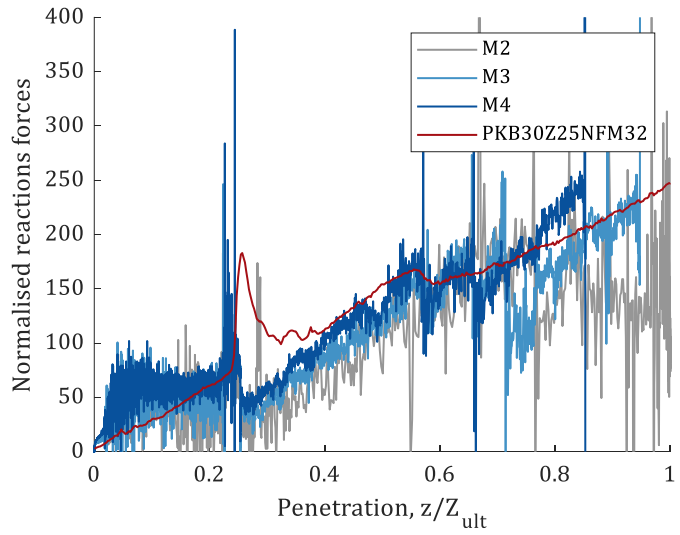


Figure 4-31 M2~M4 results

The result comparison from models M2~M4 is shown in Figure 4-31. Excessive distortions appeared in M3 at penetration $z/Z_{ult} = 0.94$, with the linear bulk viscosity, ζ_l, and quadratic

bulk viscosity, ζ_q, doubled. Given that significantly fewer elements had been used in M1, this excessive distortion should be attributed to the increase of bulk viscosity, instead of the increase of element size. This increase of ζ nevertheless reduced data oscillations. Further improvement was obtained in M4 when the requested number of outputs, N_{rd}, was increased from 500 per stage, to 2000 per stage (4000 in total), though fewer elements were used.

M4~M7: Threshold of ζ and effects of time scale, T

To find the threshold of ζ that could achieve stable computation, both ζ_l and ζ_q were gradually decreased from M4 to M7. The results comparison of the models is shown in Figure 4-32.

M5 and M6 still aborted due to excessive element distortions, but at later time steps than their predecessors. Given that the same $\hat{\rho}$ had been used in M1, this problem should not be attributed to the increased $\hat{\rho}$ in M5 and M6. However, the comparison between M5 and M7, indicated that this distortion could be due to the compressed time scale in the pre-contact stage. Longer T could further contribute to the stability of the model, but was time-consuming. Thus, the time scale of 1s was retained for further studies.

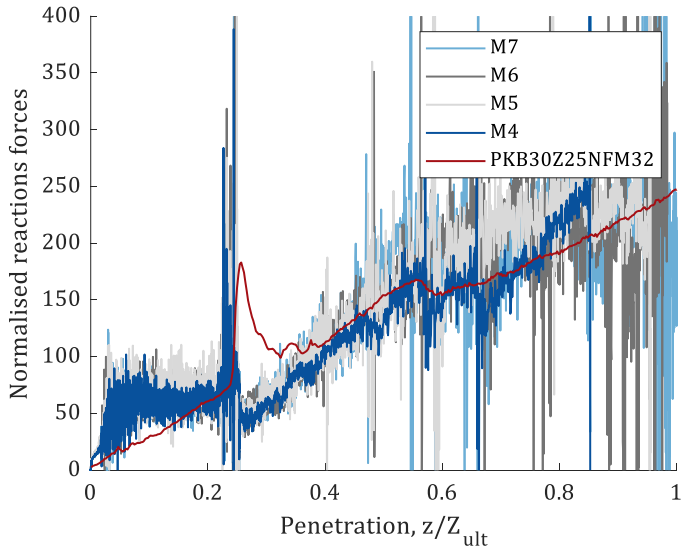


Figure 4-32 M4~M7 results (reversed sequence for improved illustration)

M8: final refinement

Combining the observations from M1 to M7, M8 achieved the best results among the models, as shown in Figure 4-33. The variation of reaction forces from M8 showed consistent trends compared to those in the experiment. The data jumps at plate-boulder contact were fully eliminated, though with an underestimation of peak contact loading of around 25%. Most data points also fell within the error band of ±25%. Large data jumps still appeared in the later stage of the computation, but returned to the trendline afterwards. These data jumps could be due to the random contact between the plate and the plate sleeve during penetration. Eliminating the gap between the plate and sleeve would further mitigate the data jumps, as presented in Section 4.7.

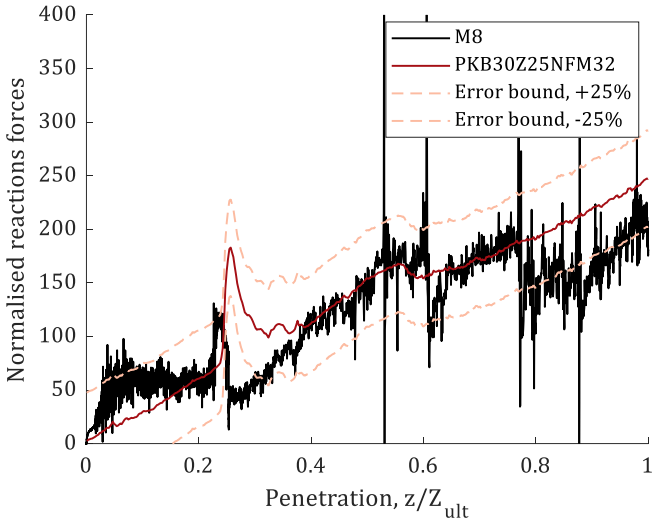


Figure 4-33 M8 results and error measures

4.6.5 EFFECTS OF REFINEMENTS

The previous refinement of models was based on the comparison of the reaction forces from the experiments and the numerical models. However, another informative parameter would be

the displacements of the plate tip, which would also reveal the trajectory and the deformation patterns of the plate.

To determine the true deformation pattern from the experiment, four additional control points, named as DeFlection (DF) points, were added to the final step of the photograph for PIV analysis, as shown in Figure 4-34. Following the same procedures of locating the initial component positions in Section 4.6.1, the object-space coordinates of the four DF points were determined. Setting DF1 to be the origin of the displacement plot, the red line presented in Figure 4-34 shows the approximated trajectory of the plate by linearly connecting the four DF points.

The plate trajectories from analyses M1 to M8 displayed softer behaviours not seen in the experiment. This softness was probably due to boundary effects, discussions of which are in Section 4.7 based on various experiments.

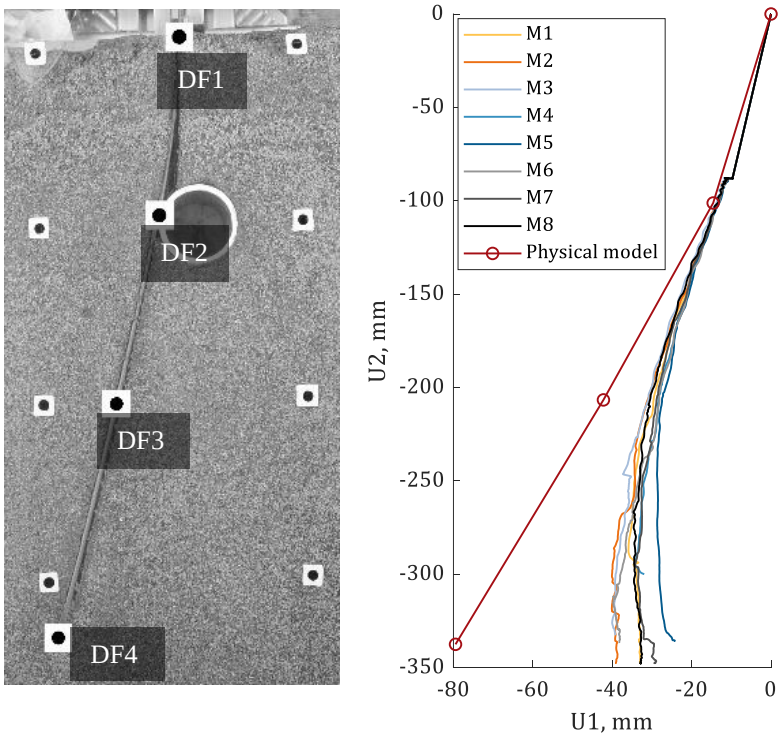


Figure 4-34 Comparison of plate trajectory

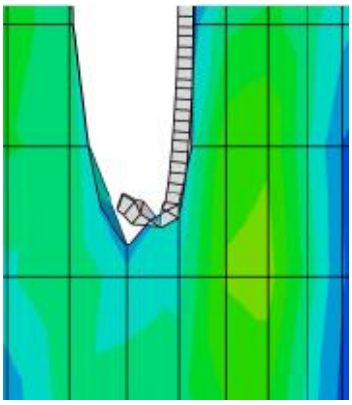


Figure 4-35 Abnormal distortions of Lagrangian elements (M7)

The trajectories in Figure 4-34 were divided into three threads: a) M2, M3, M6, b) M1, M4, M7, M8, and c) M5. No common feature could be found in thread a), given that both the meshing scheme and the bulk viscosity of the model have been changed, and two out of three models had been aborted. However, thread b) suggested that the model would give consistent results if the meshing scheme remained identical, regardless of the changes in relation to the model bulk viscosity, mass scaling factor, or time scale. Though increasing the bulk viscosity would mitigate the oscillations of the results, it would increase the computing time and make the model less stable in terms of the deformation of the Lagrangian elements. An example extracted from M7 can be seen in Figure 4-35. Therefore, further numerical simulations keep the bulk viscosity of the model at the default values of $\zeta_l = 0.06$ and $\zeta_q = 1.2$ (ABAQUS, 2014).

4.7 RESULT COMPARISON

Three experiments conducted using clay were simulated using the refined model properties. The soil strength of each test was measured once the experiment was completed, using either Shear Vane Tests (SVT), or Fall Cone Tests (FCT). An example of SVT results can be seen in Figure 4-36, where the undrained shear strength was measured at 25 mm and 50 mm below the

soil surface, then every 50 mm from there to the bottom of the sample. Tests were performed at five vertical alignments across the sample, labelled A to E from left to right. Results indicated that the undrained shear strength of the softened clays was consistent with depth, except in the proximity of the interface of the clay blocks (z = 450 mm), where the soil strength dropped below 10 kPa. The average value of the measured points was then taken after eliminating these exceptions and used in the numerical models.

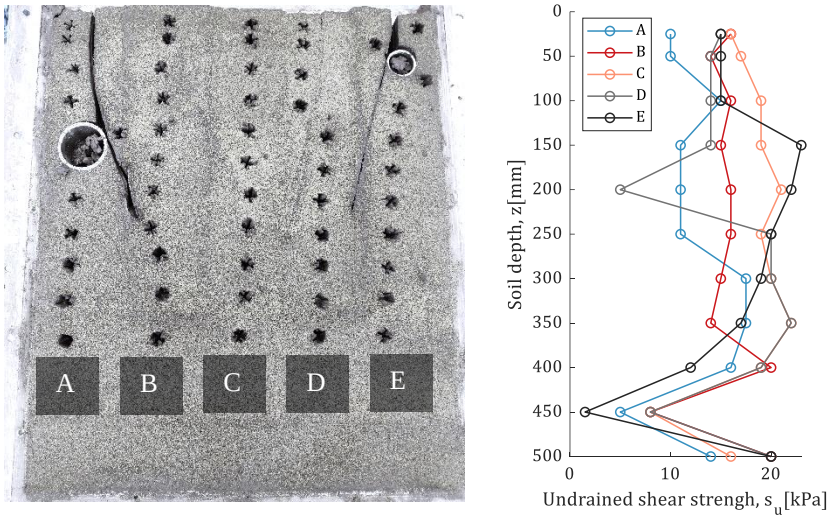


Figure 4-36 Shear vane test and results

The FCTs were conducted as a supplement to SVTs for two clay tests. A 30° cone apparatus with a mass of 32.8 g was used for the measurement. An empirical equation (Canelas *et al.*, 2018) was used to convert the penetration depth, d [mm], to the undrained shear strength s_u:

$$s_u = k(m \cdot g/d^2) \qquad \text{Eqn. 4-5}$$

where k is the cone coefficient and was taken as 0.8, g [m/s^2] is the acceleration of gravity, and m [g] is the mass of the cone. Nine clay blocks were taken from the calibration chamber, covering the penetrating area of the plate, as well as the interacting area between the plate and the boulder. The nine samples were divided into three groups, samples 1 to 3 were taken from the depth range 0 to 150 mm, samples 4 to 6 from 150 to 300 mm, and samples 7 to 9 from 300

to 450 mm. The result of the FCTs can be seen in Figure 4-37, and an average value of nine data points, 16.98 kPa, was used in the numerical models for further analysis.

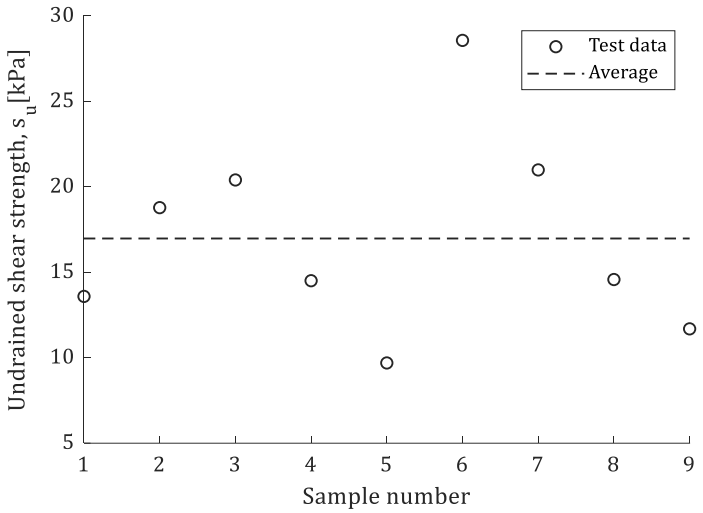


Figure 4-37 Fall cone test results

Test 1: PKB30Z20CFM32

Figure 4-38 presents the key results of the experiment and the numerical simulation of Test 1 (PKB30Z20CFM32). The undrained shear strength of the clay was $s_u = 16.5$ kPa. The embedment depth of the boulder was ~20% of the ultimate plate penetration depth, $Z_b = 0.2Z_{ult} = 70$ mm. The measured contact eccentricity, e was 4.65mm, ~10.3% of the boulder diameter $b = 45$ mm.

The tip deflection shown in Figure 4-38 (b) was 54.96 mm in the numerical model, and 67.91 mm in the physical model. The numerical model underestimated the ultimate tip deflection, D_{ult} [m], by around 19%. However, the plate trajectory predicted by the numerical model was consistent with the experiment.

The normalised reaction forces predicted by the numerical model also revealed the key features of the experiment, as presented in Figure 4-38 (c). The peak force at the plate-boulder contact

predicted by the numerical model was 25% larger than the experiment. Though most data fell within the error band of ±25%, large oscillations appeared in the later part of the computation, where coarse elements were encountered by the plate tip.

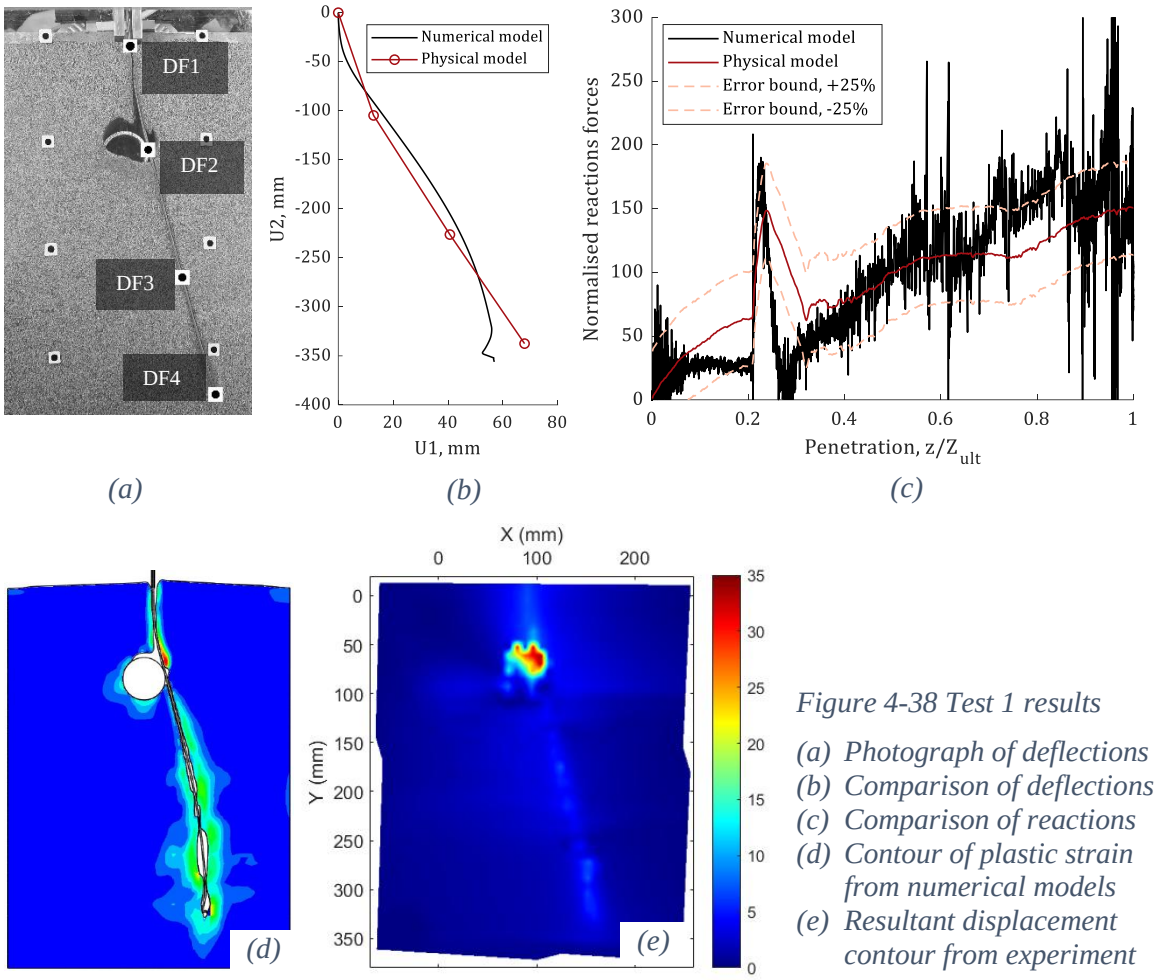


Figure 4-38 Test 1 results

(a) Photograph of deflections
(b) Comparison of deflections
(c) Comparison of reactions
(d) Contour of plastic strain from numerical models
(e) Resultant displacement contour from experiment

The movement of soil particles is represented by the plastic strain contours from the numerical model (Figure 4-38 (d)), and by the resultant displacement contour from PIV analysis (Figure 4-38 (e)). The plate trajectory was unclear from PIV analysis. This was because the deformation clustered around the boulder, termed gapping, was much larger than the area of soil moved by the plate, giving less clear colouration to the plate trajectory in the plot. This gapping did not cause significant plastic strain in the numerical model, and thus was not presented in the plot Figure 4-38 (d). Nevertheless, the shape of gapping predicted by the

numerical model was consistent with the physical model. In general, the numerical model could provide reasonable descriptions of the soil flow, as well as other key features including plate deflections and reaction forces, for Test 1.

Test 2: PKB50Z50CFM32

Figure 4-39 presents the key results of Test 2 (PKB50Z50CFM32). The undrained shear strength of the clay was $s_u = 16.9$ kPa. The embedment depth of the boulder was around 50% of the ultimate plate penetration depth, $Z_b = 0.5Z_{ult} = 175$ mm. The measured contact eccentricity, e was 8.11mm, around 10.8% of the boulder diameter $b = 75$ mm.

At the same penetration level $Z = 318.6$ mm, the tip deflection shown in Figure 4-39 (b) was 116.8 in the numerical model, and 95.7 mm in the physical model. Therefore, the numerical model overestimated the ultimate tip deflection, D_{ult}, by around 22%, though the overall prediction of the plate trajectory had consistent trends to those observed in the physical model.

Figure 4-39 (c) gives a comparison of the normalised reaction forces from the experiment and the numerical model. The peak force at the plate-boulder contact predicted by the numerical model was 18% smaller than that measured by the experiment. The majority of data fell within the error band of $\pm 25\%$, and large oscillations again appeared in the later part of the computation, which could be due to the application of coarse elements. The large deflection could also contribute to the rising normalised reaction force due to the extended contact area between the plate and soil.

Figure 4-39 (d) (e) give the soil flow in the numerical and physical models, respectively. The large deformation on top of the boulder in the physical model (Figure 4-39 (e)) was due to the falling of sand particles on the soil surface when the underlying soil was stretched and separated from the Perspex window due to the downward movement of the boulder. This *stretching*

mechanism was because the wet clay was stuck onto the boulder surface and was excluded from the numerical model. Therefore, at this point in the numerical model, significantly less plastic strain was observed than in the experiment. However, the numerical model did develop a gap of similar shape to the experiment. Despite some discrepancies, the numerical model again revealed the key features of the test.

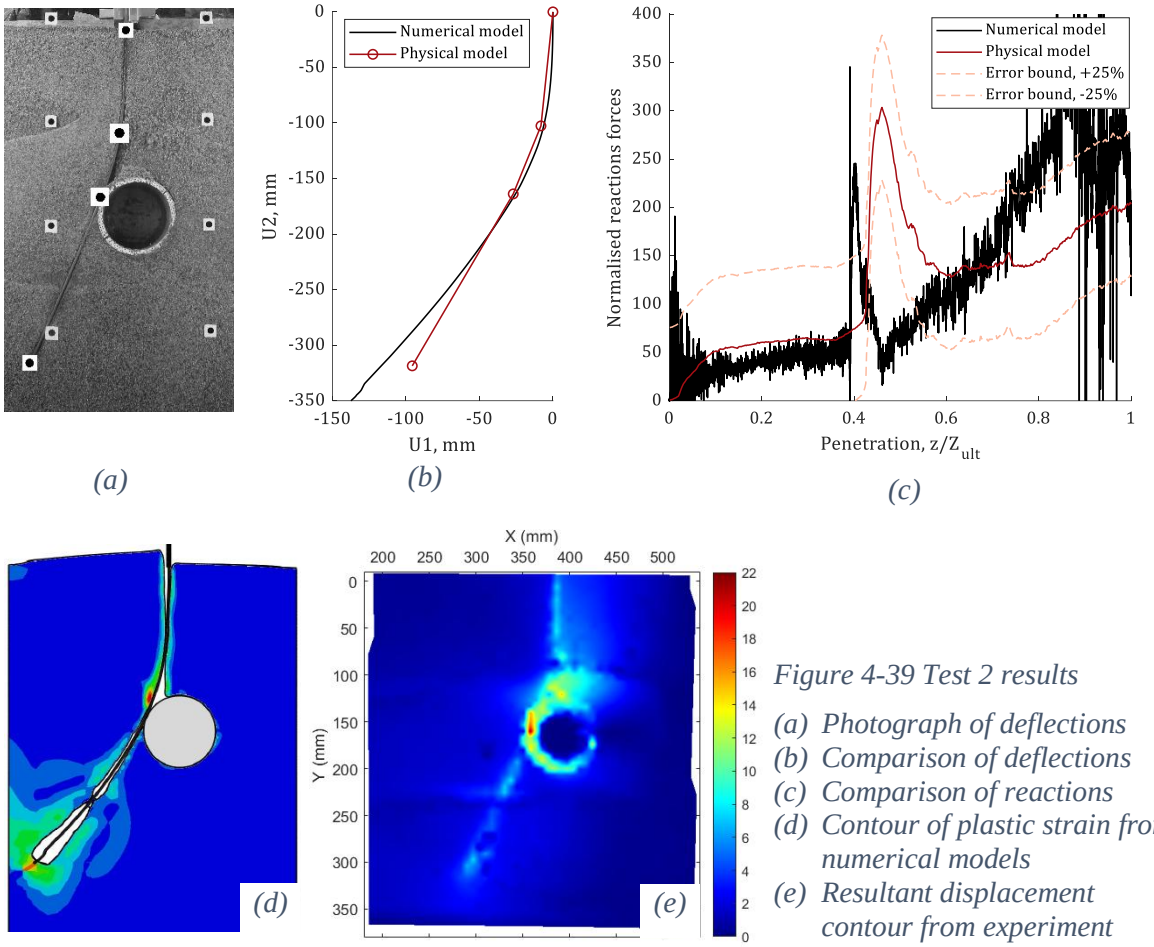


Figure 4-39 Test 2 results

(a) Photograph of deflections
(b) Comparison of deflections
(c) Comparison of reactions
(d) Contour of plastic strain from numerical models
(e) Resultant displacement contour from experiment

Test 3: PKB30Z70CFM32

The key results of Test 3 (PKB30Z70CFM32) are presented in Figure 4-40. The strength of the clay was $s_u = 16.5$ kPa. The embedment depth of the boulder was around 0.49 of the ultimate plate penetration depth, $Z_b = 0.49Z_{ult} = 173$ mm. The measured contact eccentricity, e was 17 mm, around 37% of the boulder diameter $b = 45$ mm.

The tip deflection in Figure 4-38 (b) was 64.44 mm in the numerical model, and 64.66 mm in the physical model. The numerical model therefore had a slight overestimation of D_{ult} [m] around 0.34%. The plate trajectory predicted by the numerical model was also consistent with the experiment.

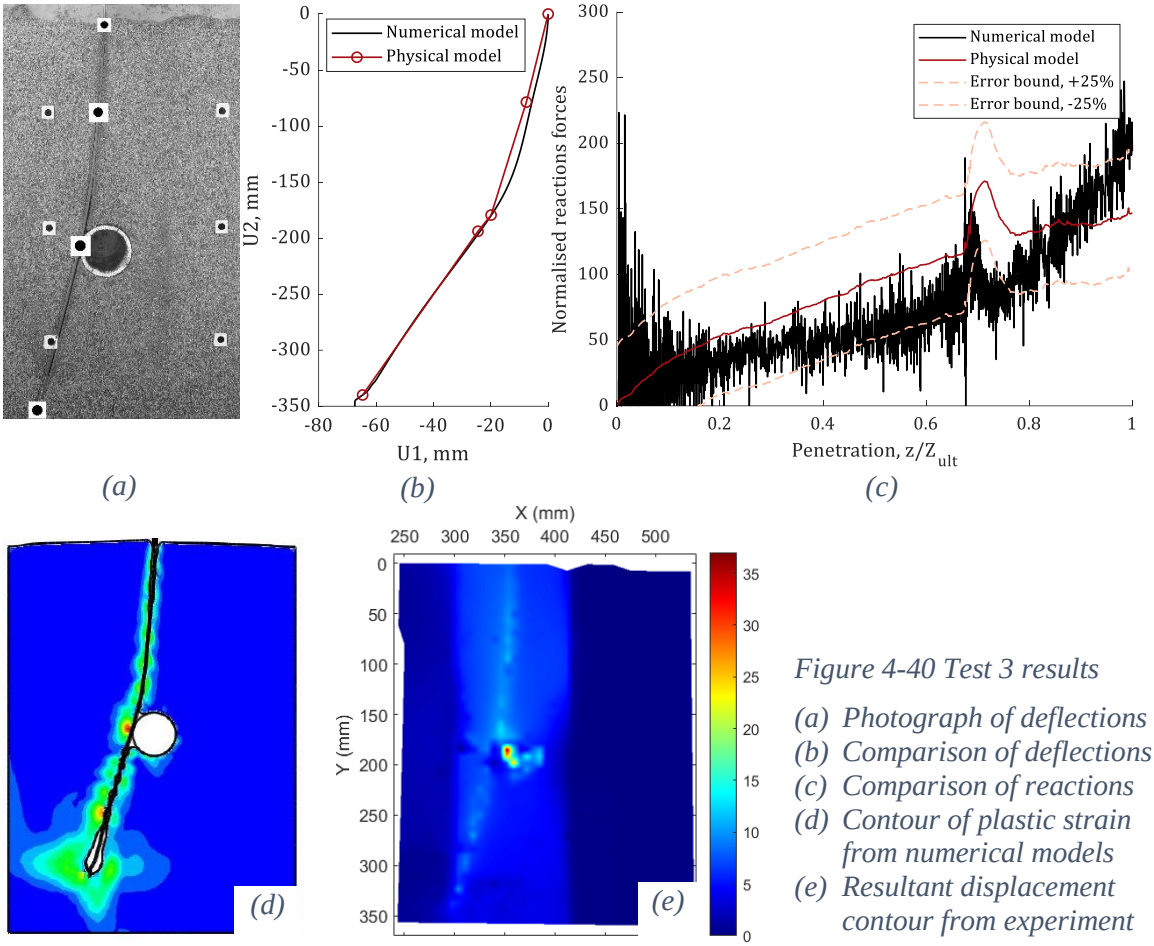


Figure 4-40 Test 3 results

(a) Photograph of deflections
(b) Comparison of deflections
(c) Comparison of reactions
(d) Contour of plastic strain from numerical models
(e) Resultant displacement contour from experiment

The peak normalised reaction force predicted by the numerical model was 6.9% smaller than the experiment. As presented in Figure 4-40, the majority of data fell within the error band of $\pm 25\%$, with a tendency of overprediction in the later part of the computation. This tendency could be due to the use of coarse elements.

The soil flow presented by the numerical model (Figure 4-40 (d)) was also comparable to the physical model Figure 4-40 (e). The systematic downward movement presented in the physical

model between $x = 300{\sim}400$ mm was due to the overall slipping of the clay block that was vertically placed in the calibration chamber. A gap was present below the clay block, leading to this overall downward movement under gravity and the downward forces from the actuator. This downward movement was considered to have negligible effects on the experiment, since it only lasted for a short period compared to the time span of the experiment. The soil then stabilised afterwards.

Based on these results, the numerical model could be regarded as reliable in describing the interactions of plate and soil flow for Test 3.

4.8 SOIL FUNCTION ANALYSIS

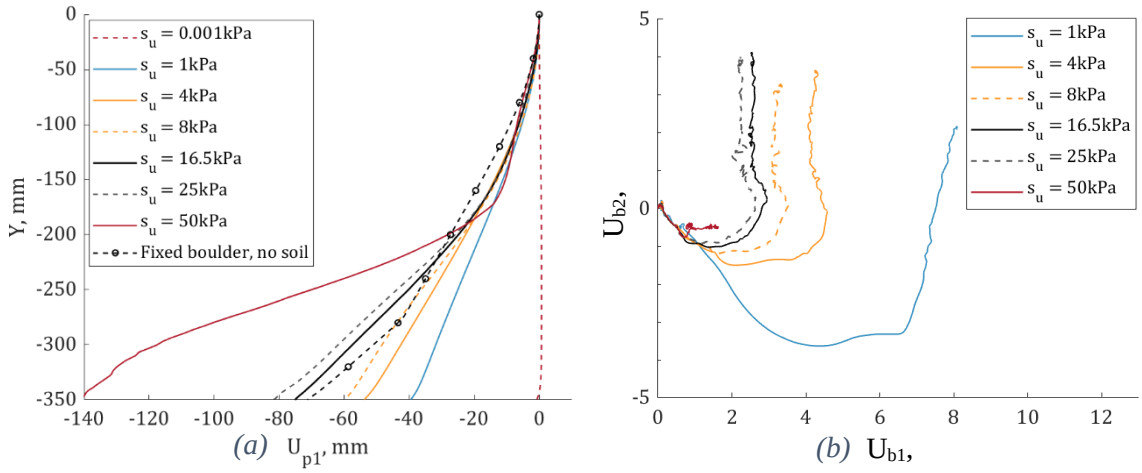


Figure 4-41 Result comparison

(a) Effects of soil strength on plate deflection in numerical simulations;
(b) Effects of soil strength on boulder movement in numerical simulations

Close observation of the deflected shape in the testing in Section 4.7 indicated minimal curvature in the plate after the boulder collision. Additional numerical models were established to investigate how the soil properties affect the deflected geometry. In these models, the soil strength ranged from 0.001 kPa to 50 kPa, with $E_s = 500 s_u$. The minimum value of s_u simulated the scenario of no soil present. A special model with no soil and a fully fixed boulder

was also established. The plate deflection is plotted in Figure 4-41 (a), with the horizontal and vertical boulder displacements (U_{b1} and U_{b2}) plotted in Figure 4-41 (b). The boulder in the model with $s_u = 0.001$ kPa was pushed downward as the plate advanced until U_{b2} = -157 mm and U_{b1} = 17 mm; this case is excluded from Figure 4-41 (b) to avoid distorting the scale. Together, Figure 4-41 indicates that the boulder acted as an obstacle, resulting in the plate deflecting upon collision and preventing the plate from returning to its initial uncurved shape. During the subsequent buckling process, the stronger soils constrained the boulder movement, preserving the penetration direction along the deflected plate tip.

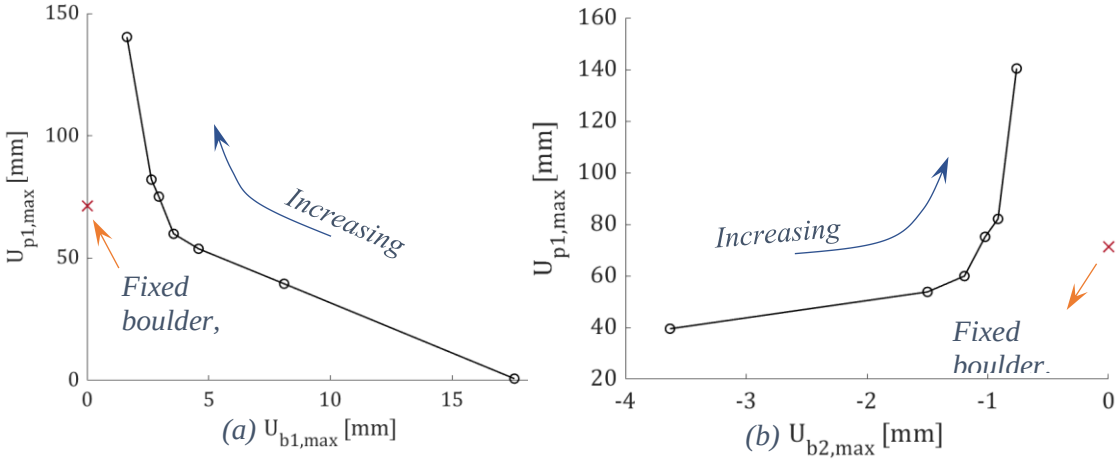


Figure 4-42 Plot of plate deflection and boulder movement in numerical simulations (a) $U_{p1,max}$ against $U_{b1,max}$; (b) $U_{p1,max}$ against $U_{b2,max}$

A more precise illustration can be seen in Figure 4-42, which presents the variation of the maximum plate tip deflection, $U_{p1,max}$, against the maximum horizontal boulder displacement in the horizontal ($U_{b1,max}$) and vertical ($U_{b2,max}$) directions. In these plots, an increase in soil strength, denoted by the blue arrow, results in a decrease in boulder movement but an increase in plate deflection. The model with a fixed boulder and no soil is denoted by a red cross. Without soil, the plate deflection was much smaller than when the soil had a strength of s_u = 50 kPa, even though the boulder cannot move. However, the deflection was comparable to

cases where $s_u = 16.5$ kPa. This finding supports the idea that the soil can prevent the recovery of plate curvature and preserve the deflected direction of tip penetration.

In addition to strength, s_u, the soil stiffness E_s has a similar influence on the boulder-plate interaction. Figure 4-43 (a) and (b) present a comparison between the model with $E_s = 50s_u$, which gave results similar to the experimental condition, and a model with $E_s = 500s_u$. The plate deflection in Figure 4-43 (a) for the model with $E_s = 500s_u$ was 74.8 mm, which was 16% higher than with $E_s = 50s_u$. This increase in tip deflection is due to the less mobile boulder, with maximum horizontal and vertical displacements 6% and 64% lower than with $E_s = 50s_u$ in Figure 4-43 (b). The effect of E_s on the tip deflection behaviour appears to be less critical than that of s_u.

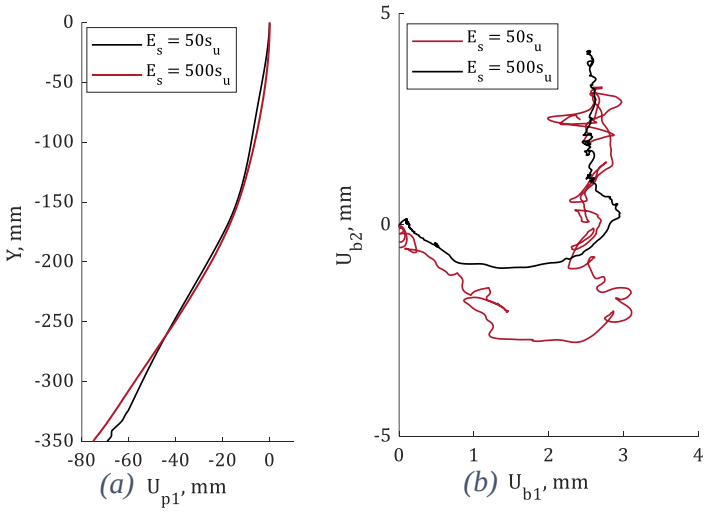


Figure 4-43 Effects of soil Young's modulus, E_S
(a) Comparison of plate deflection; (b) Comparison of boulder movement

4.9 CONCLUDING REMARKS

This chapter presented details of the preparation and execution of the physical modelling of the plate penetration problem. The key results of the physical model were compared with 2D

numerical models established in Abaqus. These 2D numerical models followed the essence of the conceptual 2D models in Chapter 3, but with refinements to accommodate the experiment conditions. The refinements included:

1) The contact conditions, or, specifically, the friction coefficient at the interface of model components,
2) The initial locations and contact eccentricities of the physical models, which were determined using control point analysis imbedded in GeoPIV-RG,
3) The initial imperfections of the Duralumin plate, which was modelled as horizontal displacement at the plate tip in the pre-contact stage.

The discrepancies between numerical and experimental plate deflections could be due to either of the following reasons:

1) Larger resistance due to the boundary effects, which could lead to significant underestimations of the deflection, especially for cases with large deflections, where the tip was approaching the vertical boundaries of the model, such as the example test (Section 4.6.5) and Test 1 (Section 4.7),
2) Weightless soil, which leads to greater heaving predicted in the numerical model than occurs experimentally, such as was observed in Test 2, reducing the lateral soil resistance.

In general, the numerical model provided results within an error range of 25%. Within the range where finer elements were used a narrower error range was achieved. Considering the simplifications which were necessary in the numerical model, this error could be tolerated through the application of a suitable safety factor. Further refinement of the model could be realised by:

1) Using refined elements throughout the model,

2) Extending the boundaries, or RoI, of the modelled area,
3) Taking soil weight into consideration,
4) Using the true time scale of the test.

These methods could benefit the reliability of the numerical model, but with the consequence of excessively long computing time given current technological constraints. However, this may become feasible in the future when more advanced computing techniques or algorithms are developed.

Based on our current results, the 2D numerical models using Abaqus CEL could be benchmarked by the designed physical modelling methods in this research. With 18 CPU processors and the modelling conditions described above, the computing time of the 2D numerical models, which was between 10~20 hours, was acceptable. The consistency between the calibrated numerical simulation and the physical model proved that the 2D model was benchmarked.

The additional investigation based on the calibrated model also revealed the key features of the physical models. During the penetration, the boulder acted as an obstacle, resulting in the plate deflecting at collision, as well as preventing the plate from returning to its initial uncurved shape. The soil, meanwhile, constrained the boulder movement, further prevented the recovery of plate curvature, and preserved the deflected direction of tip penetration. The tip deflection was more sensitive to the shear strength of soil, compared with the stiffness.

CHAPTER 5 THREE-DIMENSIONAL PILE PENETRATION

5.1 INTRODUCTION OF TRUNCATED 3D SIMULATION

To reduce the computing time of full-scale 3D simulations, the effects of D/t ratio ranging from 50 to 200 were tested on truncated 3D models. In these models, only a quarter of the pile section in proximity to the boulder collision was simulated. This section presents an overview of the truncated 3D model, including the model geometry in Section 5.1.1, the material properties in Section 5.1.2, and the boundary conditions and motion controls in Section 5.1.3.

5.1.1 MODEL GEOMETRY

Figure 5-1 shows the geometries of the truncated 3D model with its top view, where the boulder is in the shape of a hemisphere, positioned to collide with the truncated pile. The adopted pile wall thickness was $t = 0.1$ cm, simulating a typical value of offshore monopiles. The model width was $W = R + 100t$, and the soil height was $H = z_{ult} + 50t$, where R was the pile radius from the origin to the centreline of the pile wall, and z_{ult} was the ultimate penetration depth of the pile. A void layer of height $H_V = 5t$ was also included above the free surface of the soil, enabling soil heave. The longitudinal length of the pile section was $L = 250t$. Given

that only a quarter of the pile was simulated, the arc length of the pile section became $C = \pi R/2$. To resolve the issue of poor element aspect ratio along the pile centreline, a central cut-out with a radius of $X_0 = 10t$ was created. The detailed meshing scheme in relation to this cut-out is presented in Section 5.3.1.

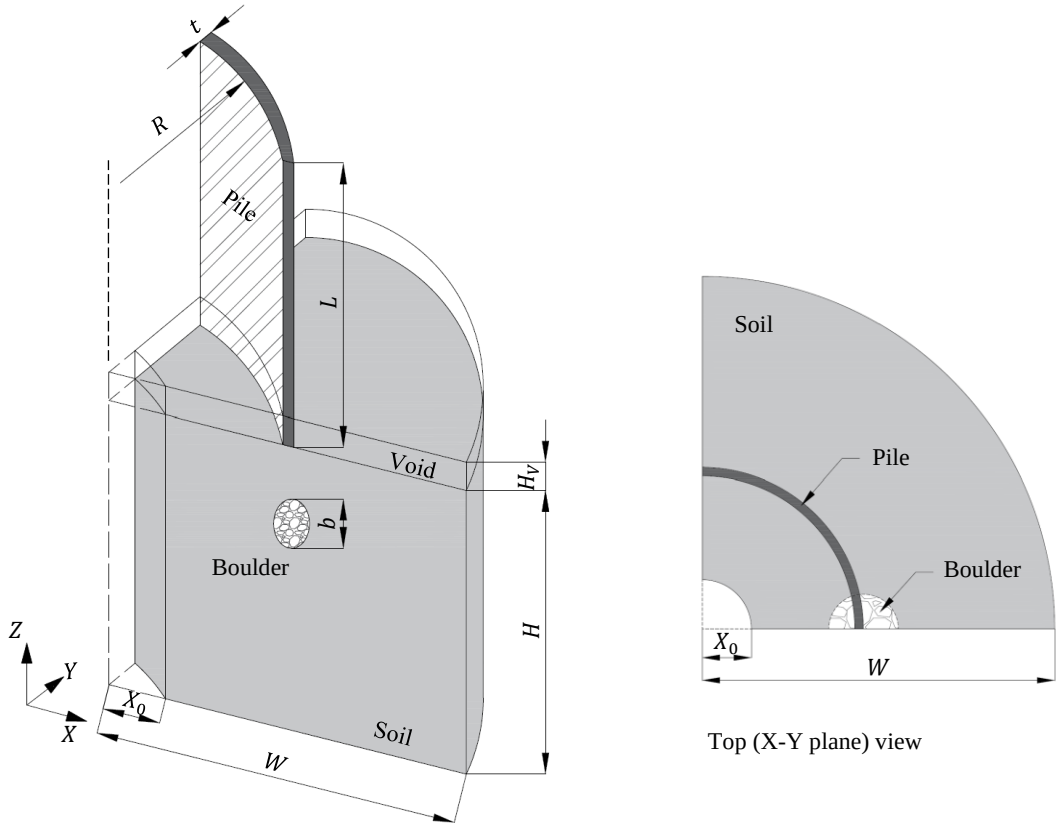


Figure 5-1 Schematic geometries of the truncated 3D models

5.1.2 MATERIAL PROPERTIES

The adopted material properties are listed in Table 5-1. The plastic strengths of both the pile steel and the soil are governed by the von Mises failure criterion. The mechanical properties of high-strength steel, S355, were used for the pile. The typical density of steel was used for the simulation. A stiff clay with an undrained shear strength of $s_u = 200$ kPa and Young's

modulus $E_s = 500s_u$ was used for the soil, the properties of which were homogeneous along the depth. The typical density of saturated clay was used.

Table 5-1 Material properties

Pile section	$E_p = 210\text{GPa}$	$\sigma_Y = 355\text{MPa}$	$\nu_p = 0.3$	$\rho_p = 7.85e3\text{kg/m}^3$
Soil	$E_s = 100\text{MPa}$	$s_u = 200\text{kPa}$	$\nu_s = 0.49$	$\rho_s = 2.0e3\text{kg/m}^3$
Boulder	Rigid body			

5.1.3 Boundary conditions and motion control

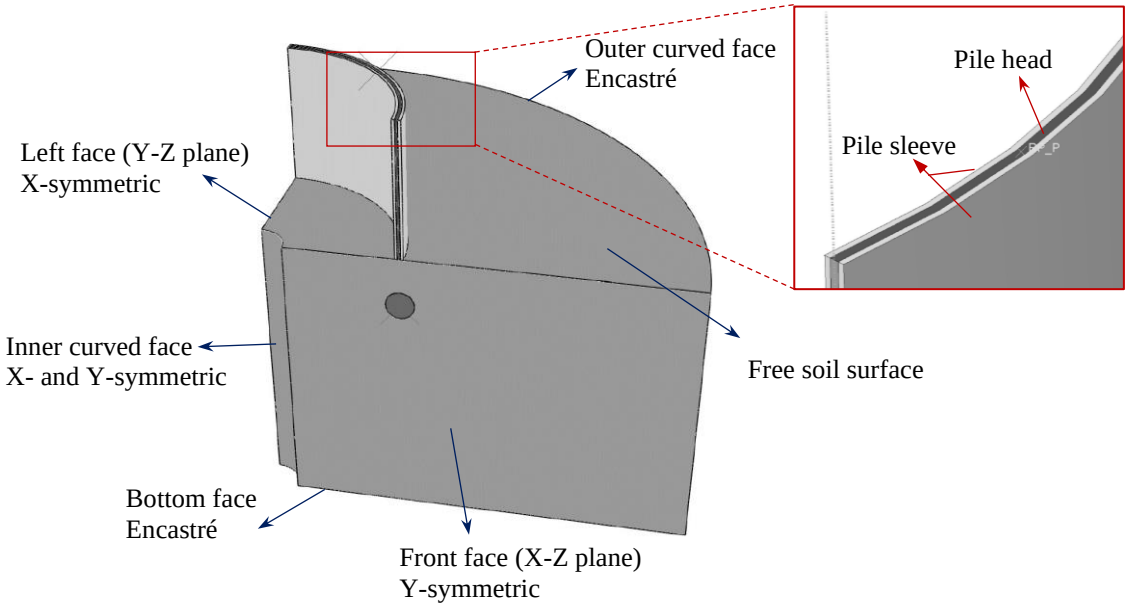


Figure 5-2 Boundary conditions of truncated 3D models

Figure 5-2 shows the boundary conditions of the truncated 3D models. The encastré condition was assigned to the bottom and the outer curved surface of the model, while the top surface of the soil was left free. Symmetrical boundary conditions were assigned to the truncated faces of the model. As labelled in Figure 5-2, the front face with the truncated boulder was parallel to the X-Z plane; therefore, the Y-symmetrical boundary conditions were applied. The left face, where no boulder existed, was on the Y-Z plane, the X-symmetrical boundary conditions were

therefore applied. The same symmetrical boundary conditions were also applied on the plie edges on the corresponding surfaces. The curved surface resulting from the central cut-out was labelled as inner curved face, with both X- and Y-symmetrical boundary conditions assigned enabling the soil movement in the Z direction only.

Similar to the 2D models, a rigid pile sleeve was added to the model to prevent Euler buckling of the pile in the air, as shown in the zoomed inset in Figure 5-2. The pile head was modelled as a rigid surface controlled by a reference point. The ultimate penetration depth, z_{ult}, was assigned to the reference point as a vertical displacement. To save computing time, the period of this penetration was defined as 1 s. A smooth variation of the displacement was used to prevent data spikes due to the sudden change of the velocity field, as shown in Figure 5-3, while still providing an average penetration speed of z_{ult} per second.

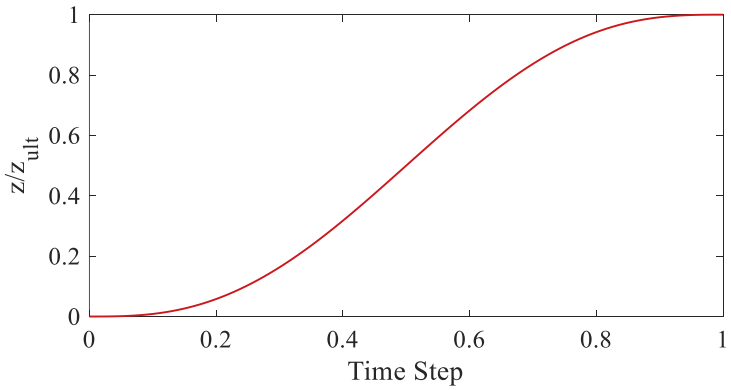
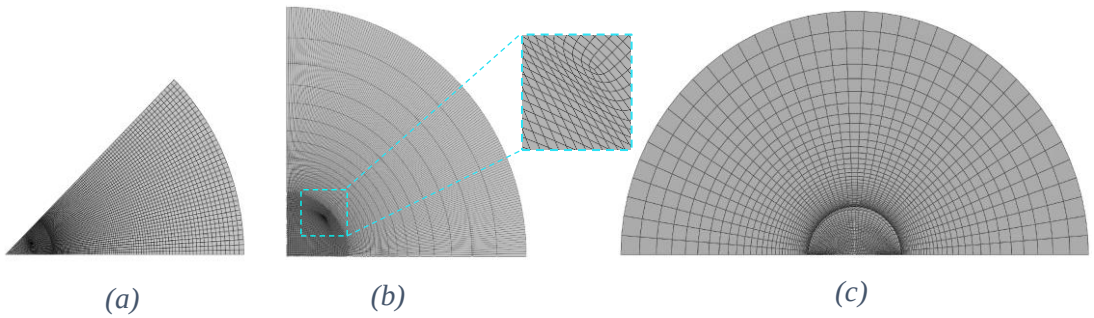


Figure 5-3 Smooth variation of penetration speed

5.2 VIABILITY OF TRUNCATED MODEL

Before further investigations based on the truncated (quarter pile) model, the normalised reaction force at the pile head was first compared between three models with different angular extents, as shown in Figure 5-4. Figure 5-5 gives the comparison of the normalised vertical reaction forces. The coarsest mesh was used to save computing time, with the minimum

element length $l_{min} = t$, and the maximum element length $l_{max} = 10l_{min}$. The model SP45-$t/1$ had its revolution angle equal to 45°, which meant the pile section was one-eighth of a circular pile, while the model SP180-$t/1$ had a half pile included. SP45-$t/1$ gave the same results as SP90-$t/1$, while SP180-$t/1$ had overestimations up to 6.73%. This overestimation could be due to the automatic mesh optimisation in Abaqus, which slightly changed the element distribution despite the identical definition of l_{min} and l_{max}. Nevertheless, the similarities of the results indicated that the 90° models could give accurate results for pile penetration problems, allowing the pile-boulder interaction studies to be carried out on smaller-scale models.



(a) *(b)* *(c)*

Figure 5-4 Top view of Abaqus models with different angular extent (Abaqus-generated mesh) (a) 45° model;(b)90° model; (c) 180° model

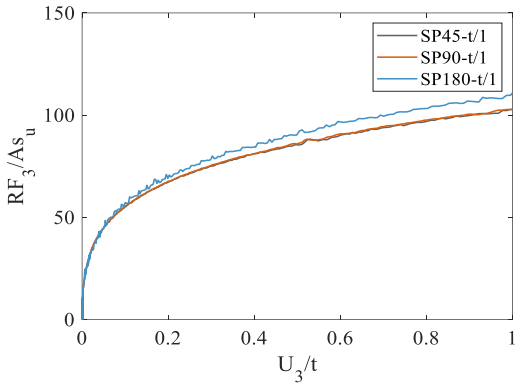


Figure 5-5 Comparison of different model angles

Figure 5-4 also reveals another issue related to the Abaqus-generated mesh. Highlighted by the blue square in Figure 5-4 (b), the angle (45° and 90°) along the centreline of the pile leads to an area of Eulerian elements with poor aspect ratios. These elements, as discussed in Section 5.4.1, may result in longer computing time. To resolve this problem, a modification to the model geometry was conducted, with a user-defined algorithm for the mesh generation, as discussed in the next section.

5.3 MODEL CONSTRUCTION

Instead of building the various required models in Abaqus CAE, a MATLAB code was established to generate the input file directly. This section follows the sequence of the input file information, presenting the algorithms that were included in the MATLAB code. Section 5.3.1 to Section 5.3.3 give the detailed meshing scheme of each of the model components. This approach directly defined the coordinates of each node, avoiding node drifting due to the automatic mesh optimisation in Abaqus, thus maintaining consistency between different models. Section 5.3.4 then presents the surface definition methods serving for the definition of boundary conditions, while Section 5.3.5 describes the calculation of the initial effective volume fraction for the Eulerian elements.

5.3.1 EULERIAN DOMAIN AND SOIL GENERATION

The Eulerian element EC3D8R was used for the soil. The Eulerian domain was divided into four parts by two planes: the pile trajectory and the free surface of the soil. As shown in Figure 5-6 (a) ~ (c), finer elements were clustered around the pile trajectory and the soil surface, while coarser elements were spread towards the model boundaries. Though no partitioning was conducted on the part, six boundaries were defined, three horizontal and three vertical. Figure 5-6 (a) gives the positions and the names of these boundaries, while Figure 5-6 (b) and (c)

present the relationship between the model components and the boundaries. These boundaries marked the commencing and the termination of mesh construction in MATLAB, without (at this stage) additional physical constraints of boundary conditions.

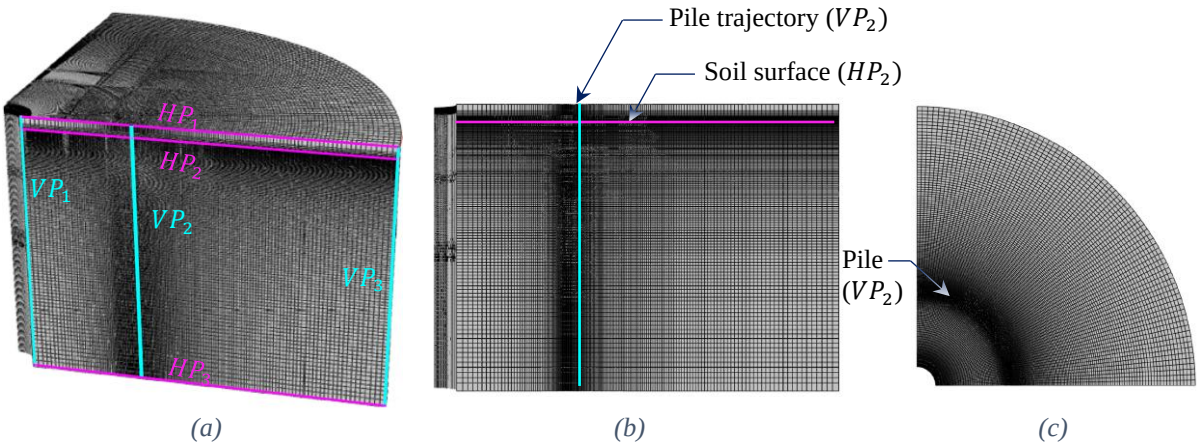


Figure 5-6 Eulerian domain meshing scheme (HP – horizontal plane, VP – vertical plane) (a) General view; (b) X-Z plane view; (C) Top view (X-Y plane)

The nodal coordinates in the X- and Z-directions were first defined on the X-Z plane by sequentially accumulating the element length from the finer boundaries. Defining that the minimum element length was l_{min} [m], the maximum element length was l_{max} [m], and the distance between the two boundaries was l_{dis} [m], the increasing bias ratio of two adjacent elements, q, became

$$q = \frac{l_{dis} - l_{min}}{l_{dis} - l_{max}} \qquad \textit{Eqn. 5-1}$$

By multiplying the bias ratio, the element length of the i^{th} element starting from the finest element became

$$l_{elem,i} = l_{min} q^{i-1} \qquad \textit{Eqn. 5-2}$$

If $l_{elem,i} > l_{max}$, $l_{elem,i} = l_{max}$. Defining that the X-coordinate of the initial boundary was X_0 and that of the end boundary was X_t, the new nodal coordinate, X_i, in each iteration became

$$X_i = X_0 + \sum_{i=1} l_{elem,i} \qquad \textit{Eqn. 5-3}$$

If $X_t - X_i < l_{max}$, $X_i = X_t$ and the iteration ended, ensuring an integer element count. Recalling the model geometry in Figure 5-1, X_0 was equal to the radius of the inner curved surface, while X_t was equal to the model width W, namely $X_0 = 10t$ and $X_t = R + 100t$. The Z-coordinate on the X-Z plane also follows the same procedure as Eqn. 5-1 to Eqn. 5-3. These coordinates were then propagated towards the Y-Z plane by creating radial sections with an increasing angle, $\Delta\theta$. The increasing angle was determined to ensure that the element length around the pile was approximately equal to the pile wall thickness, t, which gave

$$\Delta\theta = \frac{\theta_R}{\mathrm{fix}(R\theta_R) + 1} \qquad \textit{Eqn. 5-4}$$

where θ_R was the total subtended angle of the model, which was $\pi/2$ in these simulations. The function fix(·) in the denominator of Eqn. 5-4 rounds the argument to the nearest integer towards zero. The nodal coordinates, (X_i, Z_i), on the X-Z plane were then updated on the j^{th} section as

$$X_{i,j} = X_i \cos\big(\Delta\theta(j-1)\big) \qquad \textit{Eqn. 5-5}$$

$$Y_{i,j} = X_i \sin\big(\Delta\theta(j-1)\big) \qquad \textit{Eqn. 5-6}$$

$$Z_{i,j} = Z_i \qquad \textit{Eqn. 5-7}$$

Additional constraints were added to Eqn. 5-5 and Eqn. 5-6,

$$\text{If } \left|X_{i,j}\right| < 10^{-10},\ X_{i,j} = 0;$$

$$\text{If } \left|Y_{i,j}\right| < 10^{-10},\ Y_{i,j} = 0;$$

which eliminated any floating-point rounding errors, ensuring that the nodes were strictly in alignment with the boundaries on the X-Z and Y-Z planes.

Table 5-2 gives the element sizes at the mesh boundaries. Note that the horizontal boundaries (HP) control the vertical element length, while the vertical boundaries (VP) control the horizontal. The horizontal element length at VP_1, the inner curved face, was proportional to that at VP_3, the outer curved face, as shown in Table 5-2. An investigation of the mesh sensitivity is discussed in Section 5.4.1, during which the ratio between l_{max} and l_{min} was kept at a certain value. This relationship ensured an appropriate aspect ratio of an element where both l_{min} and l_{max} existed.

Table 5-2 Mesh boundaries and element sizes

Boundary	Element size
HP_1	l_{max}
HP_2	l_{min}
HP_3	l_{max}
VP_1	$l_{max}R/(W-R)$
VP_2	l_{min}
VP_3	l_{max}

5.3.2 PILE AND PILE SLEEVE GENERATION

The pile and the pile sleeve used the same meshing scheme. The fully integrated eight-node hexahedron element, C3D8, was uniformly distributed throughout these parts.

To capture the radial deflection of the pile, multiple elements were assigned across the pile wall thickness. Investigations of sensitivity to the element number across the thickness are presented in Section 5.4.1. Because the pile sleeve was simulated as a rigid body, only one element was assigned across the pile sleeve thickness.

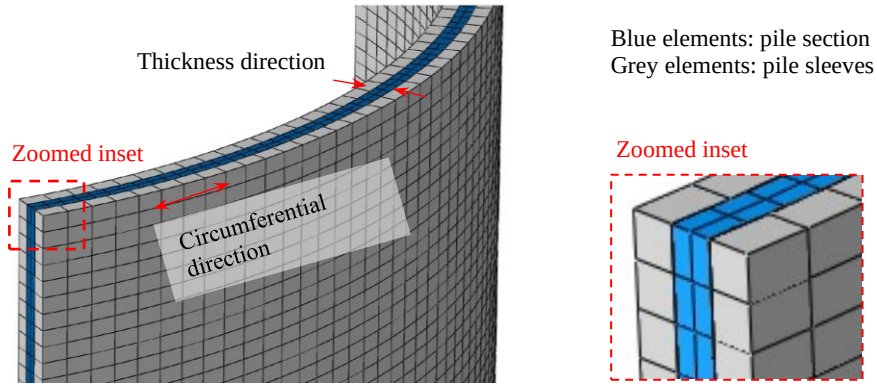
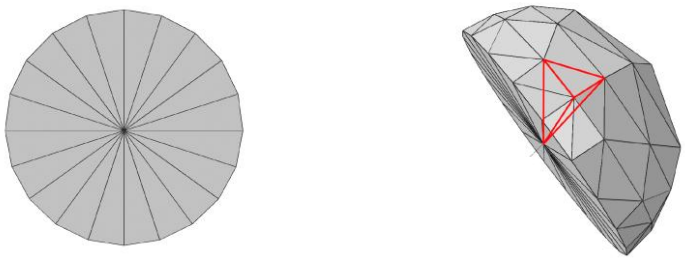


Figure 5-7 Meshing direction of pile section and pile sleeves

The element length was approximately equal to t in both the circumferential and the longitudinal direction of the pile. This element assignment was consistent with the calibrated 2D model in Chapter 4. Coarser elements were assigned to the pile sleeve, as shown in Figure 5-7, with element length equal to t in the longitudinal direction and $1.5t$ in the circumferential direction. The nodal coordinate generation followed the algorithm from Eqn. 5-3 to Eqn. 5-7, except that the element length, $l_{elem,i}$, was a constant in Eqn. 5-3.

5.3.3 BOULDER GENERATION

The meshing scheme of the boulder focused on preserving the surface curvature. Because the boulder was modelled as a rigid body, the distribution of the internal elements was less important. Therefore, the surface triangular facets were simply connected to the origin of the hemisphere to complete the mesh using four-node tetrahedral elements, C3D4, as shown in Figure 5-8. Though the mid-side node of quadratic tetrahedral elements, C3D10, could improve the approximation of the curved surface, increasing the number of C3D4 elements will also have the same accuracy. The element C3D4, in addition, also has a simpler node projection procedure in the algorithm presented in this section.



(a) *(b)*

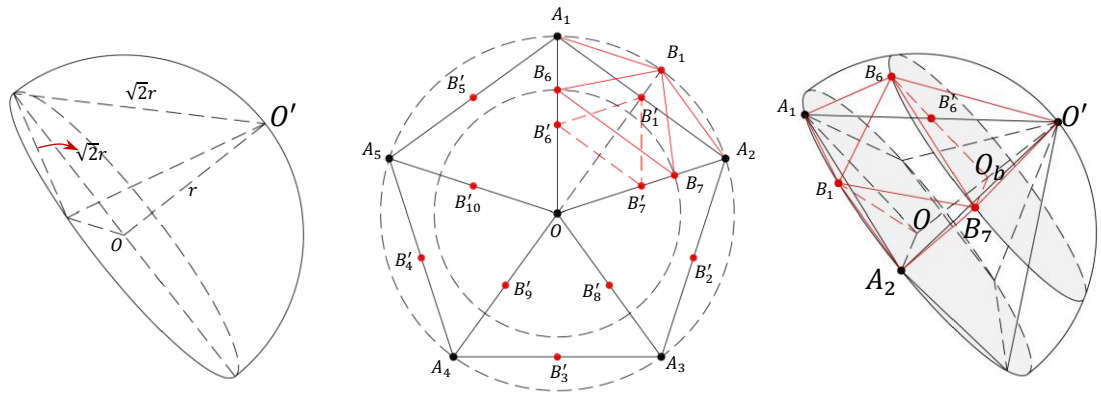
Figure 5-8 Boulder mesh example with second-order refinement of icosahedron
(a) X-Z plane view; (b) General view with a highlighted tetrahedral element shape

The surface curvature was preserved by a modified icosahedral discretisation scheme. The original scheme was used to obtain the solution of a partial differential equation; and that solution could be represented by a sphere (Baumgardner & Frederickson, 1985). The scheme first projected twelve vertices onto the sphere, giving a regular icosahedron; then refined the solution by connecting the midpoints of the edges (Baumgardner & Frederickson, 1985). Given that, in our problem, the discretised domain was a hemisphere, a polyhedral cone became a more appropriate projection compared to the regular icosahedron.

Figure 5-9 (a) shows the geometrical model that was used to obtain the optimum polyhedral cone shape, whose lateral surfaces should approximate equilateral triangles. Defining that the radius of the hemisphere was r, the side number of the polygon base was n, the equation built upon the perimeter of the base became

$$n\sqrt{2}r = \pi r \qquad \textit{Eqn. 5-8}$$

Taking n as an integer, Eqn. 5-8 gave $n \approx 5$. Therefore, the optimum cone shape was a pentagonal pyramid, referred to as the *base layer*. The further refinement had two steps: locating the midpoints of the edges, and projecting the midpoints onto the curved surface.



(a) *(b)* *(c)*

Figure 5-9 Schematic illustration of boulder meshing scheme

(a) Optimum cone shape calculation;
(b) Plane view of first-order node refinement and projection example;
(c) 3D view of first order node refinement and projection example, node B_6

Figure 5-9 (b) gives an illustration of the refinement procedure in a plan view without perspective, while Figure 5-9 (c) shows a three-dimensional view. Point O was the origin of the hemisphere, and points $A_1 \sim A_5$ were the five vertices on the circumference. The pyramid is composed of O' and $A_1 \sim A_5$ was the base layer of the refinement. Points $B'_1 \sim B'_{10}$ were the midpoints, whose coordinates were the average of the corresponding edge vertices. Three projected points, B_1, B_6, and B_7 are marked in the figure as examples. The solid red lines

symbolise the new refined element edges, while the dashed red lines are the auxiliary lines locating the nodes.

The midpoint projection was straightforward for the circumferential points, such as $B_1' \sim B_5'$. Taking B_1' for example, given the coordinates of $O(x_o, y_o, z_o)$ and B_1' $(x_{b1}', y_{b1}', z_{b1}')$, the vector $\overrightarrow{OB_1'}$ was obtained as

$$\overrightarrow{OB_1'} = [x_{ob1}', y_{ob1}', z_{ob1}'] = [x_{b1}' - x_0, y_{b1}' - y_0, z_{b1}' - z_0] \quad \textit{Eqn. 5-9}$$

Vector $\overrightarrow{OB_1}$ was then obtained by multiplying the normalised $\overrightarrow{OB_1'}$ with the radius, r,

$$\begin{aligned} \overrightarrow{OB_1} &= [x_{ob1}, y_{ob1}, z_{ob1}] \\ &= [x_{b1} - x_0, y_{b1} - y_0, z_{b1} - z_0] = \frac{\overrightarrow{OB_1'}}{\left\|\overrightarrow{OB_1'}\right\|} \cdot r \end{aligned} \quad \textit{Eqn. 5-10}$$

Eqn. 5-10 would thus give the coordinates of the projected point $B_1(x_{b1}, y_{b1}, z_{b1})$. The validity of Eqn. 5-9 and Eqn. 5-10 was confirmed by the fact that the points O, B_1', and B_1 were on the same circular plane, with the same Y-coordinates, namely

$$y_o = y_{b1}' = y_{b1} \quad \textit{Eqn. 5-11}$$

Eqn. 5-11 was also used for defining the circular plane that navigated the projection of the midpoints on the lateral edges, such as $B_6' \sim B_{10}'$. Taking the projection of B_6' as an example, given the coordinates of $B_6'(x_{b6}', y_{b6}', z_{b6}')$, the origin of the new circular plane O_b was then known as (x_0, y_{b6}', z_0). As shown in Figure 5-9 (c), points O, B_6, and O_b formed a right triangle. Following the Pythagorean theorem, the radius of the plane, r_b, was given as

$$r_b = \sqrt{r^2 - (y_0 - y'_{b6})^2} \qquad \textit{Eqn. 5-12}$$

Substituting Eqn. 5-12 into Eqn. 5-11, the position of the projected point B_6 was obtained. The calculation was realised by iterations in MATLAB. Figure 5-10 presents the refinement process from the base layer to the third-order refinement, in both general view and a perspective from the X-Z plane. The refinement with higher order is feasible but was less necessary, given that the boulder was simulated as a rigid body. Therefore, the third-order refinement was used for the 3D simulations in the following research.

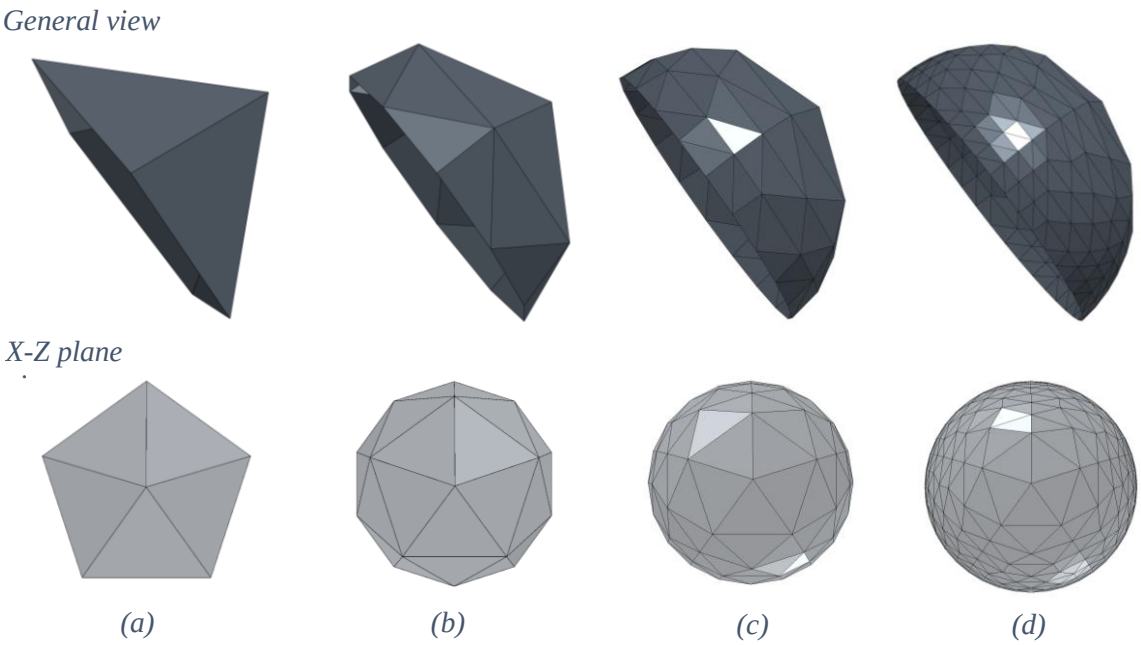


Figure 5-10 Boulder surface mesh refinement in 3D
(a) Base layer; (b) First-order refinement; (c) Second-order refinement; (d) Third-order refinement

5.3.4 Surface definitions and reference points

The surface definitions served for the definition of boundary conditions, as well as the motion control of the Lagrangian components. The surfaces were first defined by a group of nodes, whose coordinates satisfied the filtering conditions. The numbers of these nodes were recorded,

and the relevant elements were then collected if four out of the eight nodes within the hexahedral element (EC3D8R for the soil and C3D8 for the pile) were in the node assembly of the surface. The surface names and the corresponding filtering conditions for the nodal coordinates are listed in Table 5-3.

Table 5-3 Surface definition and nodal filtering conditions

Part	Surface name	Filtering conditions	
Eulerian domain	X-Z plane	$y_i = 0$	
	Y-Z plane	$x_i = 0$	
	Inner curved face	$x_{i,j} = X_0 \cdot \cos(\Delta\theta(j-1))$	- See Eqn. 5-5
	Outer curved face	$x_{i,j} = W \cdot \cos(\Delta\theta(j-1))$	- See Eqn. 5-6
	Bottom face	$z_i = 0$	
Pile	Pile head	$z_i = H + L$	- See Figure 5-1

Reference points, in addition, were used to control the motion of nodes and elements that had rigid body definitions. A list of the reference points and the controlled nodes is presented in Table 5-4. The vertical movement along the Z-axis of the pile was assigned to M-PL, with restrictions to the other five degrees of freedom, while the encastré condition of the pile sleeve was controlled by M-PS. The reference point of the boulder, M-BD, had Y-symmetrical boundary conditions, restricting the out-of-plane movement of the boulder.

Table 5-4 Reference point definition and slave nodes

Part	Reference point name	Location	Controlled nodes
Pile	M-PL	Centre of pile head	Pile head surface nodes
Pile Sleeve	M-PS	Centre of pile head	Pile sleeve nodes
Boulder	M-BD	Origin of boulder	Boulder nodes

5.3.5 CALCULATIONS OF EFFECTIVE VOLUME FRACTION

The Effective Volume Fraction (EVF) is the ratio of the filled volume to the total volume of an Eulerian element. The calculation of EVF was element-based. According to the positions of the element vertices, the element was divided into two primary categories, above the soil and below the soil. The elements below the soil were further divided into three sub-categories depending on the relative positions of the element vertices and the boulder.

The categories and the corresponding classification criteria are listed in Table 5-5, where $\boldsymbol{v}_i$ was an 8×3 matrix, containing the coordinates of the eight vertices of the examined i^{th} element. The vector $\boldsymbol{D}_i$ was 8×1, which recorded the distances between the vertices and the origin of the boulder. Each distance was compared with the boulder radius, $b/2$, to determine whether the vertex was inside or outside of the boulder.

Table 5-5 EVF calculation categories and classification criteria

Category	Description		Criterion	EVF
I	Above the soil, the void layer		$\text{all}(\boldsymbol{v}_i(:,3) \geq H) = 1$	0
II	Below the soil		$\text{all}(\boldsymbol{v}_i(:,3) \geq H) = 0$	[0,1]
	II.1	All outside of the boulder	$\text{all}(\boldsymbol{D}_i \geq b/2) = 1$	1
	II.2	All inside of the boulder	$\text{all}(\boldsymbol{D}_i \leq b/2) = 1$	0
	II.3	Partially outside/inside of the boulder	$\text{all}(\boldsymbol{D}_i \geq b/2) = 0$ & $\text{all}(\boldsymbol{D}_i \leq b/2) = 0$	(0, 1) Further partition of the element.

As shown in Table 5-5, the function $\text{all}(\cdot)$ was used in this decision process, which would return the logical value "1" if all the inequalities within were true, otherwise, return logical 0. The EVF calculation for element categories I, II.1, and II.2 was straightforward. For category

II.3, the hexahedral elements were further partitioned into 1000 sub-elements. These sub-elements again went through the classification and calculation in Table 5-5, the EVF value of which would be referred to as EVF_i. Whenever category II.3 was encountered, the sub-element was assigned $\mathrm{EVF}_i = 0.5$. Therefore, the EVF assigned to the partitioned element became $\mathrm{EVF} = \sum \mathrm{EVF}_i /1000$.

Another attempt at EVF calculation for the elements in category II.3 was to calculate analytically the overlapped volume of a hexahedral element and the hemispherical boulder. The algorithm started with locating the intersection between each element edge and the curved boulder surface. These intersections were connected and formed into a flat surface dividing the element into two polyhedrons. The volumes of the two polyhedrons were then calculated, which, divided by the entire volume of the element, resulted in the EVF value. This volume calculation added complexities to the algorithm due to the irregularities of the polyhedron shapes. An additional step, meanwhile, was required to determine which polyhedron should be filled with soil. Compared with the subdivision method presented above, these additional complexities did not bring additional accuracy to the EVF calculations. Therefore, the subdivision method was used for the subsequent simulations.

5.4 INVESTIGATION OF MODEL ROBUSTNESS

The calibrating process of the 2D models in Chapter 3 provided a guideline for the establishment of the 3D models. This section, as an extension to the guideline, presents an investigation routine to increase the robustness of the model. This routine attempted to quantify the influence of different model properties, including the mesh sensitivities in Section 5.4.1, and the contact properties in Section 5.4.2. The pile penetration speed and the effect of soil weight were considered less affected by the change of model geometry. Therefore, investigations of these two aspects were not included in the 3D simulations.

Except for the mesh sensitivity test for the pile, the boulder was temporarily removed from the models during the present investigation, with a curved flexible pile penetrating into the saturated clay. Therefore, Prandtl's mechanism (Prandtl, 1921) and Salgado's piecewise equation (Salgado *et al*., 2004) for strip footing penetration were again used to assess the results. To save computing time, this investigation was based on smaller-scale 45° models, and a discussion in Section 5.4.1 will show that the failure mechanisms are not affected by the model size. Thus, the smaller models are representative and can be used for the verification of the quarter-pile models.

5.4.1 MESH SENSITIVITIES

The mesh sensitivity test was carried out for the Eulerian domain and the pile. During the test, the mesh was first generated by Abaqus, without the central cutout, see Figure 5-4. These Abaqus-generated models ran through a convergence test, giving the most robust mesh scheme. This scheme was then used as the reference for the MATLAB-generated models, proving that the input file generation described in Section 5.3 was valid. Note that this MATLAB model verification was only carried out for the mesh schemes, because the other aspects of the MATLAB model were identical to the Abaqus-generated model.

Eulerian domain mesh sensitivity test

The viability test of the model in Section 5.2 suggested that the model with an angular extent of 90° could reduce to 45° without affecting the normalised vertical reaction force. To reduce the computing time, the investigation of mesh sensitivity used 45° models.

Recalling Section 5.3.1, the maximum element size was fixed to ten times the minimum, $l_{max} = 10l_{min}$. Therefore, this sensitivity test focused on determining an optimum l_{min},

resulting in the number of elements under the pile tip, n_{pt}, as marked by the light blue area in Figure 5-11 (a). The models were thus named as SP45-t/n_{pt}. The pile was penetrated into the ground to the depth of $z_{ult} = 10t$ within one second in models from SP45-$t/2$ to SP45-$t/10$, which showed a convergence trend with the increase of n_{pt}.

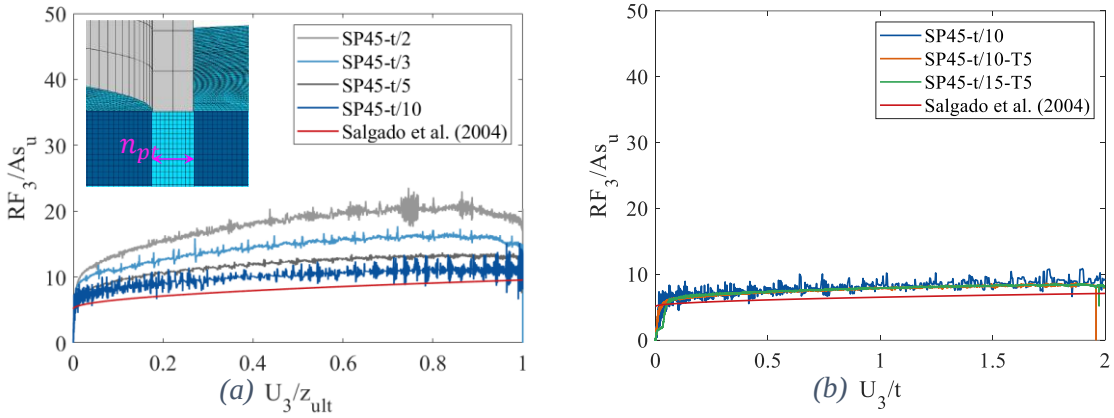


Figure 5-11 Eulerian domain mesh sensitivity test
(a) Comparison of different mesh schemes; (b) Convergence of penetration speed

To investigate whether the slight overestimation of SP45-$t/10$ was due to the penetration speed, an additional two models, SP45-$t/10$-$T5$ and SP45-$t/15$-$T5$ were established. The model SP45-$t/10$-$T5$ had the same meshing scheme as SP45-$t/10$, but with the penetration depth decreased from $10t$ to $2t$ in one second, simulating a slower penetration speed. The model SP45-$t/15$-$T5$, on the other hand, had the same speed as SP45-$t/10$-$T5$, but further increased n_{pt} to 15. The result comparison of SP45-$t/10$ and the two additional models is presented in Figure 5-11 (b), suggesting that the result has reached a converged state with the model SP45-$t/10$. Further increasing n_{pt} or decreasing the penetration speed did not improve the accuracy of the model, but helped reduce the data oscillation. The overestimation of the Abaqus model compared with the reference solution was because of the effect of material mass, further discussion of which is given in Section 5.4.3.

Considering that the model SP45-$t/5$ could give a smoother reaction curve compared to SP45-$t/10$, the following simulation used $l_{min} = t/5$. The relationship between the l_{max} and l_{min}, however, was further optimised during the verification of the MATLAB-generated models. The details of this optimisation are presented later in this section.

Pile mesh sensitivity test

The pile mesh sensitivity test focused on the number of elements across the wall thickness, n_t. The element sizes in the vertical and the circumferential directions, however, were kept equal to the wall thickness, t, as shown in the detailed view of the pile mesh in Figure 5-12 (a). To save computing time, the Eulerian soil was removed from the model. A 90° truncated pile (a quarter pile), with dimensions $D = 100t$ and $L = 50t$, was jacked towards a boulder with a diameter ten times the wall thickness, $b = 10t$. The boundary conditions of the pile edges were kept the same as those described in Section 5.1.3. Therefore, the model in fact simulated the condition where a pile hit two boulders at symmetrical positions. A preliminary study of a full pile model (not shown) suggested that negligible deformation was found along the pile edge without boulder collisions. Therefore, this boundary condition was considered appropriate.

The top view and the general view of the model are shown in Figure 5-12 (b) and Figure 5-12 (c), respectively, with the model SP90-$n_t = 3$ as an example. The penetration depth of the pile was $20t$, and the boulder was fully fixed halfway down the plate trajectory.

To control the deflection direction, the contact eccentricity was $0.05b$ to the left of the boulder origin. In this way, the tip was certain to deflect towards the left of the boulder. An example of the deformed shape can be seen in Figure 5-12 (d), while a quantitative comparison is in Figure 5-12 (e). Though with slight differences, the model with $n_t = 2$ gave consistent results with $n_t = 3$, with a relative error of 1.18%. Considering that the computing time was governed by

the pile elements due to their small size and high stiffness, the following simulations used two elements across the pile wall thickness.

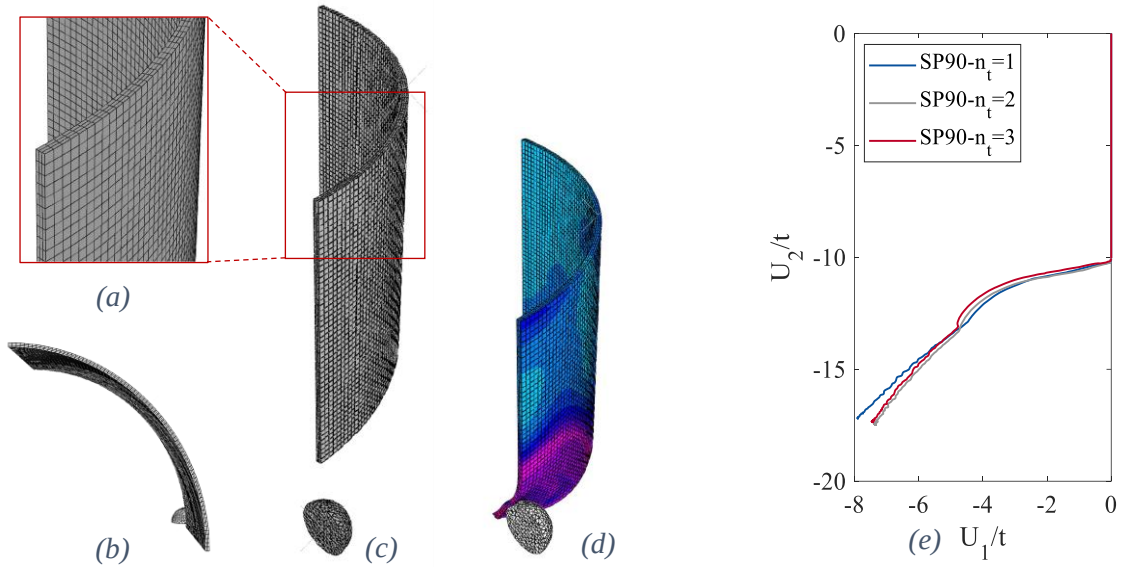


Figure 5-12 Pile mesh sensitivity test

(a) Zoomed picture of pile mesh in model SP90-n_t=3; (b) Top view of the model SP90-n_t=3;
(c) General view of the model SP90-n_t=3;
(d) Deformed pile with von Mises stress contour in SP90-n_t=3;
(e) Plots of pile tip trajectories of three models

Verification of MATLAB-generated model

Two quarter-pile models were established using Abaqus CAE as references for the verification of the MATLAB-generated models, coded as ABQ-0.1t-t and ABQ-cut-0.2t-t. Model ABQ-0.1t-t did not have the central cutout, and was a duplicate of SP45-t/10 in the previous discussion. Model ABQ-cut-0.2t-t, on the other hand, had the central cutout as shown in Figure 5-1, and a smaller ratio between l_{max} and l_{min}, namely $l_{max} = 5l_{min}$. This smaller ratio gave results comparable with $l_{max} = 10l_{min}$, in spite of a larger l_{min} ($l_{min} = 0.2t$). This relationship was adjusted to maintain an appropriate aspect ratio of the elements in the area near the internal cuts. The same meshing scheme was used in the MATLAB-generated model.

As shown in Figure 5-13, the MATLAB model gave consistent results with the two Abaqus models. Therefore, the 3D simulations in this research used $l_{max} = 5l_{min}$, and $l_{min} = 0.2t$.

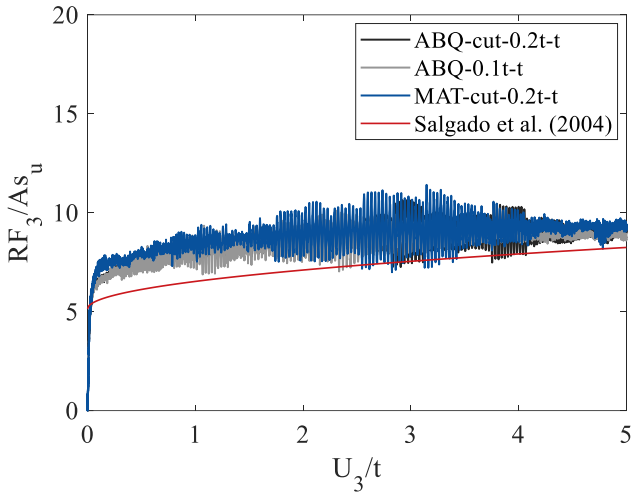


Figure 5-13 MATLAB-generated model verification

5.4.2 CONTACT PROPERTIES

The investigation of the contact properties between the pile and the soil focused on the effects of different Coulomb friction coefficients, μ. To reduce the computing time, the coarsest meshing scheme with $n_{pt} = 2$ was adopted for these simulations.

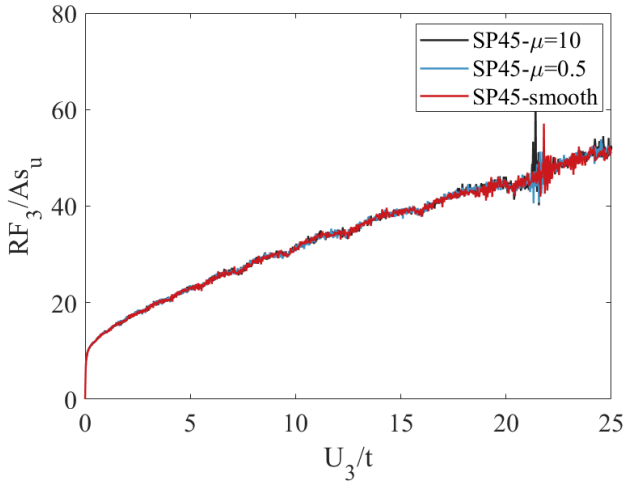


Figure 5-14 Effect of friction coefficient

A total stress friction model suitable for pile installation problems was achieved by 1) defining a high μ value enabling the rapid build-up of interfacial friction with normal stress and 2) limiting the maximum shear stress to be equal to the undrained shear strength of the clay, s_u. Two μ values were tested, $\mu = 0.5$ and 10. An additional model with smooth contact was also included for comparison.

Figure 5-14 indicates that the contact friction coefficient has a negligible effect on the pile penetration. The investigation in Chapter 4 (Section 4.6.2), in addition, suggested that μ would have little influence on the plate deflection. The penalty algorithm used for friction calculation, however, may extend the computing time when dealing with complicated interactions such as the presence of a boulder. Therefore, the following simulations used the frictionless contact condition, $\mu = 0$.

5.4.3 Mass scaling

To explore the potential for reducing the computing time, the effect of mass scaling was investigated by modifying the material densities. The coarsest meshing scheme was again adopted for computational efficiency, while the models with their corresponding material densities and computing time are listed in Table 5-6. The CPU time in the table resulted from computations with parallelisation using 18 processors.

Table 5-6 Material densities for mass scaling investigation

Model name	ρ_{soil} [kg/m^3]	ρ_{pile} [kg/m^3]	Computing time [h: min: s]
SP45-0.1	200	785	02:00:03
SP45-1	2000	7850	00:46:30
SP45-10	20000	78500	00:23:07

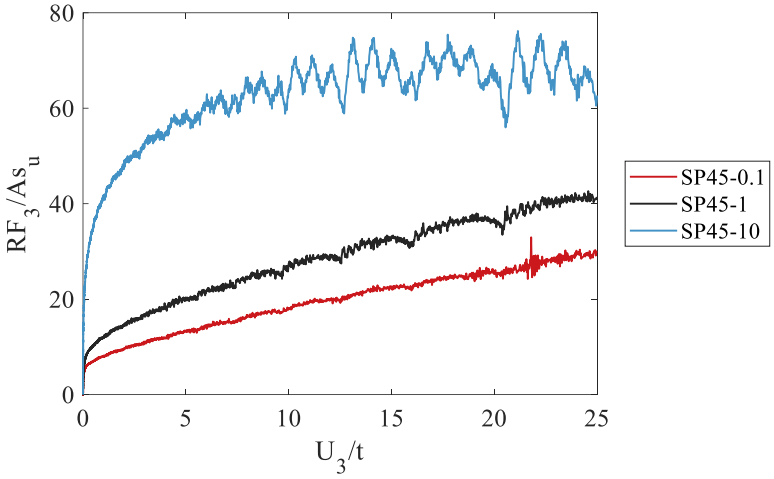


Figure 5-15 Effect of mass scaling

The vertical reaction force was again extracted from the pile head and normalised for comparison. Multiplying the material density by a factor of 10 could save half of the computing time (Table 5-6). However, as shown in Figure 5-15, the larger material density resulted in an exaggerated reaction force at the pile top. Therefore, the real material densities were adopted for the 3D simulations in this study.

5.5 3D PARAMETRIC STUDY

Three groups of parametric studies were conducted based on the 3D models, focusing on the factors introduced by the geometry changes compared with the 2D models. Section 5.5.1 focuses on the effects of D/t ratio, covering the range from 50 to 200. The boulder was placed slightly outside the pile. Because of the asymmetric condition on the two sides of the pile wall, Section 5.5.2 investigates the scenario where the boulder was slightly inside the pile. The boulder depth was then investigated in Section 5.5.3. A flat-plate model was also established for each group. An example of a pile model and its corresponding flat-plate model is shown in Figure 5-16. The flat-plate models had the same model setups as the corresponding 3D models, helping to establish connections between the 2D and 3D simulations. These models could be

regarded as an extreme condition of the curved pile and thus set a reference for the tip deflection.

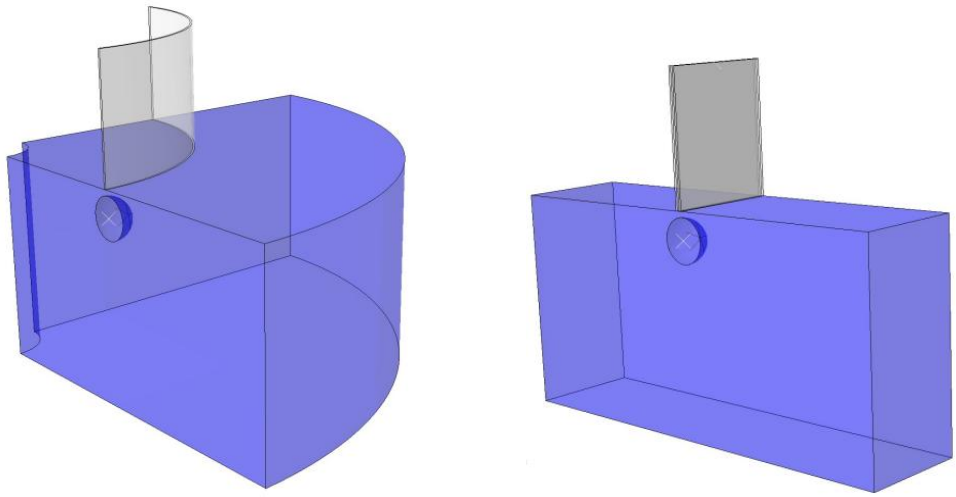


Figure 5-16 Example of pile model and corresponding flat-plate model (with transparency)

5.5.1 Effect of D/t ratio

Five models were included for the parametric study of the pile geometry, coded by "D" plus the D/t ratio ranging from 50 to 200. These piles were penetrated into the soil until $z_{ult} = 50t$. The eccentricity between the pile and the boulder was $e = 0.1b$, with the boulder centre $0.1b$ to the external side of the pile wall centreline. The boulder diameter was increased from $10t$ in the previous analyses to $20t$. This is because, from a preliminary study, the boulder with $10t$ could not cause sufficiently large tip deflections with the given material properties to give worthwhile results for further analyses. The boulder depth, $z_b = 0.05z_{ult}$, and the contact eccentricity were the most influential conditions obtained from the 2D parametric study in Chapter 3. A flat-plate model was also established with the same modelling conditions. The model thickness along the Y-axis was $50t$, more than two times the boulder radius. As the primary deformation was concentrated near the X-Z plane, this thickness was considered adequate.

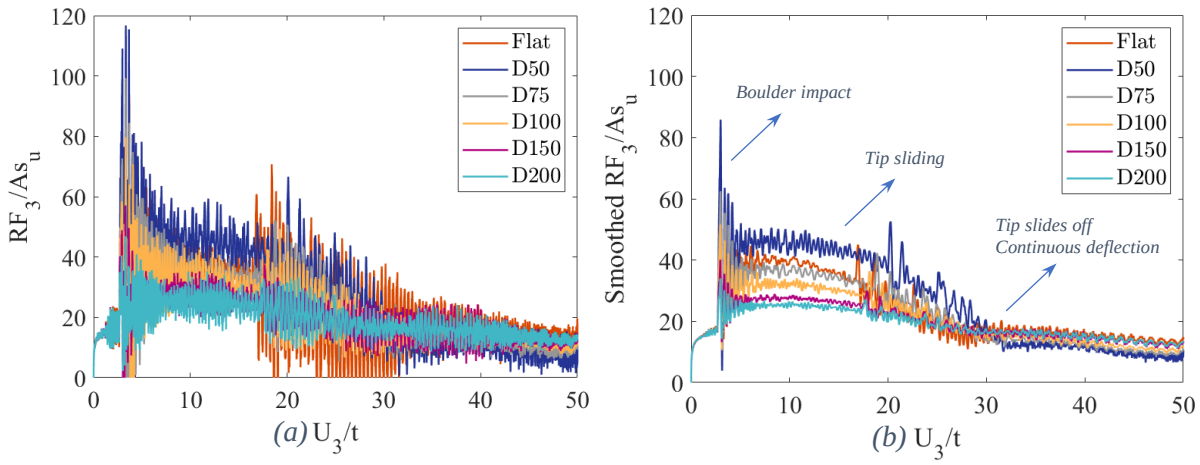


Figure 5-17 Variation of normalised reaction force with pile D/t ratio
(a) Raw data; (b) Smoothed data

Figure 5-17 (a) shows the normalised vertical reaction force from the pile tip extracted from the model, while Figure 5-17 (b) shows the filtered data with a window size of 15 data points. The data suggest a negative correlation between the reaction force and the D/t ratio of the pile. The reason behind this perhaps lies in the geometry of the pile section. For a given t, a larger D/t ratio results in a longer arc length along the circumference of the pile. Consequently, when a boulder strikes the pile, the area impacted along this arc is in a relatively smaller portion compared to piles with smaller D/t ratios. This hypothesis could be upheld by the comparison between the flat-plate model and model D75. With a model thickness of $50t$, the bottom area of the flat plate model is $50t^2$, while in D75, the bottom area is around $58t^2$. Therefore, instead of a minimum limit for all pile models, the flat model gives the reaction force comparable to the model with $D/t = 75$, as shown in Figure 5-17 (b).

Similar force-displacement trends can be observed from the plots. As shown in Figure 5-17 (b), a sudden increase first appears at the moment of boulder impact, followed by a gradual decrease while the pile interacts and slides across the boulder surface. A second turning appears when the tip leaves the boulder, which has a consistent depth of $\widetilde{U}_3 \approx 30$, regardless of the D/t ratio. This observation is comparable with those revealed by the tip trajectories in Figure 5-18.

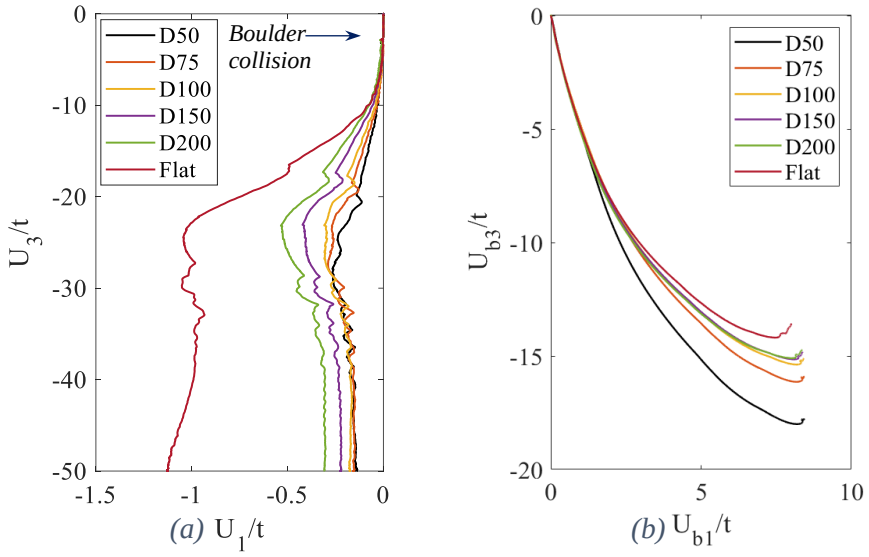


Figure 5-18 Effects of pile D/t ratio

(a) Comparison of tip trajectories; (b) Comparison of boulder displacements

The tip trajectories in Figure 5-18 (a) indicate that the tip deflection increases as the D/t ratio increases. The maximum deflection after the boulder impact occurs when the pile has penetrated a distance ranging from $20t$ to $25t$, followed by a recovery until around $\widetilde{U}_3 \approx 30$, regardless of the D/t ratio. This deflection recovery occurs when the pile tip leaves the boulder, corresponding to the second turning point in Figure 5-17 (b).

As shown in Figure 5-18 (b), the final horizontal displacement of the boulder, meanwhile, remains at around $8t$, regardless of the pile D/t ratio. This could explain the consistency of the recovery depth as previously discussed. The vertical displacement, however, presents a negative correlation with the D/t ratio. This observation was consistent with those in Chapter 4 – the boulder with larger displacements would cause less deflection at the tip. A stiffer (lower D/t ratio) pile exhibited greater resistance to radial stresses from the boulder. Consequently, the pile could transport the boulder along a more extended trajectory before sliding off it at a deeper depth. Therefore, the pile with a smaller D/t ratio would be expected to have less deflection, especially with the recovery after it leaves the boulder.

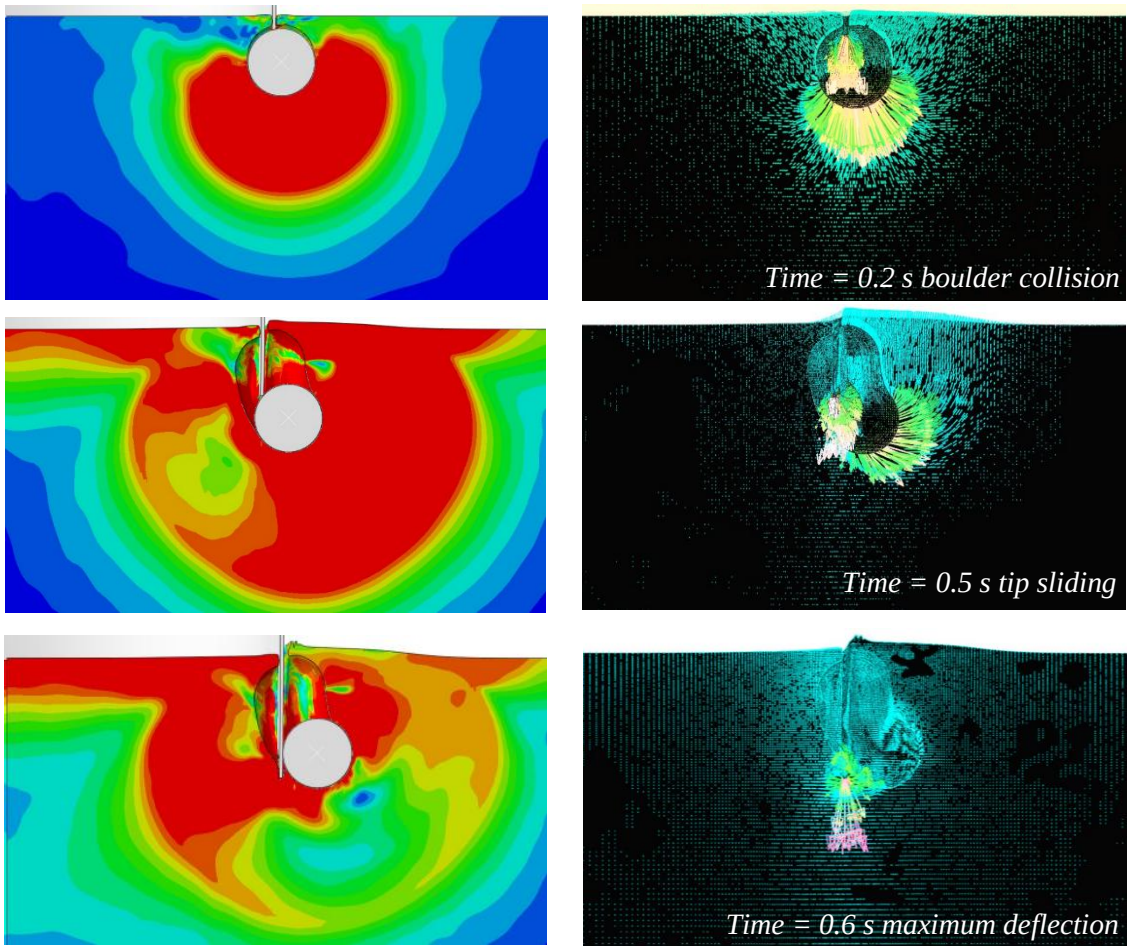


Figure 5-19 Stress contour(left) and velocity field (right) of model D200 at selected time steps

Figure 5-19 gives the stress contour and the velocity field of the soil at selected time steps – at boulder collision, during tip sliding, and at the moment of maximum tip deflection. For a clearer presentation, the boulder and the pile were removed in the plot of the velocity field. Therefore, the particle movement of the soil behind the boulder is also visible. This area of soil is influenced by the pile penetration only and thus has a smaller affected range compared with the soil on the front surface. The figure indicates that the soil behaviour is dominated by the boulder movement before the maximum tip deflection. Afterwards, the boulder becomes steady and the soil is mainly affected by the advancing pile.

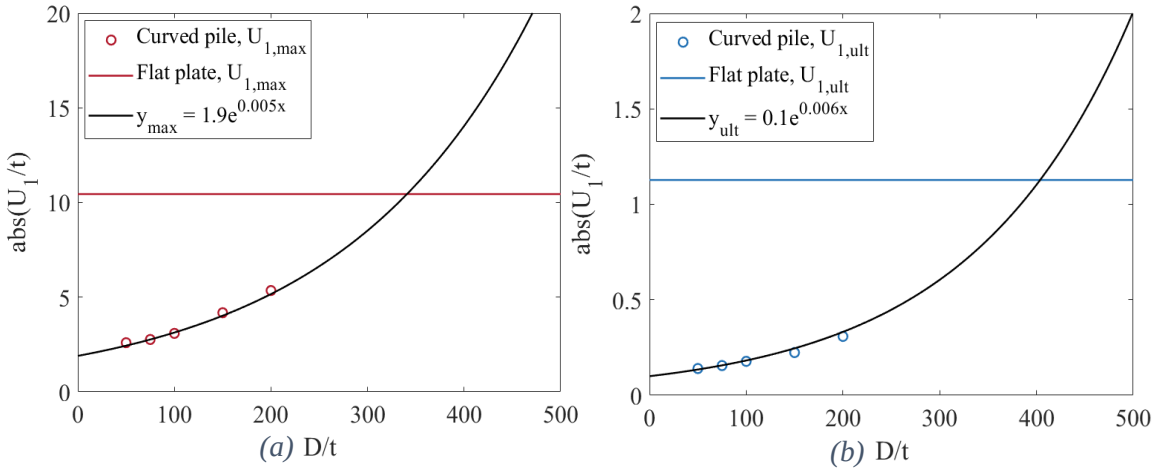


Figure 5-20 Comparison of the tip deflection and the numeric fit
(a) Maximum tip deflection; (b) Ultimate tip deflection

Figure 5-20 gives a comparison of the tip deflections, both the maximum at the depth around $25t$, $U_{1,max}$, as well as the recovered status at the end of simulations, $U_{1,ult}$. The absolute value on the vertical axis was to compensate for the positive definition of the X-axis in Abaqus. Piecewise equations established the relationship between the tip deflection and the D/t ratio for both plots,

$$\frac{U_{1,max}}{t} = 1.9e^{0.005D/t} \qquad \textit{Eqn. 5-13}$$

$$\frac{U_{1,ult}}{t} = 0.1e^{0.006D/t} \qquad \textit{Eqn. 5-14}$$

Eqn. 5-13 suggests that the pile with $D/t \approx 340$ would have comparable behaviour with a flat plate, while Eqn. 5-14 suggests $D/t \approx 400$. A comparison of the two equations indicated similar constants of D/t, and the maximum deflection is around 19 times the recovered, namely $U_{1,max} \approx 19U_{1,ult}$.Based on the observation in Figure 5-18 (a), a minimum of $30t$ would be required for the pile tip to fully recover to a stable state, enabling the application of Eqn. 5-14. A detailed discussion of the prediction of the tip deflections will be presented in Section 5.6.

It should be noted, however, that the above equations were specifically applicable to boulders deviating to the outside of the pile. Other scenarios involving no contact eccentricity and boulders deviating inside the pile will be discussed in the next section.

5.5.2 Effect of contact eccentricity

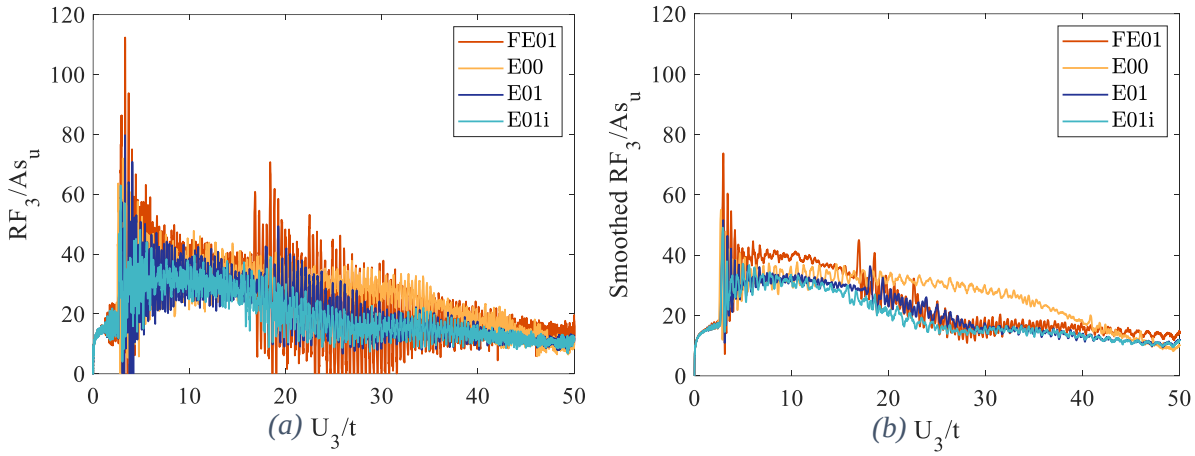


Figure 5-21 Effect of contact eccentricity
(a) Raw data; (b) Smoothed data

Three models were included for the parametric study of the contact eccentricity between the pile and boulder, where the D/t ratio was kept at 100 and the boulder diameter, $b = 20t$. The model is coded by "E" plus the value of $\tilde{e}$ without the decimal point. The model E01i contained a boulder positioned on the internal side of the pile wall. A corresponding flat-plate model, FE01 was also included for comparison.

A comparison of the reaction force at the pile top is presented in Figure 5-21. The oscillating raw data in Figure 5-21 (a) were again smoothed with a window size of 15 data points, as shown in Figure 5-21 (b). The similarity between FE01, E01 and E01i suggests that the reaction force tends not to be influenced by the position of the boulder, as long as the size and the normalised contact eccentricity are the same. The second turning point in these three models was again at the depth of $\widetilde{U}_3 \approx 30$. In E00, meanwhile, a much deeper transition was observed,

indicating a prolonged process of tip sliding across the boulder surface. Figure 5-22 (a) shows the tip trajectories of the models, where the flat-plate model has been excluded for a clearer figure scale. The plot shows a consistent trend as suggested by the reaction force in Figure 5-21.

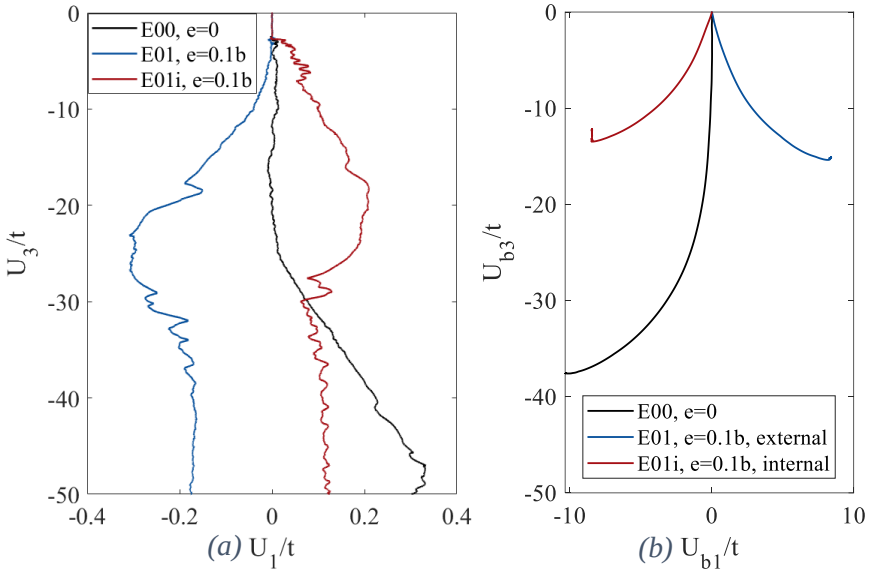


Figure 5-22 Effect of contact eccentricity
(a) Comparison of tip trajectories; (b) Comparison of boulder displacements

Though having similar reactions, E01i gave a smaller ultimate tip deflection of $0.12t$, around 70% of that in E01 ($0.17t$). The largest deflection occurred when there was no contact eccentricity, in model E00. Figure 5-23 presents the velocity field in the soil at time step 2000 of model E00, just before the boulder started moving inside the pile. The figure suggests that soil from outside the pile was flowing towards the inside of the pile, along with the boulder moving towards the pile centre. This transportation took an extended contact period of the pile and boulder compared with E01i, where the eccentricity favoured the lateral movement of the boulder. Larger deflection therefore occurred at the tip in E00. In addition, because the pile tip remained contact with the boulder until a depth of around $47t$, the recovery distance was constrained, leaving the tip deflection at a higher level.

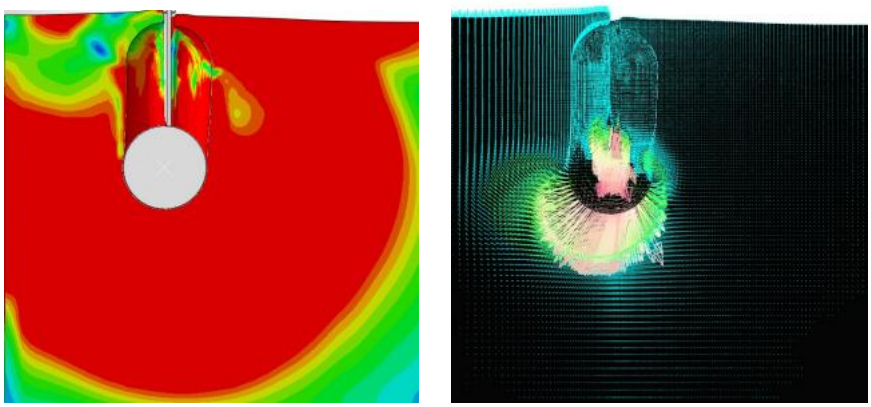


Figure 5-23 Stress contour and velocity field of model E00 in soil at time step 2000

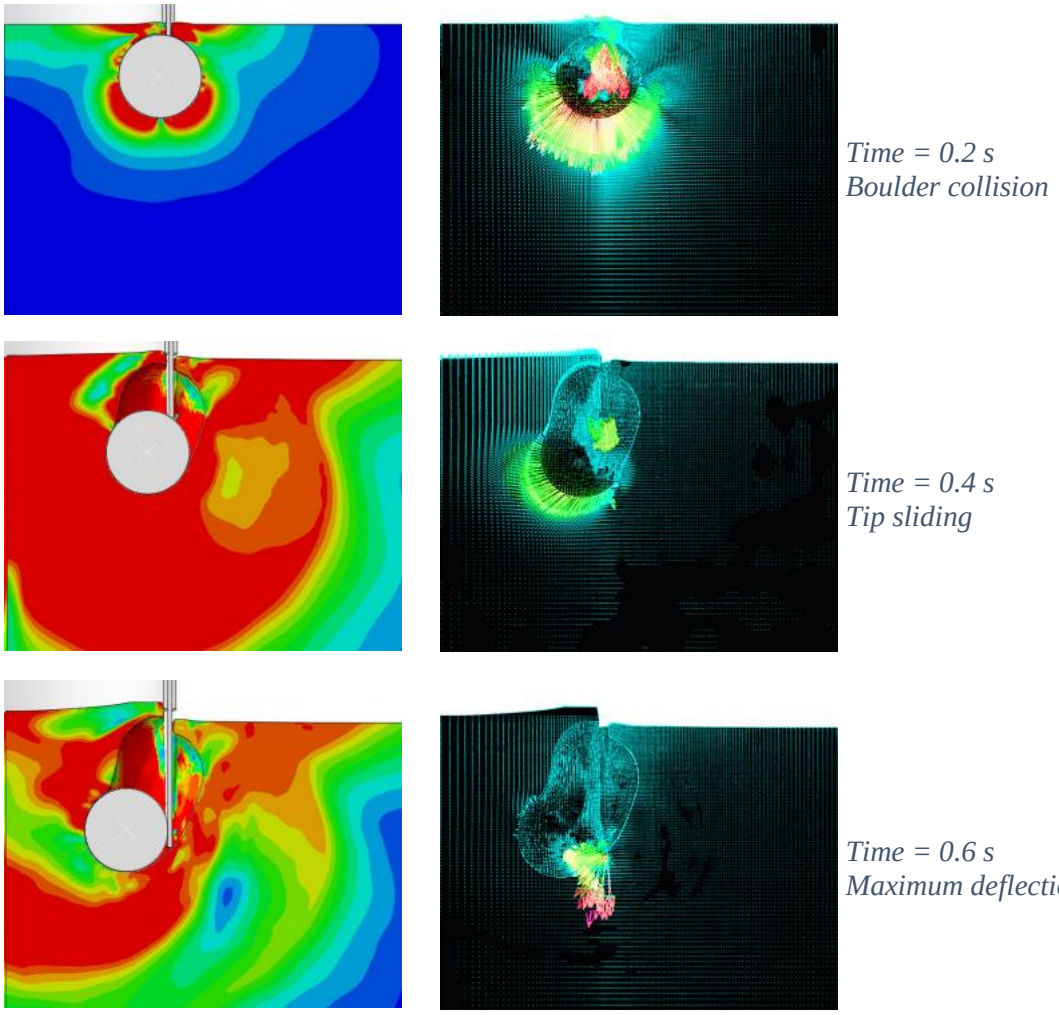


Figure 5-24 Stress contour and velocity field of model E01i at selected time steps

A similar distance enabling the development and recovery of the tip deflection was also found in the models E01 and E01i. In the case of model E00, it appeared that a greater distance was

required to achieve maximum deflection. Nonetheless, it is noteworthy that there was no contact eccentricity within the distance encompassing approximately $25t$ out of the total $47t$. Once the eccentricity appeared, the developing distance was again within the range of $20t$ ~ $25t$, as suggested in Section 5.5.1. Therefore, the developing distance should be defined as the distance between the first occurrence of contact eccentricity and the occurrence of $U_{1,max}$.

Figure 5-24 shows the stress contour and velocity field of model E01i at selected time steps, including the boulder collision, during the tip sliding, and at the moment of maximum tip deflection. Though at different depths, the velocity field of model E01i at boulder collision has a similar pattern to that in E00 when the boulder starts moving sideways (Figure 5-23). As in the previous model, the soil behaviour is dominated by the boulder movement before the maximum tip deflection, while afterwards, the pile penetration becomes dominant.

5.5.3 Effect of boulder depth

Six models were established for the parametric study of the boulder depth. The model code "Z05" denotes $z_b = 0.5z_{ult}$ and "Z005", $z_b = 0.05z_{ult}$. The model E00 in the last section is also included here. Though the boulder impact was at $z_b = 0.05z_{ult}$ in E00, the boulder deviation occurred when $z_b = 0.5z_{ult}$. Hence, a comparison was conducted between E00 and models E01Z05 and E01iZ05 in an effort to identify common aspects of the pile-boulder interaction. The model E00 is coded as E00Z005 to keep the consistency with the other models. Two flat-plate models, each with the respective boulder depths, were also established to serve as reference analyses. The contact eccentricity in both flat-plate models remained at $0.1b$, coded with FE01Z05 and FE01Z005, respectively.

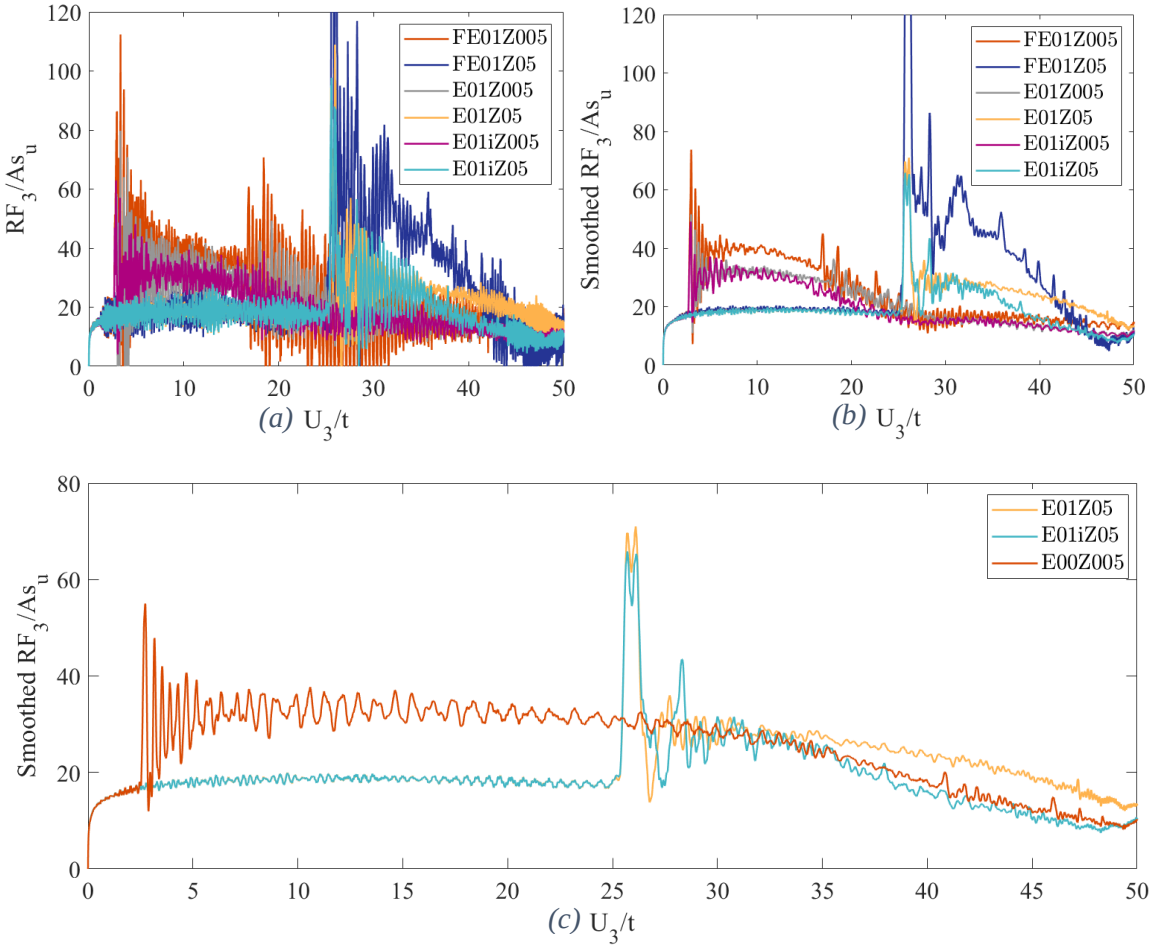


Figure 5-25 Effect of boulder depth

(a) Raw data; (b) Smoothed data; (c) Comparison with E00Z005

Figure 5-25 (a) and (b) show the raw and smoothed reaction force from the pile top, while the comparison with E00Z005 is presented independently in Figure 5-25 (c) for a clearer view. The reaction forces of the pile models have comparable magnitudes at each corresponding stage, at boulder collision and during tip recovery. This observation indicates that the instantaneous contact force between the pile and the boulder is less likely to be affected by the soil mass lying above. Other factors, such as the penetration speed, may become important. The large contact force in model FE01Z05 was due to the decrease of model dimension, specifically the decrease in model thickness from $50t$ as in FE01Z005 to $25t$. Recalling Figure 5-18, where lower D/t ratio will lead to larger reaction force at and after boulder impact, the shorter plate length tends to have the same effect when the same size boulder is encountered.

Despite the difference of boulder position, Figure 5-25 (c) shows that the reaction force of E00Z005 is comparable to E01Z05 and E01iZ05. Because the boulder in E00Z005 moved towards the pile centre, mode similarities can be found between this model and E01iZ05. Figure 5-25 (c) further indicates that the interaction force between the pile and the boulder dominates the vertical reaction force of the pile.

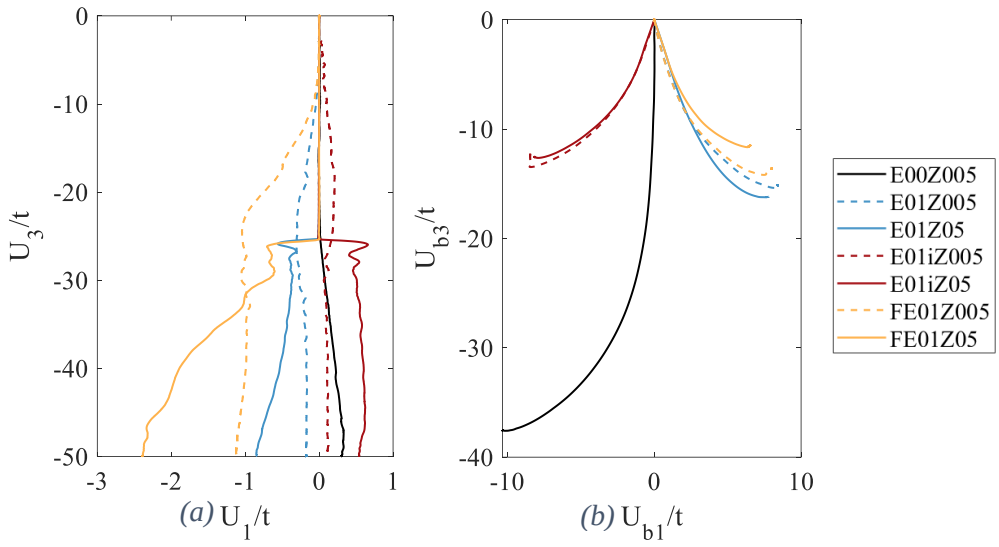


Figure 5-26 Effect of boulder depth

(a) Comparison of tip trajectories; (b) Comparison of boulder displacements

As shown in Figure 5-26 (a), in contrast to the 2D models, the deeper boulder results in larger tip deflections. This, as explained in Section 5.5.2, could be due to the limited recovery distance after the boulder impact. Despite the differences in boulder depths, the (absolute) ultimate tip deflections7 of models with internal boulders exhibited a similar relationship to those with external boulders. In model E01iZ005, $U_{1,ult} = 0.12t$, around 70% of that in E01Z005, which gave $U_{1,ult} = 0.17t$. Similarly, in model E01iZ05, $U_{1,ult} = 0.54t$, around 64% of that in E01Z05, which gave $U_{1,ult} = 0.85t$. This consistency could be due to the similar boulder movements in Figure 5-26 (b). The non-eccentric boulder in E00 had larger horizontal displacement compared with that in E01iZ05, but still led to larger tip deflections than the

latter. This was probably because the duration of contact interaction between the pile and boulder in E00 was much longer than that in E01iZ05.

5.6 CONNECTION BETWEEN 2D AND 3D SIMULATIONS

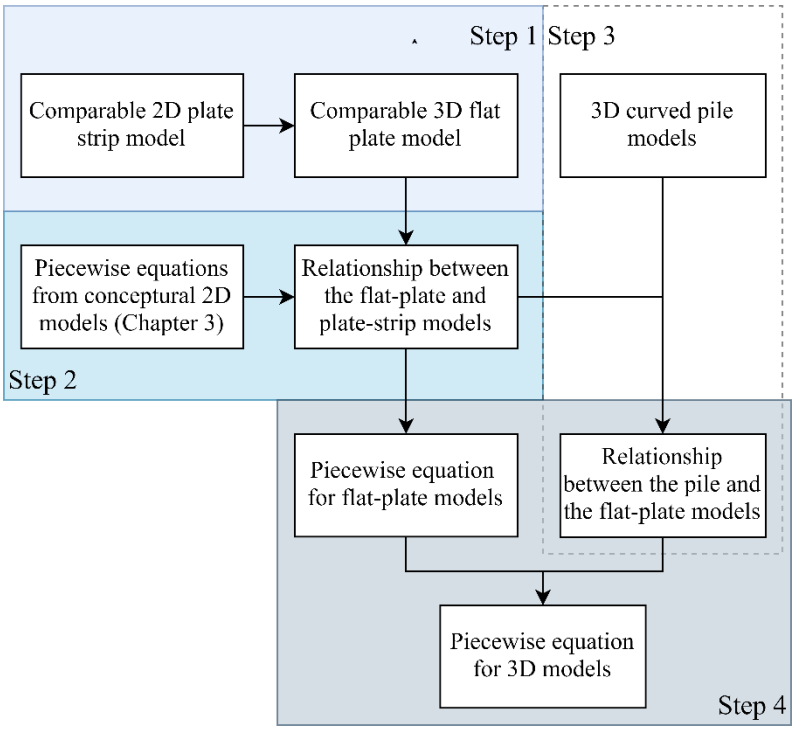


Figure 5-27 Workflow building the connection between 2D and 3D simulations

Figure 5-27 gives the workflow of this research that seeks to establish the connections between the 2D and 3D simulations, linking the deliverables in Chapter 3 and Chapter 5. This connection enables the quick estimation of the tip deflection due to boulder impact by using 2D simulations and piecewise equations taking account of the D/t effect. A description of the establishment procedure is given in Section 5.6.1, while the result generalisation can be seen in Section 5.6.2.

5.6.1 CONNECTION ESTABLISHMENT

The connection establishment has four steps, as shown in Figure 5-27:

Step 1: Six 3D flat-plate models and their 2D plate-strip counterparts were created to investigate the relationship between the 3D flat-plate (FP) and the 2D plate strip (SP) model. The model pairs are listed in Table 5-7.

Table 5-7 Parameters of verification models

Model pair	e/b	z_{ult}	$\tilde{b}$	$\tilde{z}_b$
FP1-SP1	0.1	$50t$	10	0.05
FP2-SP2				0.5
FP3-SP3			15	0.05
FP4-SP4				0.5
FP5-SP5			20	0.05
FP6-SP6				0.5

Figure 5-28 (a) shows the tip trajectories of the flat plate models. The boulders buried at deeper depths tend to induce a plateau in the trajectory as the plate tip slides off the boulder. This plateau appears in models FP2, FP4, and FP6, with an increased magnitude as the boulder diameter increases. This is because the deeper boulder presents greater resistance to the movement of the advancing plate, resulting in larger final deflections at the plate tip.

The trajectories of the flat-plate models, in addition, feature two salient points – the maximum deflection before deflection recovery, $U_{1,max}$, and the termination of recovery $U_{1,r}$, as marked in Figure 5-28 (a). The trajectories of the plate-strip models in Figure 5-28 (b), however, present a generally monotonic behaviour. Piecewise equations predicting the magnitude of $U_{1,max}$ and $U_{1,r}$ were therefore formulated in relation to the ultimate tip deflection in the 2D (SP) models, $U_{1,sp}$,

$$\frac{U_{1,max}}{t} = 0.2e^{\frac{0.2U_{1,sp}}{t}}, \qquad R^2 = 0.83 \qquad \textit{Eqn. 5-15}$$

$$\frac{U_{1,r}}{t} = \frac{0.1U_{1,sp}}{t}, \qquad R^2 = 0.89 \qquad \textit{Eqn. 5-16}$$

When the plate passes the recovery point, the ultimate tip defection, $U_{1,ult}$, is given as

$$\frac{U_{1,ult}}{t} = \frac{0.1U_{1,sp}}{t} + 0.1, \qquad R^2 = 0.85 \qquad \textit{Eqn. 5-17}$$

Eqn. 5-15 to Eqn. 5-17 were the numeric fit and, for the convenience of implementation, the simplest forms of formulae were adopted. The predictions of the two equations are within an error band of ±20%. A more accurate form could be to incorporate an additional term taking account of the effect of boulder depth. Eqn. 5-15 to Eqn. 5-17 built a relationship between the quarter-pile models and their flat-plate counterparts, contributing to the algorithm of result generalisation from 2D to 3D studies.

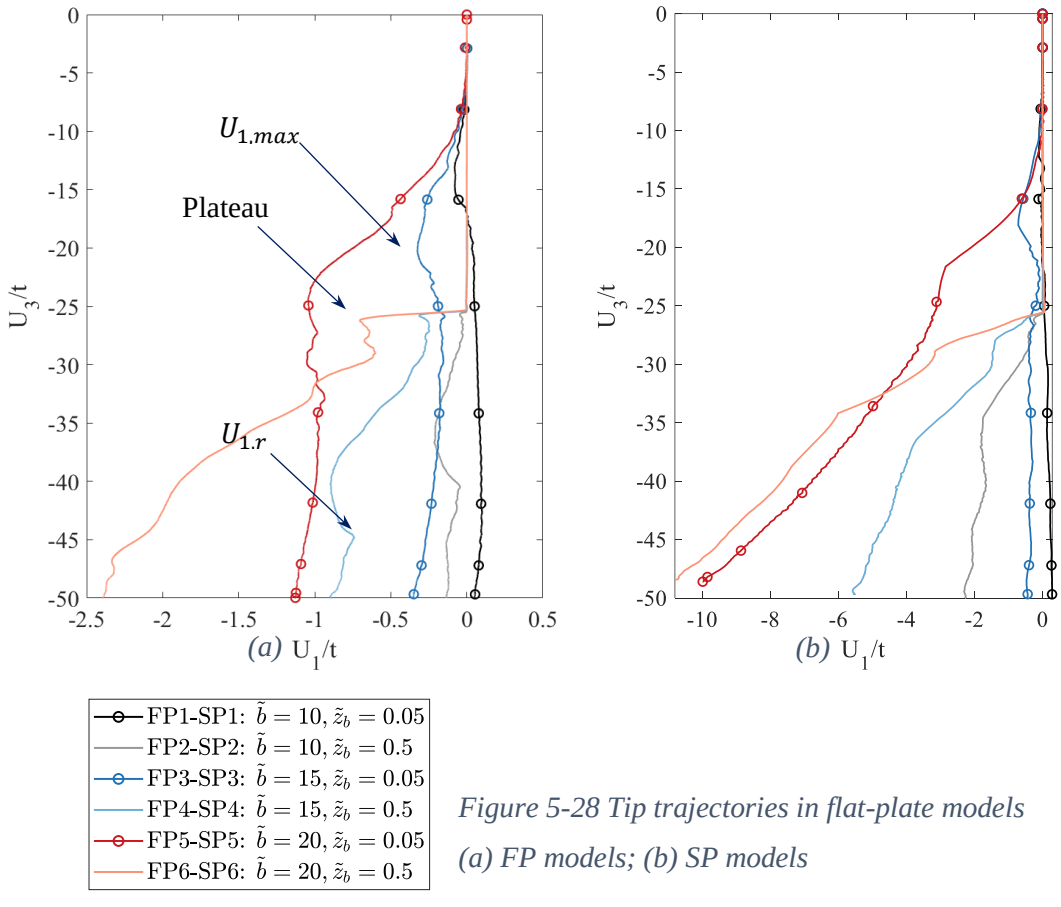


Figure 5-28 Tip trajectories in flat-plate models (a) FP models; (b) SP models

Step 2: The piecewise equations generated from the 2D parametric study described the relationship between the ultimate tip deflection of a 2D model and the corresponding parameters. The equations are summarised in Table 5-8, which provided a database of 2D tip deflections without conducting the CEL analysis and thus saved the computing time.

Table 5-8 Piecewise equations from 2D parametric study (Chapter 3 recap)

Parameter		**Equation**	
Boulder diameter	$\frac{b}{t}$	$\frac{U_{1,sp}}{z_{ult}} = 0.01\frac{b}{t} - 0.038$	*Eqn. 5-18*
Contact eccentricity	$\frac{e}{b}$	$\frac{U_{1,sp}}{z_{ult}} = 83.3e^{-21.2\frac{e}{b}} - 83.3e^{-21.5\frac{e}{b}}, \quad \frac{e}{b} \in [0.05,0.4]$	*Eqn. 5-19*
Boulder depth	$\frac{z_b}{z_{ult}}$	$\frac{U_{1,sp}}{z_{ult}} = -11.8\left(\frac{z_b}{z_{ult}}\right)^{5.2} + 0.06, \quad \frac{z_b}{z_{ult}} \in (0,0.35]$	*Eqn. 5-20*
Relative stiffness	$r_E = \frac{E_p}{E_s}$	$\frac{U_{1,sp}}{z_{ult}} = 0.012r_E^{0.21} - 3.2 \times 10^{-6} r_E$	*Eqn. 5-21*
Relative strength	$r_\sigma = \frac{\sigma_Y}{s_u}$	$\frac{U_{1,sp}}{z_{ult}} = -5.3 \times 10^{-5} r_\sigma + 0.12, \quad r_\sigma \in [500,2000]$	*Eqn. 5-22*

With $U_{1,sp}$ calculated from Table 5-8, the corresponding tip deflections of flat plates from Eqn. 5-15 to Eqn. 5-17 can be obtained. When coupling effects (Section 3.4.7) need to be considered, the piecewise equations in the table may no longer be applicable. A 2D plate strip model will need to be created to obtain $U_{1,sp}$. The computing time for a 2D model was under two hours on a workstation with 18 CPUs. This represents a notable reduction in computing time compared to a full-scale (360°) 3D model with the same model properties, which typically takes around two months to process.

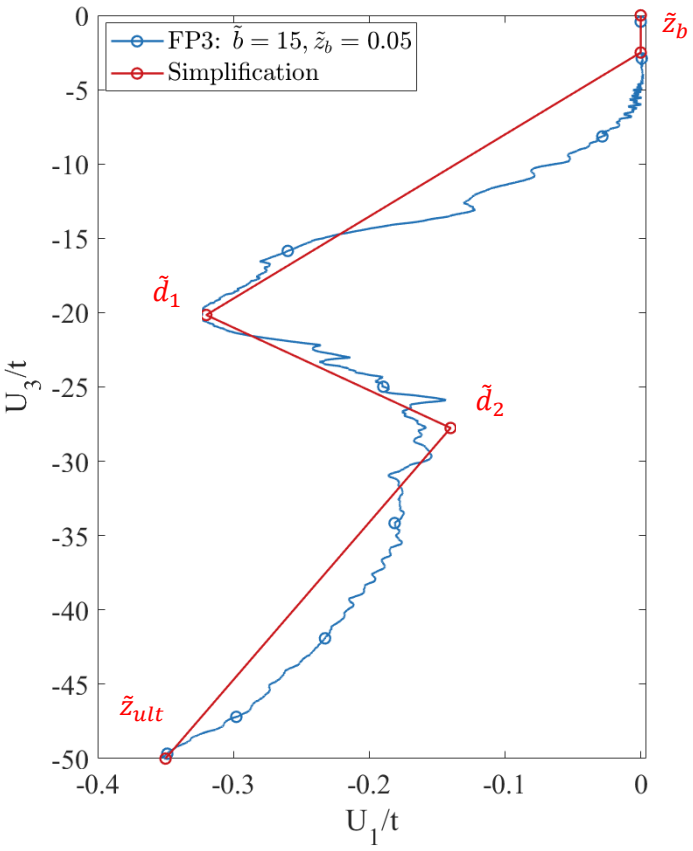


Figure 5-29 An example of tip trajectory simplification

Step 3: With the determined $U_{1,max}$ and $U_{1,r}$, the trajectory of the plate tip is simplified as four linear segments in Figure 5-29. The turning point $\tilde{d}_1$ $(= d_1/t)$ symbolises the normalised depth of $U_{1,max}$ with respect to t, and $\tilde{d}_2$ $(= d_2/t)$ is the normalised depth of $U_{1,r}$. It is found that, as shown in Figure 5-28, $\tilde{d}_1$ is linearly correlated to $\tilde{z}_b$, regardless of the initial boulder depth. The linear relationship is given as

$$\tilde{d}_1 = \tilde{z}_b + \tilde{b} - 2.5 \qquad \textit{Eqn. 5-23}$$

where $\tilde{z}_b = z_b/t$. The difference between $\tilde{d}_2$ and $\tilde{d}_1$ remains around 5, regardless of the boulder diameter or the boulder depth. Therefore, once $\tilde{d}_1$ is determined, $\tilde{d}_2$ can be estimated as $\tilde{d}_2 = \tilde{d}_1 + 5$. If the penetration depth of a flat plate is z_{ult}, the evolution of the normalised

tip deflection of a flat plate, $\widetilde{U}_{1,flat}$, can be calculated based on three interpolation equations, characterising the simplified linear tip trajectories in each segment,

$$\text{when } \tilde{z}_b < \tilde{z}_{ult} \leq \tilde{d}_1, \qquad \widetilde{U}_{1,flat} = \widetilde{U}_{1,max}\frac{z_{ult} - z_b}{d_1 - z_b}$$

$$\text{when } \tilde{d}_1 < \tilde{z}_{ult} \leq \tilde{d}_2, \qquad \widetilde{U}_{1,flat} = \widetilde{U}_{1,max} - \left(\widetilde{U}_{1,max} - \widetilde{U}_{1,r}\right)\frac{z_{ult} - d_1}{d_2 - d_1}$$

$$\text{when } \tilde{z}_{ult} > \tilde{d}_2, \qquad \widetilde{U}_{1,flat} = \widetilde{U}_{1,ult}$$

Step 4: The relationship between the flat plate and curved pile models has been discussed in Section 5.5.1 and Section 5.5.3. A key finding was that the tip trajectory between the two sets of models had similar patterns, with similar $\tilde{d}_1$ and $\tilde{d}_2$. This means an additional classification of the penetration depth, such as in Step 3, is not required. The tip deflection of the pile can be directly transferred from the plate deflection, given as

$$\widetilde{U}_{1,pile} = 0.2e^{0.005D/t}\widetilde{U}_{1,flat} \qquad \textit{Eqn. 5-24}$$

where $\widetilde{U}_{1,pile}$ and $\widetilde{U}_{1,flat}$ refer to the normalised displacement of the corresponding structure in any requested point. Eqn. 5-24 based on the relationship between $\widetilde{U}_{1,max,pile}$ and $\widetilde{U}_{1,max,flat}$ (recall Eqn. 5-13), which is a conservative calculation of the ultimate deflection of the pile, $\widetilde{U}_{1,ult,pile}$ (recall Eqn. 5-14).

5.6.2 Tip deflection generalisation

The calculation from Step 1 to Step 4 enables a quick evaluation of the likely extent of tip buckling with an error band of $\pm$ 20%. An estimation of the safety range of four parameters was obtained using the described approach, including boulder diameter, contact eccentricity, boulder depth, and relative strength. The generalisation excluded the impact of relative stiffness due to its minimal influence. Attempts at investigating the coupling effect of two parameters

are also conducted by incorporating the piecewise equations, but a case-specific numerical simulation is still recommended during the design stage in practice.

Boulder size

To obtain the safety envelope with respect to the boulder size, the boulder depth was kept at $10t$, with $\tilde{z}_{ult} \in [50, 200]$. The mechanical properties were taken as $r_\sigma = 1000$, $r_E = 10000$, and the contact eccentricity remained 0. Boulders with diameters ranging from $5t$ to $50t$ were investigated.

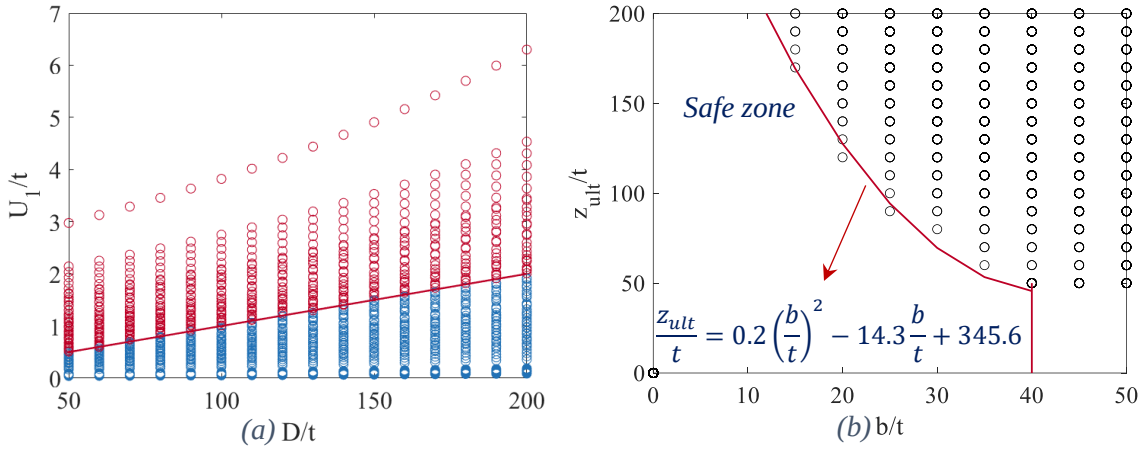


Figure 5-30 Result generalisation with respect to boulder size
(a) Plot of tip deflection; (b) Safety envelope

Figure 5-30 (a) gives the plot of the normalised tip deflection against the D/t ratio of the pile section. The failure criterion of out-of-roundness in API Specification 2B (API, 2002) was adopted for the evaluation. The red dots in the figure symbolise the region where the deflections are larger than $0.01D$, which is indicated by the solid red line. This red line becomes the safety envelope in Figure 5-30 (b), where the failed data points are plotted in the plane of $\tilde{z}_{ult}$-$\tilde{b}$. In this plot, the vertical axis denotes the penetration depth that is required for the failure to occur with the designated boulder depth. The equation of the envelope in Figure 5-30 (b) was determined from numeric fitting and has a cut-off at $\tilde{b} = 40$, beyond which a pile failure could

be envisaged regardless of the penetration depth. Though the deflection value exists when $\tilde{b} = 0$, it does not have physical meanings as the required penetration depth resulting in pile failure is beyond the maximum z_{ult} value considered.

It should be noted that the envelope presented in Figure 5-30 (b) assumes an idealised condition, where the pile hits the boulder centre precisely. In practice, however, this coincidence cannot hardly be guaranteed. The boulder size effect was therefore incorporated with the following analysis of contact eccentricity.

Contact eccentricity with boulder size extrapolation

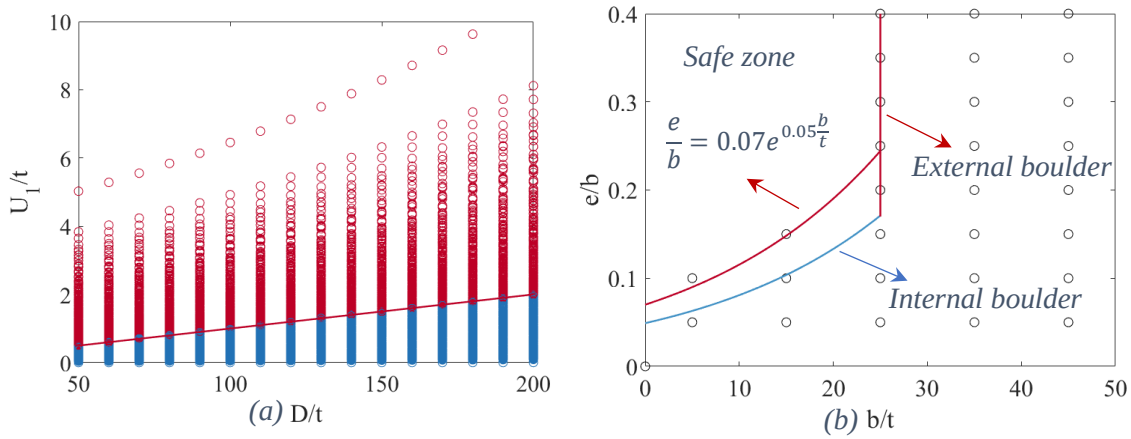


Figure 5-31 Result generalisation with respect to contact eccentricity
(a) Plot of tip defection; (b) Safe envelope

During this generalisation, the boulder was again placed at $10t$, with $\tilde{z}_{ult} \in [50, 200]$. The mechanical properties were taken as $r_\sigma = 1000$, $r_E = 10000$. The contact eccentricity ranged from $\tilde{e} = 0.05$ to 0.4. The boulder diameter was within $\tilde{b} \in [5, 50]$ with a linear extrapolation from $\tilde{b} = 10$ used to incorporate the effect of the external boulder into the result generalisation. The deflection resulting from internal boulders was taken as 70% of that from corresponding external boulders.

Figure 5-31 (a) gives the plot of the normalised tip deflection due to external boulders against the D/t ratio of the pile section, with the solid red line indicating $0.01D$ out-of-roundness deflection. Figure 5-31 (b) plots the failed data points in the plane of $\tilde{e}$-$\tilde{b}$, the red line is the safety envelope for external boulders, and the blue line for the internal boulders.

With eccentricity, the pile has the possibility to buckle even when the boulder diameter is at the smallest value $\tilde{b} = 5$. Beyond $\tilde{b} = 25$, the pile would fail regardless of the contact eccentricity or the penetration depth. In practice, the precise contact eccentricity is hard to determine prior to installation. Based on Figure 5-31 (b), a recommendation would be that, when $\tilde{b} \leq 5$, it might not pose a significant issue if the pile does not hit the boulder near its centre. For the scenarios when $5 < \tilde{b} \leq 20$, hitting the pile around its periphery might not cause significant failure.

Boulder depth with boulder size extrapolation

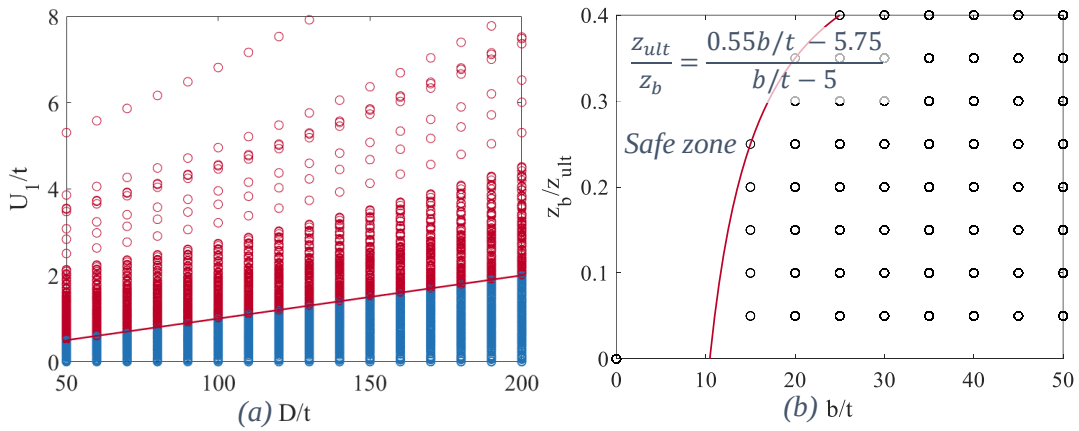


Figure 5-32 Result generalisation with respect to boulder depth
(a) Tip deflections; (b) Safety envelope

This investigation covered the boulder depth $z_b \in [0.05, 0.4]z_{ult}$, where $\tilde{z}_{ult} \in [50, 200]$. The boulder diameter range was $\tilde{b} \in [5, 50]$. The contact eccentricity was excluded, as a refined

coupling algorithm was required for the consideration of a third nonlinear equation (Eqn. 5-19). The mechanical properties were kept as $r_\sigma = 1000$, $r_E = 10000$.

Figure 5-32 (a) gives the plot of the normalised tip deflection due to different boulder depths, with the solid red line indicating $0.01D$ out-of-roundness deflection, while Figure 5-32 (b) shows the failed data points with a safety envelope. The envelope is comparable to those obtained for boulder diameter in Figure 5-30 (b), where the boulder with $\tilde{b} \leq 10$ is less likely to cause tip failure without contact eccentricity. When $\tilde{b} \geq 25$, on the other hand, the tip buckling is deemed certain to occur, regardless of the boulder depth or the contact eccentricity (recall Figure 5-31).

Relative strength with boulder size extrapolation

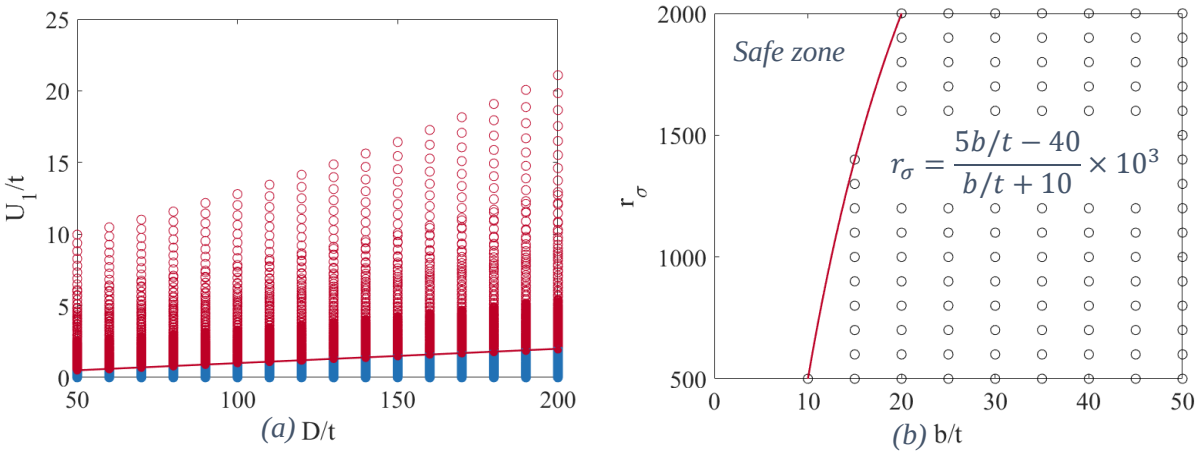


Figure 5-33 Result generalisation with respect to relative strength
(a) Tip deflections; (b) Safety envelope

This result generalisation covers a range of relative strengths of $r_\sigma \in [500, 2000]$. Given that the typical yield strength of steel for offshore use is around 350 MPa, the considered range of r_σ gives s_u from around 175 kPa to 700 kPa, in the regime of stiff to extremely stiff clay. Boulders with diameters ranging from $\tilde{b} = 5$ to 50 were buried at a depth of $10t$, with $\tilde{z}_{ult} \in$

[50, 200]. No contact eccentricity was included and the relative stiffness remained $r_E = 10000$.

The tip deflections with the $0.01D$ limit line and the safety envelope are presented in Figure 5-33 (a) and (b), respectively. Boulders with $\tilde{b} \leq 10$ are mostly in the safe zone, except for $\tilde{b} \leq 10$ at $r_\sigma = 500$. Beyond $\tilde{b} = 10$, the boulder may lead to tip failure depending on the value of the relative strength. Weaker soils (giving higher r_σ) are safer because it is easier for the pile to push the boulder out of the way.

5.7 CONCLUDING REMARKS

This chapter first presents a detailed procedure for establishing a 3D model containing the interactions of pile, boulder, and soil. Various model properties, including the mesh sensitivity, the contact condition, and mass scaling, were investigated to obtain the optimum modelling conditions. These investigations focused on the model performance due to the pile curvature, which can be regarded as compensation for the investigation in Section 3.3. The key findings of this additional investigation include

1) The convergence of the model is not only dependent on the finest element in the proximity to the pile trajectory, but also the element quality at distance. The automatic mesh generation in Abaqus may result in elements with poor aspect ratios for pile models without central cutouts. Though these elements are clustered around the pile centre, instead of the pile trajectory, they still elongate the computing time and slow down the convergence speed. The optimisation of the model with the central cutout and the meshing algorithm established in MATLAB compensated for this insufficiency, providing converged results a bit coarser than the Abaqus-generated model;

2) The reaction force of the pile is not affected by the definition of the frictional behaviour at the pile-soil interface. However, it may be affected by the definition of material densities. Increasing the material density will reduce the computing time, with an exaggeration of the pile reaction force. This exaggeration implies the instability of the model performance. Unlike the investigation of soil weight in Section 3.3.4, where gravitational force was considered, simply altering the material density should not introduce further changes to the model reactions. Therefore, simulations using Abaqus CEL are recommended to use either small densities excluding the exaggerating effect, or using the practical density of the material, giving results comparable to $1g$-condition (recall Section 3.3.4).

Further studies based on the truncated 3D model mainly focused on the possible changes due to the pile geometry, including the variation of tip deflection against the D/t ratio, and the comparison between the scenarios with internal and external boulders with different depths. The flat-plate model, under comparable modelling conditions, was also set up as a reference point for bridging the connections between 2D and 3D simulations. The comparison between the tip trajectories suggested that, in contrast to the monotonic increase observed in the 2D models, the 3D models presented a phenomenon of tip recovery after the boulder impact. Throughout the process, the tip deflection initially increased to a peak value upon sliding off the boulder, then rebounded to a certain distance as the boulder was pushed away, reaching a steady state. Subsequently, the tip continued to deflect at a generally constant rate until the penetration ceased. The piecewise equations linking the 2D and 3D models were accordingly divided into three segments.

Using the deliverables from the 2D parametric study, safety envelopes were established with respect to the boulder diameter, the contact eccentricity, the boulder depth, and the relative

strength between the pile and the soil. These envelopes provided a quick evaluation of whether the tip deflection would happen with corresponding parameters. Alternatively, when dealing with a more intricate coupling effect involving three or more parameters, it is advisable to opt for a 2D calculation. In this scenario, the 3D tip deflection can be obtained through the piecewise equations previously suggested, linking the 2D and 3D analysis.

CHAPTER 6 CONCLUSION

6.1 OBJECTIVES AND OUTCOMES

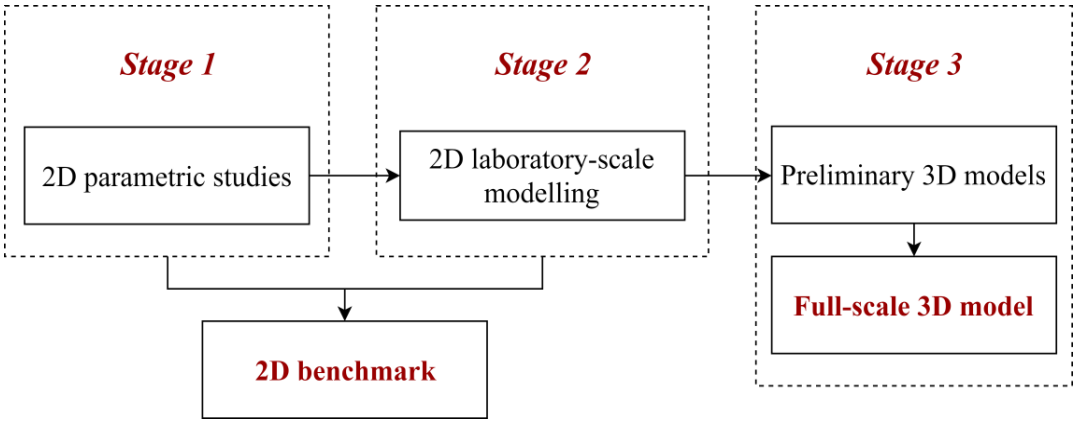
The research focused on the progressive bucking of monopiles due to boulder impact during installation, with the aim of establishing a reliable calculation approach in describing the interactions between pile, boulder, and soil. Recalling the research framework in Figure 1-17, the objectives and the outcomes of each stage are listed as follows:

Stage 1: This stage aimed at identifying the sensitivities of the influencing factors. A 2D parametric study was established using Abaqus CEL. A newly established sensitivity index suggested that the boulder size would affect the tip deflection most. Though a quantitative analysis of the boulder shape was not conducted in this research, a flipping mechanism was found for the boulders. Meanwhile, it was observed that the longer the boulder axis aligned with the tip trajectory after flipping, the greater the tip deflection. This flipping mechanism is regarded as one of the innovative findings of this research.

Stage 2: Serving as a validation approach to the 2D simulations, laboratory-scale physical modelling was subsequentially established at this stage. The thesis provides a detailed operating procedure, including the apparatus setup for PIV analysis, the preparation of clay samples, and the calibration of the numerical model. Though the PIV analysis has been used in various research, this thesis is one of the few that provides a detailed description of the

experimental procedure, which could serve as a guideline for future research. An extended study based on the calibrated 2D numerical models indicated two functions of the soil: it tends to maintain the deflected direction of the pile tip while also constraining the movement of the boulder. The latter effect causes the boulder to occupy the trajectory of the pile tip, further amplifying the tip deflection. This soil function has not been mentioned in previous literature, which could be regarded as the second innovative finding of this research.

Stage 3: Finally, the 3D simulations were conducted, providing the effect of the D/t ratio of the pile. The connections between the 2D and 3D analysis were described by piecewise equations. These equations were then implemented in the development of safety envelopes, indicating the possibility of tip buckling under given circumstances. The piecewise equations provide an efficient approach for evaluating tip deflection through hand calculations, serving as a practical rule of thumb for monopile design.



Recall Figure 1-18 Research framework

In short, the deliverables of this research are primarily threefold:

1) The verification process of establishing a numerical model that can provide reliable descriptions of the interaction between pile, boulder, and soil;
2) A convenient laboratory-scale test for efficient validation of the numerical model;

3) A series of piecewise equations linking the 2D and 3D analysis, accompanied by safety envelopes as a byproduct, indicating the possibility of top buckling under specific model conditions.

6.2 CHAPTER SUMMARIES AND CONTRIBUTIONS

Each of the primary outcomes summarised in Section 6.1 represents a chapter from Chapter 3 to Chapter 5. A more detailed summary of each chapter is presented as follows:

Chapter 3 Two-Dimensional Plate Penetration

Benchmarking: To save computing time, a plane-strain model was established in Abaqus CEL, where the model thickness was much smaller than the width and height of the model. To investigate whether this model was applicable, two classical geotechnical problems, the reaction force of strip footing penetration and the failure envelope of boulder rotation, were established as benchmarks. The model results were compared with either existing solutions or verified numerical techniques. The agreement between the model results and the reference solutions validated the effectiveness of the established equivalent 2D model in addressing the interactions between the rigid structure and the soil.

Optimum modelling condition: A preliminary model was subsequentially established, which involved a flexible plate strip penetrating into the soil. The objective of this model was to identify the properties that would ensure stable and dependable performance. Investigations based on this preliminary model included the mesh sensitivities of the Eulerian soil and the Lagrangian plate strip, the effect of the penetration speed, and the effect of soil weight. In contrast to the common practice in literature, where the pile was simulated as a cylindrical shell, it was recommended to use solid elements to represent the pile. Because it was found that the software had trouble considering the effect of shell thickness when it interacted with an

Eulerian material. The shell element, as a consequence, would underestimate vertical soil resistance from the pile base, adding conservatisms to the pile design.

The investigation of the penetration speed, meanwhile, suggested that a quicker penetration speed could save the computing time, but would exaggerate the pile reactions. A normalising scheme was established to mitigate this exaggeration, while a critical penetration speed was found when it was equal to the pile wall thickness.

The investigation of soil weight was realised by varying the gravitational acceleration of the model, from $0g$ to $10g$. It was found that the model with $0g$ and $1g$ would give comparable results. Models with accelerations other than $0g$ and $1g$ are not common for pile installation problems. However, the investigation indicated the potential interaction between the boulder and the soil at depth, where the gaps formed due to the boulder movement would be filled by the falling soil. Given that the additional stress wave may be induced by gravitational accelerations higher than 0, the simulation was recommended to use $0g$.

2D parametric study: With the verified model properties, the parametric study based on the 2D model investigated the effect of five independent normalised parameters, including the boulder diameter, the boulder depth, the contact eccentricity, the relative strength and the relative stiffness between the pile and the soil. Piecewise equations were established to characterise the relationship between the tip deflection and the corresponding parameters. A new index, meanwhile, was created to evaluate the parameter sensitivity. A radar plot composed of the indices suggested that the boulder size was the most influential factor in tip buckling, while the soil stiffness was the least. Qualitative descriptions, meanwhile, were also given with respect to the effect of boulder shape and tip geometry (chamfer effect). It was found that the tip deflection was determined by the axis occupying the plate trajectory after

boulder rotation. Longer axes would lead to more significant tip deflection. The chamfered tip, meanwhile, would decrease the lateral resistance of the pile and cause larger tip deflections.

Chapter 4 Laboratory-Scale Physical Modelling

Experiment: A laboratory-scale physical modelling was proposed for the validation of the 2D numerical models. The physical model was also considered to be in a plane-strain condition, as the model thickness was much smaller than its width and height. Similar to the 2D numerical model, a plate strip was penetrated into the saturated clay and collided with a rigid boulder buried in the designated position prior to the test. The interactions between the plate, the boulder, and the soil were recorded by photos and went through the PIV analysis. The vertical reaction force from the plate top and the tip trajectories were extracted from the experiment and then compared with the numerical models simulating the test. This experiment was likely the first to employ PIV analysis for a scenario involving the interaction of soil with two objects, one flexible and one rigid. The success of the experiment relied heavily on details, particularly when using saturated clay and a thin plate strip. However, once prior experience with the experiment is established, as discussed in the chapter, this small-scale testing approach should prove to be an effective tool for validating the numerical model.

Calibration: These experiments were then simulated using the same modelling techniques shown in Chapter 3. The interfacial contact properties were defined as smooth in Chapter 3, but were supplemented for the experiment to achieve a better agreement with the test results. It was found that, however, the friction coefficient at the interface between the buried structures and the soil had little influence on the tip deflection. The smooth contact condition was therefore adopted in later simulations due to the consideration of model stability. The improvement of the numerical model, in addition, focused on the model stability, the reduction of computing time, and the mitigation of data oscillation. These improvements did not

compromise the validity of the outcomes obtained from the uncalibrated models in Chapter 3. Because these additional modifications improved the smoothness of the reaction forces on the plate top, but were considered to have little influence on the tip deflection.

At this point, the numerical model was considered validated, enabling the 3D simulation of a full-scale pile. The underlying concept was that, given the calibration of the numerical model using the physical model, it would reliably predict pile deflection as long as the same model properties were employed.

Soil function: An additional investigation was conducted based on the calibrated model. This investigation aimed to determine whether the agreement between the test and the numerical model was merely coincidental. However, it unexpectedly yielded insights into the mechanisms of tip deflection by revealing the soil functions during the buckling process – it constrained the boulder movement, further prevented the recovery of plate curvature, and preserved the deflected direction of tip penetration.

Chapter 5 Three-Dimensional Pile Penetration

Model construction: Instead of building the model directly using Abaqus CAE, a MATLAB scheme was developed to generate the input file for the 3D simulation. The scheme mitigated the insufficiencies of the mesh optimisation by specifically defining the coordinates of each node. The obtained model was able to give results of the same accuracy with the Abaqus-generated models, while with coarser elements. Additional analyses of the contact properties were conducted based on the pile penetration model without boulders, which was comparable to the strip footing penetration model for 2D analysis. The consistency of the reaction force from the pile top with various frictional conditions proved that the developed 3D model could give reliable descriptions of pile penetration problems. Because the 3D simulation is usually

time-consuming, the effect of mass scaling was also investigated by varying the material densities. It was found that larger material densities could reduce the computing time effectively, but with the consequence of exaggerating the results. Therefore, the true densities of materials were recommended for the simulations.

Effect of D/t ratio: Parametric studies were then conducted to investigate the effect of D/t ratio of the pile and the position of the boulder. A positive correlation between the D/t ratio and the tip deflection was found from the analysis. In contrast to the 2D model, where the boulder induced a monotonic increase in the tip deflection, the pile curvature gave more lateral resistance to the structure, and the tip deflection could be divided into three stages after the boulder impact. As the tip slid across the boulder surface, the deflection gradually increased to a maximum value. After the tip slid off the boulder, a recovery in deflection was observed, followed by a gradual increase in deflection as the pile penetrated into the soil. With the same boulder size and contact eccentricity, the distance for the development of the maximum deflection remained consistent, regardless of the boulder position. In addition to the external boulder, the internal boulder was also simulated, giving a tip deflection of around 70% of that induced by its external counterpart.

Another difference between the 2D and 3D analysis was in relation to the boulder depth. Unlike the 2D models, where a shallower boulder would induce larger tip deflection, the 3D model was found to be more sensitive to the deeper boulder. This was considered a consequence of the recovery effect from the pile D/t ratio. With a deeper boulder depth, the tip had limited recovery distance after the boulder impact. In 2D models, on the contrary, an earlier boulder impact would allow for a longer development of monotonically increasing tip deflections.

Result generalisation from 2D to 3D analysis: To connect the 2D and 3D analysis, the flat-plate models were first established as counterparts for 3D models. The flat-plate model was

considered as an upper limit to the pile models with $D/t \to +\infty$. A relationship regarding the variations of the D/t ratio was subsequentially established.

The direct connection between the 3D pile model and the 2D plate strip model seemed difficult due to the effect of D/t ratio. Therefore, the flat-plate model was employed as a bridge, giving the segmental equations connecting its tip deflection at three penetration stages to the final deflection of a 2D counterpart. Together with the effect of D/t ratio derived from the previous step, these segmental equations completed the connections between the 2D and 3D analysis. A workflow of this procedure is summarised in Figure 6-1. The piecewise equations obtained from the 2D parametric study in Chapter 3 were also used to predict the tip deflections for 3D models under different model conditions. This approach provided safety envelopes for boulder size, boulder depth, and contact eccentricity, which can be used for a quick evaluation of the possibility of tip bucking in practice.

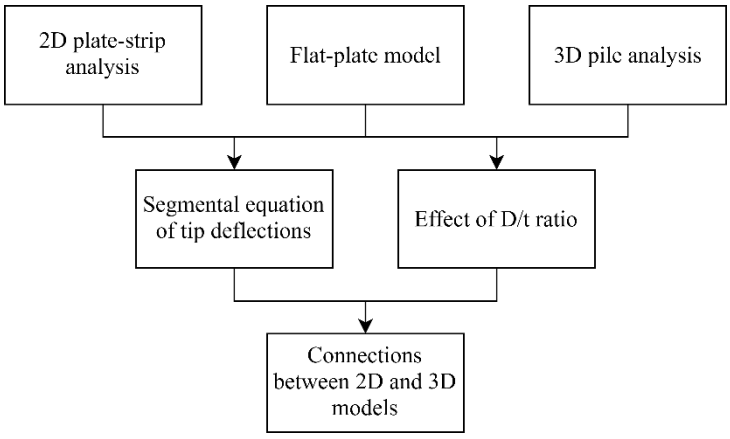


Figure 6-1 Workflow connecting the 2D and 3D analysis

6.3 LIMITATIONS AND FUTURE WORK

The limitations of the research came from the material definition and the parameter scope in the numerical models.

Material definition: The numerical model used homogeneous von Mises elastic-perfectly plastic material for the saturated clay. This linearised material model could not capture the non-linear behaviour or the change of pore-water pressure of soils during the pile installation. Given that the simulation was dependent on Abaqus CEL, this simplification was inevitable as E3D8R was the only applicable element in the software. Further work, however, could be conducted by developing a used-defined element incorporating the software. Alternatively, developing an efficient CEL scheme where a more complicated constitutive model of the soil can be implemented.

The elastic-perfectly plastic model was also used for the pile, excluding the potential hardening or softening plastic behaviour as the progressive deflection developed. These plastic behaviours may decelerate or accelerate the defection rate after the initial dent caused by boulder impact. The use of advanced constitutive models, however, would increase computing cost, resulting in longer computing time and perhaps less stable performance. Future studies could focus on the influence of different constitutive models, provided that an efficient computing method is available.

Boulder cracks: Another simplification was the rigid definition of the boulder, which, in reality, would present a brittle failure due to the pile impact. The computation of crack propagation in boulders needs an advanced numerical approach, such as the eXtended Finite Element Method (XFEM). The method uses the *a priori* knowledge of crack development as an enrichment solution, describing the brittle failure of a structure with prescribed crack locations. However, these advanced numerical techniques are usually time-consuming. Given the computational expense associated with the CEL approach, combining it with such methods would further increase computational costs. Further work related to this aspect has two options: incorporating XFEM with the CEL scheme in 2D models, the 3D results can be obtained using

the generalisation approach proposed in this research; alternatively, using XFEM to analyse the brittle failure of the boulder independently, and incorporating the result with the pile penetration model.

Parameter scope: The parametric study in 2D analysis involved the coupling effect of two parameters. Introducing a third parameter could potentially change the defection behaviour; however, this would necessitate tripling the number of models required for the analysis. The analysis of boulder shapes faced similar limitations. Rather than providing a quantified evaluation for elliptical and diamond boulders, discussions related to these shapes remained qualitative. Increasing the number of models could compensate for the deficiencies, resulting in a significant increase in the computing time if the current computing approach is employed. An alternative, however, could be to build a relationship between the boulder movement and the pile deflection. Therefore, the analysis will be able to focus only on the boulder movement, reducing the computing cost by eliminating the flexible piles. However, for this approach to be effective, a reliable reference model is required, which this research aims to establish.

REFERENCES

ABAQUS. (2014). 14.1.1 Eulerian analysis Products: Abaqus/Explicit Abaqus/CAE. In *Abaqus 6.14 Documentation*.

Adrian, R. J. (1991). Particle-Imaging Techniques for Experimental Fluid Mechanics. *Annual Review of Fluid Mechanics*, *23*(1), 261–304. https://doi.org/10.1146/annurev.fl.23.010191.001401

AISC. (1989). *AISC335-89: Specification for structural steel buildings, Allowable Stress Design and Plastic Design*. American Institute of Steel Construction, Inc.

Aldridge, T., Carrington, T., & Kee, N. (2005). Propagation of pile tip damage during installation. *Frontiers in Offshore Geotechnics*, 823–828. https://doi.org/10.1201/NOE0415390637.ch94

Alm, T., Snell, R. O., Hampson, K. M., & Olaussen, A. (2004). Design and Installation of the Valhall Piggyback Structures. *Offshore Technology Conference*, 3–6.

Anandavijayan, S., Mehmanparast, A., & Brennan, F. (2018). A numerical analysis of the effects of manufacturing processes on material pre-strain in offshore wind monopiles. *Procedia Structural Integrity*, *13*, 953–958. https://doi.org/https://doi.org/10.1016/j.prostr.2018.12.178

API. (2002). *Specification 2B: Specification for the Fabrication of Structural Steel Pipe* (6th ed.).

API. (2014). *API RP 2A-WSD: Planning, Designing, and Constructing Fixed Offshore Platforms - Working Stress Design* (22nd ed.).

Bakroon, M., Daryaei, R., Aubram, D., & Rackwitz, F. (2018). Multi-Material Arbitrary Lagrangian-Eulerian and Coupled Eulerian- Lagrangian methods for large deformation geotechnical problems. In A. S. Cardoso, J. L. Borges, P. A. Costa, A. T. Gomes, J. C. Marques, & C. S. Vieira (Eds.), *Numerical Methods in Geotechnical Engineering IX: Proceedings of the 9th European Conference on Numerical Methods in Geotechnical Engineering (NUMGE 2018)* (Issue June 25-27, pp. 673–681). CRC Press.

Bakroon, M., Daryaei, R., Aubram, D., & Rackwitz, F. (2019). Numerical evaluation of buckling in steel pipe piles during vibratory installation. *Soil Dynamics and Earthquake Engineering*, *122*(July), 327–336. https://doi.org/10.1016/j.soildyn.2018.08.003

Baumgardner, J. R., & Frederickson, P. O. (1985). ICOSAHEDRAL DISCRETIZATION OF THE TWO-SPHERE*. In *SIAM J. NUMER ANAL* (Vol. 22, Issue 6). https://epubs.siam.org/terms-privacy

Benn, D. I., & Evans, D. J. A. (2010). *Glaciers & Glaciation* (2nd ed.). Hodder Education.

Benson, D. J. (1992). Computational methods in Lagrangian and Eulerian hydrocodes. *Computer Methods in Applied Mechanics and Engineering*, *99*, 235–394. https://doi.org/10.1016/0045-7825(92)90042-i

BGS. (2022, December 5). *GeoIndex Offshore Map*. British Geological Survey. https://mapapps2.bgs.ac.uk/geoindex_offshore/home.html

BOEM. (2020). *Comparison of Environmental Effects from Different Offshore Wind Turbine Foundations* [U.S. Dept. of the Interior, Bureau of Ocean Energy Management, Office of Renewable Energy Programs]. https://www.boem.gov/sites/default/files/documents/environment/Wind-Turbine-Foundations-White%0APaper-Final-White-Paper.pdf

Boyce, J. I., & Eyles, N. (2000). Architectural element analysis applied to glacial deposits: Internal geometry of a late Pleistocene till sheet, Ontario, Canada. *GSA Bulletin*, *112*(1), 98–118. http://pubs.geoscienceworld.org/gsa/gsabulletin/article-pdf/112/1/98/3385508/i0016-7606-112-1-98.pdf

Broos, E., Sibbes, R., & de Gijt, J. (2017). Widening a harbour basin, demolition of a deep sea quay wall in Rotterdam. *COME2017: Decommissioning of Offshore Geotechnical Structures*, *April*, 251–262.

BS EN 10002-1:2001. (2001). Metallic materials - Tensile testing - Part 1: Method of tests at ambient temperature. In *Metallic materials - Tensile testing* (Issue September). Europena Commitee for Standardization.

Byrne, B. W. (2011). Foundation Design for Offshore Wind Turbines. In *Geotechnique Lecture* (Issue November). https://eng.ox.ac.uk/media/9490/geotechnique_lecture_bwb_2011_web.pdf

Byrne, B. W., & Houlsby, G. T. (2015). Helical piles: An innovative foundation design option for offshore wind turbines. *Philosophical Transactions of the Royal Society A: Mathematical, Physical and Engineering Sciences*, *373*(2035). https://doi.org/10.1098/rsta.2014.0081

Cai, S., & Deeks, A. J. (2005). Axi-symmetric dynamic finite element analysis of cylindrical shells with initial distortion. *Computers and Structures*, *83*, 1834–1848. https://doi.org/10.1016/j.compstruc.2005.02.019

Calladine, C. R. (1986). Analysis of Large Plastic Deformations in Shell Structures. In B. L., F. R., & V. R. (Eds.), *Inelastic Behaviour of Plates and Shells. International Union of Theoretical and Applied Mechanics*. https://doi.org/10.1007/978-3-642-82776-1_4

Canelas, D., Fernandes, I., & Lopes, M. D. G. (2018). Use of Fall Cone Test for the determination of undrained shear strength of cohesive soils. *MATEC Web of Conferences*, *251*. https://doi.org/10.1051/matecconf/201825104067

Carrara, S., Alves Dias, P., Plazzotta, B., & Pavel, C. (2020). *Raw materials demand for wind and solar PV technologies in the transition towards a decarbonised energy system* [JRC Publications Office of the European Union]. https://doi.org/10.2760/160859

Clarke, B. G. (2018). The engineering properties of glacial tills. *Geotechnical Research*, *5*(4), 262–277. https://doi.org/10.1680/jgere.18.00020

DESNZ. (2023). *UK Energy Trends July to September 2023* (Issue September) [Department for Energy Security and Net Zero]. https://www.gov.uk/government/statistics/energy-trends-section-6-renewables

DNV. (2016). *DNVGL-ST-0126 - Support structures for wind turbines* (Issue April). Det Norske Veritas Germanischer Lloyd.

DNV. (2018). *Classification Notes No. 30.1 Buckling Strength Analysis of Bars and Frames , and Spherical Shells*.

DNV. (2019). *DNVGL-RP-C202 Recommended Practice: Buckling strength of shells*.

DNV. (2023a). *DNV-CG-0128 Class guideline: Buckling* (Issue December).

DNV. (2023b). *ENERGY TRANSITION OUTLOOK 2023: A global and regional forecast to 2050* [DNV]. https://www.dnv.com/energy-transition-outlook/index.html

Dreimanis, A. (1989). Tills: their genetic terminology and classification. In R. P. Goldthwait & C. L. Matsch (Eds.), *Genetic Classification of Glacigenic Deposits* (pp. 17–84).

Dunne, H. P. (2017). *Finite Element Limit Analysis of Offshore Foundations on Clay*. University of Oxford.

Durning, P., & Rennie, I. (1978). Determining pile capacity and pile driveability in hard, overconsolidated Noth Sea clay. *SPE European Petroleum Conference*.

Elkhouly, A. (2020). *The Analysis of Different Pile Types for Use in Marine Infrastructure*. NERKEN SCHOOL OF ENGINEERING.

EN 1993-1-6. (2007). *Eurocode 3 - Design of steel structures - Part 1-6: Strength and Stability of Shell Structures*. European Committee for Standardisation.

EN1993-1-1. (2005). *Eurocode 3: Design of steel structures - Part 1-1: General rules and rules for buildings*.

Erbrich, C. T., Barbosa-Cruz, E., & Barbour, R. (2011). Soil-pile interaction during extrusion of an initially deformed pile. *Symposion on Frontiers of Offshore Geotechnics II*, 489–494. https://doi.org/doi:10.1201/b10132-62 10.1201/b10132-62

Folk, R. L. (1959). Practical Petrographic Classification of Limestones. *AAPG Bulletin*, *43*(1), 1–38. https://doi.org/10.1306/0BDA5C36-16BD-11D7-8645000102C1865D

Gargarella, P. (2018). Numerical study of flint/boulder behaviour during pile driving. In *POLITECNICO DI TORINO*. Politecnico di Torino, Collegio di Ingegneria Civile.

Gerwick Jr., B. C. (1968). PRESTRESSED CONCRETE PILES. *PCI Journal*, *13*(5), 66–93. https://doi.org/10.15554/pcij.10011968.66.93

Gourvenec, S., Randolph, M., & Kingsnorth, O. (2006). Undrained Bearing Capacity of Square and Rectangular Footings. *International Journal of Geomechanics*, *6*(3), 147–157. https://doi.org/10.1061/(asce)1532-3641(2006)6:3(147)

GWEC. (2023a). *Global Offshore Wind Report 2023* [Global Wind Energy Council]. https://gwec.net

GWEC. (2023b). Global Wind Report 2023 [Global Wind Energy Council]. In *GWEC*. https://gwec.net/wp-content/uploads/2023/04/GWEC-2023_interactive.pdf

Hamann, T., Qiu, G., & Grabe, J. (2015). Application of a Coupled Eulerian-Lagrangian approach on pile installation problems under partially drained conditions. *Computers and Geotechnics*, *63*, 279–290. https://doi.org/10.1016/j.compgeo.2014.10.006

Holeyman, A., Peralta, P., & Charue, N. (2015). Boulder-soil-pile dynamic interaction. In Meyer (Ed.), *Frontiers in Offshore Geotechnics III* (pp. 563–568). Taylor & Francis Group.

Holeyman, A., Whenham, V., Peralta, P., Ballard, J.-C., & Pulukul, S. C. (2020). VIBRATORY INSTALLATION STUDY OF A MONOPILE IN DENSE SAND. *ASME 2020 39th International Conference on Ocean, Offshore and Arctic Engineering OMAE2020*.

Houlsby, G. T., & Puzrin, A. M. (1999). The bearing capacity of a strip footing on clay under combined loading. *Proceedings of the Royal Society A: Mathematical, Physical and Engineering Sciences*, *455*(1983), 893–916. https://doi.org/10.1098/rspa.1999.0340

HSE. (2001). *A study of pile fatigue during driving and in-service and of pile tip integrity*.

ISO. (2020). *ISO 19902 INTERNATIONAL STANDARD: Petroleum and natural gas industries - Fixed steel offshore structures* (2nd ed.).

Jiang, Z. (2021). Installation of offshore wind turbines: A technical review. *Renewable and Sustainable Energy Reviews*, *139*. https://doi.org/https://doi.org/10.1016/j.rser.2020.110576

Ko, J., Jeong, S., & Kim, J. (2017). Application of a Coupled Eulerian-Lagrangian technique on constructability problems of site on very soft soil. *Applied Sciences (Switzerland)*, *7*(1080). https://doi.org/10.3390/app7101080

Kong, D. (2015). *Large displacement numerical analysis of offshore pipe-soil interaction on clay*. University of Oxford.

Kong, D., Martin, C. M., & Byrne, B. W. (2017). Modelling large plastic deformations of cohesive soils using sequential limit analysis. *International Journal for Numerical and Analytical Methods in Geomechanics*, *41*(18), 1781–1806. https://doi.org/10.1002/nag.2700

Kramer, G. (1996). *Investigation of the Collapse Mechanism of Open Ended Piles during Installation*. *June*, 105.

Kyriakides, S., & Babcock, C. D. (1982). Experimental Determination of the Propagation Pressure of Circular Pipes. *American Society of Mechanical Engineers (Paper)*, *103*(November 1981).

Le, V. H., Akdag, C. T., Aubram, D., Daryaei, R., & Rackwitz, F. (2023, October). Experimental investigations on monopile tip buckling during impact driving. *Innovative Geotechnologies for Energy Transition SUT 2023*. https://www.researchgate.net/publication/374194655

Li, J., Li, Z., Jiang, Y., & Tang, Y. (2022). Typhoon Resistance Analysis of Offshore Wind Turbines: A Review. *Atmosphere*, *13*(3), 451. https://doi.org/https://doi.org/10.3390/atmos13030451

Martin, C. M. (1994). Physical and numerical modelling of offshore foundations under combined loads. In *University of Oxford* (p. 306).

Martin, C. M. (2011). The use of adaptive finite-element limit analysis to reveal slip-line fields. *Geotechnique Letters*, *1*(2), 23–29. https://doi.org/10.1680/geolett.11.00018

Merritt, A. S., Schroeder, F. C., Jardine, R. J., Stuyts, B., Cathie, D., & Cleverly, W. (2012). Development of pile design methodology for an offshore wind farm in the north sea. *Offshore Site Investigation and Geotechnics 2012: Integrated Technologies - Present and Future, OSIG 2012*, *i*, 439–447.

Mourillon, N. K. N. (2015). *Stability analysis quay structure at the Amazonehaven port of Rotterdam*. Delft University of Technology.

Nietiedt, J. A. (2022). *Pile Tip Damage and Extrusion Buckling Assessment through Centrifuge Modelling and Large Deformation Finite Element Analysis* (Issue March). The University of Western Australia.

Nietiedt, J. A., Randolph, M. F., Doherty, J. P., & Gaudin, C. (2022). Numerical assessment of tip damage during pile installation in boulder rich soils. *Geotechnique*. https://doi.org/10.1680/jgeot.21.00395

Noh, W. F. (1963). *CEL: A time-dependent, two-space-dimensional, coupled Eulerian-Lagrange code (No. UCRL-7463)*. https://www.osti.gov/servlets/purl/4621975

Norsok. (2012). *N-004 NORSOK STANDARD: Design of steel structures*.

OWIC. (2019). *The UK Offshore Wind Industry : Supply Chain Review* (Issue January).

Palmieri, F., Mclennan, D., Ciruela-Ochoa, F., Cunningham, A., Go, J., Morrison, P., Tejada, C., Perikleous, G., Brandt, J., & Lubek, M. (2023). hree-dimensional finite element modelling to assess the damage due to boulder impact during pile installation. In Zdravkovic L, Kontoe S, & Taborda DMGTsiampousi A (Eds.), *10th European Conference on Numerical Methods in Geotechnical Engineering*. https://doi.org/10.53243/NUMGE2023-330

Prandtl, L. (1921). Eindringungsfestigkeit und Festigkeit von Schneiden. *Angew. Math. U. Mech*, *1*(15), 15–20.

Qiu, G., Henke, S., & Grabe, J. (2011a). Application of a Coupled Eulerian-Lagrangian approach on geomechanical problems involving large deformations. *Computers and Geotechnics*, *38*(1), 30–39. https://doi.org/10.1016/j.compgeo.2010.09.002

Qiu, G., Henke, S., & Grabe, J. (2011b). Application of a Coupled Eulerian-Lagrangian approach on geomechanical problems involving large deformations. *Computers and Geotechnics*, *38*(1), 30–39. https://doi.org/10.1016/j.compgeo.2010.09.002

Randolph, M. F. (2018). Potential Damage to Steel Pipe Piles During Installation. *IPA News Letter*, *3*(1), 3–10.

Randolph, M., & Gourvenec, S. (2011). Offshore geotechnical engineering. In *Offshore Geotechnical Engineering*. Spon Press.

RenewableUK. (2016). *Offshore Wind Energy powering the UK since 2000: Owners' Workshop Manual*.
RenewableUK. (2022). *Offshore Wind Project Timelines 2022*. www.RenewableUK.com
Richards, I. (2019). *Monopile foundations under cyclic lateral loading*. University of Oxford.
Richards, I. A., Bransby, M. F., Byrne, B. W., Gaudin, C., & Houlsby, G. T. (2021). Effect of Stress Level on Response of Model Monopile to Cyclic Lateral Loading in Sand. *Journal of Geotechnical and Geoenvironmental Engineering*, *147*(3), 04021002. https://doi.org/10.1061/(asce)gt.1943-5606.0002447
Rooz, A. F. H., & Hamidi, A. (2019). A numerical model for continuous impact pile driving using ALE adaptive mesh method. *Soil Dynamics and Earthquake Engineering*, *118*(December 2018), 134–143. https://doi.org/10.1016/j.soildyn.2018.12.014
Rystad Energy. (2023). *The State of the European Wind Energy Supply Chain* (Issue April). Rystad Energy, Wind Europe.
Salgado, R., Lyamin, A. V., Sloan, S. W., & Yu, H. S. (2004). Two- and three-dimensional bearing capacity of foundations in clay. *Géotechnique*, *54*(5), 297–306. https://doi.org/10.1680/geot.54.5.297.46720
Sherman, D. R. (1977). *Tentative Criteria for Structural Applications of Steel Tubing and Pipe*. Commitee of Steel Pipe Producers, American Iron and Steel Insititute.
Song, G. (2020). *The use of protective structures to reduce tunnelling induced damage to buildings* (Issue September). The University of Nottingham.
Stanier, S. A., Dijkstra, J., Leśniewska, D., Hambleton, J., White, D., & Muir Wood, D. (2016). Vermiculate artefacts in image analysis of granular materials. *Computers and Geotechnics*, *72*, 100–113. https://doi.org/10.1016/j.compgeo.2015.11.013
Steel, W. J. M., & Spence, J. (1983). On propagating buckles and their arrest in sub-sea pipelines. *Proceedings of the Institution of Mechanical Engineers, Part A: Journal of Power and Energy*, *197*(2), 139–147. https://doi.org/10.1243/PIME_PROC_1983_197_015_02
Stevens, R. F., Westgate, Z., & Kocijan, J. (2019). Assessing the Pile Driving Risk Due to the Presence of Boulders. *Offshore Technology Conference*, *May*. https://doi.org/10.4043/29668-ms
Taras, A., Nseir, J., & Boissonnade, N. (2014). Cylindrical shell buckling strength according to the "overall method" of Eurocode 3 - Background and applicability to the design of high strength steel circular hollow sections. *Structural Stability Research Council Annual Stability Conference, SSRC2014*, 446–465.
The Crown Estate. (2023). *Offshore wind report 2022*.
Timoshenko, S., & Gere, J. M. (1961). *Theory of elastic stability* (2nd ed.). McGraw-Hill.
Timoshenko, S. P., & Gere, J. M. (1985). *Theory of elastic stability* (2nd ed.). McGraw-Hill Book Company, Inc.
U.S. Department Of Energy. (2023). *Offshore Wind Market Report: 2023 Edition*.
Wheeler, L. N., Take, A., & Hoult, N. A. (2016). Measurement of rail deflection on soft subgrades using DIC. *Proceedings of the Institution of Civil Engineers: Geotechnical Engineering*, *169*(5), 383–398. https://doi.org/10.1680/jgeen.15.00171
White, D. J., Take, W. A., & Bolton, M. D. (2003). Soil deformation measurement using particle image velocimetry (PIV) and photogrammetry. *Geotechnique*, *53*(7), 619–631. https://doi.org/10.1680/geot.2003.53.7.619
White, D. J., Take, W. A., Bolton, M. D., & Munachen, S. E. (2001). A deformation measurement system for geotechnical testing based on digital imaging, close-range photogrammetry, and PIV image analysis. *15th International Conference on Soil Mechanics and Geotechnical Engineering*, 539–542. http://www-civ.eng.cam.ac.uk/geotech_new/people/bolton/mdb_pub/109_ICSMGE_2001_proc_539_542.pdf
White, D., Take, A., & Bolton, M. (2001). Measuring soil deformation in geotechnical models using digital images and PIV analysis. *10th International Conference on Computer Methods and Advances in Geomechanics*, *May*, 997–1002. http://www-civ.eng.cam.ac.uk/geotech_new/people/bolton/mdb_pub/99_IACMAG_2001_Proc_997_1002.pdf
Wierzbicki, T., & Bhat, S. U. (1986). Initiation and Propagation of Buckles in Pipelines. *International Journal of Solids and Structures*, *22*(9), 985–1005.
Wind Europe. (2021). *Offshore wind in Europe - Key trends and statistics 2020*.
Wind Europe. (2023). *Offshore wind energy 2023 mid-year statistics* (Issue August).
Xiao, Z., Fu, D., Zhou, Z., Lu, Y., & Yan, Y. (2019). Effects of strain softening on the penetration resistance of offshore bucket foundation in nonhomogeneous clay. *Ocean Engineering*, *193*(March), 106594. https://doi.org/10.1016/j.oceaneng.2019.106594
Zhang, Y. D., Tan, T. S., & Leung, C. F. (2005). Application of particle imaging velocimetry (PIV) in centrifuge testing of uniform clay. *International Journal of Physical Modelling in Geotechnics*, *1*, 15–26.